Modelling and efficient characterization of enzyme-mediated response to antibiotic treatments

Virgile Andreani

INSTITUT POLYTECHNIQUE DE PARIS

NNT : 2020IPPAX108

Thèse de doctorat

Modelling and Efficient Characterization of Enzyme-Mediated Response to Antibiotic Treatments

Thèse de doctorat de l'Institut Polytechnique de Paris
préparée à l'École polytechnique

École doctorale n°626 École doctorale de l'Institut Polytechnique de Paris (ED IPP)
Spécialité de doctorat : Physique

Thèse présentée et soutenue à Paris, le 17 décembre 2020, par

VIRGILE ANDREANI

Composition du Jury :

Marie Doumic Directrice de recherche, Inria, CNRS and Sorbonne University	Présidente du jury
Rosalind Allen Professor of Biological Physics, Edinburgh University	Rapportrice
Tobias Bollenbach Professor of Biological Physics, Cologne University	Rapporteur
Philippe Glaser Directeur de recherche, Institut Pasteur	Examinateur
Lingchong You Professor of Biomedical Engineering, Duke University	Examinateur
Grégory Batt Directeur de recherche, Inria and Institut Pasteur	Directeur de thèse

MODELLING AND EFFICIENT CHARACTERIZATION OF ENZYME-MEDIATED RESPONSE TO ANTIBIOTIC TREATMENTS

VIRGILE ANDREANI

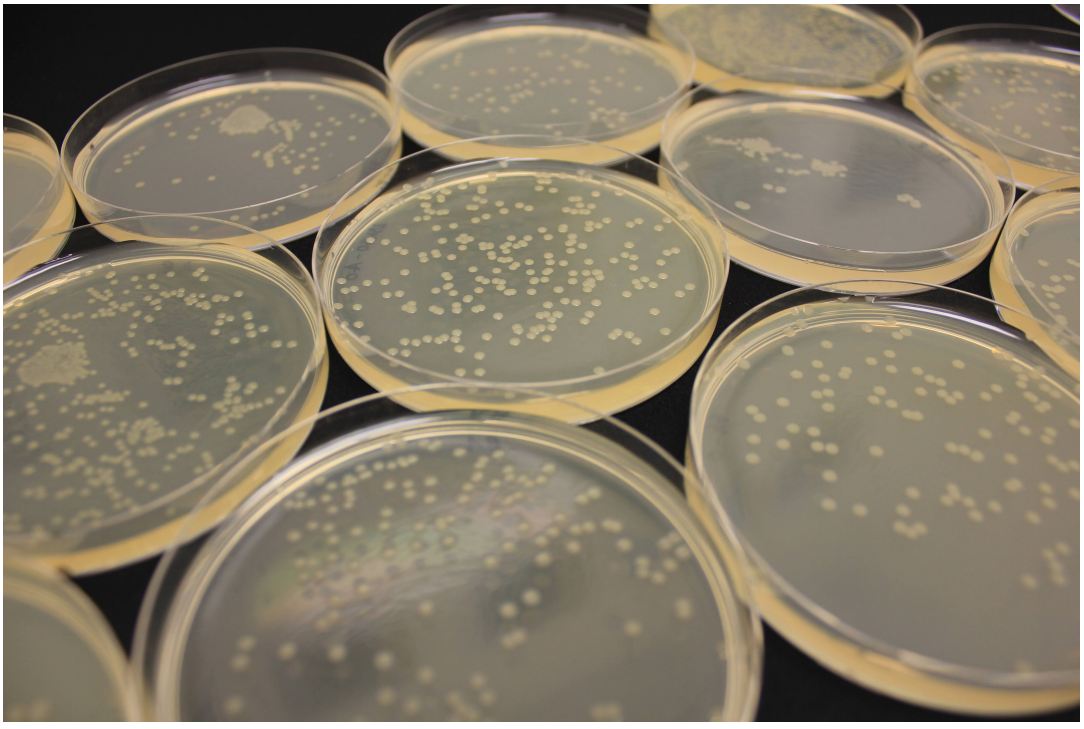

December 2020

1 http://creativecommons.org/licenses/by-nc/4.0/

Considerate la vostra semenza;
fatti non foste a viver come bruti,
ma per seguir virtute e canoscenza.

— Dante Alighieri, *Inferno*

À mon grand-père, Gérard Pertica

ACKNOWLEDGEMENTS

I would like to thank here all the people who helped me or were close to me during these few years.

Tout d'abord, mon directeur de thèse Grégory Batt que j'ai le plaisir de connaître depuis mon master. Sa curiosité, sa passion et sa rigueur ont favorisé la grande qualité de nos échanges scientifiques. Le fait que nous ayons eu des parcours différents a quant à lui contribué à leur richesse. J'ai eu la chance de bénéficier avec lui de conditions de travail privilégiées, et sa confiance et son style de supervision m'ont permis de m'aventurer dans les directions de recherche qui m'intéressaient le plus, ce dont je lui suis très reconnaissant. Il m'a également accordé la supervision de deux étudiants en stage de master, expérience dont j'ai beaucoup appris.

As put by Claude Lévy-Strauss, "*The scientist is not a person who gives the right answers, he is one who asks the right questions.*" In this respect, I had the great chance to meet Lingchong You and Hannah Meredith at the beginning of my thesis, who introduced me to the field and asked me the right questions. Lingchong kindly welcomed me for two work visits at Duke University, and helped to guide my early work on this subject. I also would like to thank specially Hannah, who I had the real pleasure to work with during the first couple of years. I am convinced that there could not have been a better start for me and this project. Hannah gave her time generously to teach me basic biology and train me in lab work. Moreover, all the time spent working together, in the same lab or an ocean apart, trying to make sense of our data and models, represent to me what an ideal collaboration should be.

J'aimerais remercier particulièrement Philippe Glaser et son équipe, notamment Adriana, Isabelle et Nicolas, qui ont tous donné de leur temps pour répondre à mes questions parfois naïves sur les bactéries, les antibiotiques, les techniques pour les étudier, et qui m'ont également donné accès à leur catalogue de souches.

I would also like to thank warmly the rest of my jury: the president Marie Doumic, and the two reviewers Rosalind Al-

len and Tobias Bollenbach, whose works have been sources of inspiration for me all through these years.

Ce travail a été réalisé au sein de deux équipes successives : Lifeware, équipe-projet Inria, puis Inbio, équipe mixte Inria et Institut Pasteur. Étant un des doctorants qui ont connu la transition de Lifeware à InBio, j'ai eu le plaisir de bénéficier des discussions d'informatique théorique du bâtiment 8 de Rocquencourt, un peu éloignées de ce que j'ai fait par la suite mais pas trop : comme pour faire la liaison, le bâtiment 8 de l'Institut Pasteur fut le premier bâtiment qui a hébergé l'équipe InBio après sa séparation avec Lifeware. L'équipe Commands est également une équipe Inria que je peux difficilement considérer comme séparée compte tenu des collaborations et liens étroits que nous entretenons. Cela a été un vrai plaisir de partager bureaux, labo, repas, et discussions scientifiques et autres pendant toutes ces années avec toutes ces personnes. I would also like to thank Shuang Li and Albin Salazar, two master students whose projects I was given the chance to supervise.

Even if we were not directly in contact during my thesis, I would like to address special thanks to some of my former teachers and mentors, who were the main contributors to the development of my set of skills and interests, notably Stéphan Fauve, Werner Krauth, Jean Vuillemin and Thomas Monz.

Je n'oublie pas les amis qui m'ont aidé à avancer, prendre du recul ou me changer les idées : les fidèles d'IRC Aurore, Élie et Thomas, mes redoutables adversaires puis coéquipiers de concours de programmation Rayan et Yoann, mais aussi Anna, Basile, Damien, Étienne, Florent, Gianluca, Guillaume, Iris, Julien, Patricia, Pierre(s), Ze, et toutes les autres personnes qui ont joué un rôle important et particulier auprès de moi ces dernières années.

J'adresse des remerciements tout particuliers à mes sœurs et mes parents pour leur amour et leur soutien indéfectibles. J'ai eu la chance de grandir proche de mes grands-parents, qui ont toujours tenu une place particulière dans ma vie et sans lesquels je serais très différent aujourd'hui. Je veux saluer aussi ma famille un peu plus éloignée, dont je percevais également l'attention bienveillante.

Enfin, ces deux dernières années auraient été très différentes sans Anđela, qui m'a soutenu, aidé, encouragé, fait réfléchir et rêver plus que je n'aurais pensé possible. Merci de partager ton monde avec le mien.

RÉSUMÉ

La résistance aux antibiotiques est reconnue comme l'un des plus grands dangers contemporains de santé publique. Dans les laboratoires hospitaliers, la susceptibilité d'une souche bactérienne à un antibiotique donné est quantifiée par sa Concentration Minimale Inhibitrice (CMI) : la dose minimale d'antibiotique nécessaire pour inhiber la croissance de la souche pendant 24 heures. Cette valeur joue un rôle central dans les décisions de traitements prises par le personnel soignant.

Or, la CMI est une mesure reposant sur un unique point de temps, et ne peut pas rendre compte de tous les aspects de la réponse d'une souche à un traitement. Pourrait-on obtenir une évaluation plus informative de la résistance d'une souche à un antibiotique, en exploitant sa courbe de croissance entière ? Pourrait-on également faire en sorte que ce diagnostic soit réalisable dans un environnement hospitalier, où la densité optique de la culture est souvent la seule observable disponible ? Ce problème est complexe, notamment parce que les antibiotiques β-lactams provoquent la filamentation des cellules, ce qui décorrèle la densité optique de la culture du nombre de cellules vivantes qu'elle contient.

Dans cette thèse, nous développons un modèle mathématique de la réponse de populations bactériennes à des β-lactams, qui rassemble les différents types de résistance (résistance, tolérance, résilience) au sein d'un même cadre. Considérant les trois échelles : moléculaire, de la cellule et de la population, ce modèle offre des prédictions simultanées de la densité optique et du nombre de cellules, ainsi que de leur distribution de longueurs. Son cœur est constitué d'un modèle dit de croissance-fragmentation : une équation aux dérivées partielles considérant explicitement la distribution des tailles des cellules et son évolution en réponse à l'antibiotique qui déclenche leur filamentation. Or, le modèle à dérivées partielles n'est pas idéal pour l'optimisation numérique, et notamment pour l'inférence de paramètres. Nous décrivons donc le passage à un modèle compagnon à équations différentielles ordinaires, qui se prête mieux à une calibration efficace. Ce passage est réalisé à l'aide d'approximations soigneuses des moments partiels de la dis-

tribution des longueurs des cellules. On montre alors que les deux modèles, à dérivées partielles et ordinaires, satisfont quantitativement diverses observations empiriques réalisées sur des populations bactériennes, et bien connues dans le domaine.

La calibration de ce modèle sur un ensemble d'isolats cliniques a été rendue possible par l'analyse en rétro-ingénierie d'un lecteur de plaques commercial et le développement d'un pilote open source pour celui-ci, nous permettant d'en faire un usage programmatique, ainsi que par le choix d'algorithmes d'optimisation numérique efficaces et robustes. Nous montrons que les valeurs estimées de plusieurs des paramètres du modèle peuvent être expliquées par la présence de gènes et de mutations facteurs de résistance. Alors que tous les paramètres du modèle sont en principe identifiables, la plupart des isolats cliniques n'expriment qu'un sous-ensemble des comportements autorisés par le modèle. Par conséquent, les valeurs estimées pour les paramètres inutilisés par une souche donnée sont aléatoires et inutilisables. Nous proposons une méthode pour regrouper les souches similaires, malgré la présence de telles non-identifiabilités, en utilisant les intervalles de confiance des valeurs estimées plutôt que les valeurs elles-mêmes. Nous observons alors l'émergence de trois classes distinctes : sensibles, tolérantes et résilientes, et résistantes. En comparaison avec le système classique SIR (susceptibles, intermédiaires, et résistantes), ces classes dégagent des explications plus riches du comportement des isolats, et permettent également une exploitation directe pour du traitement optimal.

CONTENTS

ACRONYMS

API	Application Programming Interface
CAT	Collective Antibiotic Tolerance
CDC	Centers for Disease Control
CFU	Colony Forming Unit
CMA-ES	Covariance Matrix Adaptation Evolution Strategy
CV	Coefficient of Variation
EDTA	Etylenediaminetetraacetic acid
ESBL	Extended Spectrum β-lactamase
LHS	Latin Hypercube Sampling
MBRT	Methylene Blue Dye Reduction Test
MDK	Minimum Duration for Killing
MIC	Minimum Inhibitory Concentration
MLE	Maximum Likelihood Estimator
OD	Optical Density
ODE	Ordinary Differential Equation
PBP	Penicilin Binding Protein
PCA	Principal Component Analysis
PDE	Partial Differential Equation
PK/PD	Pharmacokinetic/Pharmacodynamic
scMIC	single-cell MIC
SIR	Sensitive / Intermediate / Resistant
t-SNE	t-distributed Stochastic Neighbour Embedding

1 INTRODUCTION

1.1 MOTIVATION

Antibiotic resistance is widely recognized as one of the biggest threats to global health. The first strain resistant to penicillin was discovered in 1942, only one year after the release of the drug. Since then, not one antibiotic was spared by resistant strains, to a point where antibiotic resistance has become a norm rather than an exception among pathogens, a situation unlikely to ever change. The United States public health institute (Centers for Disease Control (CDC)) even refers to our times as a "post-antibiotic era" (Centers for Disease Control and Prevention (U.S.) 2019).

To put this number into perspective, over 1 million people died of COVID-19 this year.

Antibiotic resistance claims more than 700 000 lives every year, globally, and this toll is estimated to surge in the next years, reaching 10 million lives per year by 2050 ("Tackling Drug-Resistant Infections Globally: Final Report and Recommendations" 2016). This plague does not know continents, borders, age, health or immunity: it threatens literally everyone, everywhere, at all time. The discovery of new antibiotics, either fortuitous or deliberate, seems to become increasingly challenging as time passes. An important concept appeared in response to this assessment is antibiotic stewardship. In the words of the CDC, it is an effort to measure and improve how antibiotics are prescribed and used.

Antibiotic treatment is indeed a double-edged sword. While the purpose of antibiotic treatments is to decrease the bacterial charge of infections, a side effect of antibiotic exposure is a selection pressure driving the evolution of mutations decreasing the susceptibility of the bacteria to the drug (Greulich, Waclaw, and Allen 2012; Baym et al. 2016). This puts clinicians in the delicate situation of trying to fill the two objectives, not always compatible, of healing a person of a specific infection, and protecting the population by preventing the emergence of resistant mutants. Guidelines are published and regularly updated by public health agencies, based on a metric quantifying the resistance of a strain, the Minimum Inhibitory Concentration (MIC):

the minimal antibiotic dose needed to inhibit the growth of a given cell inoculum for 24 hours (Gould and MacKenzie 2002).

However, antibiotic response is multidimensional, and quantifying it only with the 24-hour time point is a gross approximation (Brauner et al. 2016; Balaban et al. 2019). Indeed, under the umbrella term "antibiotic resistance," one traditionally separates the possible responses in different components: resistance, tolerance, persistence, and resilience. *Resistance*, strictly speaking, is the ability of strains to grow under high antibiotic doses. Resistant strains under high antibiotic dose behave in similar ways than without antibiotic, in general thanks to mutations making their constituents much less sensitive to the drug. *Tolerant* strains, however, are defined by the ability to survive a transient exposure to antibiotic. The antibiotic might affect them, but not kill them instantly, such that their growth can restart once the antibiotic is removed. *Persistence* is an extreme case of tolerance, and caused by a genetically identical, but phenotypically different, subpopulation of cells with an almost zero growth rate. Not growing often confers a protection from the antibiotic. Non-growing cells are then virtually immortal. By unclear mechanisms, persisters are formed, and woken up stochastically (Harms, Maisonneuve, and Gerdes 2016). If a persister wakes up after the antibiotic was removed, it can grow and reconstitute the cell population. Finally, *resilience*, a term borrowed from population ecology, refers to the capacity of a population to recover from a perturbation. Population regrowth being only possible after the removal of the antibiotic, mechanisms implemented by the cells to actively degrade the antibiotic can be understood as participating in the resilience of the population. Starting here, in this document, "resistance" alone will refer to this specific definition, but "antibiotic resistance" has to be understood as the umbrella term.

The variety of possible responses makes it challenging to identify quickly and accurately the efficiency of a given antibiotic on a given strain. Comparing the MIC with two tabulated breakpoints defined by the public health agencies, one can assign to each pair strain/antibiotic a label "S" for Sensitive, "I" for Intermediate, or "R" for Resistant. The antibiogram, a standard technique used in all clinical laboratories around the world, also delivers the same information. The Sensitive / Intermediate / Resistant (SIR) classification is the basis of decision for choosing an appropriate antibiotic to treat a given infection. However, as the "S" treatment options become increasingly rarer, clinicians

are driven to start considering "I" options as possible treatment opportunities, requiring stronger doses.

One of the most used families of antibiotics is β-lactams. They contain antibiotics such as penicillin, ampicillin, amoxicillin, or cefotaxime. They are known to interfere with the cell wall formation, which eventually leads to cell lysis. The main bacterial defence mechanism against this type of antibiotic is the expression of an enzyme able to degrade the antibiotic, called β-lactamase. β-lactamases are known to be active both in the periplasm of cells, and in the environment, where they are released upon cell lysis. Outside the cells, the enzymes continue to degrade the antibiotic to the benefit of other cells. This mutualistic mechanism is called Collective Antibiotic Tolerance (CAT).

This complex dynamics is the consequence of the interplay between three fundamental scales. The lowest level is that of biochemical molecular reactions between the antibiotic and the molecules that it binds to, targets or β-lactamases. The middle level is that of the cell itself, experiencing direct consequences of the biochemical level ranging from changes in growth rate or cell morphology, to lysis. Finally, the highest level is that of the cell population, and is necessary to explain CAT.

Quantifying this system with only the MIC is not fully satisfying. Indeed, although low MICs (category "S") lend themselves well to treatment, intermediate and high MICs (categories "I" and "R") do not really describe the behaviour of the strains, because the MIC is a final time point. We lack an understanding of the dynamics of "I" and "R" strains, which is why treatments in "I" conditions are often gambles. Our assessment is that neither the MIC nor the SIR system are explainable, and that the antibiogram is possibly not appropriate any more for the post-antibiotic era. However, the full 24-hour dynamics of a culture of cells treated with antibiotics is much richer than just its final state.

Acquiring a full growth curve in a clinical setting can be done with an automated optical plate reader: alternating incubation and measurement phases, this device can record the Optical Density (OD) of a number of cell cultures (typically 96) every couple of minutes over several days, the OD of a cell culture being considered approximately proportional to its biomass. Acquiring other types of data, like microscopy or growth curve in cell numbers, seems too costly either in equipment or time for a typical hospital laboratory. Despite this, the data contained in 24 hours of optical density measurements "only" remains much

richer than just its final point, thus, the exploitation of an optical plate reader became our model of data acquisition.

However, we quickly discovered a modelling barrier preventing the use of this data. As we saw, β-lactams, through the disruption of cell wall related activity, cause drastic changes in the cell morphology. These changes result in a decorrelation of biomass and number of cells: as a matter of fact, the ratio between the observed optical density and the number of living cells can change by 3 to 4 orders of magnitude over the first few hours of an experiment. To our knowledge, inferring cell numbers from optical density data in presence of β-lactam-induced cell filamentation has never been successfully addressed.

In summary, motivated by the rise of antibiotic resistance imposing to treat cells with antibiotics towards which they are ever less susceptible, we resolved to try improving the explainability of the response of strains to antibiotics. *Could we get a more informative assessment of antibiotic resistance by exploiting the whole growth curve?* Importantly, we should limit ourselves to OD data, since only this is directly applicable in a clinical setting.

1.2 APPROACH

The data that we want to use is both rich and poor. Rich, because it is a full 24-hour optical density growth curve. Poor, because it shows only one surface view of a system with much more depth. In fact, we are actually facing an information challenge, and our capacity to overcome the modelling challenges will be dependent on the quality of the data. The necessary first step will then be to ensure excellent experimental conditions allowing the acquisition of informative data over long time periods. Notably, the automation of data acquisition is a key factor of experimental reproducibility.

Secondly, we need to acquire a global picture of the behaviour of the system, at all scales involved: molecular, cell-level and population. The best way to assess our knowledge about a system is to recreate it. Mathematical modelling is the framework of choice to create and simulate systems. We will then build a model of antibiotic resistance, ideally sufficiently generic to be applied to a large class of antibiotics and isolates. To stay relevant to clinical measurements, we have to consider that the input of this model could exclusively consist in OD growth curves.

Thus, the model needs to bridge the apparent decorrelation between the OD and the number of cells.

To challenge the model and verify both its generality and practical use, we need to assemble samples of various pathogenic strains as diverse as possible. The automated experimental platform built for this purpose will help carry out quantitative measurements on these strains, while a robust, versatile and efficient optimization framework will help fit the model to the data. In this way, we could describe strains by their associated model parameters, instead of just the value of the MIC.

Once confirmed that the mathematical model is a reliable description of the response of the strains to antibiotic treatments, we can use it to answer the original question: How much information can we get by exploiting the full OD response? More specifically, can we make sense of parameter values, better than of the MIC? Could we propose a classification that is more exploratory and more explainable than SIR? And what could we learn from the model about the respective roles of resistance, tolerance, resilience or persistence in the responses of the strains to treatment?

1.3 CONTRIBUTIONS

This thesis presents several methodological and theoretical contributions made on the way to answer these questions. These developments were both inspired and validated by original data collected from a collection of clinical isolates.

We propose to our knowledge the first model of bacterial resistance, tolerance and resilience to β-lactams able to predict simultaneously the number of cells and optical density of a cell culture submitted to complex antibiotic treatments. This Partial Differential Equation (PDE) model, based on a growth-fragmentation equation, describes the evolution of the length distribution of the population of cells. It relies on a limited number of simple biological hypotheses, backed up by both data and literature. The PDE model is not very practical for numerical optimization, notably for parameter inference. We therefore describe the passage to a companion Ordinary Differential Equation (ODE) model, involving careful approximations of the partial moments of the first model. Both of these models behave as expected by several well-known phenomenological observations in the β-lactam literature.

The experimental validation of these models was performed through its application to a collection of pathogenic clinical isolates of *E. coli*. The experimental conditions were carefully choosen to create highly informative experiments. Notably, we propose methods improving the reliability of cell counting with Colony Forming Units (CFUs), and of plate reader experiments. First, we describe a bayesian method for cell counting allowing the computation of estimates of cell number and confidence intervals from any number and combination of dilutions and platings, starting with one unique count. Second, we show how to reverse engineer a commercial plate reader, in order to develop an Application Programming Interface (API) offering a full programmatic control of the machine through a custom Python library, `platerider`.

For our work, assessing the identifiability of the model is critical. After consideration of the noise model of the observation process, following the approach of A. Raue et al. (2009), we demonstrate with a profile likelihood analysis that it is possible to recover most parameters of the model on a simulated dataset. For this, we had to give great care to the robustness of the global optimization problems, as well as to the efficiency of local optimization problems.

Finally, we show that our approach is superior to the standard MIC metric and SIR classification with respect to understanding and being able to predict both intuitively and quantitatively the response to a treatment *in vitro*. On real datasets, we found a good agreement between measurable predictions of the model and experiments, even beyond OD (microscopy, cell number). We also found a tight agreement between the parameters of the model and the antibiotic resistance genes contained in each cell's genome. This inspires confidence in the fact that the inferred model parameters are a mapping of concrete biological properties of the strains. We also propose a clustering method robust to unidentifiabilities that allows to separate the collection into three classes of strains of noticeably different phenotypes, and responsive to different treatment strategies. The three phenotypes can be described as sensitive, tolerant/resilient and resistant. The model itself has value, since it contributes to the understanding of these three separated classes as three parts of a shared continuum. Notably, the rate of cell death depends only on their length, which makes tolerance by filamentation an essential factor of the effectiveness of the treatment.

1.4 OUTLINE

After this introduction, the second chapter (2) describes the experimental conditions that we engineered in order to make experiments as reproducible as possible. After discussions on the medium composition, the influence of preculture, and the steps taken to avoid excessive evaporation, we discuss the calibration of the plate reader. Then, we introduce the bayesian cell counting method. In a second part, we present the process of reverse-engineering of the plate reader and introduce the custom driver `platerider`.

The third chapter (3) is dedicated to the models. After a theoretical introduction on the necessary biological notions, we derive the growth-fragmentation model, with the detail of each of its constituents. In the following part, we derive its companion ODE model. This involves the extraction of partial moments from the main model, which we do by partially solving it in appropriate conditions. We then demonstrate the agreement of the model with several well-known observations.

The fourth chapter (4) starts with the detail of the optimization methods required to fit the model to data efficiently. In a second part, we employ the profile likelihood framework to understand the specific unidentifiabilities of the model, which becomes important later. We also show that the calibration of the model on OD and number of cells first, then on OD only, is doable.

In the fifth chapter (5), we combine the theoretical and methodological work exposed on the first three chapters, and apply them to the characterization of a collection of nine pathogenic clinical isolates. After a description of the strains and their antibiotic resistance enzymes, we present the ensemble of the data obtained on them and how they guided us in the model development. We discuss then the biological relevance of the calibrated parameter values. Then, we discuss clustering methods to organize the nine 17-parameter vectors, and show that we can categorize them in three classes: sensitive, tolerant/resilient, and resistant. Finally, we present two experimental artefacts that the model does not capture.

Finally, in the sixth and last chapter (6), we explicit the gains in explainability and practicality offered by this unifying model encompassing resistance, tolerance and resilience. We also discuss the theoretical and practical contributions of this thesis and suggest further research perspectives as well as applications of the model.

2 QUANTITATIVE MEASUREMENTS

The purpose of science being to understand the world, progress in science is deeply connected with progress in theories and technologies that enable the recording of accurate data about the world.

The earliest traces of systems of measurements date as early as the 3rd or 4th millennia BC, from Ancient Egypt and Mesopotamia and were developed to quantify goods such as cattle or seeds, or to keep track of the passage of time. Most measurement systems at the time were based on objects readily available by anyone anywhere, such as body parts. The practicality of this kind of measurement unit comes with obvious reproducibility issues. An early measurement system less prone to observer variability was that of time, that consisted during the night of the observation of the time of rise of a set of chosen stars above the horizon.

Many scientific discoveries were concomitant with the invention of the technology that enabled them. To cite only a few of the best known, Galileo's telescope allowed him in 1610 to discover notably the phases of Venus and the moons of Jupiter, two observations which led him to refute Ptolemy's geocentric model of the solar system. The precise interferometer developed by Albert Abraham Michelson and Edward Morley allowed them in 1887 to exhibit an evidence against the theory of ether (a medium supposedly necessary for the propagation of light). More recently, the construction of LIGO, a light interferometer of outstanding precision, enabled the observation of gravitational waves, a prediction of general relativity.

Although a technological development seems to be the cause of a scientific breakthrough in a large quantity of cases, scientific discoveries are sometimes made through not technological but methodological advances. From a strictly technological standpoint, Louis Pasteur's experiments on spontaneous generation in 1859 (Pasteur 1922–1939) only required him to slightly modify standard glassware, which someone could have done decades, if not centuries earlier. But it is his protocol and rigour that were the main ingredients in his discovery.

Sometimes even, the experimental data is available and the discovery is just waiting for it to be examined under a new light. This new light can be provided by a change of paradigm in the underlying model of the system, or by technological advances in data analysis. Munafò et al. (2017) cite several examples of breakthroughs achieved by reinterpretation of preexisting data. Recently, the rise of machine learning and artificial intelligence allowed revisiting quantities of existing data and extract from them new information unreachable so far, from planet discovery (Shallue and Vanderburg 2018) to dolphin communications (Frasier et al. 2017).

In some cases, the careful revisiting of data collection and analysis methods also allows detecting and correcting mistakes or misinterpretations that were done by the authors of the original analysis. Houle et al. (2011) cites a series of examples caused by either sloppy data collection, mishandling of units or logical flaws in the data analysis. Popular statistical tools such as p-values are reportedly often misused or misunderstood (Colquhoun 2014; Greenland et al. 2016).

In the context of a reproducibility crisis (Ioannidis 2005; Baker 2016), researchers began to automate and standardize the main parts of scientific data processing. Reproducible automated data collection relies on the use of open lab equipment with accessible APIs allowing seamless integration in a heterogeneous experimental platform. Open hardware allows unlimited customization with widely accessible tools such as 3d-printers and cheap electronic cards. Lab equipment with open software can be made to work in use cases not envisioned by their constructors.

Experimental and computational protocols themselves are freely exchanged on several emerging dedicated platforms, either community-driven or backed by scientific publishers. Quantitative models are also shared on open repositories such as Biomodels (Li et al. 2010) in the standardized format SBML, allowing an easier reproducibility of simulations.

As robotic lab equipment is starting to appear to enable researchers to automate themselves their processes, some companies emerged (Transcriptic n.d.) to propose fully integrated solutions for on-demand cloud lab, the experiments being done in fully automated robotic labs supposedly improving the conditions of reproducibility.

These solutions can be expensive and not practical to set up in a lab with limited space or resources. Wanting to design a

dynamical model of antibiotic resistance bridging the individual cell and cell population levels, we investigated a few relevant data collection options. One tool to observe the behaviour of individual cells can be an optical microscope associated with microfluidic chips known as mother machines (P. Wang et al. 2010). Acquiring the microscope and designing and building the chips are expensive and time-consuming processes that not every lab can afford. To track the growth of a population of cells, a microplate reader is typically used. This device repeatedly measures the absorbance of wells where cells grow in culture medium. The growing biomass in the well diffuses light and the data collection can happen without intervention for long durations (several days), which makes this a good way to obtain longitudinal temporal data. A flow cytometer is a third kind of device that can bridge both individual cell and population levels by collecting individual cell data for several tens of thousands of cells. The type of data collected by flow cytometers are typically related to the fluorescence of individual cells, as well as their forward and side scatters, loosely linked to dimensions and composition of the cell.

Each of these tools (microscope, plate reader and flow cytometer) would be a valuable asset for the study of our system. But we decided to explore what was possible to be done with only the most common and most affordable one, the plate reader. Indeed, a quality absorbance plate reader can be acquired for a couple of tens of thousand of euros, a fraction of the cost of a microscope or of a flow cytometer. Affordability, low maintenance and easy handling make of this device the most effective option to study this kind of system. It is conceivable for example, to install a plate reader in a medical laboratory. This is why our experimental platform and processes gravitate around a plate reader as the main measuring instrument.

To extract the most of the data, appropriate experimental conditions ensuring suitable levels of reproducibility need to be carefully designed and respected. The purpose of this chapter is to account for this work.

Our main measurement device is a multimode micro-plate reader of model Spark and brand Tecan (Ltd n.d.), bought in late 2017 for this work. The majority of experiments performed consist in growing pathogenic bacteria in a solution of culture medium, and applying antibiotics at different times while tracking the growth of the cells by absorbance measurements. Cells were occasionally counted by spreading a known volume of the

solution on an agar plate and counting the number of colonies after incubation. We also occasionally used a microscope to determine estimates of the length distribution and viability of cells.

The sources of measurement errors in these processes are the biological systems themselves and the way that they are handled, the measurement devices, and the data analysis. In the first part of this chapter we describe the actions we took to make the measurements as meaningful and reproducible as possible. In the second part we introduce `platerider`, a custom driver that we wrote for the plate reader to allow its integration in the context of an automated lab.

2.1 EXPERIMENTAL CALIBRATIONS

2.1.1 Choice of the medium composition

Two main classes of media are used to grow microorganisms: *defined* and *complex* media. A defined medium is one that was prepared by adding in known quantities its constituents to pure water. The nature and quantities of nutrients and salts are just sufficient to support growth, or to reach a given physiological state. A complex medium is one created with a number of highly nutritious substances such as digests of microbial, animal, or plant products, but whose exact compositions are unknown (Madigan et al. 2017).

Lysogeny Broth (LB), a complex medium introduced by Bertani (1951), is one of the most used media to grow microorganisms. However, the physiology of bacteria growing in LB changes when some of its several constituents starts lacking, which happens as early as OD = 0.3 (C. H. Wang and Koch 1978; Sezonov, Joseleau-Petit, and D'Ari 2007). The complexity of the medium also creates reproducibility issues and makes it inappropriate for quantitative studies (Hiroshi 2009). A clinical argument also suggests, contrary to common practice, that MICs should be measured in poor rather than rich media (Elf et al. 2006).

The use of a defined medium seemed a necessity for our study. M9 is a minimal medium also widely used. It is composed of a mixture of salts (Merck n.d.)

- 6.78 g/L Na_2HPO_4

- 3 g/L KH_2PO_4
- 1 g/L NH_4Cl
- 0.5 g/L NaCl
- 0.24 g/L $MgSO_4$ (optional)
- 0.01 g/L $CaCl_2$ (optional)

to which one can add the required amount of glucose, possibly completed with casamino acids.

The use of a culture medium instead of another, besides the difference in growth rates, can also cause significant qualitative behaviour changes, as shown in figure 2.1. Two strains (IB34 and IB36) were grown in the same conditions except for the culture medium (M9 with 1% glucose, or LB). The growth of both of these strains is much faster in LB than in M9. For both strains, the death phase is more pronounced in LB than in M9. Lastly, the resistant strain IB36 appears much more resistant in LB than in M9, as a 8 mg/L antibiotic dose can prevent its full growth for more than 16 hours in M9 but doesn't affect it in LB.

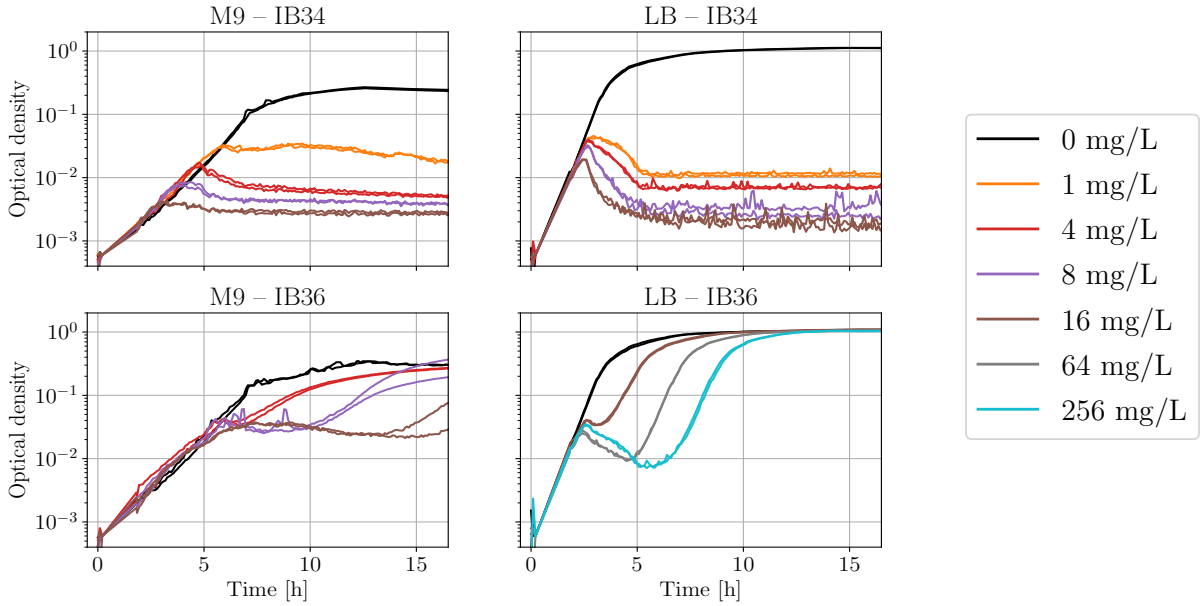

Figure 2.1: Comparison of M9 and LB for the growth of two strains with X mg/L of cefotaxime.

The standard recipe for M9 does not specify the concentration of glucose, which is left free for the experimentalist to adapt to their requirements. Our goal was to pick a glucose concentration that would facilitate the modelling and the analysis of the data.

To do so, growth curves were measured in M9 prepared with different glucose concentrations, as shown on figure 2.2. The

initial growth phase is carried at identical growth rates for the different concentrations. The only notable difference between the different media is the OD where the growth of the population stops. This optical density is the *carrying capacity* of the medium.

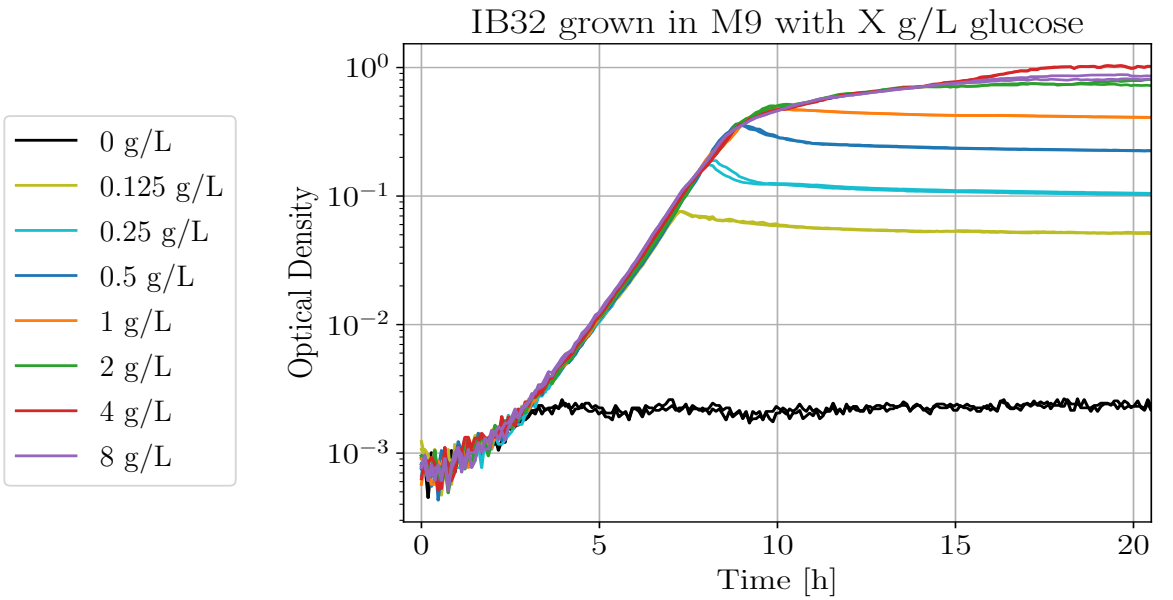

Figure 2.2: Growth of a strain in M9 with increasing glucose concentrations.

The sharp growth arrests seen from 0 g/L to 1 g/L are characteristic of a carbon-limited medium (Wanner and Egli 1990). The softer deceleration observed for 2 g/L and above reveals that at these concentrations, growth is eventually limited by something else than glucose: either the depletion of some other nutrient, or the acidification of the medium.

The cell population eventually settles for a steady-state density, that is a function of the initial concentration of glucose. This function is plotted in figure 2.3.

The strict proportionality between the initial glucose concentration and the carrying capacity of the medium, at low concentrations, confirms that the glucose is limiting in this region. The proportionality law seems valid until 2 g/L, but for this value, the carrying capacity is reached after a slow down of the growth, as seen on figure 2.2. At 4 g/L, we can guess that a significant amount of glucose remains unused even after a long time.

To not overcomplexify the model, we chose to use the maximum glucose concentration that resulted in a clear carbon-limited growth, i.e. 1 g/L, because this type of dynamics is

usually well described by simple mathematical models (Monod 1949; Senn et al. 1994; Lendenmann, Snozzi, and Egli 2000). It has also the advantage to maintain the whole curve in the linear zone of the plate reader, as demonstrated in section 2.1.4.

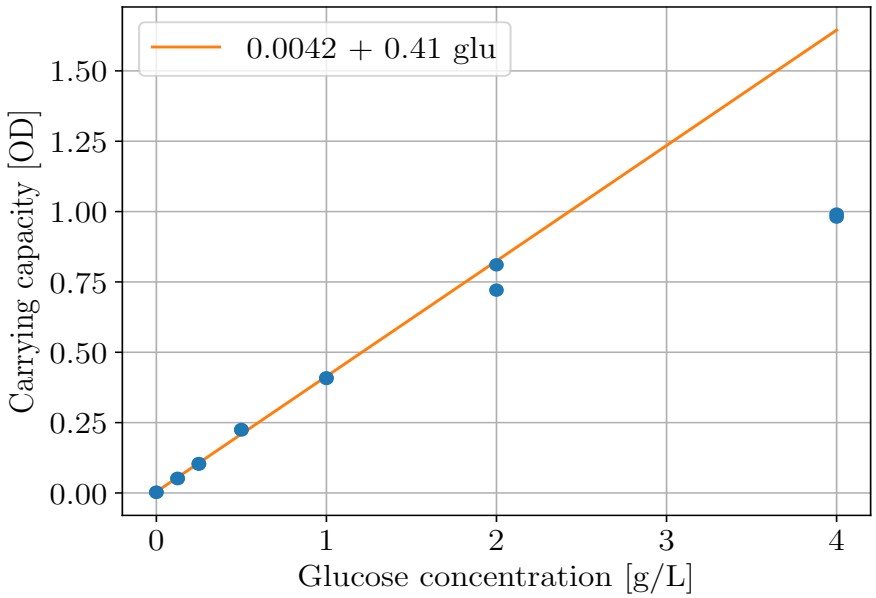

Figure 2.3: Carrying capacity for IB32 in M9 as a function of the glucose concentration. A fresh culture of cells in M9 1 g/L glucose was diluted 100 times to prepare these cultures, which explains the value of the y-axis intercept.

2.1.2 Assessment of the influence of preculture

Life phases of a cell culture in batch[1] are usually described by a succession of phases described first in detail by Buchanan (1918). A complete and accurate model of the ensemble of this process would be a huge task. Usually, one or two consecutive phases are considered at a time. Their mathematical description can involve complex mathematical techniques (Alonso, Molina, and Theodoropoulos 2014 for example use stochastic differential equations to model the lag phase).

Again to make the interpretation of the observations as easy as possible, an effort was made to simplify the observed dynamics. The lag phase was completely avoided by a 3-hour preculture

1 Batch culture and continuous culture are two modes of cultures of cells. In batch, the culture medium is in limited quantity and available from the beginning of the experiment. In continuous culture, fresh culture medium is added to the culture at a given rate as used medium and cells are flushed away from the bioreactor at the same rate.

of the cells in the morning of the experiment, following an overnight, as shown in figures 2.4 where the inoculum[2] consisted of cells directly resuspended from an overnight, and 2.5, where the cells were first resuspended in fresh medium, then diluted 5 times, and let grow for 3 hours prior to starting the experiment.

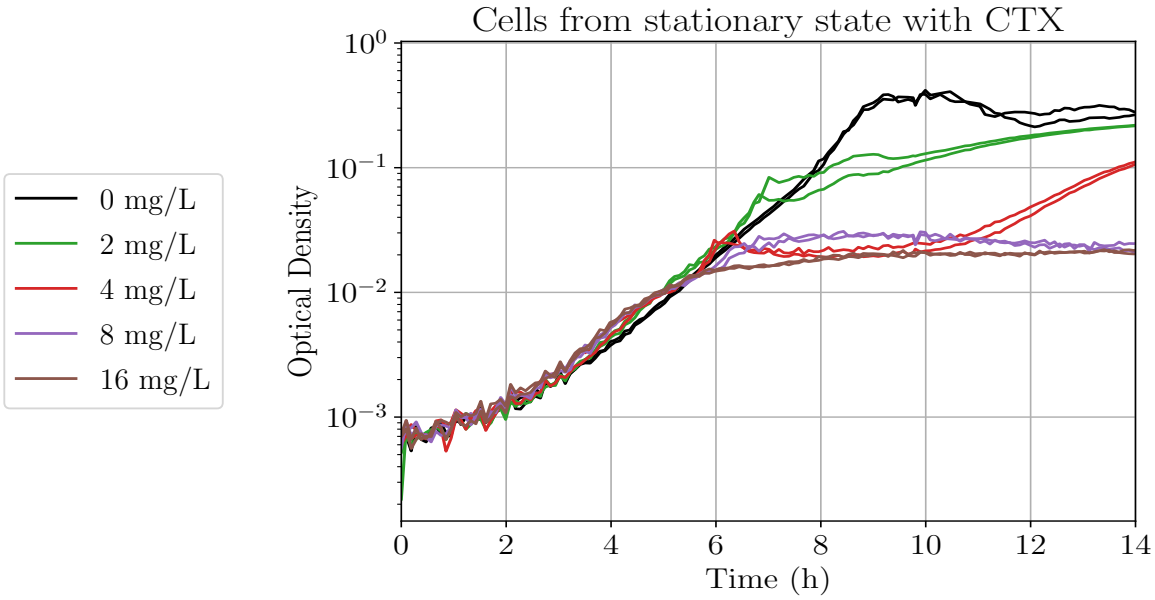

Figure 2.4: Cells starting directly from the overnight culture without preculture.

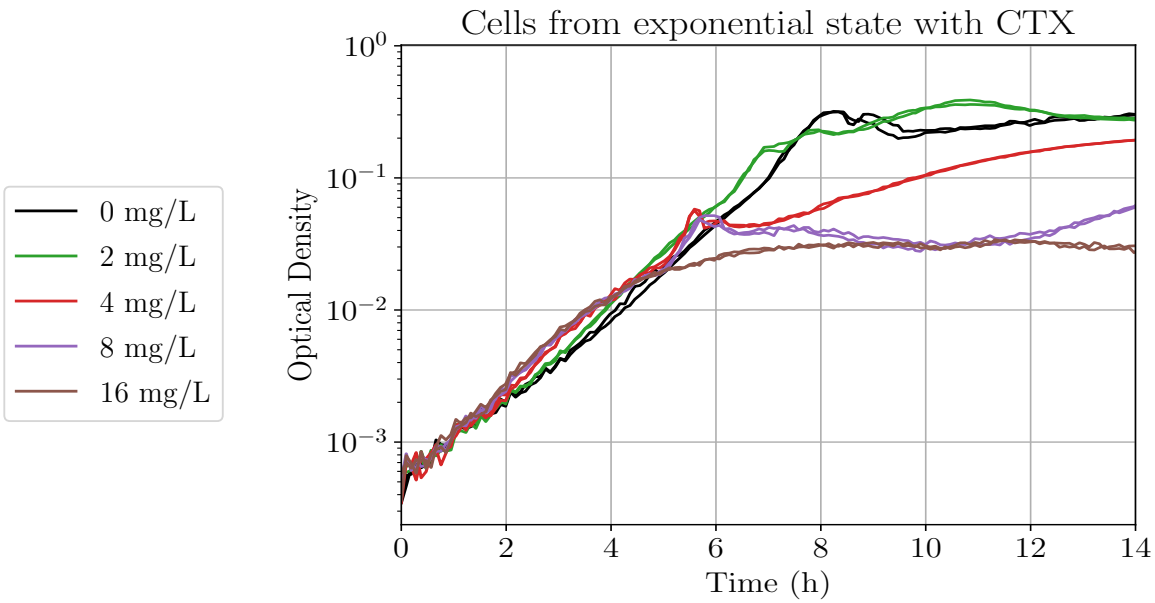

Figure 2.5: Cells starting after a 3-hour preculture.

2 The inoculum is the starting cell density in an experiment.

There is a difference of one hour between the instants when these two cultures reach an optical density of 10^{-2}. It is clear that the preculture manages to avoid the lag phase, because in this case the experiment starts with cells that are already in exponential phase. This makes their growth much easier to model.

Another notable observation from these figures is that the state of the cells at the beginning of the experiment influences their resistance to antibiotics. Indeed, 4 mg/L of cefotaxime can prevent the growth of cells (below 0.1) starting from stationary state for 14 hours, but the same dose of antibiotic can only maintain exponentially growing cells below the same threshold for 10 hours.

A determination of MIC would then yield different results depending on the state of the cells at the beginning of the experiment. To avoid these issues, cells are precultured after overnight for most of the experiments in this work.

2.1.3 Quantification of evaporation

The typical growth rate of bacteria is on the order of one generation per hour. Starting from 5×10^5 cells/mL which is the recommended starting inoculum for MIC determination by EUCAST (2020b), 11 generations are needed to go to 1×10^9 cells/mL, which is the typical carrying capacity for the medium used. With a generation time of around an hour, at least a dozen of hours are required to observe an unperturbed cell growth. Upon antibiotic exposure, the growth is altered and a full population recovery can be delayed by several hours too. It is then reasonable to expect to be able to measure cell growth over 24 hours in good conditions.

The optimal growing temperature for enterobacteria being 37 °C, the growth medium is subject to significant evaporation throughout the experiment. Without precaution, the whole plate (96 wells of 200 µL each) dries out in 14 to 19 hours.

Common solutions to this problem involve covering each well with a couple of drops of mineral oil, or using a transparent plate lid. These methods make evaporation almost negligible at the timescale of a day, but they do not allow to perform a crucial operation in our experiments: the automatic injection of antibiotic during the experiment. However, the plate reader[3]

3 Tecan Spark

that we chose to acquire comes equipped with a "humidity cassette": a metallic box where the plate is kept closed between measurements. The cassette has compartments that can be filled with water, to saturate the surroundings of the plate with water vapour and slow down the evaporation of the wells. The lid of the cassette can be removed and replaced by the plate reader with an electromagnet to allow for measurements and injections.

Figure 2.6: Humidity cassette. Picture credit: Chetan Aditya.

The question is to determine whether the use of the cassette has any noticeable effect compared to the sole plate, and how to use it at best.

To evaluate its effectiveness, a 96-well plate was prepared with 200 µL of water per well. The plate was weighted empty and with the water. The plate reader was programmed to incubate the plate at 37 °C for 5 or 10 minutes, then to open the lid of the cassette and make a full OD scan of the plate, at two different speeds. In one case, the box was opened for 33 s with a periodicity of 645 s, and in the other, the box was opened for 52 s with a periodicity of 352 s.

At different points during the experiment, the plate was taken out of the device and weighted to measure the remaining volume of water. We noted that the water evaporated faster for the more open schedule, as seen in figure 2.7.

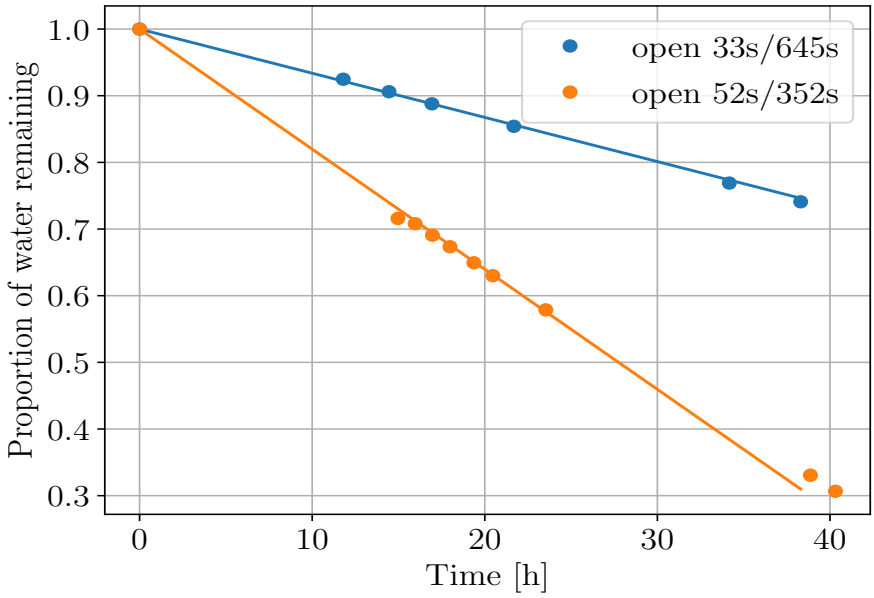

Figure 2.7: Proportion of water remaining in the plate as a function of time.

Plotted as a function not of the experiment time but of the cumulative open time of the cassette, the two evaporation profiles overlap, as seen in figure 2.8.

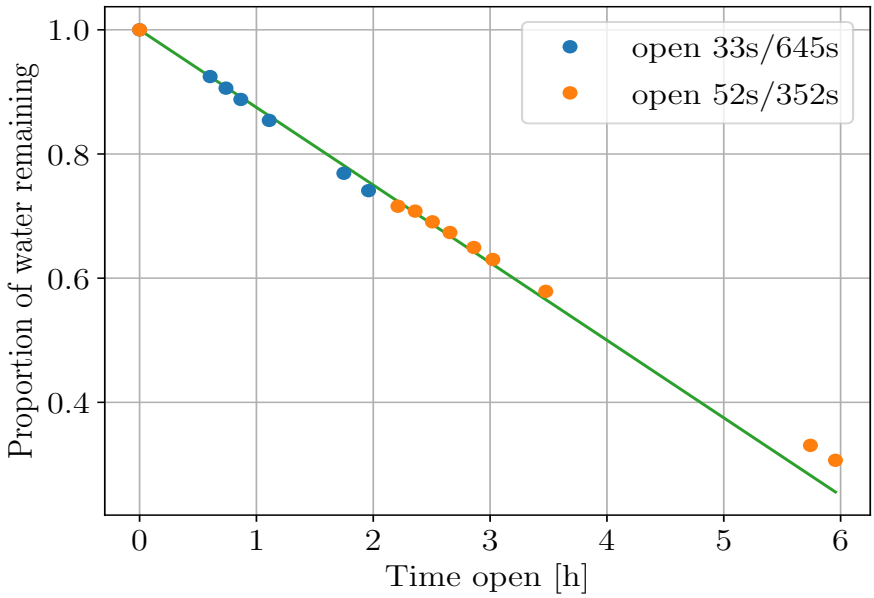

Figure 2.8: Proportion of water remaining in the plate as a function of open lid time.

Consequently, evaporation happens at a constant speed, and only when the lid is lifted. This information is crucial in the

design of long experiments, where a compromise has to be found between the frequency of measurements and the speed of evaporation. Indeed, although evaporation does not affect the OD in first approximation (because it increases the density of cells by the same factor that it reduces the light path), it does concentrate the chemicals in the well.

2.1.4 Correction of the non-linearity of OD

The optical density is a convenient, quick and non-destructive method to measure the biomass of cells in solution. Although usually considered as a proxy for the number of cells when the morphology of cells is constant, in the general case, as put by Koch (1961), "Absorbancy measurements [...] are more nearly a measure of bacterial mass than of bacterial numbers."

This was demonstrated by a number of theoretical studies on optical considerations of the scattering of light by colloidal particles of different shapes and sizes (Koch 1961, 1968), as well as by experimental studies (Koch 1970; Stevenson et al. 2016; Beal et al. 2019).

A calibration process of OD measurement devices is recommended. Following Stevenson et al. (2016) and Koch (1961), the optical density measured from a solution with a density of bacteria of n (cells/mL) can be written as

$$OD = k\,n\,(1 - \alpha\,n) + OD_0$$

where k and α depend on the size and shape of the bacteria. The constant offset OD_0 was added to take into account the absorbance of the non-biological components in the light path, such as the bottom of the plate and the culture medium itself. To identify these parameters, two strains in different conditions were diluted by different factors from a highly concentrated culture. The optical density values returned by the plate reader were plotted accordingly in figure 2.9.

The purpose of testing cells in stationary and exponential phase was to check if the quadratic coefficient depended on the size of the cells (cells in stationary phase being smaller than cells in exponential phase). It seems that this is not the case.

The parameters k and α are different for each strain and each cell morphology. The determination of k, the proportionality constant between the number of cells and their optical density, for many strains and many conditions, would require an infeasible number of cell counts.

Although the linear coefficient k varies widely as shown by Stevenson et al. (2016), it is possible that the coefficient of the quadratic term is less subject to change. To check that, the measured optical density is plotted against the linear term of

the OD, $k\,n$. This term is proportional with the number of cells because it is also proportional with the dilution factor. The plotted equation on figure 2.10 is then

$$OD = OD_0 + x - \frac{\alpha}{k}x^2$$

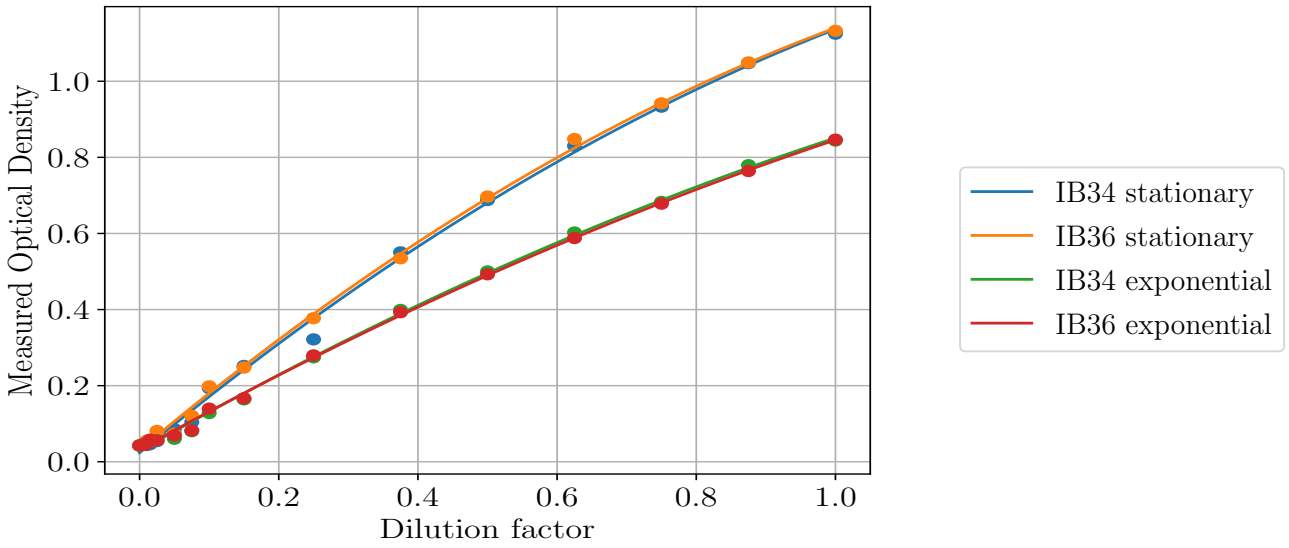

Figure 2.9: Measured optical density of cells after a dilution of a given factor, for two strains and two conditions.

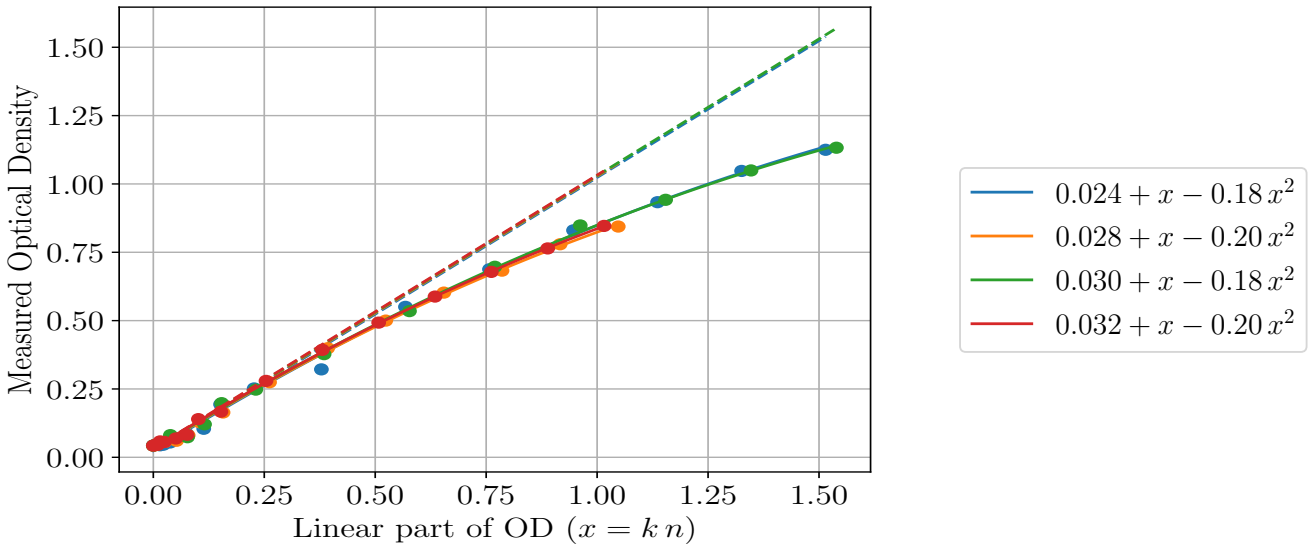

Figure 2.10: Measured optical density plotted as a function of its linear part. The dashed lines mark the tangents at the origin. The Coefficient of Variation (CV) of the fits on the constant term is 40%, whereas it is only 10% on the quadratic factor.

The superposition of the curves in this figure show that $\frac{\alpha}{k}$ is a conserved quantity for our experimental setup, equal to 0.2. This figure also shows that the linear approximation is valid up to ODs around 0.3.

If we stay within this region, which is the case with the chosen concentration of glucose, the quadratic correction is not needed. We then come back to a relation $OD = OD_0 + k\,n = OD_0 + k'm$ where m is the biomass of the bacteria. This last relation is more appropriate for our study where cell size is expected to vary widely during the course of the experiment, as a consequence k varies as well. On the contrary, k' is assumed constant.

2.1.5 An economical bayesian cell counting method

Although OD is a reliable way to measure the biomass of a cell culture, relating this information to the number of cells is difficult when the biomass per cell is changing during the experiment. This happens during normal growth curves, as cells go from a growing phase to the next, and this also happens as a result of antibiotic action, since β-lactams are known to induce severe morphological changes in bacteria. To know the number of cells, we are then reduced to counting them.

State of the art

Whether for sanitary checks of water and food, for scientific research on soil samples, or for routine health analyses, counting cells is one of the most classical problems in microbiology. Nonetheless, counting protocols have been identified for at least a century as problematic with respect to accuracy and reproducibility (Wyant 1921; Pamphilon et al. 2013), and new methods as well as technological advances never stopped being developed as ways to make this process more practical and trustworthy.

A plethora of methods have been developed to count cells, directly or indirectly, by various physical phenomena (Patterson 1979). The specificities of some of these methods allow different features such as the ability to assess not only the number but the viability of cells, or the possibility to count inanimate particles like pollens or colloidal spheroids. Some of these methods are more suitable for eukaryotes than prokaryotes notably because of the size of the cells.

The most intuitive counting method is probably direct visual counting, such as can be done under a microscope. In order to

determine a density of cells, a hemocytometer is typically used, which provides chambers of defined volumes where cells can be counted. A direct counting method that doesn't require the use of a hemocytometer is called the ratio method, and consists of mixing the unknown sample with a colloidal solution of given density and counting the ratio of particles (Takahasi, Ishida, and Kurokawa 1964). Direct counting of cells can also be done by a device designed to manipulate individual cells, such as a flow cytometer.

Cells being too small to be identified without this kind of precision devices, all the other counting methods can only be indirect.

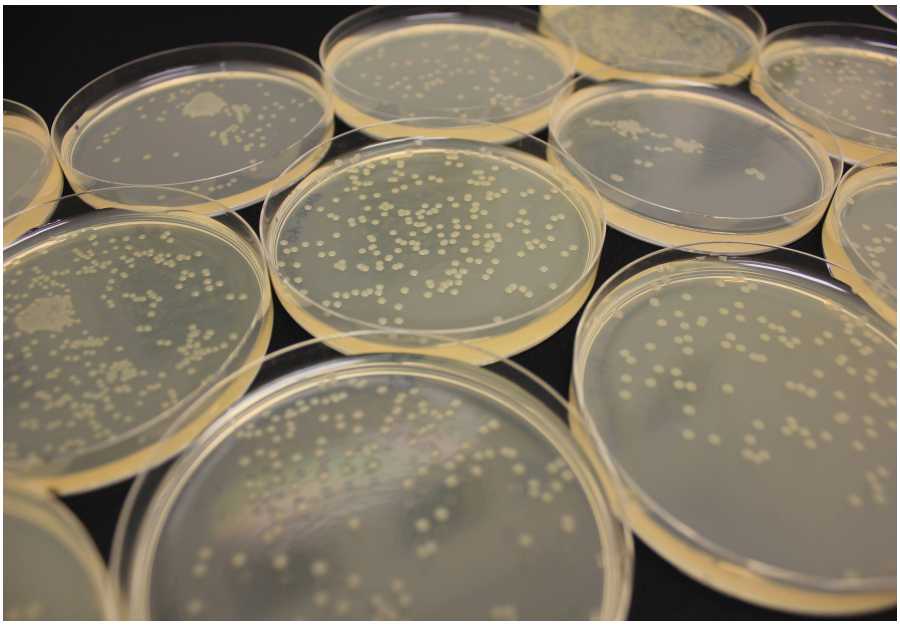

Figure 2.11: A few agar plates with bacterial colonies for the CFU counting method. Picture credit: Anđela Davidović.

The most employed of the indirect methods is the CFU method. It relates with the observation that a single cell deposited at the surface of an agar plate will, after 12 to 16 hours of incubation, form a colony of several billions of bacteria, visible to the naked eye. Spreading on an agar plate a small volume of the initial solution will then provide a number of dots easy to enumerate, and working backwards with the dilution factor allows to estimate the cell density in the original sample. Several methods exist to perform this operation, among which the "pour-plate" (where the cells are mixed with the gel) and "surface-spread" (where the cells are spread on top of it) methods (Hedges 2002). When no prior information is available about the expected number of

cells, the operator performs serial dilutions and prepares several plates with different dilution factors, in order to maximize the chances to obtain a plate with a number of cells suitable for manual counting (not too high for time reasons and to prevent crowding of cells, and not too low for statistical reasons). A number of authors have for a century analysed this problem, since the pioneering statistical analysis of Fisher, Thornton, and Mackenzie (1922). Jennison and Wadsworth (1940) discuss the contributions of the two main sources of uncertainties in this process: the *dilution* error, coming from the imprecision of the pipettes used by the operator to perform the dilutions, and the *distribution* error, intrinsic error due to the sampling of a finite number of discrete entities. In a thorough analysis, Hedges (2002) adds a third source of uncertainty which is the possibility that two cells randomly land close to each other on the plate, growing into a single colony. This leads to an underestimation of the number of plated bacteria. Hedges then computes optimal number of CFUs to aim for in order to minimize the error, for given experimental conditions. More recently, Ben-David and Davidson (2014) proposed an algorithm to choose the serial dilution that minimizes the error made in the cell count estimation.

Counting CFUs by eye and hand for this common technique can be tedious. This is why recent years have seen the development of several automated or semi-automated techniques to make this task easier. Clarke et al. (2010) developed a MATLAB script to analyse pictures and detect colonies automatically. Brugger et al. (2012) have an integrated hardware and software platform facilitating the task of taking correct pictures of the agar plates and analysing them. Geissmann (2013) developed the open software `OpenCFU` in an attempt to push a wider adoption of automated image analysis methods. Machine-learning approaches have also been proposed in (Hilsenbeck et al. 2017; Khan et al. 2018; Berg et al. 2019).

All these methods require the use of numerous plates especially for the first run of an experiment, when the expected number of cells is unknown. For this reason, more efficient methods have been developed which consist in performing all the serial dilutions on the same plate (Miles, Misra, and Irwin 1938; Jett et al. 1997).

The other counting methods are even more indirect as they do not permit the visualization of cells nor colonies.

Methylene Blue Dye Reduction Test (MBRT) is a chemical method allowing a coarse estimation of the quantity of microorganisms in a sample and is typically used for milk. The OD is a broadly used measurement that relies on the fact that cells in suspension diffuse incident light. Although efficient and practical, this method suffers from flaws. Indeed, it is difficult to calibrate, and the OD relates rather to the biomass than to the cell number (Stevenson et al. 2016). In presence of cells of varying sizes and shapes, the number of cells is then difficult to access. Another physical method relies on the propagation in the culture not of light, but of electrical current (DeBlois and Bean 1970).

Two rather exotic but ingenuous methods allow the estimation of cell count without actually counting them. One of them relies on the time that it takes to a cell sample to grow to a set threshold (Hazan et al. 2012). If we assume exponential growth, this time is an affine function of the logarithm of the initial number of cells. Another one, dating more than a century, has been named the "most probable number" method (Phelps 1908). It consists, like the CFU method, of serial dilutions, but the cells are not counted. Rather, the cells are kept in liquid phase and the dilutions are labelled as "positive" or "negative" whether they contain at least a cell or none (whether bacterial growth happened or not is visible without instrument after incubation). The proportions of positive and negative samples at different dilutions permits a probabilistic evaluation of the initial number of cells, as explained thoroughly by McCrady (1915) and Cochran (1950).

A review on a number of these methods considering their different features has been done by Hazan et al. (2012). It can be noted that several commercial devices have been developed to make cell counting more convenient and reliable, such as (Johnston 2010). A review of two of these semi-automated or automated measurement devices can be seen in (Cadena-Herrera et al. 2015).

Bayesian estimation for CFU counting

We do not know of a statistical study of cell counting done in a Bayesian framework. This is surprising, because it seems quite a natural approach, as in contrast with frequentist methods, it allows to easily combine the knowledge of several observations to improve the accuracy of the estimation.

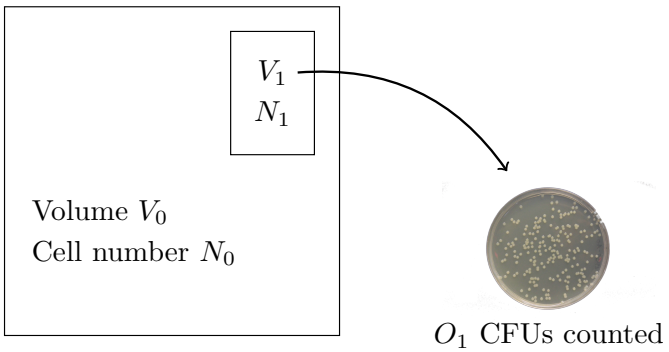

Figure 2.12: Schematical representation of the problem.

Consider an initial volume V_0 containing N_0 cells. A smaller volume V_1 is sampled from V_0 with N_1 cells, which is a random variable. This volume is spread on a plate and the cells are counted after incubation. What can we say about the initial number of cells N_0 after observing O_1 colonies on the plate?

We search for the probability $p(N_0 = N|N_1 = O_1)$. This probability can be expressed with Bayes' theorem:

$$p(N_0 = N|N_1 = O_1) = \frac{p(N_1 = O_1|N_0 = N)p(N_0 = N)}{p(N_1 = O_1)}$$

The denominator can be expanded by summing over all the possible initial numbers of cells:

$$p(N_0 = N|N_1 = O_1) = \frac{p(N_1 = O_1|N_0 = N)p(N_0 = N)}{\sum_{M\in\mathbb{N}} p(N_1 = O_1|N_0 = M)p(N_0 = M)}$$

The direct problem that appears on the right-hand side of the equation, consists of calculating the distribution of sampled cells from a known initial problem. Except in the two extreme cases where all or none of the volume is sampled (that would result in all or none of the cells sampled), the ratio of sampled cells can be quite different from the ratio of volumes, because of the *distribution* error (Jennison and Wadsworth 1940; Hedges 2002). This effect is exacerbated by low numbers of cells. A more accurate model for the sampling of cells is one where each cell has the same probability to be sampled, this probability being equal to the ratio of volumes. So if we sample half the volume, each cell has a 50% chance of being sampled, which does not mean that half the cells will necessarily be sampled. In this context, the probability that a given number of cells is sampled is given by the binomial distribution:

$$p(N_1 = O_1 | N_0 = N) = \binom{N}{O_1} \left(\frac{V_1}{V_0}\right)^{O_1} \left(1 - \frac{V_1}{V_0}\right)^{N-O_1}$$

Hedges (2002) suggests that the distribution error dominates the dilution error. This observation seems to be confirmed by nine plating replicates from a single well. As can be seen in figure 2.13, the spread of the resulting distribution of colony numbers is comparable to what it would be accounting for only the distribution error.

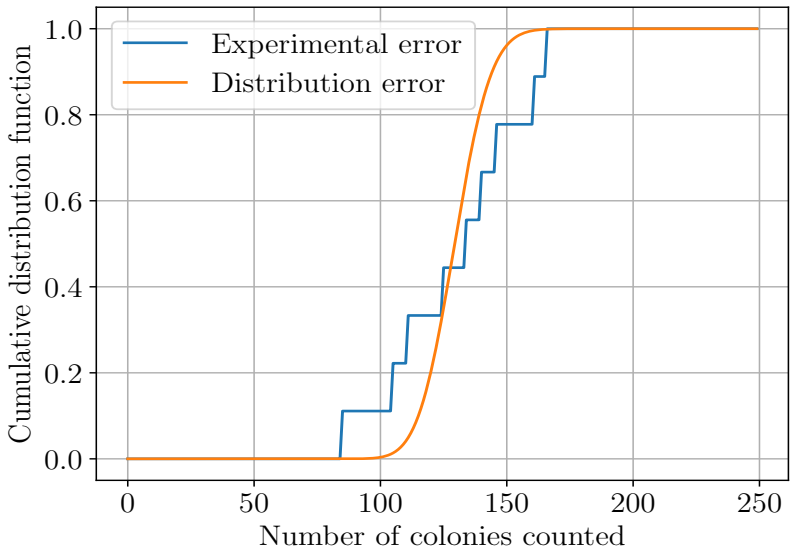

Figure 2.13: Nine plates were spread one after each other from the same cell culture, with a dilution factor of 1/1000. The initial culture has an OD of 0.0005 and contains about 130000 cells.

The binomial distribution can then be considered as a reasonable model for the cell sampling.

The original conditional probability can be rewritten, in all generality:

$$
\begin{aligned}
&p(N_0 = N | N_1 = O_1) \\
&= \frac{\binom{N}{O_1}\left(\frac{V_1}{V_0}\right)^{O_1}\left(1-\frac{V_1}{V_0}\right)^{N-O_1} p(N_0 = N)}{\sum_{M\in\mathbb{N}}\binom{M}{O_1}\left(\frac{V_1}{V_0}\right)^{O_1}\left(1-\frac{V_1}{V_0}\right)^{M-O_1} p(N_0 = M)} \\
&= \frac{\binom{N}{O_1}\left(1-\frac{V_1}{V_0}\right)^{N} p(N_0 = N)}{\sum_{M\in\mathbb{N}}\binom{M}{O_1}\left(1-\frac{V_1}{V_0}\right)^{M} p(N_0 = M)}
\end{aligned}
$$

Choosing a prior can be a delicate problem. In our case, we know that the initial number of bacteria is necessarily larger or equal than the number of colonies counted. We also know that it cannot exceed a reasonable biological limit. The maximal optical density measured in our experimental setting is in the order of 1, which corresponds at best to a billion of bacteria per cubic millilitre. The initial volume being a fifth of a millilitre, the maximum possible number of bacteria in the original sample is on the order of 200 millions. We will use a uniform prior over the interval $[O_1, L]$ where L is this upper limit.[4] The uniform prior is typically used to describe a lack of information.

$$
\begin{aligned}
&p(N_0 = N | N_1 = O_1) \\
&= \frac{\binom{N}{O_1}\left(1-\frac{V_1}{V_0}\right)^{N} \frac{\Theta(L-N)}{L-O_1+1}}{\sum_{M=O_1}^{L}\binom{M}{O_1}\left(1-\frac{V_1}{V_0}\right)^{M} \frac{1}{L-O_1+1}} \\
&= \frac{\binom{N}{O_1}\left(1-\frac{V_1}{V_0}\right)^{N} \Theta(L-N)}{\sum_{M=O_1}^{\infty}\binom{M}{O_1}\left(1-\frac{V_1}{V_0}\right)^{M} - \sum_{M=L+1}^{\infty}\binom{M}{O_1}\left(1-\frac{V_1}{V_0}\right)^{M}}
\end{aligned}
$$

The first term of the denominator can be expressed with the negative binomial formula: $\frac{1}{(1-x)^{r+1}} = \sum_{k=r}^{\infty}\binom{k}{r}x^{k-r}$

4 In reality, if the optical density is also measured, one can have some information on the number of cells. Knowing that the average length of bacteria can go from a couple to a hundred of micrometers for extremely elongated cells, the prior can be restricted to two decades instead of 6 or 7. In practice, the uniform prior is sufficiently robust so that this doesn't change much the results.

$$
\begin{aligned}
&p(N_0 = N | N_1 = O_1) \\
&= \frac{\binom{N}{O_1}\left(1-\frac{V_1}{V_0}\right)^N \Theta(L-N)}{\left(\frac{V_0}{V_1}\right)^{O_1+1}\left(1-\frac{V_1}{V_0}\right)^{O_1} - \sum_{M=L+1}^{\infty}\binom{M}{O_1}\left(1-\frac{V_1}{V_0}\right)^M} \\
&= \frac{\binom{N}{O_1}\left(\frac{V_1}{V_0}\right)^{O_1+1}\left(1-\frac{V_1}{V_0}\right)^{N-O_1}\Theta(L-N)}{1-\sum_{M=L+1}^{\infty}\binom{M}{O_1}\left(1-\frac{V_1}{V_0}\right)^{M-O_1}\left(\frac{V_1}{V_0}\right)^{O_1+1}} \\
&= \binom{N}{O_1}\left(\frac{V_1}{V_0}\right)^{O_1+1}\left(1-\frac{V_1}{V_0}\right)^{N-O_1}\frac{\Theta(L-N)}{1-Y(O_1, L, V_1/V_0)}
\end{aligned}
$$

where Y corresponds to the sum in the denominator in the previous line.

The last fraction tends towards 1 when $L \to \infty$. For $N \leq L$, this fraction doesn't depend on N and acts as a normalizing factor. Consequently, for L sufficiently large such that it doesn't touch the posterior ($L \gg O_1 \frac{V_0}{V_1}$), we can ignore this factor.

We then have the final formula, that allows to express the initial conditional probability as a negative binomial distribution[5] of parameters $n = O_1 + 1$, $k = N - O_1$ and $p = \frac{V_1}{V_0}$:

$$
\boxed{p(N_0 = N | N_1 = O_1) = \binom{N}{O_1}\left(\frac{V_1}{V_0}\right)^{O_1+1}\left(1-\frac{V_1}{V_0}\right)^{N-O_1}}
$$

This formula allows to determine the expected value of the initial number of cells, which is the average of the distribution. The average of k in the negative binomial distribution is $\frac{n(1-p)}{p}$, to which we have to add O_1 to obtain the average of N, which gives, after calculation:

$$
E[N_0 | N_1 = O_1] = O_1 \frac{V_0}{V_1} + \frac{V_0 - V_1}{V_1}
$$

5 In this parameterization, the negative binomial distribution describes the number of failures k in iid Bernoulli trials before n successes occur, if the probability of success of each trial is p.

The standard deviation of this distribution[6] is given by $\frac{\sqrt{n(1-p)}}{p}$:

$$\sigma = \frac{V_0}{V_1}\sqrt{(O_1+1)\left(1-\frac{V_1}{V_0}\right)}$$

The cumulative distribution function of this distribution is $I_p(r, k+1)$ where $I_x(a,b)$ is the regularized incomplete beta function[7]:

$$CDF(N) = I_{\frac{V_1}{V_0}}(O_1+1, N-O_1+1)$$

Its quantiles can be extracted by root finding of the function `scipy.special.betainc`. Even more conveniently, everything can be solved with the `stats` module of `scipy`:

```
from scipy.stats import nbinom

def n0_95ci(dilution, cfus):
    '''
    Returns (mean, lb95ci, ub95ci) for the inferred
    distribution of number of cells before a dilution
    that leads to a given cfu count.
    '''
    dist = nbinom(n=cfus+1, p=dilution, loc=cfus)
    return (dist.mean(), *dist.interval(0.95))
```

6 We can check here that these two values make sense on a few extreme cases. In the first case, $V_1 = 0$. If no volume was sampled, nothing can be deduced about the initial culture, and consequently the distribution diverges. In the second case, $V_1 = V_0$. This corresponds to spreading the total volume of the solution. In this case, we find $E[N_0|N_1 = O_1] = O_1$ and $\sigma = 0$, as expected.

7 The incomplete beta function is defined in terms of the beta function $B(a,b) = \int_0^1 t^{a-1}(1-t)^{b-1}\,\mathrm{d}t$ and the incomplete beta function $B(x;a,b) = \int_0^x t^{a-1}(1-t)^{b-1}\,\mathrm{d}t$ as $I_x(a,b) = \frac{B(x;a,b)}{B(a,b)}$.

PARALLEL DILUTIONS The same framework can be applied just as easily to more complex sampling scenarios, for example if two plates are spread one after each other from the same culture with possibly different dilution factors. As an example, consider that after the first volume V_1 was sampled, another volume V_2 is sampled from the same culture and spread on another plate. Then we have:

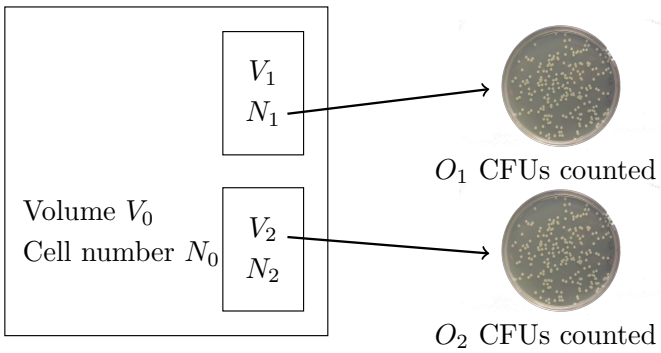

Figure 2.14: Schematical representation of the problem of parallel dilutions.

$$
\begin{aligned}
&p(N_0 = N | N_1 = O_1 \wedge N_2 = O_2) \\
&= \frac{p(N_1 = O_1 \wedge N_2 = O_2 | N_0 = N) p(N_0 = N)}{p(N_1 = O_1 \wedge N_2 = O_2)} \\
&= \frac{p(N_2 = O_2 | N_0 = N \wedge N_1 = O_1) p(N_1 = O_1 | N_0 = N) p(N_0 = N)}{p(N_1 = O_1 \wedge N_2 = O_2)} \\
&= \frac{\binom{N-O_1}{O_2} \left(\frac{V_2}{V_0 - V_1}\right)^{O_2} \left(1 - \frac{V_2}{V_0 - V_1}\right)^{N-O_1-O_2} \binom{N}{O_1} \left(\frac{V_1}{V_0}\right)^{O_1} \left(1 - \frac{V_1}{V_0}\right)^{N-O_1} p(N_0 = N)}{p(N_1 = O_1 \wedge N_2 = O_2)}
\end{aligned}
$$

The denominator, expressed as a sum over M like previously, can be simplified as following, if we again take the uniform prior:

$$
\begin{aligned}
&p(N_1 = O_1 \wedge N_2 = O_2) \\
&= \left(\frac{V_1}{V_0}\right)^{O_1} \left(1 - \frac{V_1}{V_0}\right)^{O_2} \left(\frac{V_2}{V_0 - V_1}\right)^{O_2} \left(\frac{V_0}{V_1 + V_2}\right)^{1+O_1+O_2} \binom{O_1 + O_2}{O_1}
\end{aligned}
$$

This goes back in the original formula:

$$
\begin{aligned}
&p(N_0 = N | N_1 = O_1 \wedge N_2 = O_2) \\
&= \frac{\binom{N-O_1}{O_2}\left(\frac{V_2}{V_0-V_1}\right)^{O_2}\left(1-\frac{V_2}{V_0-V_1}\right)^{N-O_1-O_2}\binom{N}{O_1}\left(\frac{V_1}{V_0}\right)^{O_1}\left(1-\frac{V_1}{V_0}\right)^{N-O_1}}{\left(\frac{V_1}{V_0}\right)^{O_1}\left(1-\frac{V_1}{V_0}\right)^{O_2}\left(\frac{V_2}{V_0-V_1}\right)^{O_2}\left(\frac{V_0}{V_1+V_2}\right)^{1+O_1+O_2}\binom{O_1+O_2}{O_1}} \\
&= \frac{\binom{N-O_1}{O_2}\binom{N}{O_1}}{\binom{O_1+O_2}{O_1}}\frac{\left(1-\frac{V_2}{V_0-V_1}\right)^{N-O_1-O_2}\left(1-\frac{V_1}{V_0}\right)^{N-O_1}}{\left(1-\frac{V_1}{V_0}\right)^{O_2}\left(\frac{V_0}{V_1+V_2}\right)^{1+O_1+O_2}} \\
&= \binom{N}{O_1+O_2}\left(1-\frac{V_2}{V_0-V_1}\right)^{N-O_1-O_2}\left(1-\frac{V_1}{V_0}\right)^{N-O_1-O_2}\left(\frac{V_1+V_2}{V_0}\right)^{1+O_1+O_2} \\
&= \binom{N}{O_1+O_2}\left(\frac{V_1+V_2}{V_0}\right)^{1+O_1+O_2}\left(1-\frac{V_1+V_2}{V_0}\right)^{N-O_1-O_2}
\end{aligned}
$$

Where we recognize, as previously, a negative binomial distribution of parameters $n = O_1 + O_2 + 1$, $k = N - O_1 - O_2$ and $p = \frac{V_1+V_2}{V_0}$. This shows that in this framework, sampling two different volumes and counting them independently is exactly equivalent as sampling the sum of the volumes in one time. When appropriate, one could take advantage of this property by summing the counts of several plates sampled from the same well, to improve the accuracy of the estimation. A frequentist investigation on the usefulness of averaging over dilutions can be found in (Hedges 2002).

SERIAL DILUTIONS In another typical situation, the dilution factor necessary to sample a countable number of bacteria from a well is too large to do it in one step. Then a first volume V_1 is sampled, fresh medium is added to this volume to reach a volume V_0', and a second volume V_2 is taken from this intermediate sample and then spread on a plate. We only count the number of cells contained in V_2 and observe O_2 colonies. In these conditions,

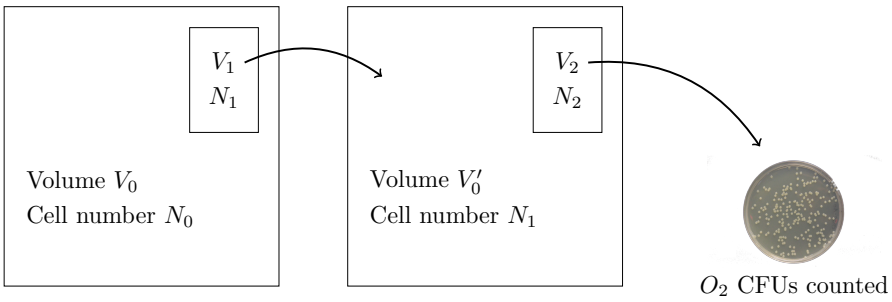

Figure 2.15: Schematical representation of the problem of serial dilutions.

$$
\begin{aligned}
&p(N_0 = N | N_2 = O_2) \\
&= \frac{p(N_2 = O_2 | N_0 = N) p(N_0 = N)}{p(N_2 = O_2)} \\
&= \frac{\sum_{O_1=O_2}^{N} p(N_2 = O_2 | N_1 = O_1) p(N_1 = O_1 | N_0 = N) p(N_0 = N)}{p(N_2 = O_2)} \\
&= \frac{\sum_{O_1=O_2}^{N} \binom{O_1}{O_2} \left(\frac{V_2}{V_0'}\right)^{O_2} \left(1 - \frac{V_2}{V_0'}\right)^{O_1 - O_2} \binom{N}{O_1} \left(\frac{V_1}{V_0}\right)^{O_1} \left(1 - \frac{V_1}{V_0}\right)^{N - O_1} p(N_0 = N)}{p(N_2 = O_2)}
\end{aligned}
$$

The sum in the numerator can be written

$$
\begin{aligned}
&\sum_{O_1=O_2}^{N} \binom{O_1}{O_2} \left(\frac{V_2}{V_0'}\right)^{O_2} \left(1 - \frac{V_2}{V_0'}\right)^{O_1 - O_2} \binom{N}{O_1} \left(\frac{V_1}{V_0}\right)^{O_1} \left(1 - \frac{V_1}{V_0}\right)^{N - O_1} \\
&= \left(\frac{V_2}{V_0'}\right)^{O_2} \left(\frac{V_1}{V_0}\right)^{O_2} \sum_{O_1=O_2}^{N} \binom{N}{O_1} \binom{O_1}{O_2} \left(1 - \frac{V_2}{V_0'}\right)^{O_1 - O_2} \left(\frac{V_1}{V_0}\right)^{O_1 - O_2} \left(1 - \frac{V_1}{V_0}\right)^{N - O_1} \\
&= \binom{N}{O_2} \left(\frac{V_1 V_2}{V_0 V_0'}\right)^{O_2} \sum_{O_1=O_2}^{N} \binom{N - O_2}{O_1 - O_2} \left[\frac{V_1}{V_0}\left(1 - \frac{V_2}{V_0'}\right)\right]^{O_1 - O_2} \left(1 - \frac{V_1}{V_0}\right)^{N - O_1} \\
&= \binom{N}{O_2} \left(\frac{V_1 V_2}{V_0 V_0'}\right)^{O_2} \sum_{X=0}^{N - O_2} \binom{N - O_2}{X} \left[\frac{V_1}{V_0}\left(1 - \frac{V_2}{V_0'}\right)\right]^{X} \left(1 - \frac{V_1}{V_0}\right)^{N - O_2 - X} \\
&= \binom{N}{O_2} \left(\frac{V_1 V_2}{V_0 V_0'}\right)^{O_2} \left[\frac{V_1}{V_0}\left(1 - \frac{V_2}{V_0'}\right) + 1 - \frac{V_1}{V_0}\right]^{N - O_2} \\
&= \binom{N}{O_2} \left(\frac{V_1 V_2}{V_0 V_0'}\right)^{O_2} \left(1 - \frac{V_1 V_2}{V_0 V_0'}\right)^{N - O_2}
\end{aligned}
$$

Leading to the same answer as before, the dilution factor being the product of the serial dilutions:

$$\boxed{p(N_0 = N|N_2 = O_2) = \binom{N}{O_2}\left(\frac{V_1V_2}{V_0V_0'}\right)^{O_2+1}\left(1-\frac{V_1V_2}{V_0V_0'}\right)^{N-O_2}}$$

COMBINATIONS We saw that in parallel, dilutions factors are added to each other, and in series, they are multiplied together. One can show that these two laws combine as expected.

If, from a volume V_0, a volume V_1 is extracted and completed until V_0' with fresh medium, then from this new volume V_2 is sampled and plated, and from the initial volume, V_3 is directly sampled and plated, and the two plates are counted with respectively O_2 and O_3 colonies, then the probability distribution on the initial number of cells is

$$\begin{aligned}&p(N_0 = N|N_2 = O_2 \wedge N_3 = O_3)\\ &= \binom{N}{O_2+O_3}\left(\frac{V_3}{V_0}+\frac{V_1V_2}{V_0V_0'}\right)^{O_2+O_3+1}\left(1-\frac{V_3}{V_0}-\frac{V_1V_2}{V_0V_0'}\right)^{N-O_2-O_3}\end{aligned}$$

PROBABILISTIC PROGRAMMING These derivations, although tedious, are tractable. To investigate more complex situations, for example to integrate the dilution errors, probabilistic programming is the ideal tool. `PyMC3` (Salvatier, Wiecki, and Fonnesbeck 2016) is one of the most accessible frameworks allowing to describe these problems in Python.

To go back to the case of a simple dilution, with a normal multiplicative dilution error, the program that computes the mean and the 95% confidence interval is the following:

```
import pymc3 as pm
from scipy.stats.mstats import mquantiles

def n0_95ci_pymc(dilution, cfus, nmax=1e9, nbsamples=10000):
    '''
    Returns (mean, lb95ci, ub95ci) for the inferred
    distribution of number of cells before a dilution
    that leads to a given cfu count.
    With probabilistic programming.
    '''
    with pm.Model():
        n0 = pm.DiscreteUniform('n0', lower=0, upper=nmax)
        dilf = pm.Normal('dilf', mu=1, sigma=0.02)
        pm.Binomial('obs', n0, dilution*dilf, observed=cfus)
        trace = pm.sample(nbsamples, tune=nbsamples//2)
    mean = trace['n0'].mean()
    lb95ci, ub95ci = mquantiles(trace['n0'], [0.025, 0.975])
    return (mean, lb95ci, ub95ci)
```

CONCLUSION OF CELL COUNTING As we will see in chapter 4, model calibration relies not only on data values but also on their uncertainties. Evaluating uncertainties with CFU counting is classically done by making typically 3 replicates of each plate. However, if we want data on the number of cells every two hours during 24 hours, in an experiment done with 6 antibiotic concentrations, the number of time points is 78. Replicating each plate 3 times is infeasible experimentally, so we needed a way to compute confidence intervals with only one plate.

Moreover, the first time that we do an experiment, we do not really know what number of cells to expect, and the dilutions are not optimized. Being able to infer average numbers and confidence intervals from only one plate per time point allows to optimize the dilutions in case we want to repeat the experiment, without spending too much time or resources in the preview experiment.

2.2 DEVELOPMENT OF A CUSTOM PLATE READER DRIVER

The instrument that we chose to carry out our experiments, Tecan Spark (figure 2.16), is a versatile multimode plate reader that can be purchased with an injector module able to dispense in the plate small volumes of up to two reagents, at any time during the experiment.

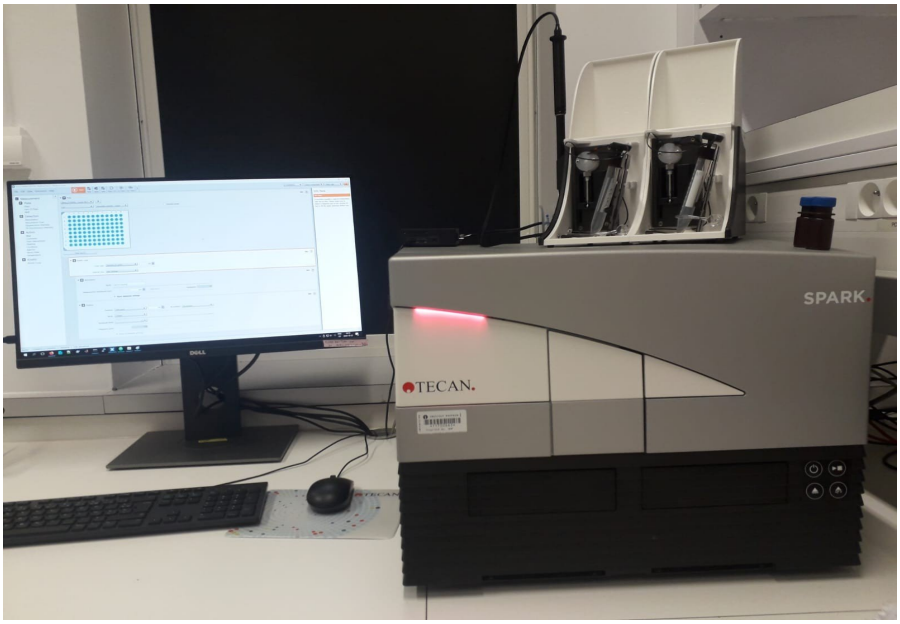

Figure 2.16: Tecan Spark with injectors. Picture credit: Chetan Aditya.

It is an automated device controlled by a computer to whom it is connected via USB. The programming of the device is done through the Windows software SparkControl, licensed by Tecan, offering a graphical programming interface and a live visualization of results. A protocol is specified in this software as a sequence of instructions (such as taking an OD measurement, shaking the plate, or incubating it) assembled by dragging graphical blocks in succession to create a program (figure 2.17).

It is difficult to make a software both accessible for novice users, and powerful for power-users. In this case, it is clear that the engineers and developers of SparkControl made the choice to enable people without programming experience to easily design protocols for the plate reader. Unfortunately, SparkControl is of limited help for complex static protocols (through limitations in the nesting of loops for example), and almost unable to

implement any dynamic protocols, i.e. protocols that might depend on the data measured.

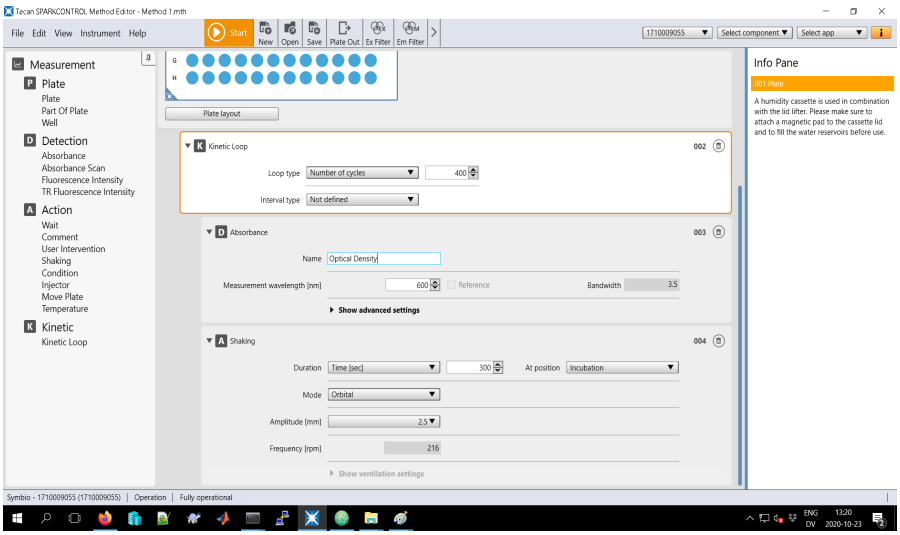

Figure 2.17: SparkControl, the Tecan software to program the plate reader. This protocol represents 400 OD measurements of the whole plate, separated with 5 minutes of shaking.

A classical way to enable tech-savy users to use a piece of equipment as they please, is to expose to them a documented and updated low-level programming API.

Unfortunately, Tecan was unable to propose us an API satisfying our requirements. A meager Visual Basic API exists but only allows to perform a couple of high-level operations, like execute a protocol already programmed with SparkControl.

Without any help from the constructor, we then undertook to reverse-engineer the plate reader in order to build ourselves a suitable API. The reverse-engineering of a device is a process consisting of its careful auscultation in order to build a precise understanding of its hidden internal functions. This understanding is needed to gain the ability to interact with the device, disguised as the official driver, in order to make it execute any arbitrary succession of commands, that could not be done in the official way. It is also a risky process, because it is a non recognized use of the device that might void its guarantee, and give direct access to potentially dangerous low-level functions of the device, without the safety checks performed by the official interface.

2.2.1 Reverse-engineering of a lab device

General informations

The Spark plate reader has a modular design and can be bought with in one of several configurations consisting of a list of modules. The base module, necessary for the use of the plate reader, is the "Plate transport" module. We bought the plate reader with the optional "Absorption," "Fluorescence" and "Injectors" modules.

Upon connection of the Spark USB cable to a computer, three USB devices appear and introduce themselves with their `idVendor` and `idProduct` numbers, that all USB devices possess, and that uniquely identify respectively their manufacturer and their model. Tecan has its own `idVendor`, the hexadecimal number `0x0c47`, registered under the description `TECAN AUSTRIA`. It is common to the three devices. They have their specific `idProduct` numbers:

- `0x8026` corresponds to `ABSORPTION`;
- `0x8027` corresponds to `FLUORESCENCE`;
- `0x8028` corresponds to `PLATE_TRANSPORT`.

Interestingly, the injectors module does not have a dedicated USB device; upon further inspection we discovered that the injectors are managed by the plate transport module.

First contact

The easiest way to understand how to communicate with the plate reader is to observe how the official software SparkControl does it. This can be done with the open-source software Wireshark (Combs 2020), specialized in the interception and analysis of network packets, but which can also be used for USB.

Wireshark is opened and setup to spy on the USB connection used between the computer and the plate reader. The recording is launched, then the plate reader is connected to the computer and SparkControl automatically starts an initialization phase which is entirely recorded by Wireshark.

During this phase, SparkControl and the plate reader exchange messages in a custom protocol. Some of the bytes can be interpreted as ascii characters. An extract of the initialization sequence is reproduced below, together with the decoded ascii on the right. The non-printable bytes are marked with a dot.

```
computer -> Spark  01:01:00:11:3f:49:4e:53     ....?INS
                   54:52:55:4d:45:4e:54:20     TRUMENT
                   53:54:41:54:45:4c           STATEL

computer <- Spark  81:01:00:0b:53:54:41:54     ....STAT
                   45:3d:52:45:41:44:59:aa     E=READY.

computer -> Spark  01:02:00:15:48:57:42:55     ....HWBU
                   54:54:4f:4e:20:41:4c:4c     TTON ALL
                   3d:44:49:53:41:42:4c:45     =DISABLE
                   44:53                       DS

computer <- Spark  81:02:00:00:83              .....
```

After investigation, guessing and error, the general structure of a message appeared:

```
81:01:00:0b:53:54:41:54:45:3d:52:45:41:44:59:aa
AA CC 00 LL _________Message text__________ XX
```

- `AA` is a message identifier, with a value either 01, 81, 82, 83, 84, 85, 86, 87 or 88 depending on the type of message;
- `CC` is a message counter, incremented by 1 at each message. A message answering to another one shares the same message counter;
- `00` is always `00`;
- `LL` is the length of the text length in this message;
- After the length comes the text of the message;
- The messages ends with `XX` which is a message checksum: it is the binary XOR of all the rest of the message, in such a way that the binary XOR of all the message including this byte is `00`.

With this information and the library `PyUSB` (*PyUSB* (version 1.0) 2020), we were able to craft and send our own USB messages for the plate reader, as well as read its answers. With the example of the recorded initialization sequence, we were also able to write a python script to initialize the plate reader ourselves.

Format of the data

The next step is to understand how to interpret the data sent by the plate reader following a request for an absorbance reading. The message text corresponding to absorbance readings cannot

be interpreted as ascii: it is a binary blob which we must learn how to make sense of.

SparkControl has a setting that allows choosing how many reads per well the plate reader will do. We noticed that the size of the packets changes for different values of this setting: 80 bytes for 20 reads, and 4 bytes for 1 read. Which must mean that each read is sent individually and represented over 4 bytes.

Setting up a plate with high OD and low OD wells, we could then compare the values themselves, read per read.

```
       high OD       low OD
hex: 9f:01:0d:95 | 9f:94:75:34
hex: 9c:55:0d:57 | a0:fe:76:7c
hex: 9f:db:0d:9e | a3:05:78:33
hex: 9e:96:0d:7a | a1:17:77:14
```

The four high OD reads correspond to the same well, and likewise for the low OD reads. Their values should then be similar. Looking at these values, what jumps to the eye is that the first and third bytes are almost constant, whereas the second and fourth are more variable. This is a hint that the first and third bytes can be the most significant bits of a number, and the second and fourth are the least significant ones. It leads into interpreting these four bytes as two 2-byte integers:

```
       high OD       low OD
hex: 9f:01|0d:95 | 9f:94|75:34
int: 40705| 3477 | 40852|30004
hex: 9c:55|0d:57 | a0:fe|76:7c
int: 40021| 3415 | 41214|30332
hex: 9f:db|0d:9e | a3:05|78:33
int: 40923| 3486 | 41733|30771
hex: 9e:96|0d:7a | a1:17|77:14
int: 40598| 3450 | 41239|30484
```

The values of these numbers remind of the way that optical density is measured, as a function of the ratio of the incident and transmitted lights. We understand that the first number is a measurement of the power of the incident light, and the second is a measurement of the transmitted light. Hence the first result, that looks like an optical density:

$$\log_{10}\left(\frac{\Phi_{\text{in}}}{\Phi_{\text{tr}}}\right)$$

```
       high OD       low OD
hex: 9f:01|0d:95 | 9f:94|75:34
```

```
int: 40705| 3477 | 40852|30004
log:    1.068         0.132
hex: 9c:55|0d:57 | a0:fe|76:7c
int: 40021| 3415 | 41214|30332
log:    1.069         0.133
hex: 9f:db|0d:9e | a3:05|78:33
int: 40923| 3486 | 41733|30771
log:    1.070         0.132
hex: 9e:96|0d:7a | a1:17|77:14
int: 40598| 3450 | 41239|30484
log:    1.071         0.131
```

Measurement model

At this point, one needs to understand how the data is measured in order to properly interpret it. The absorbance is defined as the logarithm of the ratio of the power of the incident over transmitted light by a sample. One can imagine measuring these quantities with one light source and two photodetectors arranged as presented in the figure 2.18.

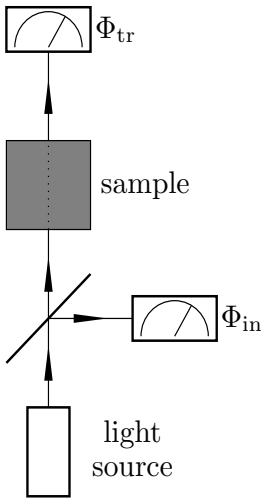

Figure 2.18: Measurement model.

However, the idealized relationship $OD = \log_{10}\left(\frac{\Phi_{in}}{\Phi_{tr}}\right)$ is not valid in the real world where neither light source or detectors are ideal. The light source emits variable amounts of light, and the detectors do not necessarily have the same gain, and also measure different background noises.

The photodetectors can be activated with the sample out of the light path, and with or without light. This mode can be used

to understand the behaviour of the different components of the design.

A series of 50 flashes was recorded, with light off, and with light on. With light off, $\Phi_{in} = 417 \pm 3$ and $\Phi_{tr} = 620 \pm 8$. With light on, $\Phi_{in} = 41688 \pm 1058$ and $\Phi_{tr} = 41283 \pm 1056$ (average $\pm$ standard deviation). The variability of the values with light on can seem important, and an important question is to determine where it comes from.

Although the measurements of incident and transmitted light with light off seem uncorrelated (correlation coefficient of 0.22), they are extremely correlated with light on (correlation coefficient of $1 - 10^{-4}$). This shows that most of the variability in the measurements comes from the light source and not from the detectors.

More formally, if x is the power emitted by the light source, then we can model the value measured by the incident light detector as

$$\Phi_{in} = G_{in}\, x + O_{in}$$

with G_{in} the gain of the detector and O_{in} its offset value due to background noise. Similarly,

$$\Phi_{tr} = G_{tr}\, x\, 10^{-OD} + O_{tr}$$

if OD is the optical density of the sample.

It is useful to make a calibration run with the sample out of the light path, to obtain values that we will call B for black (light off) and W for white (light on), where z (different from x) marks the power sent by the light source to perform this particular measurement:

$$B_{in} = O_{in} \quad B_{tr} = O_{tr} \quad W_{in} = G_{in}\, z + O_{in} \quad W_{tr} = G_{tr}\, z + O_{tr}$$

Extracting the value of OD from these measurements requires the use of all of these variables, and it can be verified that in these conditions,

$$\boxed{OD = \log_{10}\left(\frac{\Phi_{in} - B_{in}}{\Phi_{tr} - B_{tr}} \cdot \frac{W_{tr} - B_{tr}}{W_{in} - B_{in}}\right)}$$

The detectors are here supposed noiseless, but it would be interesting to investigate how to explicitly handle measurement noise, and how to make the best use of several measurements.

From our investigations it appears that SparkControl uses this formula, but with for Φ_{in} and Φ_{tr} respectively the average of the incident and transmitted light beams.

It is not very clear why taking the average of the intensities first, and then computing the OD would be better than computing the OD for all the reads, and then taking the average of the ODs obtained.

As a first approach, we did compute the individual ODs for each reading, from what we extracted not the average but the median, in order to limit the influence of outliers.

2.2.2 Design of the library `platerider`

We implemented a driver and API for the plate reader in about a thousand significant lines of code, in the programming language Python 3.

Logging is done both to the terminal (at a configurable level) and to a file (at the most detailed level), such as to not clutter the terminal with logging information, but still have everything recorded in case of need. In fact, the library has a replay mode where it reads an existing log file in place of the plate reader, replaying the exchange as it happened. This mode was especially useful for debugging.

The code is structured as follows

```
platerider/
  __init__.py           320 sloc
  bufread.py             80 sloc
  errors.py              30 sloc
  util.py                50 sloc

  module.py             150 sloc
  absorption.py         200 sloc
  fluorescence.py        10 sloc
  injectors.py           90 sloc
  plate_transport.py    140 sloc
```

`__init__.py`

This file is the entry point of every library in Python. It defines a class `Spark` and the code necessary to detect the plate reader, perform the initialization dialogue, and create as many objects as there are modules (absorption, fluorescence, plate transport, injectors). A short extract of this file is featured below.

```
class Spark:
    def __init__(self, cassette: bool = False) -> None:
        # skipped lines
        self.cassette = cassette
        self.abs = absorption.Absorption(self)
        self.flu = fluorescence.Fluorescence(self)
        self.plt = plate_transport.PlateTransport(self)
        self.inj = injectors.Injectors(self)
        LOGGER.info('Modules acquired and configured')

    def __enter__(self):
        self.plt._send_raw(b'\x02\x00\x00\x00\x02')
        LOGGER.info('Hello?')
        msg = self.plt.read(timeout=3)
        assert len(msg) == 0
        LOGGER.info('Hello!')
        sel.plt.check('?INSTRUMENT STATE', 'STATE=READY')
        LOGGER.info('Instrument ready.')
        # skipped lines
```

bufread.py

The file `bufread.py` implements the class `BufferedReader`, which is a wrapper around a USB reader, with a buffer that it uses to fix broken messages or messages that arrive in several USB packets. It runs in its own thread and continuously polls its attributed USB endpoint, stacking them up in a queue in case they are not read fast enough. This avoids the loss of messages written over by the next one in the USB port. A simplified implementation is reproduced below.

```
class BufferedReader(Thread):
    """ Runs in a thread, listens to the specified endpoint,
    fixes incomplete and multiple packages and buffers them.
    """
    def __init__(self, endpoint) -> None:
        Thread.__init__(self)
        self.endpoint = endpoint
        self.messages = queue.Queue()
        self._is_running = True
        LOGGER.info('Buffered reader created.')

    def run(self) -> None:
        LOGGER.info('Buffered reader running.')
        while self._is_running:
```

```
            try:
                packet = self._read()
                self.messages.put(packet)
            except usb.USBError:
                pass
        LOGGER.info('Buffered reader stopping.')

    def stop(self) -> None:
        LOGGER.info('Asking buffered reader to stop.')
        self._is_running = False

    def read(self, block: bool = True, timeout: int = None):
        return self.messages.get(block=block, timeout=
            timeout)

    def _read(self, timeout: int = 1000):
        # Calls 'self.endpoint.read' sufficiently many times
        # to get a complete message, checks that it is well-
        # formed and not corrupted before returning it.
```

errors.py

This file defines the errors used in the module, for example `USBTimeoutError` raised when the plate reader does not answer, or `ModuleTimeoutError`, when the plate reader says that one of its internal modules does not answer.

util.py

The file `util.py` contains the definition of two decorators used to lift and close the lid automatically. Decorators in Python are wrappers around functions. Some functions of the plate reader can only be done with the lid of the plate open, such as dispensing reagents with the injectors, or measuring the absorbance of some wells (if the humidity cassette was used). In order to avoid repeating the code for the lid opening or closing for each function that needs it, Python offers the possibility to annotate them with these decorators (examples of their use are given in the file `absorption.py`):

```
from functools import wraps

def needs_lid_open(function):
    "Decorator to mark that this method needs the lid open."
    @wraps(function)
```

```
    def wrapper(self, *args, **kwargs):
        if self.spark.cassette:
            self.spark.plt.lid_lift()
        return function(self, *args, **kwargs)
    return wrapper
```

module.py

This file defines the abstract class `Module`, that `Absorbance`, `Fluorescence`, and `PlateTransport` inherit of. It contains the code to initialize the module, retrieve its USB endpoints and communicate with it. The module exposes among others the functions `check(command, answer)` that sends a command and verifies that the answer is the one expected, `ask(command)` that sends a command and returns the answer. Every incoming and outgoing communication is logged automatically.

absorption.py

The file `absorption.py` specializes the class `Module` for its absorbance configuration. Notably, it adds a function to make the calibration described in 2.2.1, as well as functions to measure the optical density of a well, a row of wells, or the entire plate. A short extract is featured below.

```
class Absorption(module.Module):
    def __init__(self, spark) -> None:
        super().__init__(spark, idvendor=0x0c47,
                         idproduct=0x8026)
        self.bin = None
        self.btr = None
        self.win = None
        self.wtr = None

    def od(self, inc: float, tra: float) -> float:
        return np.log10(
            (inc - self.bin) / (tra - self.btr) *
            (self.wtr - self.btr) / (self.win - self.bin))

    def prepare_reference(self) -> None:
        "Fills up bin, btr, win, wtr"
        # skipped lines

    @util.needs_lid_open
    def scan_well(self, well: util.Well) -> float:
```

```
        x, y, z = well.xyz()
        self.spark.plt.send(f'SCAN X={x} Y={y} Z={z}')
        # skipped lines
        msg = self.read()
        lights = list(struct.iter_unpack('>HH', msg))
        ods = [self.od(i, t) for i, t in lights]
        # skipped lines
        return np.median(ods)
```

fluorescence.py

I never used the fluorescence module, so the code for this module is not implemented yet.

plate_transport.py

This file implements the communications with the plate transport module, which is the most important as it centralizes and coordinates the work of the other modules, and also forwards information about temperature and motors. A few representative functions of this module as reproduced below.

```
class PlateTransport(module.Module):
    def __init__(self, spark) -> None:
        super().__init__(spark, idvendor=0x0c47,
                         idproduct=0x8028)

    def hwbutton(self, enable: bool,
                 button: str = 'ALL') -> None
        action = ['DISABLED', 'ENABLED'][enable]
        self.check(f'HWBUTTON {button}={action}')

    def plate_out(self, side: str = 'RIGHT') -> None
        self.check(
            f'ABSOLUTE MODULE=MTP POSITION=OUT_{side}')

    def plate_in(self) -> None
        self.check(
            f'ABSOLUTE MODULE=MTP POSITION=PLATE_IN')

    def shake(self, mode: str = 'LINEAR',
              amplitude: int = 800,
              frequency: int = 240,
              duration: int = 3) -> None:
        self.check(
            'ABSOLUTE MODULE=MTP POSITION=INCUBATION')
```

```
        self.check(f'MODE SHAKING={mode}')
        self.check(f'SHAKING AMPLITUDE={amplitude} '
                   f'FREQUENCY={frequency}')
        self.check(f'SHAKING TIME={duration}')
        LOGGER.info(f'Shaking starts ({duration} s).')
        self.check('SHAKING STARTS', timeout=duration+2)
        LOGGER.info('Shaking ends.')
```

2.2.3 Applications of `platerider`

Basic example

This library enables the full control of the plate reader in a convenient way. For example, the full script that sets the incubation temperature to 37 °C, takes the plate in, and measures the full plate 400 times, then dispenses antibiotics in some of the wells as a function of the latest plate measurement, with 5 minutes of incubation between each measurement is the following:

```
from platerider import Spark

with Spark(cassette=True) as spark:
    spark.set_temperature_control(37)
    spark.plt.plate_out()
    input('Place plate on tray and press Enter.')
    spark.plt.plate_in()
    for _ in range(400):
        plate = spark.abs.measure_plate()
        injections = compute_injections(plate)
        for well, volume in injections.items():
            spark.inj.inject(well, disp_vol=volume)
        spark.plt.incubate(duration=300)
```

The full log is automatically saved in a file `.log`, the plate measurements are also automatically saved in a file `.csv`, as well as the injection log that is saved in another `.csv` file. Because of the dynamic nature of the protocol, this program is impossible to implement with the official software.

Dilution helper

One of the most common tasks in any microbiology laboratory is the dilution of an overnight culture to a specific optical density. Because of the non-linearity of OD (see 2.1.4), when the initial culture is of high density, it is advised to first bring it to an

intermediate OD (around 0.1), and then to the target density, in order to improve the precision of the dilution.

It is to the experimentalist to figure out the dilution factors for these two dilutions. Although not difficult, this task is somewhat tedious and prone to mistakes. The existence of a plate reader API allowing to write any arbitrary program is ideal to remedy this situation.

We wrote a command-line utility to automate this process and make it more efficient and accurate. It takes arguments to select a blank well (one filled with only medium and no cells), the target optical density desired, and the target dilution volume. The script corrects for the quadratic nonlinearity measured in 2.1.4 with a quadratic coefficient of -0.2. For example, the command to generate the instructions to follow to obtain1 mL of culture at an OD of 0.05 is the following, assuming that the blank well is F1 and the wells containing the cultures to dilute are F2 and F3:

```
dilution --blank F1 --target 0.05 --volume 1 F2 F3
```

2.3 CHAPTER SUMMARY

This chapter detailed all the work necessary for the obtention of high-quality experimental data. As explained in section 1.1, the data consists mostly of OD growth curves acquired with an optical plate reader, but it is supplemented by cell counting experiments in order to assess and challenge the model.

In a first part, we lay out our experimental setup, starting with the medium composition that we chose to measure only what is directly relevant to antibiotic resistance (2.1.1). Then, we discuss the influence of the history of the cell culture at the start of the experiment (2.1.2). In the next subparts, we focus on issues more directly related to the measuring devices: how to optimize measurements to minimize water evaporation (2.1.3), and how to correct for the non-linearity of OD measurements (2.1.4). Finally, we introduce a bayesian method of cell counting allowing to compute confidence intervals on the results, starting from one plate, and also able to combine several plates (2.1.5).

The second part of the chapter is dedicated to the reverse-engineering of the plate reader. After a tutorial on reverse-engineering a USB device, we present the library `platerider` that we developed, serving as an API allowing to programmatically

control the plate reader. Finally, we show a couple of practical applications of `platerider`.

3 RESISTANCE MODELS

As argued by Allen and Waclaw (2016), Lukačišinová and Bollenbach (2017), Lopatkin and Collins (2020) and others, quantitative modelling is a tool so important in physical and life sciences that some phenomena can escape understanding until proper care is given to the development of an appropriate mathematical model. Multiscale systems almost always fall in this category, and the development of their models is often challenging at the same time conceptually, mathematically and numerically. Although bacteria are one of the simplest life forms that we know, they possess several thousands of genes (Serres et al. 2001) and about the same number of encoding proteins. This creates several millions of potential biochemical reactions, that all happen at the same time, and of which we can observe only a fraction, with highly specialized methods.

The interactions between molecules, characterized by reaction rates and molecular constants, combine at the microscopic level of a cell into processes involving cell-level structures like cell compartments, cell wall, or microscopic quantities like the length of a cell. Further, bacteria live in populations, whether dense as in biofilms, or spread as in liquid cultures, whose macroscopic features are not to be neglected to understand the full behaviour of the system.

None of these three scales —molecular-, cell- and population-level— should be overlooked in a model with the ambition to capture the main features of the system. However, although full mappings of one level at a time have been attempted (Bhat and Balaji 2020), modelling perfectly more than one level at the same time seems irrealistic. Modelling in biology is then the art of formulating a problem, setting a bar, and knowing to pick not too little nor too much in order to answer the original question.

The goal of this chapter is to present the models that we developed during this thesis, but also the reasons that led us to add new resistance models to an growing collection, and the process that enabled us to build one, followed by another. After a short review on the current models of cell populations and of antibiotic resistance, we describe the limitations of existing models that we wanted to overcome with our approach. Then,

we explain how we adapted, modified and configured a generic growth-fragmentation model to fit our system of study, and verify that the resulting model complies with notable experimental observations. However, the simulation of this model is too costly and prevents an adequate calibration to experimental data. In a last part, we show how to decrease the complexity of the model while conserving its main features, by reducing the simulation of a whole distribution to the simulation of its first moments only.

3.1 STATE OF THE ART IN BACTERIAL POPULATION MODELLING

The dynamics of a population of cells treated with antibiotics can only be understood knowing how untreated cells grow (section 3.1.1), the molecular and cell-level actions of antibiotics (section 3.1.2), and also the modes of defence of bacteria, which includes the population effects (section 3).

3.1.1 Models of growth

The first non-trivial situation to study is the simple growth of cells in a liquid culture medium. The exponential growth is one of its most typical features (Neidhardt 1999).

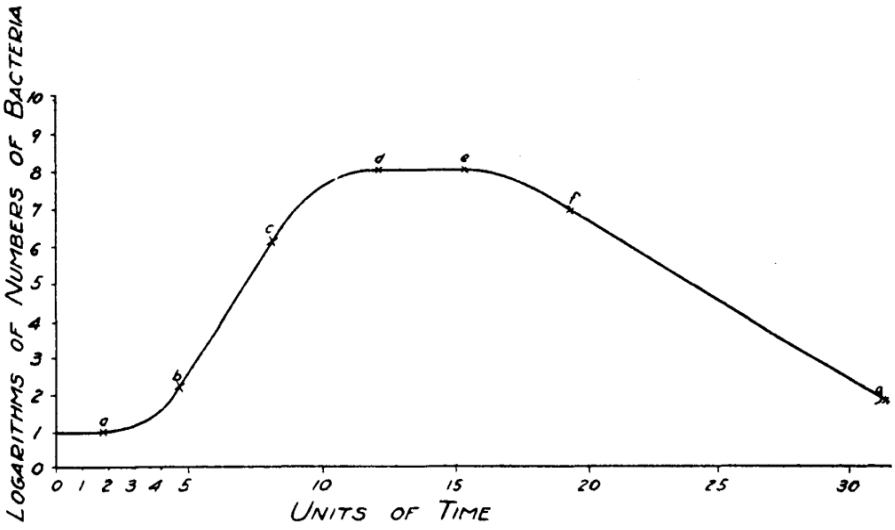

Figure 3.1: Schematic of a typical growth curve (Buchanan 1918).

Besides exponential growth, the typical growth curve is composed of several successive phases, including, such as pictured in figure 3.1:

- lag phase: the part leading to exponential growth, where the growth rate is ramping up (ab);
- exponential growth, featuring constant growth rate (bc);
- stationary phase: the part with null growth rate (de),

The universality of this curve is remarkable. Shared by most living beings including humans (Roser, Ritchie, and Ortiz-Ospina 2013), it also applies to the spread of inanimate objects such as viruses, fashions or cultural trends.

It has been extensively studied, qualitatively and quantitatively, with the first breakthrough probably being made by Monod (1941) who found an empirical mathematical relation between the concentration of nutrients in the culture medium s, and the growth rate of the bacterial population feeding on it μ, the famous Monod equation:

$$\mu = \frac{s}{K_s + s}$$

where K_s is the concentration of nutrient enabling the microorganism to grow at half its maximal speed.

Despite its age and some criticism (Condrey 1982), the Monod equation is still overwhelmingly used to model the growth of microorganisms, and efforts to improve it are generally failing to gain traction, probably because of the diminishing return that a complexification of this equation would bring (Lendenmann et al. 2000). The competing framework to model cell growth is the family of logistic functions, where the limiting growth factor is not the depletion of the nutrients but the overcrowding of the culture medium (Zwietering et al. 1990).

However, extensions to the Monod equation have been proposed to also describe the growth of cells over several substrates at the same time, situation known to provoke multiple successive exponential phases (Tsao and Hanson 1975; Egli, Lendenmann, and Snozzi 1993).

As basic as this system may seem, it already hides a great complexity. Further complexity lies in the relationship between the individual and population scales. Firstly, the individual growth rate of a cell shows periodic perturbations induced by the cell cycle. But even individual growth rates averaged over the cell cycle are in general different from one cell to another

in the same population. To a given distribution of individual growth rates corresponds a population growth rate which is in general not the average growth rate of the cells (Hashimoto et al. 2016).

3.1.2 Models of antibiotic effect

An antibiotic is a substance that disrupts one or several of the biochemical processes at play within a bacterium cell, leading to a stop or a slowing down of its growth (bacteriostatic antibiotics), or to its death (bacteriolytic antibiotics).

Several classes of antibiotics exist, that target different processes of the cell (Finberg et al. 2004). The main targeted system by the bacteriostatic antibiotics is the protein synthesis machinery (this is the mode of action of tetracyclines, chloramphenicol, macrolides, oxazolidinones, lincosamides and streptogramins). Antibiotics with a bacteriolytic action may target the synthesis of the cell wall (β-lactams or glycopeptides), the properties of the cell membrane (lipopeptides), the DNA replication (quinolones) or RNA synthesis (ansamycins).

β-lactams are one of the clinically most important classes of molecules, and were estimated to have saved directly between 80 and 200 million lives in under 80 years. Although their general mechanism of action, through interfering with the cell wall synthesis, has been known for decades, molecular details of their mechanisms, or of the role of the enzymes that they target, Penicilin Binding Proteins (PBPs), keep being discovered until today (Chung et al. 2009; Cho, Uehara, and Bernhardt 2014; Wu et al. 2014; Vigouroux et al. 2020).

Penicillin-binding proteins

A thorough review on the roles of PBPs can be found in (Sauvage et al. 2008). In *E. coli*, the consensus is that PBP3 is exclusively required for cell division (Botta and Park 1981). Inhibition of PBP3 consequently results in cell filamentation (Buijs et al. 2008). Besides PBP3, and with different affinities, β-lactams also target PBP1 and PBP2. The morphological effects induced on the cells at different antibiotic concentrations can allow to determine the relative affinities of an antibiotic on these three enzymes (Spratt 1975). The enzymes PBP1 and PBP2 are respectively involved in the reparation of wall defects (Vigouroux et al. 2020) and the maintenance of the rod cell shape (Sauvage et al. 2008).

Inhibition of PBP1 results in rapid cell lysis (Buijs et al. 2008), while inhibition of PBP2 makes cells spherical.

PBPs and β-lactams react together with an acyl-enzymatic reaction that consumes the antibiotic (Chambers, Sachdeva, and Hackbarth 1994). The PBP is inactivated while bound in the complex, which is relatively stable.

Multi-scale interactions

Even with the perfect knowledge of molecular processes, the story would be incomplete without the study of the effects that are implied at the cell level. A notable characteristic of β-lactams, because of their interference with the cell wall mechanisms, is to dramatically change the shape of the treated bacteria, creating either filaments or spheroids, depending on the main target PBP of the drug (Greenwood and Eley 1982; Buijs et al. 2008; Fredborg et al. 2015). As put by Greenwood (1977), "unless morphological observations are made, important features of antibiotic response may be missed."

A cell-level view is necessary to complement the understanding of molecular processes, as illustrated by the phenomenon of phenotypic tolerance. A cell is said to exhibit phenotypic tolerance when its current physiological state allows it to tolerate antibiotics. Non-growing cells (also called persisters), are prime examples of phenotypic tolerance (Wood, Knabel, and Kwan 2013), as well as auxotrophic cells (Elaine Tuomanen 1986).

The presence of persisters in a population brings the need to consider a third plane of interest: the level of the population itself. Indeed, a genotypically homogeneous, but phenotypically heterogeneous cell population made of sensitive cells and persisters, might recover thanks to stochastic awakening of the persisters (Windels et al. 2019), once the antibiotic passed. The dynamics of the population then cannot be understood by only considering molecular or cell-level processes. A complete model of the response of cells to antibiotics must then include aspects of the three levels: molecular, cell, and population (Allen and Waclaw 2016).

3.1.3 Antibiotic resistance models

As put by Levy and Marshall (2004), on the 15 known classes of antibiotics, none has escaped to resistance so far. Resistance mechanisms are of diverse origins and modes of actions (Hogan

and Kolter 2002). Among the most common are the expression of efflux pumps extracting antibiotics out of the cell, modification of porins or cell permeability to antibiotic, modification or change of the target protein to foil the antibiotic attacks. The acquisition of these defences can be made by *de-novo* mutation or horizontal gene transfer (transfer of genetic material between cells of the same population).

Biofilms, or compact 3-dimensional bacterial assemblies are also known to defy antibiotic treatments. The limited antibiotic penetration, the accumulation of resistance enzymes and the decreased growth rate are all factors increasing the tolerance of a biofilm to antibiotics, making them effective illustrations of CAT.

The major mechanism of defence for Gram-negative against β-lactams is the secretion of an enzyme able to actively degrade the antibiotic: the β-lactamase (Bush 2018). Reported almost at the same time as the beginning of use of antibiotics (Abraham and Chain 1940), a range of enzymes as varied as the antibiotics themselves has now been observed in bacteria around the world (Bush and Jacoby 2010).

β-lactamases are not only active in the cell, but also outside. Indeed, once produced in the cytoplasm, β-lactamases are transported through the cytoplasmic membrane. In gram-positive bacteria, β-lactamases can either adhere electrostatically to the cell wall, or be released in the cell culture. In gram-negative bacteria, that possess another membrane outside of the cell wall, they are not released outside the cell until the cell lyses (Livermore 1997).

In both cases, once in the environment, β-lactamase is able to degrade the antibiotic that has not yet entered cells. This mechanism can lead to a curious dynamics: the more cells are lysed in the first place, the more enzyme is released, and the more effective is the antibiotic degradation. β-lactamases are one of the possible explanations of the Eagle effect, a paradoxical degradation of an antibiotic efficiency at high doses (Eagle 1948; Eagle and Musselman 1948).

This already links the three scales again: a molecular factor is released into the environment at the occasion of cell lysis, and degrades then the remaining antibiotic for the benefit of the population. Most resistance phenomena are direct consequences of the deep interconnection of the molecular, cell and population levels (Srimani et al. 2017; Artemova et al. 2015).

Different approaches have been tried in order to describe the variety of possible responses of bacterial populations to antibiotic treatments. Bottom-up approaches simulating individual cells in order to generate a population dynamics include cellular automata (Ben-Jacob et al. 1994) and agent-based simulations (Murphy, Walshe, and Devocelle 2008). This angle elegantly illustrates the emergence of complexity, but requires massive computational resources. On the opposite, top-down approaches explicit the dynamics of state variables such as the population size. More efficient from a computational point of view, they often take the form of systems of ODEs. They however hardly cover more than the population scale, ignoring largely the molecular and cell levels and thus cannot be rich enough to encompass the full spectrum of the antibiotic response. Between these two kinds of approaches, PDE models can bridge the scales of population and individual, by considering a spatial dimension as in the case of biofilms or cultures on gelose, or describe a heterogeneity in the population (Pienaar et al. 2009).

However, starting this thesis, we did not know of a model rooted in molecular mechanisms, considering the changes in the cell morphology subsequent to these processes, and describing population-level observables accessible by measurement such as optical density or number of viable cells. This chapter is dedicated to the development of such a model.

3.1.4 A resistance and resilience model

Most recently, in collaboration with Hannah R. Meredith et al. (2018), we contributed to the development, calibration and interpretation of a model of antibiotic resistance allowing us to introduce to the community the notion of resilience, borrowed from ecology.

Calibrating this model to clinical isolates, a global sensitivity analysis allowed us to classify its parameters into the ones contributing mostly to resistance, or mostly to resilience.

However, this first model conflates the notions of number of cells and optical density into a single variable n, ignoring the filamentation that can cause the optical density to increase while n remains constant. Moreover, it makes the assumption that the bacteriolytic action of the antibiotic is immediate. Indeed, as soon as the variable a is updated with the concentration of antibiotic in the medium, the lysis rate l becomes positive, which causes an instantaneous decrease of the net growth rate $g - l$,

and an increase of everything that is a consequence of cell lysis, such as releasing of β-lactamase or recycled nutrients in the culture medium.

As shown on figure 3.2, we know from growth curves that the effect of antibiotic treatment on the optical density can follow the treatment by several hours, and we also know from CFU counts that the antibiotic can immediately stop the growth of the number of cells, but does not make this number decrease until the moment when the optical density drops too.

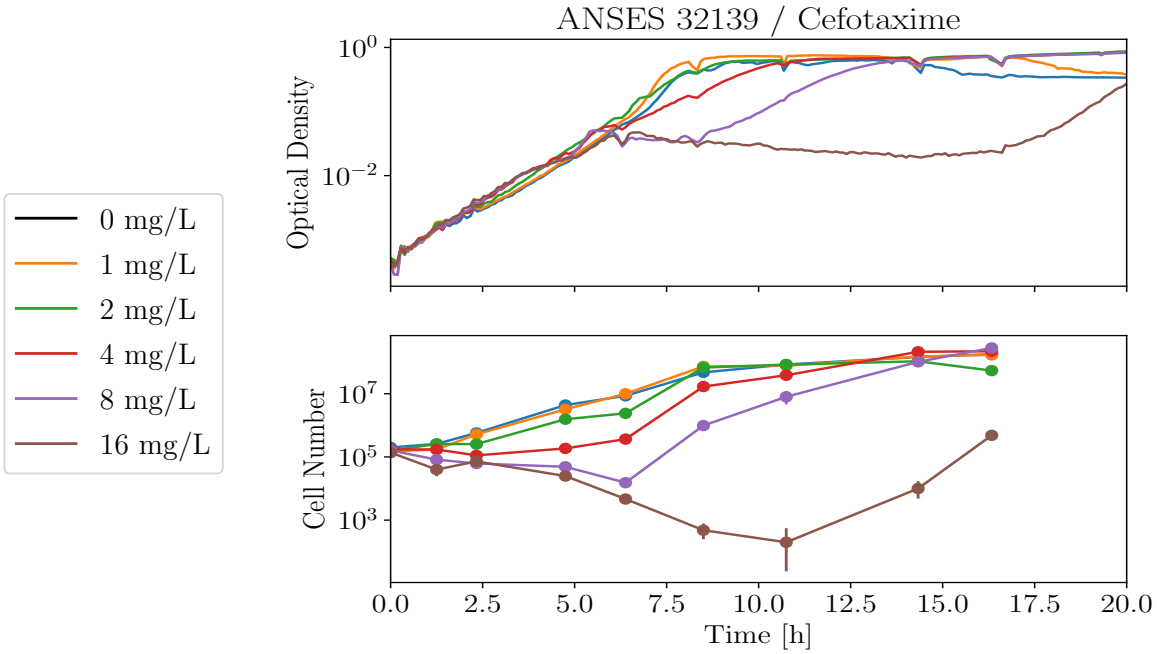

Figure 3.2: Simultaneous measurements of optical density and number of cells for a resistant strain treated at $t = 0$ with increasing doses of cefotaxime. The error bars are the 95% confidence intervals computed with the method in section 2.1.5.

The inability for the model to describe the first "lag" phase, before the antibiotic-induced death affects the OD, forced us to set the initial time of our simulations at the moment when the OD drops, on this graph at $t = 6$ h. Starting from this point, we could model the rest of the OD but parameters obtained from fitting this model were difficult to interpret biologically, because the number of viable cells at this point depends strongly on the antibiotic dose, in a range covering two or three orders of magnitude.

Moreover, not being able to simulate the bacterial response for 3 to 6 hours following the addition of antibiotic prevents the

simulation of experiments involving repeated treatments, which are the basis for the search of optimal treatment regimens.

The inability to properly calibrate biologically meaningful parameters, the awkwardness of ad-hoc manual fitting procedures, the impossibility to access the actual number of cells, and the inability to simulate the entirety of the bacterial response, then pushed us to search for an improved model.

3.2 A TOLERANCE, RESISTANCE AND RESILIENCE MODEL

3.2.1 The growth-fragmentation equation

Hall and Wake (1989) popularized in mathematical biology a fundamental equation otherwise known as growth-fragmentation, describing the distribution of entities experiencing continuous growth and sudden divisions. This framework seems perfectly suited to describe a bacterial population, especially when the length of the cells takes an important role in their dynamics, like in our system where antibiotics cause the cells to filament, which affects their viability as well as their optical density.

Hall and Wake (1989) start with a very general setting where the density of cells of length ℓ at time t is represented by the function $n(\ell, t)$[1]. Formally, for an infinitesimally small $\mathrm{d}\ell$, if $N_{[\ell,\ell+\mathrm{d}\ell]}(t)$ is the number of cells of length comprised between ℓ and $\ell + \mathrm{d}\ell$ at time t, then

$$N_{[\ell,\ell+\mathrm{d}\ell]}(t) = n(\ell, t)\,\mathrm{d}\ell$$

The cells experience a continuous elongation with a speed $g(\ell, t)$ that depends on their length. This means that $g(\ell, t)$ is the temporal derivative of the length ℓ of a cell.

With a rate $f(\ell, t)$ that also depends on its length, a cell also experiences fission into α cells of equal sizes (each of them a fraction $1/\alpha$ of the dividing cell). The original paper did not include a death rate, but we will add it as $d(\ell, t)$, as it is necessary to account for the effect of a bacteriolytic antibiotic.

The division rate in the original paper is noted $b(\ell, t)$. We changed it here to $f(\ell, t)$ because b is more natural for β-lactamase.

To derive the PDE, it is useful to draw a diagram with the flows between infinitesimal elements, like in figure 3.3.

1 Formally, this means that at time t, the number of cells of length comprised between ℓ and $\ell + \mathrm{d}\ell$ is equal to $n(\ell, t)\,\mathrm{d}\ell$, in the limit where $\mathrm{d}\ell$ tends to zero.

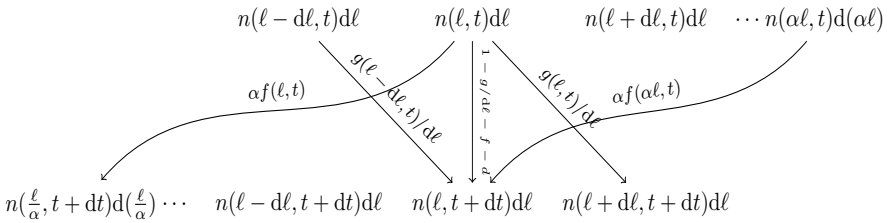

Figure 3.3: Diagram of the flows between infinitesimal elements. Contributions to $n(\ell, t + \mathrm{d}t)\,\mathrm{d}\ell$ come from the neighbouring infinitesimal elements, and also from $n(\alpha\ell, t)\,\mathrm{d}(\alpha\ell)$, the element containing the cells of sizes $\alpha\ell$ to $\alpha\ell + \alpha\,\mathrm{d}\ell$ that can divide into cells of sizes ℓ to $\ell + \mathrm{d}\ell$.

This schematic allows to establish the infinitesimal equation

$$\begin{aligned} n(\ell, t + \mathrm{d}t)\,\mathrm{d}\ell = {} & n(\ell - \mathrm{d}\ell\,, t)\,\mathrm{d}\ell\; g(\ell - \mathrm{d}\ell\,, t)\frac{\mathrm{d}t}{\mathrm{d}\ell} \\ & + n(\ell, t)\,\mathrm{d}\ell \left(1 - g(\ell, t)\frac{\mathrm{d}t}{\mathrm{d}\ell} - f(\ell, t)\,\mathrm{d}t - d(\ell, t)\,\mathrm{d}t\right) \\ & + \alpha\, n(\alpha\ell, t)\,\mathrm{d}(\alpha\ell)\, f(\alpha\ell, t)\,\mathrm{d}t \end{aligned}$$

The first α in the term α^2 comes from the size $\alpha\,\mathrm{d}\ell$ of the infinitesimal element containing the cells of size $\alpha\ell$ that can divide into cells of size ℓ. The second α comes from the fact that each of these cells divides into α smaller cells. The correctness of this factor becomes clear in the calculation of the evolution of the total number of cells (equation 3.3).

that leads to the PDE

$$\frac{\partial n}{\partial t} + \frac{\partial (g\, n)}{\partial \ell} = -n(\ell, t) f(\ell, t) - n(\ell, t) d(\ell, t) + \alpha^2 n(\alpha\ell, t) f(\alpha\ell, t) \tag{3.1}$$

One can introduce here the variable $N(t) = \int_0^\infty n(\ell, t)\,\mathrm{d}\ell$ representing the total number of cells at the time t. As Hall and Wake (1989) state, as this study is done in simplified conditions with infinite nutrient supply, there is no non-trivial steady-state of this equation: only in very specific conditions will the number of cells remain constant. The interesting object is rather the normalized size distribution: $y(\ell, t) = \frac{n(\ell, t)}{N(t)}$, such that $\int_0^\infty y(\ell)\,\mathrm{d}\ell = 1$. Unlike n, which grows exponentially just like the number of cells, y is normalized and will stabilize to the stationary size distribution if it exists. If it exists, we can then separate variables and write $n_\infty(\ell, t) = y_\infty(\ell) N_\infty(t)$. Like Hall and Wake (1989), we will qualify this regime of *steady size* regime.

Hall and Wake (1989) then go on with the search of y_∞ in the particular case $f(\ell, t) = f$ and $g(\ell, t) = g$. But we can push the general case a bit further:

Equation 3.1 can be rewritten in terms of y:

$$\frac{1}{N}\frac{\mathrm{d}N}{\mathrm{d}t}y+\frac{\partial y}{\partial t}+\frac{\partial(g\,y)}{\partial \ell}=-y(\ell,t)f(\ell,t)-y(\ell,t)d(\ell,t)+\alpha^2 y(\alpha\ell,t)f(\alpha\ell,t) \tag{3.2}$$

It is possible to find an expression for $\frac{\mathrm{d}N}{\mathrm{d}t}$, by integrating equation 3.1 taking boundary conditions to forbid cells of zero or infinite sizes: $n(0,t)=n(\infty,t)=0$

$$\begin{aligned}\int_0^\infty \frac{\partial n}{\partial t}\,\mathrm{d}\ell+\int_0^\infty \frac{\partial(g\,n)}{\partial \ell}\,\mathrm{d}\ell &= -\int_0^\infty (f+d)n\,\mathrm{d}\ell+\int_0^\infty \alpha^2 n(\alpha\ell,t)f(\alpha\ell,t)\,\mathrm{d}\ell\\ \frac{\mathrm{d}N}{\mathrm{d}t}+[g(\ell,t)n(\ell,t)]_0^\infty &= -\int_0^\infty (f+d)\,n\,\mathrm{d}\ell+\alpha^2\int_0^\infty n(\ell,t)f(\ell,t)\frac{\mathrm{d}\ell}{\alpha}\\ \frac{\mathrm{d}N}{\mathrm{d}t}+0 &= \int_0^\infty (f(\alpha-1)-d)\,n\,\mathrm{d}\ell\end{aligned}$$

$$\text{hence}\quad \frac{\mathrm{d}N}{\mathrm{d}t}=N\int_0^\infty [(\alpha-1)f(\ell,t)-d(\ell,t)]y(\ell,t)\,\mathrm{d}\ell \tag{3.3}$$

The average length $L(t)=\int_0^\infty \ell y(\ell,t)\,\mathrm{d}\ell$ is an important quantity to compute. Integrating equation 3.2 after multiplying it by ℓ, we now need the boundary condition $\lim_{\ell\to\infty}\ell\,y(\ell,t)=0$. Because the integral of y is finite, y is integrable, which gives this limit. The detail of the calculations follows:

$$\begin{aligned}\frac{\mathrm{d}L}{\mathrm{d}t}+\int_0^\infty \ell\frac{\partial(g\,y)}{\partial \ell}\,\mathrm{d}\ell &= -\int_0^\infty (f+d)\ell\,y\,\mathrm{d}\ell\\ &\quad +\alpha^2\int_0^\infty \ell\,y(\alpha\ell,t)f(\alpha\ell,t)\,\mathrm{d}\ell-\frac{1}{N}\frac{\mathrm{d}N}{\mathrm{d}t}L\\ \frac{\mathrm{d}L}{\mathrm{d}t}+0-\int_0^\infty g\,y\,\mathrm{d}\ell &= -\int_0^\infty (f+d)\ell\,y\,\mathrm{d}\ell\\ &\quad +\alpha^2\int_0^\infty \frac{\ell}{\alpha}y(\ell,t)f(\ell,t)\frac{\mathrm{d}\ell}{\alpha}-\frac{1}{N}\frac{\mathrm{d}N}{\mathrm{d}t}L\\ \frac{\mathrm{d}L}{\mathrm{d}t}-\int_0^\infty g\,y\,\mathrm{d}\ell &= -\int_0^\infty \ell\,d\,y\,\mathrm{d}\ell-\frac{L}{N}\frac{\mathrm{d}N}{\mathrm{d}t}\end{aligned}$$

With equation 3.3, we get

$$\frac{\mathrm{d}L}{\mathrm{d}t}=\int_0^\infty [g(\ell,t)-(\alpha-1)f(\ell,t)L+d(\ell,t)L-\ell\,d(\ell,t)]y(\ell,t)\,\mathrm{d}\ell \tag{3.4}$$

Another quantity of interest is the optical density of the solution, which is proportional to its biomass: $OD \propto N\,L$ (Koch 1961). The net growth rate is defined by the logarithmic derivative of the optical density:

$$\frac{1}{OD}\frac{\mathrm{d}OD}{\mathrm{d}t} = \frac{1}{N\,L}\frac{\mathrm{d}N\,L}{\mathrm{d}t} = \frac{1}{N}\frac{\mathrm{d}N}{\mathrm{d}t} + \frac{1}{L}\frac{\mathrm{d}L}{\mathrm{d}t}$$

With equations 3.3 and 3.4, we obtain

$$\frac{1}{OD}\frac{\mathrm{d}OD}{\mathrm{d}t} = \frac{1}{L}\int_0^\infty [g(\ell,t) - \ell\, d(\ell,t)]y(\ell,t)\,\mathrm{d}\ell \tag{3.5}$$

We can see here that if g, f and d are chosen independent of time, y can reach a steady state y_∞. In this case, in the limit of large time, we have

$$N_\infty(t) \propto \mathrm{e}^{\lambda_0 t}$$
$$OD_\infty(t) \propto \mathrm{e}^{\lambda_0 t}$$
$$L_\infty(t) = \frac{\kappa}{\lambda_0}$$

$$\text{where } \kappa = \int_0^\infty [g(\ell) - \ell\, d(\ell)]y_\infty(\ell)\,\mathrm{d}\ell$$
$$\text{and } \lambda_0 = \int_0^\infty [(\alpha-1)f(\ell) - d(\ell)]y_\infty(\ell)\,\mathrm{d}\ell$$

are two constants independent of time. λ_0 is called the Malthus exponent. This shows, as expected, an exponential growth (or decay, depending on the sign of λ_0) of the number of cells and of the optical density, with the same growth rate λ_0.

The objective of the next three subsections is to find appropriate forms for the three functions of the model $g(\ell,t)$, $f(\ell,t)$ and $d(\ell,t)$. We will then find that α, the division factor, also needs a special treatment.

3.2.2 Elongation speed $g(\ell,t)$

Hall and Wake (1989) investigated the case of a constant elongation speed: $g(\ell,t) = g_1$. In this case, cells elongate at a speed that does not depend on their length. However, several studies showed (Collins and Richmond 1962; Rolinson 1980; Tanouchi et al. 2017) that the elongation speed of a cell is rather proportional to the cell length itself, and remains mostly unperturbed

by antibiotic treatment. As we saw in the last section, whether the elongation of a single cell constant or linear in ℓ, or any other function, y_∞ adapts to produce eventually an exponential increase of the number of cells and the optical density, of rate λ_0, which does not depend on g. One can then wonder where g, a single-cell quantity, can induce a change in N or OD, population-level variables.

The influence of g can be seen in the transient filamentation phase following an addition of antibiotic, where different elongation speeds can provoke different population-level behaviours.

Cell death can be ignored for a few hours following addition of antibiotic, because as we will see in 3.2.4, cells do not die until they reach a certain length.

Indeed, in this initial regime of a few hours, cell death can be neglected. The antibiotic affecting the division rate, let us imagine a concentration of antibiotic high enough to reduce this rate to zero. We will study how taking $f(\ell, t) = 0$ and $d(\ell, t) = 0$ affects the evolution of the number of cells, optical density, and of the average length of cells.

For the number of cells, equation 3.3 reduces to $\frac{\mathrm{d}N}{\mathrm{d}t} = 0$, which makes sense because new cells are only produced as a result of cell divisions. From equations 3.4 and 3.5, the average length and the optical density increase following

$$\frac{\mathrm{d}OD}{\mathrm{d}t} = N\frac{\mathrm{d}L}{\mathrm{d}t} = N\int_0^\infty g(\ell, t)y(\ell, t)\,\mathrm{d}\ell$$

With a constant elongation speed $g(\ell, t) = g_1$, we have

$$\frac{\mathrm{d}OD}{\mathrm{d}t} = N\frac{\mathrm{d}L}{\mathrm{d}t} = Ng_1$$

hence $L(t) = L(0) + g_1\,t$ and $OD(t) = OD(0) + N(0)\,g_1\,t$.

With a linear elongation speed $g(\ell, t) = g_e\,\ell$, we have

$$\frac{\mathrm{d}OD}{\mathrm{d}t} = N\frac{\mathrm{d}L}{\mathrm{d}t} = Ng_eL$$

hence $L(t) = L(0)\,\mathrm{e}^{g_e\,t}$ and $OD(t) = OD(0)\,\mathrm{e}^{g_e\,t}$.

As shown in figure 2.5, the OD in the initial growth phase is always exponential, which rules out the constant elongation speed, while a function of the form $g(\ell, t) = g_e\,\ell$ is compatible with the experiments.

In reality, we work in batch, so the growth conditions change drastically throughout the experiment. Bacterial growth transforms an initial state with fresh medium and available nutrients into a depleted environment unsuitable for more growth in about ten hours. The change of state of the growth medium has to be reflected in the growth rate of the population and one of the most common ways to do so is to use Monod's equation,

that relates the net growth rate of a cell population $G(t)$ to the concentration of sugar in the environment $s(t)$: $G(t) = \mu \frac{s(t)}{K_s + s(t)}$. The net growth rate of the population is the logarithmic derivative of the optical density, the quantity shown on equation 3.5. Ignoring death for an instant and taking $g(\ell, t) = g_e \, \ell$, we can compute

$$\begin{aligned} G(t) &= \frac{1}{OD} \frac{\mathrm{d}OD}{\mathrm{d}t} \\ &= \frac{1}{L} \int_0^\infty g_e \, \ell \, y(\ell, t) \, \mathrm{d}\ell \\ &= \frac{g_e}{L} \int_0^\infty \ell \, y(\ell, t) \, \mathrm{d}\ell \\ G(t) &= g_e \end{aligned}$$

This shows that in reality, we have to consider g_e not as a constant but as a function of time, which we just determined as being equal to $G(t)$. Hence, our final elongation speed is

$$g(\ell, t) = G(t) \, \ell = \mu \frac{s(t)}{K_s + s(t)} \ell \tag{3.6}$$

3.2.3 Division rate $f(\ell, t)$

The original article of Hall and Wake (1989) considers the division rate constant and independent of ℓ. Even outside the antibiotic context, this assumption can seem a little strong and disconnected from biological realities. Indeed, it is well established that cells do not divide at any time, but only during a particular phase of the cell cycle (J. D. Wang and Levin 2009). However, tracking the details of the cell cycle for each cell would require the model to account not only for the length of the cells but also for their cell-cycle age. In practice, similar models with a continuous division rate, smoothed over the cell cycle, manage to approximate the steady-state distribution to a satisfying amount (Cullum and Vicente 1978).

In fact, it is difficult to see how to improve substantially the model while conserving a similar complexity for the division rate, or what benefits a complexification of this function would bring. We will then take

$$f(\ell, t) = f(t)$$

where the dependency in t stands for the effect of the antibiotics and remains to be determined. As shown by several studies, one of the actions of β-lactams is to bind to PBP3, disrupting the activity of the division machinery (Chung et al. 2009; Cho, Uehara, and Bernhardt 2014). The question is then to quantitatively link the concentration of antibiotics in the solution to the division rate of the cells.

The binding of β-lactams to PBPs follows Michaelis-Menten kinetics, this result in a proportion of inactivated PBPs equal to $\frac{a}{k_1+a}$ (Chambers, Sachdeva, and Hackbarth 1994). Although the division rate of the cells has to depend on the ratio of functioning PBPs, there is no reason to believe that this dependency should be linear. To model this relation, we decided to use a generalization of the Michaelis-Menten dynamics: a Hill function. We therefore chose to model the division rate as a Hill function parameterized by three values: the maximal division rate β, the half-rate parameter k_1 and the Hill exponent h_1.

$$f(\ell, t) = \frac{\beta}{1 + \left(\frac{a(t)}{k_1}\right)^{h_1}} \tag{3.7}$$

3.2.4 Death rate $d(\ell, t)$

Cell death is intuitively associated to antibiotic activity. But in the case of β-lactams, the main direct antibiotic activity seems to be the disruption of the PBP activity, which is not directly lethal for the cell. A recent article (Vigouroux et al. 2020) shows that PBPs normally act to repair defects that naturally occur in the cell wall. Such defects left unattended could eventually cause the death of the cell.

The careful observation of the initial growth phase under antibiotics, until death occurs, for several strains including sensitive and resistant ones, can help to develop an intuition of the death mechanism.

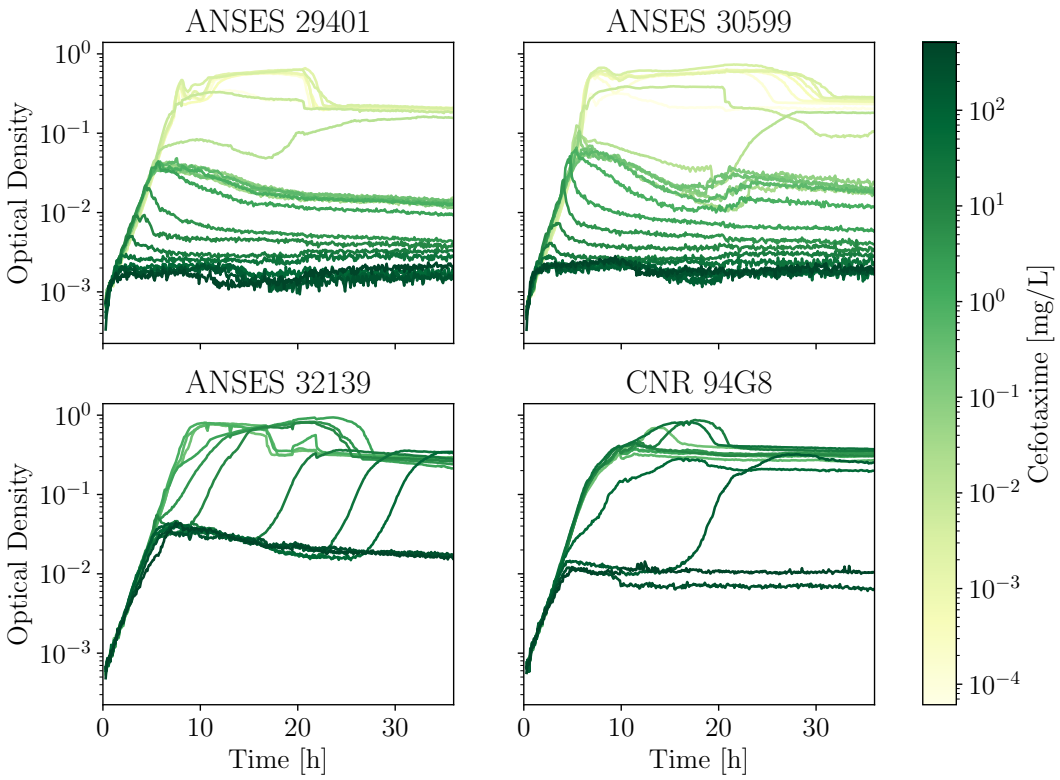

Figure 3.4: Four strains grown in the same conditions, with different initial amounts of cefotaxime. The two on the top do not possess resistance genes and are then sensitive (low MIC). The two on the bottom have the β-lactamase CTX-M-15, and CNR 94G8 additionally has OXA-181. They can be qualified as resistant strains (high MIC).

As shown in figure 3.4, the death phase seems to obey two different behaviours depending on the resistance of the strain. For weakly resistant strains, the death phase is triggered earlier with increasing antibiotic doses. For highly resistant strains, the death phase timing does not depend on the antibiotic quantity. An intermediate behaviour is observed for some mildly resistant strains. In all cases, the brusque change in net growth rate indicates that death is never established progressively but rather abruptly, like if $d(\ell, t)$ jumped suddenly from 0 to a non-null positive value that we will call γ, a constant independent on the antibiotic concentration. We now need to understand what causes this jump.

One possible explanation is a time delay, necessary for the cells to die after being penetrated with antibiotic. In this hypothesis, a series of biochemical reactions taking a given amount of time are proceeding and eventually lead to the cell lysis, in-

dependently of its other activities. As shown by the response of the sensitive strains in figure 3.4, the antibiotic, at high dose, has the ability to act almost instantly on sensitive cells: this delay would then decrease with increasing concentrations of antibiotic.

Another possible explanation is a mechanism triggered by the length of the cell. In this hypothesis, cells filament until they reach a critical length which they cannot sustain any more under this amount of antibiotic. This critical length decreases with increasing doses of antibiotic for sensitive cells, but does not depend on the antibiotic concentration for strains expressing a β-lactamase.

Whether the delay is time-based or length-based is a delicate question. However, Boman and Eriksson (1963) showed that for a given antibiotic concentration, the time to lysis is inversely proportional to the growth rate. This is consistent with the length hypothesis, as the time T to reach a length L_m from a starting length L_0 with an exponential filamentation of rate μ is $T = \frac{1}{\mu} \ln \frac{L_m}{L_0}$. This calls for a death function of the form

$$d(\ell, t) = \gamma\, \Theta(\ell - L_m) \quad \text{with} \quad \Theta(x) = \begin{cases} 0 & \text{for } x < 0 \\ 1 & \text{for } x > 0 \end{cases}$$

This is assuming that the concentration of antibiotics in the culture does not change significantly during the initial growing phase: because it is stable enough (d_a low), and cell lysis did not occur yet (b low).

However, as figure 3.4 shows, L_m depends not only on the strain (see ANSES 32139 and CNR 94G8), but also, for sensitive strains, on the antibiotic dose. In fact, plotting the ratio of optical densities when death occurs, to the initial optical density, for the two sensitive strains, yields curves that can be accurately modelled with sigmoid functions such as Hill's, as shown on figure 3.5.

Here, we will model the death rate as

$$d(\ell, t) = \gamma\, \Theta(\ell - L_m) \quad \text{with} \quad L_m = L_{min} + \frac{L_{max} - L_{min}}{1 + \frac{a}{k_2}} \tag{3.8}$$

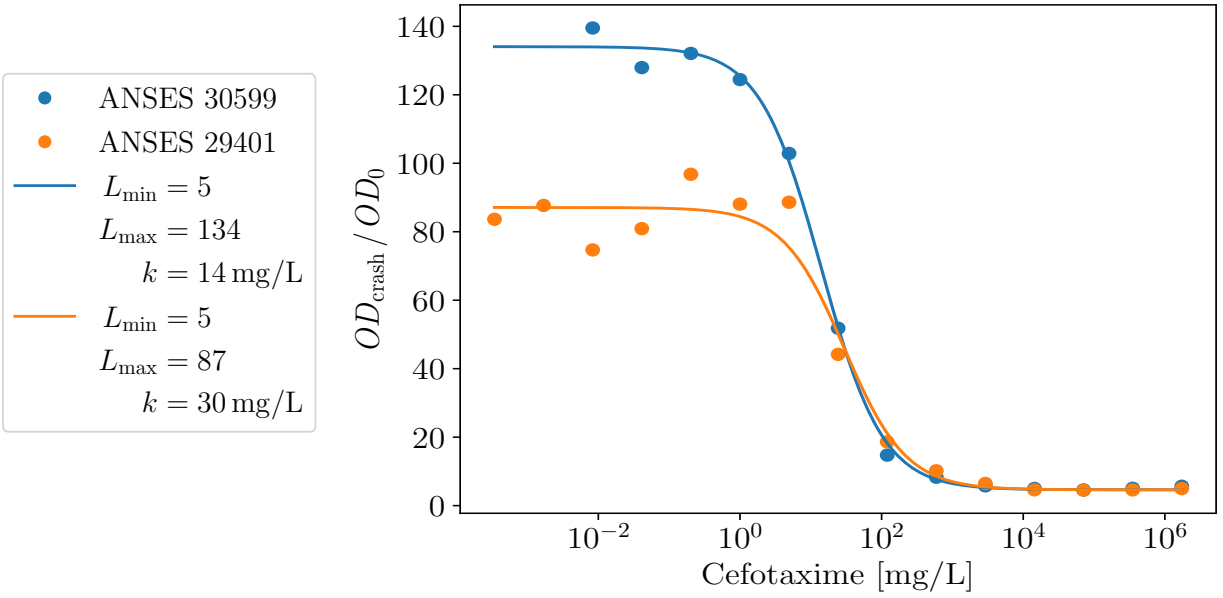

Figure 3.5: Ratio of the optical density when death occurs by the initial optical density, as a function for the antibiotic dose, for two sensitive strains. Since cells do not divide during the filamentation phase, the ratio of the optical densities is comparable with the ratio of the lengths.

For resistant strains, this ratio is independent on the antibiotic. Two ways for the formula to account for that is to either set $L_{\min} = L_{\max}$, or set k_2 to a very large value.

A simple model for the emergence of this function can be seen as following: as per (Vigouroux et al. 2020), the role of some PBPs is to repair damages that naturally occur in the cell wall with a rate $d_1\,\ell$. Assuming unimpeded PBPs can repair $r_{\max}$ wall defects per unit of time, and that antibiotics bind to PBPs following the kinetics of protein-ligand binding, then the effective repair capacity of the cell in the presence of antibiotics becomes $r = \frac{r_{\max}}{1+\frac{a}{k_2}}$. Cell lysis occurs when the rate of creating cell wall defects overcomes the rate of repairing them, hence at a length $L_{\mathrm{m}} = \frac{r_{\max}}{d_1}\frac{1}{1+\frac{a}{k_2}}$, which corresponds exactly to equation 3.8.

We will see on section 5.3 that these two antibiotic effects can be linked to two different molecular targets of the antibiotic, inhibited at different concentrations.

We identified so far two parameters related to a with the dimension of a concentration: k_1, involved in equation 3.7, and k_2, in equation 3.8. Intuitively, k_1 is the concentration of antibiotics that blocks the division mechanism, and k_2 is the concentration of antibiotics that disrupts the activity of wall-repairing proteins. These two parameters determine the shape of the antibiotic response: for resistant strains, k_1 is approachable as one of the

first concentrations of antibiotics that produces a growth curve different from the control. However, k_2 is too high to be measured. For sensitive strains, k_1 is very low, but k_2 has a finite value that produces the intermediate response in the sheaf of curves such as seen on the top row of figure 3.4.

3.2.5 Division factor α

Having determined the three unknown functions g (equation 3.6), f (equation 3.7) and d (equation 3.8), we can now insert them in the general PDE (equation 3.1). To start, let us consider the simple case of growth without antibiotics. In this case, we have $g(\ell,t) = g\,\ell$, $f(\ell,t) = \beta$ and $d(\ell,t) = \gamma\,\Theta(\ell - L_\mathrm{m})$. Within normal growth conditions, filamentation is unexpected to happen and the length of cells remains safely under L_m, so we will also take $d(\ell,t) = 0$.

In these conditions, equations 3.3, 3.4 and 3.5 become

$$\frac{\mathrm{d}N}{\mathrm{d}t} = N(\alpha-1)\beta, \quad \frac{\mathrm{d}L}{\mathrm{d}t} = (g-(\alpha-1)\beta)L \quad \text{and} \quad \frac{\mathrm{d}OD}{\mathrm{d}t} = g\,OD$$

In the most classical growth-fragmentation equation, cells grow linearly and divide exponentially. This leads to a stable steady state. Here, cells grow and divide exponentially, which intuitively explains why the steady state only exist under the condition of a kind of balance between growth and division.

Although N and OD are allowed to grow exponentially as long as the nutrients are not lacking, the average length of cells L is also exponentially growing, which is a problem. Indeed, we would expect the distribution of lengths of cells in these conditions to reach a steady state, which can only be the case if $\frac{\mathrm{d}L}{\mathrm{d}t} = 0$. But this condition is equivalent to a strict relation on the parameters of the system: $g = (\alpha-1)\beta$. An equilibrium should be found for any combination of g, α and β, which shows that one of the hypotheses considered so far is wrong.

The wrong hypothesis is that α is constant. We left it unspecified so far. Intuitively, α is the number of cells that result from the division of a larger cell. In normal conditions in bacteria, this number is 2. However, it was shown recently that not only filamenting cells contain multiple copies of their genome, they are also able to divide into multiple individuals when the antibiotic is removed (Wehrens et al. 2018).

Surprisingly, bacteria do not always divide in two, and this is needed for the model to work.

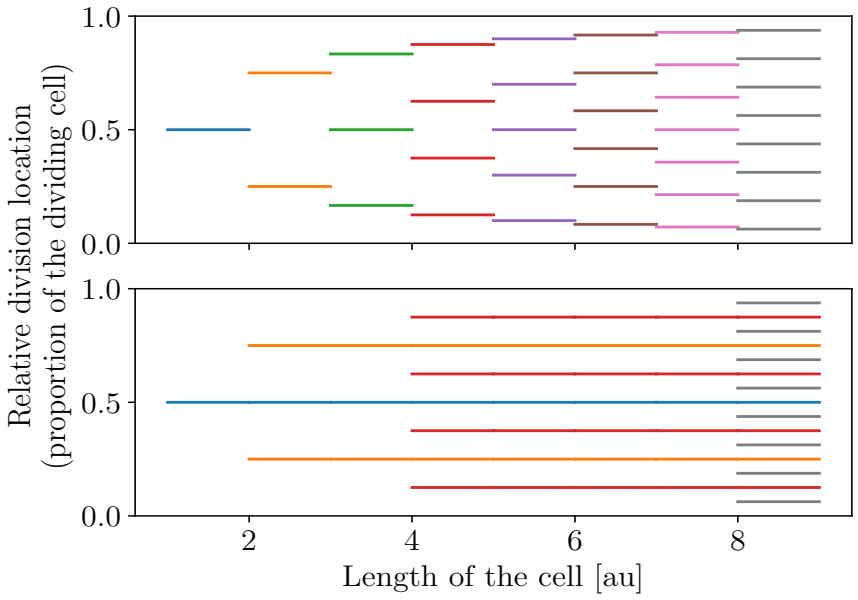

Figure 3.6: Top: relative positions of the divisions when a filamenting cell divides. Example: cells of sizes between 2 and 3 divide into 3 smaller cells, sizes between 3 and 4 divide into 4 smaller cells, etc. Figure adapted from Wehrens et al. (2018). Bottom: approximation of this mechanism to make analytical and numerical computations easier. Here, cells can only divide in a number of smaller cells that is a power of 2, depending on their length.

Figure 3.6 shows on the top panel how α changes with the cell length ℓ. In arbitrary units of length, this shows that cells of sizes between 1 and 2 divide into cells of sizes between $1/2$ and 1, cells of sizes between 2 and 3 divide into cells of sizes between $2/3$ and 1, and in general cells of sizes ranging from $i-1$ to i where i is a strictly positive integer divide into cells of sizes comprised between $\frac{i-1}{i}$ and 1. Although the representation of this mechanism in mathematical terms is possible, analytical and numerical analyses of this process seem complex. This is why we will prefer the slightly simpler mechanism appearing on the bottom of figure 3.6. In this way, cells of sizes comprised between 2^{i-2} and 2^{i-1}, with i a strictly positive integer, divide into 2^{i-1} smaller cells, of sizes between $1/2$ and 1.[2] The length 1

2 In this way of writing, $i = 1$ corresponds to cells with a length comprised between $1/2$ and 1, and that divide in 1 cell of the same size. This leads to two cancelling terms in the equation, so it does not matter if n starts at 1 or 2.

can be seen as the minimal length that a cell can have to divide. Cells of sizes lower than $1/2$ do not divide.[3]

Equation 3.1 then becomes the following equation, where the sum in the domain $[1/2, 1[$ represents the contribution of the cells from all the upper domains, that divide in increasing numbers of cells of sizes between $1/2$ and 1, like pictured in figure 3.7.

$$\frac{\partial n}{\partial t} + g\,\ell\,\frac{\partial n}{\partial \ell} + g\,n = \begin{cases} 0 & \text{for } 0 \leq \ell < \frac{1}{2} \\ f \sum_{i=2}^{\infty} (2^{i-1})^2\, n(2^{i-1}\ell, t) & \text{for } \frac{1}{2} \leq \ell < 1 \\ -n\,f & \text{for } 1 \leq \ell < L_{\mathrm{m}} \\ -n\,(f+\gamma) & \text{for } L_{\mathrm{m}} \leq \ell \end{cases} \tag{3.9}$$

By this mechanism, exponential growth of cells is balanced by a division greater than exponential, which is sufficient to create a stable steady distribution, as we will see in section 3.3.

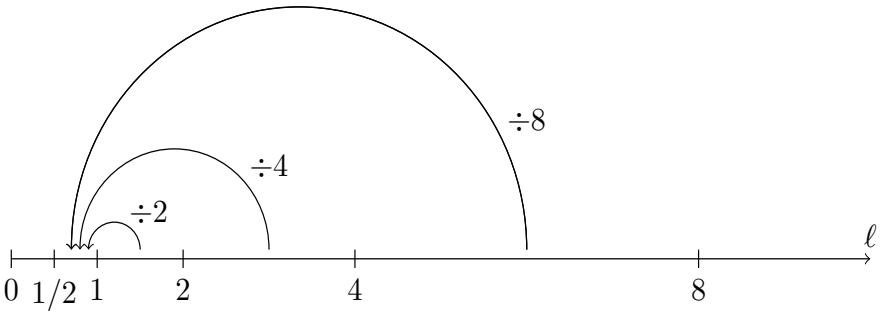

Figure 3.7: Schematic representation of the flows of cells in the model.

Although Wehrens et al. (2018) note that the fissions inside a filamented cell rarely happen all at once, they noticed that the time between divisions decreases when the length of the filament increases. For a normal cell cycle time of 60 min, the average interdivision time quickly decreases with the birth size of the cell to reach 10 min at around $\ell = 10$. At this rate, the time required for a filamented cell of size $\ell = 16$ to fully divide into individual cell units of size $\ell = 1$ is comparable to a normal cell cycle time. This justifies this simplified assumption that filamented cells can divide atomically into $\alpha > 2$ smaller cells.

3 It also does not really matter what cells smaller than $1/2$ do, because the steady state in the domain of ℓ ranging from 0 to $1/2$ is $n(\ell, t) = 0$. Indeed, cells in that domain at $t = 0$ grow and eventually become larger than $1/2$, and no new cell is ever added because all new cells have sizes between $1/2$ and 1.

3.2.6 Completing the model

Equation 3.9 describes the dynamics of the cell population, but the system contains other variables that we also need to describe.

First, the antibiotic concentration. It is a chemical species that only disappears, by two different processes: its natural degradation with a rate d_a, and its active degradation by β-lactamase contained in the environment and noted b, with a mass action law of rate k_b. The equation for a is then

$$\frac{\mathrm{d}a}{\mathrm{d}t} = -k_\mathrm{b}\, b\, a - d_\mathrm{a}\, a$$

The lysed cells and debris of lysing contribute to the optical density of the solution, they have then to be taken into account. Some debris are quickly degraded by the agitation, but some are not and remain in suspension. We note p_c the proportion of debris that are formed resistant to breaking down. We represent with the variable c the quantity of debris with a short half life, and c_r the quantity of debris that accumulate. The equations for c and c_r are then

$$\frac{\mathrm{d}c}{\mathrm{d}t} = \gamma(1-p_\mathrm{c})\int_{L_\mathrm{m}}^{\infty} \ell\, n\, \mathrm{d}\ell - d_\mathrm{c}\, c \quad \text{and} \quad \frac{\mathrm{d}c_\mathrm{r}}{\mathrm{d}t} = \gamma\, p_\mathrm{c} \int_{L_\mathrm{m}}^{\infty} \ell\, n\, \mathrm{d}\ell$$

Lysed cells release β-lactamase in the environment. Since filamenting cells duplicate their genetic material, it can be assumed that they also duplicate their proteome, meaning that the quantity of β-lactamase in a cell is proportional to its length. β-lactamase is then degraded naturally with a rate d_b. We can then establish

$$\frac{\mathrm{d}b}{\mathrm{d}t} = \gamma\, B_\mathrm{in} \int_{L_\mathrm{m}}^{\infty} \ell\, n\, \mathrm{d}\ell - d_\mathrm{b}\, b$$

Finally, the concentration of glucose in the environment, noted s, decreases when it is consumed. Noting λ the conversion factor, it comes

$$\frac{\mathrm{d}s}{\mathrm{d}t} = -\frac{g}{\lambda}\int_{0}^{\infty} \ell\, n\, \mathrm{d}\ell$$

The complete PDE system is then the following:

$$\frac{\partial n}{\partial t} + g\,\ell\,\frac{\partial n}{\partial \ell} + g\,n = \begin{cases} 0 & \text{for } 0 \leq \ell < \frac{1}{2} \\ f \sum_{i=2}^{\infty} (2^{i-1})^2\, n(2^{i-1}\ell, t) & \text{for } \frac{1}{2} \leq \ell < 1 \\ -f\,n & \text{for } 1 \leq \ell < L_\mathrm{m} \\ -(f+\gamma)\,n & \text{for } L_\mathrm{m} \leq \ell \end{cases}$$

$$\frac{\mathrm{d}s}{\mathrm{d}t} = -\frac{g}{\lambda}\int_0^\infty \ell\, n\, \mathrm{d}\ell \qquad \text{with } g = \mu\frac{s}{K_\mathrm{s}+s}$$

$$\frac{\mathrm{d}a}{\mathrm{d}t} = -k_\mathrm{b}\, b\, a - d_\mathrm{a}\, a \qquad f = \frac{\beta}{1+\left(\frac{a}{k_1}\right)^{h_1}}$$

$$\frac{\mathrm{d}b}{\mathrm{d}t} = \gamma\, B_\mathrm{in}\int_{L_\mathrm{m}}^\infty \ell\, n\, \mathrm{d}\ell - d_\mathrm{b}\, b \qquad L_\mathrm{m} = L_\mathrm{min} + \frac{L_\mathrm{max}-L_\mathrm{min}}{1+\frac{a}{k_2}}$$

$$\frac{\mathrm{d}c}{\mathrm{d}t} = \gamma(1-p_\mathrm{c})\int_{L_\mathrm{m}}^\infty \ell\, n\, \mathrm{d}\ell - d_\mathrm{c}\, c$$

$$\frac{\mathrm{d}c_\mathrm{r}}{\mathrm{d}t} = \gamma\, p_\mathrm{c}\int_{L_\mathrm{m}}^\infty \ell\, n\, \mathrm{d}\ell \qquad OD = \eta\left(\int_0^\infty \ell\, n\, \mathrm{d}\ell + c(t) + c_\mathrm{r}(t)\right)$$

Some initial conditions are set by the experiment: $s(0)$, $a(0)$, $N(0)$, and $b(0) = c(0) = c_\mathrm{r}(0) = 0$. For n, because we start the experiment with cells in exponential state (see section 2.1.2), we take the steady size distribution with no death, that we will compute in the next section (see equation 3.13): $n(\ell, 0) = N(0)\, y_{\infty,\gamma=0}(\ell)$.

In practice, it is more often $OD(0)$ that is known experimentally. In which case, $N(0)$ can be computed from $OD(0)$ and the rest of the initial conditions.

The right-hand side of the PDE involves the value of $n(\ell, t)$ in an infinite number of values of ℓ. It is a particular case of equations known as pantograph equations. This kind of dependency prevents the use of most common PDE solvers, hence we decided to implement a custom numerical method. The method used is an explicit, upwind, first order finite-difference scheme. A natural change of variables allows to simulate each domain (0 to 1/2, 1/2 to 1, 1 to 2, 2 to 4, etc.) with the same number of points, which makes the simulation efficient. We can in this way simulate until a length L, in a time proportional to $\log L$: in practice this allows to choose the upper limit of simulation as high as necessary.

This model is able to exhibit behaviours similar to sensitive, as well as resistant strains, as shown on figure 3.8.

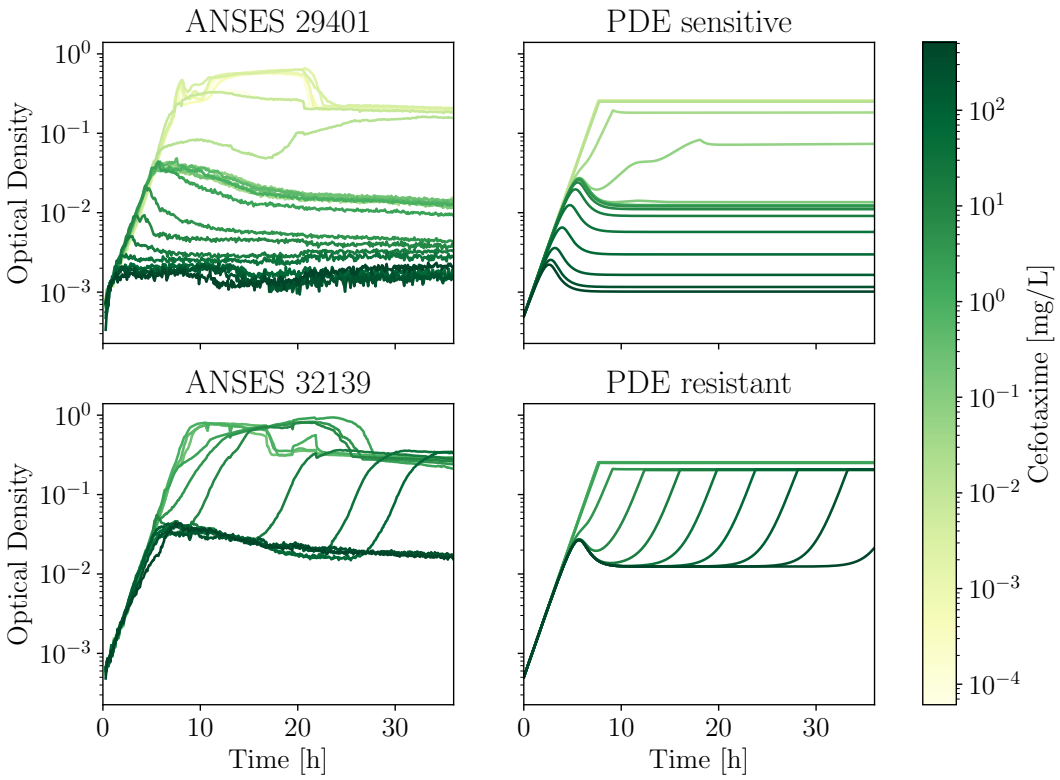

Figure 3.8: On the left are two clinical isolates (top sensitive, bottom resistant). On the right are simulations of the PDE model with similar behaviours.

3.2.7 Parameters of the PDE model

The variables and parameters of the model are presented in the following tables.

Variable	Unit	Comment
t	h	Time
ℓ	1	Cell length [au]
$n(\ell, t)$	1	Population density
$s(t)$	g/L	Concentration of nutrients
$a(t)$	mg/L	Concentration of antibiotics
$b(t)$	mg/L	Concentration of β-lactamase
$c(t)$	1	Dead degradable biomass
$c_r(t)$	1	Dead non-degradable biomass

Parameter	Unit	Comment
γ	1/h	Death rate
β	1/h	Maximal division rate
μ	1/h	Maximal growth rate
K_s	g/L	Half-velocity constant of nutrients
λ	L/g	Conversion factor from nutrients
k_1	mg/L	Conc. of antibiotics needed to stop cell division
h_1	1	Hill coefficient of this antibiotic action
k_2	mg/L	Conc. of antibiotics needed to stop defect repair
B_{in}	mg/L	Conc. of β-lactamase released by a cell of length 1
k_b	L/mg/h	Activity rate of β-lactamase
d_a	1/h	Degradation rate of antibiotics
d_b	1/h	Degradation rate of β-lactamase
d_c	1/h	Elimination rate of dead biomass
p_c	1	Proportion of non-degradable dead biomass
L_{min}	1	Minimal cell length where lysis can occur
L_{max}	1	Maximal viable cell length
η	1	Conversion between biomass and OD

3.3 SIMPLIFYING THE MODEL

It takes a few seconds to solve the PDE model for one initial condition, but it takes more than a minute to solve it for 12, which is useful to fit a range of antibiotic concentrations at the same time. In these conditions and with this number of parameters to search, an automated parameter search becomes difficult. This is because of the nature of the model: being a population model, a whole distribution needs to be simulated. It would be much more convenient to fit an ODE model containing only population-level variables such as the total number of cells N, or their average length L.

Integrating equation 3.9 on ℓ gives the expression of the temporal derivative of the total number of cells:

$$\frac{\mathrm{d}N}{\mathrm{d}t} + g\int_0^\infty \ell\frac{\partial n}{\partial \ell}\,\mathrm{d}\ell + g\,N$$
$$= f\sum_{i=2}^{\infty}\left(2^{i-1}\right)^2\int_{\frac{1}{2}}^{1} n(2^{i-1}\ell,t)\,\mathrm{d}\ell - f\int_1^\infty n\,\mathrm{d}\ell - \gamma\int_{L_\mathrm{m}}^\infty n\,\mathrm{d}\ell$$

After integration by parts on the left and change of variable on the right, we have

$$\frac{\mathrm{d}N}{\mathrm{d}t} = f\sum_{i=2}^{\infty}2^{i-1}\int_{2^{i-2}}^{2^{i-1}} n\,\mathrm{d}\ell - f\int_1^\infty n\,\mathrm{d}\ell - \gamma\int_{L_\mathrm{m}}^\infty n\,\mathrm{d}\ell$$

Introducing $y(\ell,t) = \frac{n(\ell,t)}{N(t)}$, the normalised cell density, and $Y_>(t) = \int_{L_\mathrm{m}}^\infty y(\ell,t)\,\mathrm{d}\ell$, the proportion of cells longer than L_m, we get

$$\frac{\mathrm{d}N}{\mathrm{d}t} = f\,N\sum_{i=2}^{\infty}2^{i-1}\int_{2^{i-2}}^{2^{i-1}} y\,\mathrm{d}\ell - f\,N\int_1^\infty y\,\mathrm{d}\ell - \gamma\,N\,Y_>$$

Or written differently,

$$\frac{\mathrm{d}N}{\mathrm{d}t} = N\left[f\left(\sum_{i=1}^{\infty}2^{i-1}\int_{2^{i-2}}^{2^{i-1}} y\,\mathrm{d}\ell - \int_{\frac{1}{2}}^\infty y\,\mathrm{d}\ell\right) - \gamma\,Y_>\right]$$

Because the steady-state solution for length less than $1/2$ is 0, we will consider in all the following that $\forall \ell \leq \frac{1}{2}, \forall t, y(\ell,t) = 0$. This allows to say that the sum of integrals is nothing else than α averaged over the distribution y, that we will note $\bar{\alpha}(t)$. The other integral is equal to 1. Finally,

$$\frac{\mathrm{d}N}{\mathrm{d}t} = N(t)[f(\bar{\alpha}(t) - 1) - \gamma\,Y_>(t)] \tag{3.10}$$

Let us now express equation 3.9 in terms of y:

$$\frac{\partial y}{\partial t} + g\ell\frac{\partial y}{\partial \ell} + (g + \bar{\alpha}(t)f - \gamma Y_>)y$$
$$= \begin{cases} f\sum_{i=1}^{\infty}(2^{i-1})^2 y(2^{i-1}\ell,t) & \text{for } \frac{1}{2} \leq \ell < 1 \\ 0 & \text{for } 1 \leq \ell < L_\mathrm{m} \\ -\gamma y & \text{for } L_\mathrm{m} \leq \ell \end{cases} \tag{3.11}$$

Multiplying this equation by ℓ and integrating it over ℓ brings the equation for the evolution of the average cell length:

$$\frac{\mathrm{d}L}{\mathrm{d}t} = [g - f\,(\bar{\alpha}(t) - 1)]\,L - \gamma \int_{L_\mathrm{m}}^{\infty} (\ell - L) y \,\mathrm{d}\ell$$

that we can also write with the help of $L_>(t) = \int_{L_\mathrm{m}}^{\infty} \ell\, y(\ell, t)\,\mathrm{d}\ell$:

$$\frac{\mathrm{d}L}{\mathrm{d}t} = [g - f\,(\bar{\alpha}(t) - 1)]\,L - \gamma(L_>(t) - L\,Y_>(t)) \tag{3.12}$$

For an ODE model, we need to know the temporal evolution of N and L, only as a function of other population-level quantities. Equations 3.10 and 3.12 are not satisfying yet, because they include functions whose dynamics depends on the distribution y, such as $\bar{\alpha}$, $Y_>$ and $L_>$. The goal of the rest of this section is to find how to remove y from these equations.

3.3.1 An approximation for the average division factor $\bar{\alpha}$

Let us first study the steady-state if there was no death: $y_{\infty,\gamma=0}$. First, since $L_{\infty,\gamma=0}$ must be constant, then 3.12 provides a condition on the average division factor at steady state: $\bar{\alpha}_{\infty,\gamma=0} = 1 + g/f$. Consequently, from 3.10 we have $N_{\infty,\gamma=0}(t) = N_0\,\mathrm{e}^{g\,t}$. The general PDE 3.11 simplifies and its analytical solution is now tractable:

$$\ell\, y'_{\infty,\gamma=0}(\ell) + 2\, y_{\infty,\gamma=0}(\ell) = \begin{cases} \frac{f}{g} \sum_{i=2}^{\infty} (2^{i-1})^2\, y_{\infty,\gamma=0}(2^{i-1}\ell) & \text{for } \frac{1}{2} \le \ell < 1 \\ -\frac{f}{g}\, y_{\infty,\gamma=0}(\ell) & \text{for } 1 \le \ell \end{cases}$$

The general solution of this equation for $1 \le \ell$ is

$$y_{\infty,\gamma=0}(\ell) = \frac{A}{\ell^{2+f/g}}$$

Replacing this expression in the first branch of the differential equation, we now have to solve for $\frac{1}{2} \le \ell < 1$ the following:

$$\ell\, y'_{\infty,\gamma=0}(\ell) + 2\, y_{\infty,\gamma=0}(\ell) = \frac{f/g}{\ell^{2+f/g}} \frac{A}{2^{f/g} - 1}$$

The general solution of this equation, valid for $\frac{1}{2} \le \ell < 1$, is the following:

$$y_{\infty,\gamma=0}(\ell) = \frac{B}{\ell^2} - \frac{A}{\ell^{2+f/g}} \frac{1}{2^{f/g} - 1}$$

The continuity of the solution in 1 can be proved by conservation of the flux of cells through 1.

The value of one of the integration constants can be obtained by continuity of the solution in 1: $A = B\left(1 - 2^{-f/g}\right)$, and the value of the other constant is found by normalization of $y_{\infty,\gamma=0}$ integrated over ℓ:

$$\begin{aligned}
1 &= \int_{1/2}^{\infty} y_{\infty,\gamma=0}(\ell)\,\mathrm{d}\ell \\
&= B\int_{1/2}^{1}\left[\frac{1}{\ell^2} - \frac{1}{\ell^{2+f/g}}\frac{1-2^{-f/g}}{2^{f/g}-1}\right]\mathrm{d}\ell + B(1-2^{-f/g})\int_{1}^{\infty}\frac{\mathrm{d}\ell}{\ell^{2+f/g}} \\
&= B - 2^{-f/g}B\frac{g}{f+g}(2^{1+f/g}-1) + B(1-2^{-f/g})\frac{g}{f+g} \\
1 &= B - B\frac{g}{f+g}
\end{aligned}$$

hence $B = 1 + g/f$, and finally

$$y_{\infty,\gamma=0}(\ell) = \begin{cases} \frac{f+g}{f}\,\frac{\ell^{f/g}-2^{-f/g}}{\ell^{2+f/g}} & \text{for } \frac{1}{2} \le \ell < 1 \\ \frac{f+g}{f}\,\frac{1-2^{-f/g}}{\ell^{2+f/g}} & \text{for } 1 \le \ell \end{cases} \tag{3.13}$$

From the steady-state distribution, it is possible to compute the steady-state average cell length:

$$L_{\infty,\gamma=0} = \frac{f+g}{f}\ln 2 = \bar{\alpha}_{\infty,\gamma=0}\ln 2 \tag{3.14}$$

It would be very interesting to make the calculations with the original division factor, featured on top of figure 3.6, because in this case, the relation between L and $\bar{\alpha}$ is much tighter: $L \le \bar{\alpha} \le L+1$. It is also possible that it would remove the factor $\ln 2$ throughout the calculations, caused by the discrepancy between the two scales for α shown on this figure.

That the average cell length is proportional to the average division factor is understandable, because as figure 3.6 shows, $\alpha(\ell)$ closely follows ℓ. In fact, whatever the distribution y, with or without death, their ratio is bounded: $\ell \le \alpha(\ell) \le 2\ell$, which bounds the integrals in the same way: $\forall t, L \le \bar{\alpha}(t) \le 2L$, the limit cases happening for very tight distributions. Wider cell length distributions make an average that comes closer to the center of the interval.

With $1/\ln 2 \approx 1.44$, the relation $\bar{\alpha} = L/\ln 2$ actually holds not only for the stationary distribution of cell lengths without death, but it is also a very good approximation of the non-steady state, even including death. In fact, on the numerical computations of figure 3.8 for example, this ratio is accurate at all time within 1% of relative deviation. Consequently, we will assume the following relation to always hold:

$$\bar{\alpha}(L) = \frac{L}{\ln 2} \tag{3.15}$$

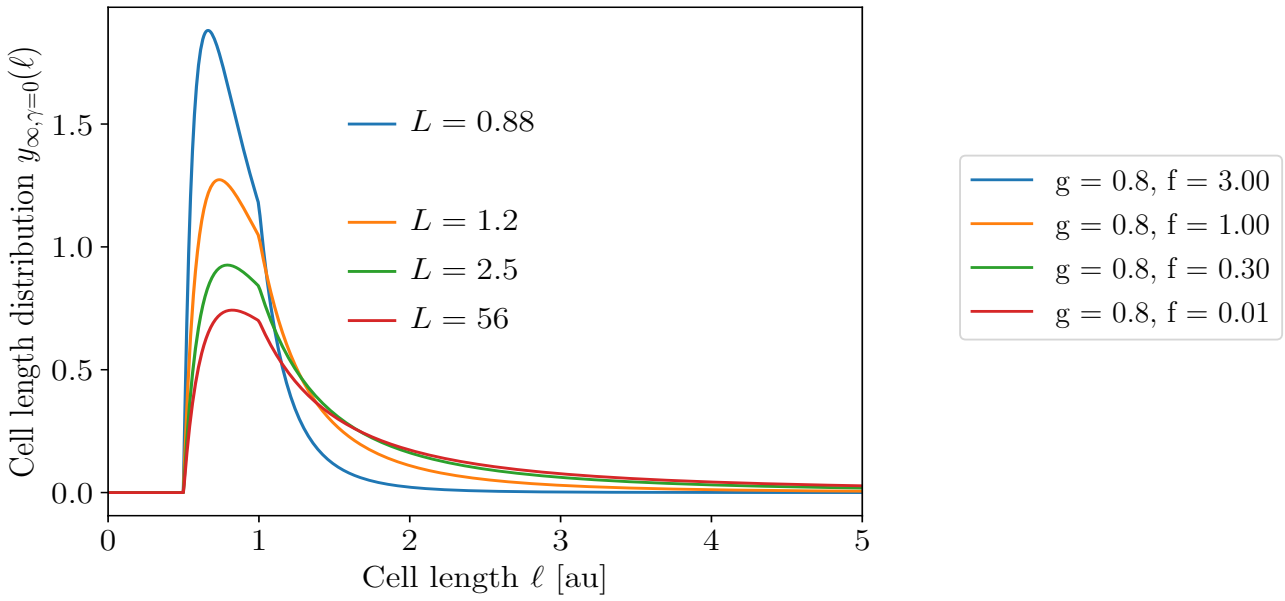

Figure 3.9: Steady-state cell size distribution without death, for several growth and cell division rates. Different parameter values can generate distributions of relatively similar shapes, albeit with different average lengths.

3.3.2 Extraction of partial moments $Y_>$ and $L_>$

It would be tempting to compute $Y_>$ and $L_>$ on the steady state without death 3.13 and use these values in the equations 3.10 and 3.12. This would be making the approximation that at any time during the experiment, if the average cell length is L, then the distribution of cells is close to the steady-state distribution with the same average length L. However, as figure 3.10 shows, the transition from a steady-state distribution with low average length to another steady-state with a larger average length does not in general go through a path of steady-state distributions of intermediate average lengths.

What actually happens is that cells do not divide almost at all any more but still elongate, so the whole distribution is shifted as a block towards increasing lengths, until $f\,\alpha^2$ becomes sufficiently high to repopulate the short lengths region despite the low division rate. The distribution is then first shifted to larger lengths, then becomes bimodal, and finally the first peak regrows to fill the target distribution while the second peak vanishes at extremely long lengths.

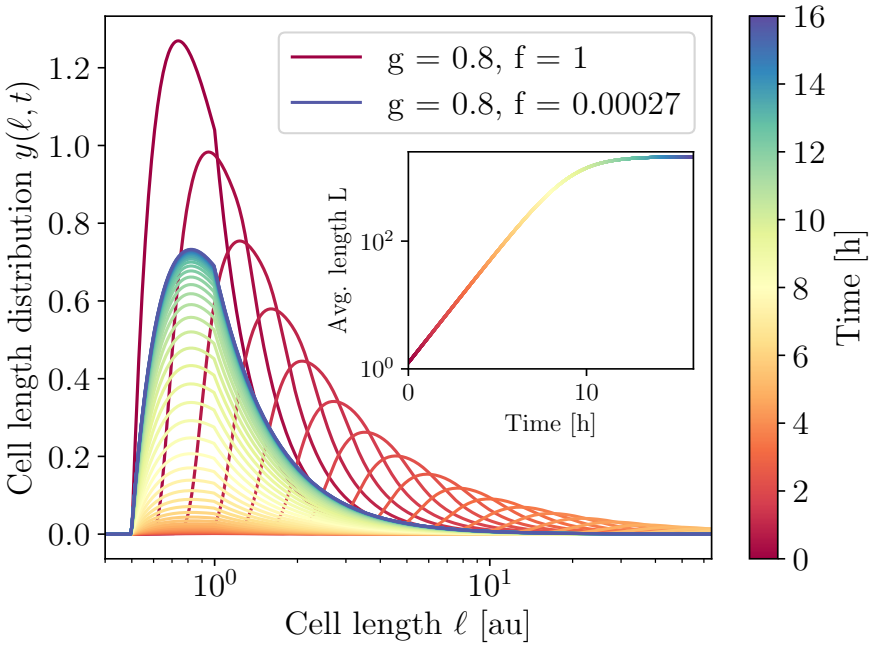

Figure 3.10: Snapshots of successive cell length distributions when an exponentially growing cell culture is treated with a dose of antibiotics that dramatically reduces its division rate, increasing its average length. Although the average length is continuously increasing from the first value (red curve, $L = 1.25$) to the last (blue curve, $L = 2067$), the transient distributions do not take the path of steady-state distributions with intermediate lengths pictured in figure 3.9.

We can model the shifted distribution, applying equation 3.11 without death or division to the initial distribution that we assume stationary and representative of conditions without antibiotics:

$$\frac{\partial y}{\partial t} + g\,\ell\,\frac{\partial y}{\partial \ell} + g\,y = 0 \quad \text{with} \quad y(\ell,0) = \begin{cases} \frac{\beta+g}{\beta}\,\frac{\ell^{\beta/g} - 2^{-\beta/g}}{\ell^{2+\beta/g}} & \text{for } \frac{1}{2} \le \ell < 1 \\ \frac{\beta+g}{\beta}\,\frac{1-2^{-\beta/g}}{\ell^{2+\beta/g}} & \text{for } 1 \le \ell \end{cases} \tag{3.16}$$

The solution of this differential equation is the following:

$$y(\ell,t) = \begin{cases} \frac{\beta+g}{\beta}\,e^{-g\,t}\,\frac{e^{-\beta\,t}\,\ell^{\beta/g} - 2^{-\beta/g}}{e^{-(2g+\beta)t}\,\ell^{2+\beta/g}} & \text{for } \frac{e^{g\,t}}{2} \le \ell < e^{g\,t} \\ \frac{\beta+g}{\beta}\,e^{-g\,t}\,\frac{1-2^{-\beta/g}}{e^{-(2g+\beta)t}\,\ell^{2+\beta/g}} & \text{for } e^{g\,t} \le \ell \end{cases} \tag{3.17}$$

We can now compute the partial moments of this distribution:

$$Y_>(t) = \begin{cases} \frac{g}{\beta}\frac{2^{\beta/g}-1}{2^{\beta/g}L_\mathrm{m}^{1+\beta/g}}\mathrm{e}^{(\beta+g)t} & \text{for } \mathrm{e}^{g\,t} \le L_\mathrm{m} \\ \frac{\beta+g}{\beta}\frac{\mathrm{e}^{g\,t}}{L_\mathrm{m}} - 1 - \frac{g}{\beta}\frac{\mathrm{e}^{(\beta+g)t}}{2^{\beta/g}L_\mathrm{m}^{1+\beta/g}} & \text{for } \frac{\mathrm{e}^{g\,t}}{2} \le L_\mathrm{m} < \mathrm{e}^{g\,t} \\ 1 & \text{for } L_\mathrm{m} < \frac{\mathrm{e}^{g\,t}}{2} \end{cases}$$

$$L_>(t) = \begin{cases} \frac{g\,(g+\beta)}{\beta^2}\frac{2^{\beta/g}-1}{(2\,L_\mathrm{m})^{\beta/g}}\mathrm{e}^{(g+\beta)t} & \text{for } \mathrm{e}^{g\,t} \le L_\mathrm{m} \\ \frac{g\,(g+\beta)}{\beta^2}\left(1+\beta\,t - \frac{\beta}{g}\ln L_\mathrm{m} - \frac{\mathrm{e}^{\beta\,t}}{(2\,L_\mathrm{m})^{\beta/g}}\right)\mathrm{e}^{g\,t} & \text{for } \frac{\mathrm{e}^{g\,t}}{2} \le L_\mathrm{m} < \mathrm{e}^{g\,t} \\ L & \text{for } L_\mathrm{m} < \frac{\mathrm{e}^{g\,t}}{2} \end{cases}$$

Observing that $L(t) = \mathrm{e}^{g\,t}L_0$ with $L_0 = \frac{\beta+g}{\beta}\ln 2$, we can replace the variable t in the equations above with its expression as a function of L and L_0, which gives

$$Y_>(L) = \begin{cases} \frac{g}{\beta}\left(1-2^{-\beta/g}\right)\left(\frac{L}{L_0L_\mathrm{m}}\right)^{1+\beta/g} & \text{for } L \le L_0L_\mathrm{m} \\ \left(1+\frac{g}{\beta}\right)\frac{L}{L_0L_\mathrm{m}} - 1 - 2^{-\beta/g}\frac{g}{\beta}\left(\frac{L}{L_0L_\mathrm{m}}\right)^{1+\beta/g} & \text{for } L_0L_\mathrm{m} \le L \le 2L_0L_\mathrm{m} \\ 1 & \text{for } 2L_0L_\mathrm{m} \le L \end{cases}$$

$$L_>(L) = \begin{cases} \frac{L}{\ln 2}\frac{g}{\beta}\left(1-2^{-\beta/g}\right)\left(\frac{L}{L_0L_\mathrm{m}}\right)^{\beta/g} & \text{for } L \le L_0L_\mathrm{m} \\ \frac{L}{\ln 2}\left[\frac{g}{\beta} + \ln\frac{L}{L_0L_\mathrm{m}} - 2^{-\beta/g}\frac{g}{\beta}\left(\frac{L}{L_0L_\mathrm{m}}\right)^{\beta/g}\right] & \text{for } L_0L_\mathrm{m} \le L \le 2L_0L_\mathrm{m} \\ L & \text{for } 2L_0L_\mathrm{m} \le L \end{cases}$$

Finally, to reduce visual noise, it can be convenient to make the double change of variable $x = \frac{L}{L_0L_\mathrm{m}}$ and $\nu = \frac{\beta}{g}$. Then we have

$$Y_>\left(x = \frac{L}{L_0L_\mathrm{m}}\right) = \begin{cases} \frac{x}{\nu}\left(x^\nu - \left(\frac{x}{2}\right)^\nu\right) & \text{for } x \le 1 \\ x - 1 + \frac{x}{\nu}\left(1 - \left(\frac{x}{2}\right)^\nu\right) & \text{for } 1 \le x \le 2 \\ 1 & \text{for } 2 \le x \end{cases} \tag{3.18}$$

$$\frac{L_>}{L_0L_\mathrm{m}}\left(x = \frac{L}{L_0L_\mathrm{m}}\right) = \begin{cases} \frac{x}{\nu\ln 2}\left(x^\nu - \left(\frac{x}{2}\right)^\nu\right) & \text{for } x \le 1 \\ x\frac{\ln x}{\ln 2} + \frac{x}{\nu\ln 2}\left(1 - \left(\frac{x}{2}\right)^\nu\right) & \text{for } 1 \le x \le 2 \\ x & \text{for } 2 \le x \end{cases} \tag{3.19}$$

We have now closed the three terms missing to express $\frac{\mathrm{d}N}{\mathrm{d}t}$ and $\frac{\mathrm{d}L}{\mathrm{d}t}$ as functions of N, L and L_m only. Figure 3.11 shows these three functions.

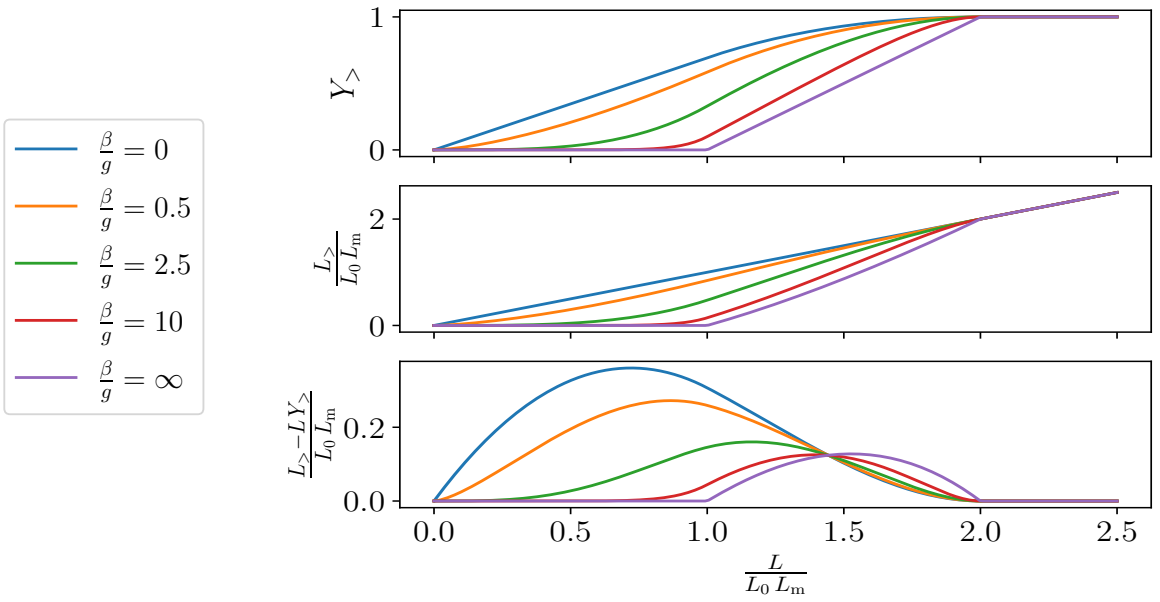

Figure 3.11: The partial moments $Y_>$, $L_>$ and $L_> - L\,Y_>$ as a function of L, for different values of the parameters.

With these expressions for $\bar{\alpha}$, $Y_>$ and $L_>$, equations 3.10 and 3.12 become respectively

$$\frac{\mathrm{d}N}{\mathrm{d}t} = N\left[f\left(\frac{L}{\ln 2} - 1\right) - \gamma\, Y_>(L)\right]$$
$$\frac{\mathrm{d}L}{\mathrm{d}t} = L\left[g - f\left(\frac{L}{\ln 2} - 1\right)\right] - \gamma(L_>(L) - L\, Y_>(L))$$

with $Y_>$ and $L_>$ as described in 3.18 and 3.19.

We can show that the term appearing in $\frac{\mathrm{d}L}{\mathrm{d}t}$, $-\gamma(L_> - L\,Y_>)$, is always negative, which shows that the lysis of long cells can only decrease the average length[4].

On real cases, these approximations are particularly accurate for small (which do not lead to death) and very large doses

4 From the definition of the partial moments,

$$L_> - L\,Y_> = \int_{L_\mathrm{m}}^{\infty} (\ell - L)\, y(\ell)\, \mathrm{d}\ell$$

If $L_\mathrm{m} \leq L$, then

$$L_> - L\,Y_> \geq \int_{0}^{\infty} (\ell - L)\, y(\ell)\, \mathrm{d}\ell = 0$$

(close to the limit case considered in the approximation) of antibiotics, but less for intermediate doses like 8 mg/L, as shown on figure 3.12. Indeed, we based our calculations on the assumption that the length distribution moves as a block. This only happens for very low division rates: high antibiotics. Of course, for low antibiotics, the perturbation to the system is minimal, which is also well captured by these formulas. In intermediate cases, when f/β is neither 0 nor 1, since the behaviour of the system is not a limit case, it is less adequately described by these terms.

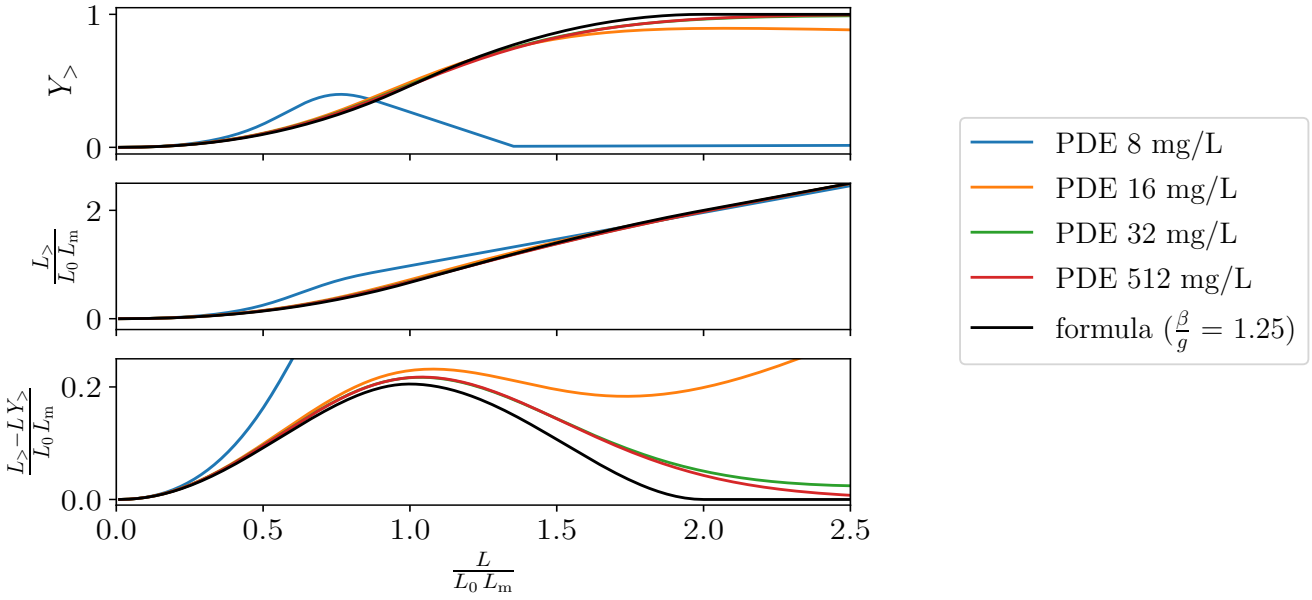

Figure 3.12: Comparison of $Y_>$, $L_>$ and $L_> - L\,Y_>$ given by the PDE simulation, and by the formulas computed in this section. The system was run with no death, no antibiotic degradation and unlimited nutrients, similarly to the conditions of figure 3.10.

It is interesting to check the accuracy of these approximations on a real case, allowing the nutrient and antibiotic concentrations to evolve as well.

The match between the PDE and the partial moment approximation is worse on figure 3.13 than on figure 3.12. Indeed, the

---

And if $L \leq L_m$, then

$$\begin{aligned} L_> - L\,Y_> &= \int_0^\infty (\ell - L)\,y(\ell)\,\mathrm{d}\ell - \int_0^{L_m} (\ell - L)\,y(\ell)\,\mathrm{d}\ell \\ &\geq \int_0^\infty (\ell - L)\,y(\ell)\,\mathrm{d}\ell - \int_0^\infty (\ell - L)\,y(\ell)\,\mathrm{d}\ell = 0 \end{aligned}$$

combined effects of cell death (which deforms the cell distribution, and generates β-lactamase that degrade the antibiotics, changing the value of the division rate f), and of the batch culture (the nutrients are depleted, which changes the value of the growth rate g) draw the system away from the idealized case pictured above in figure 3.12.

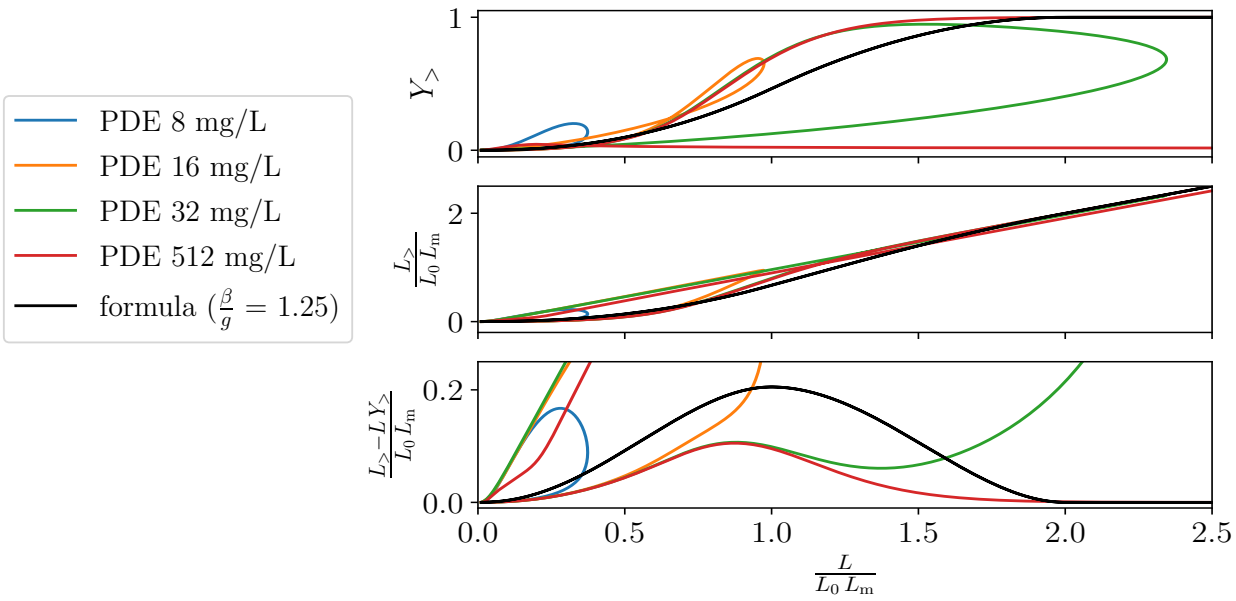

Figure 3.13: Comparison of $Y_>$, $L_>$ and $L_> - L\,Y_>$ given by the PDE simulation, and by the formulas computed in this section. The system simulates a batch experiment, similarly to the conditions of figure 3.8 (resistant case).

The loops seen on 3.13 show that the path taken for the cell distribution to increase its length is not the same as the path taken to decrease it. The simplified ODE model assumes that the same path is taken to go up and down (shown as the black curve). However, even though the path taken by the cell distribution to come back to a normal length while recovering from filamentation is quite different from the one that the ODE model assumes, this happens after massive cell death, so it only concerns very few cells, and this is what allows this approximation to work.

Knowing this, it might be possible to find simpler functions that would be equally or more performant at this dimensionality reduction. For this, one would need to determine where the function needs to be accurate and where it does not, and simplify where it can be.

3.3.3 Completing the model

We complete the model similarly as for the PDE version: the equation for the antibiotics is unchanged. The other equations have integral terms, that are substituted with their expression with the partial moments:

$$\frac{\mathrm{d}c}{\mathrm{d}t} = \gamma\,(1-p_\mathrm{c})N\,L_>(L) - d_\mathrm{c}\,c \quad \text{and} \quad \frac{\mathrm{d}c_\mathrm{r}}{\mathrm{d}t} = \gamma\,p_\mathrm{c}\,N\,L_>(L)$$

A similar substitution leads to $\frac{\mathrm{d}b}{\mathrm{d}t}$ and $\frac{\mathrm{d}s}{\mathrm{d}t}$:

$$\frac{\mathrm{d}b}{\mathrm{d}t} = \gamma\,B_\mathrm{in}\,N\,L_>(L) - d_\mathrm{b}\,b \quad \text{and} \quad \frac{\mathrm{d}s}{\mathrm{d}t} = -\frac{g}{\lambda}\,N\,L$$

Finally, we come to the complete ODE model.

The substitutions $\int_0^\infty \ell\,n\,\mathrm{d}\ell \to N\,L$ and $\int_{L_m}^\infty \ell\,n\,\mathrm{d}\ell \to N\,L_>$ are the only changes in the equations for s, a, b, c and c_r. The only real change of this model compared with the PDE is the replacement of the PDE on n with two ODEs on N and L.

$$\frac{\mathrm{d}N}{\mathrm{d}t} = N\left[f\left(\frac{L}{\ln 2}-1\right) - \gamma\,Y_>\right]$$
$$\frac{\mathrm{d}L}{\mathrm{d}t} = L\left[g - f\left(\frac{L}{\ln 2}-1\right)\right] - \gamma(L_> - L\,Y_>)$$

$$\frac{\mathrm{d}s}{\mathrm{d}t} = -\frac{g}{\lambda}\,N\,L \qquad g = \mu\frac{s}{K_s+s} \qquad \nu = \frac{\beta}{g}$$
$$\frac{\mathrm{d}a}{\mathrm{d}t} = -k_\mathrm{b}\,b\,a - d_\mathrm{a}\,a \qquad f = \frac{\beta}{1+\left(\frac{a}{k_1}\right)^{h_1}}$$
$$\frac{\mathrm{d}b}{\mathrm{d}t} = \gamma\,B_\mathrm{in}\,N\,L_> - d_\mathrm{b}\,b \qquad L_\mathrm{m} = L_\mathrm{min} + \frac{L_\mathrm{max}-L_\mathrm{min}}{1+\frac{a}{k_2}}$$
$$\frac{\mathrm{d}c}{\mathrm{d}t} = \gamma\,(1-p_\mathrm{c})N\,L_> - d_\mathrm{c}\,c \qquad L_0 = \left(1+\frac{\mu}{\beta}\right)\ln 2$$
$$\frac{\mathrm{d}c_\mathrm{r}}{\mathrm{d}t} = \gamma\,p_\mathrm{c}\,N\,L_> \qquad OD = \eta(N\,L + c(t) + c_\mathrm{r}(t))$$

$$Y_>\left(x=\frac{L}{L_0L_\mathrm{m}}\right) = \begin{cases} \frac{x}{\nu}\left(x^\nu - \left(\frac{x}{2}\right)^\nu\right) & \text{for } x \le 1 \\ x - 1 + \frac{x}{\nu}\left(1-\left(\frac{x}{2}\right)^\nu\right) & \text{for } 1 \le x \le 2 \\ 1 & \text{for } 2 \le x \end{cases}$$

$$\frac{L_>}{L_0L_\mathrm{m}}\left(x=\frac{L}{L_0L_\mathrm{m}}\right) = \begin{cases} \frac{x}{\nu\ln 2}\left(x^\nu - \left(\frac{x}{2}\right)^\nu\right) & \text{for } x \le 1 \\ x\frac{\ln x}{\ln 2} + \frac{x}{\nu\ln 2}\left(1-\left(\frac{x}{2}\right)^\nu\right) & \text{for } 1 \le x \le 2 \\ x & \text{for } 2 \le x \end{cases}$$

Similar initial conditions apply as for the PDE model: $N(0)$, $s(0)$ and $a(0)$ are known experimentally, $b(0) = c(0) = c_r(0) = 0$, and because we start the experiment with exponentially growing cells, we consider that they reached the steady size distribution, where $L(0) = L_0$.

3.3.4 Parameters of the ODE model

The two models share exactly the same variables and parameters, except for ℓ and $n(\ell, t)$ which are specific to the PDE model, and $N(t) = \int_0^\infty n(\ell, t)\,\mathrm{d}\ell$, the total number of cells, and $L(t) = \int_0^\infty n(\ell, t)\,\mathrm{d}\ell$, the average cell length in the population, specific to the ODE model. For other variables and parameters, see section 3.2.7.

3.3.5 Agreement of PDE and ODE models

Figure 3.14 compares the PDE and ODE models on a typical parameter set. Different colours represent different initial antibiotic doses, spaced between each other by a factor 2.

The overall shapes of these state variables are conserved between the two models. Globally, it seems that only the green curve, the lowest antibiotic dose that dose an effect, is in disagreement between the PDE and ODE models.

We can observe that cells gives impossible values to N. This is a typical problem of simulations that represent the number of cells as a continuous quantity, rather than a discrete one. Both the PDE and ODE models are affected by this problem.

The average cell length is also too high for some parameter values, for both models. Under the microscope, it is rare to see cells longer than a couple of hundreds of times their normal length. In this light, both models are wrong when they predict an average length larger than about 300. For the highest antibiotic doses, the predicted cell lengths are particularly unrealistic, but this is not so impactful because at this time, as the cell number suggests, there is probably not a single cell alive any more. Generally, while the antibiotic subsists, the average length tends to augment and the number of cells to decrease, and they both do so exponentially. If the antibiotic subsists for too long, both average length and cell numbers reach unrealistic values.

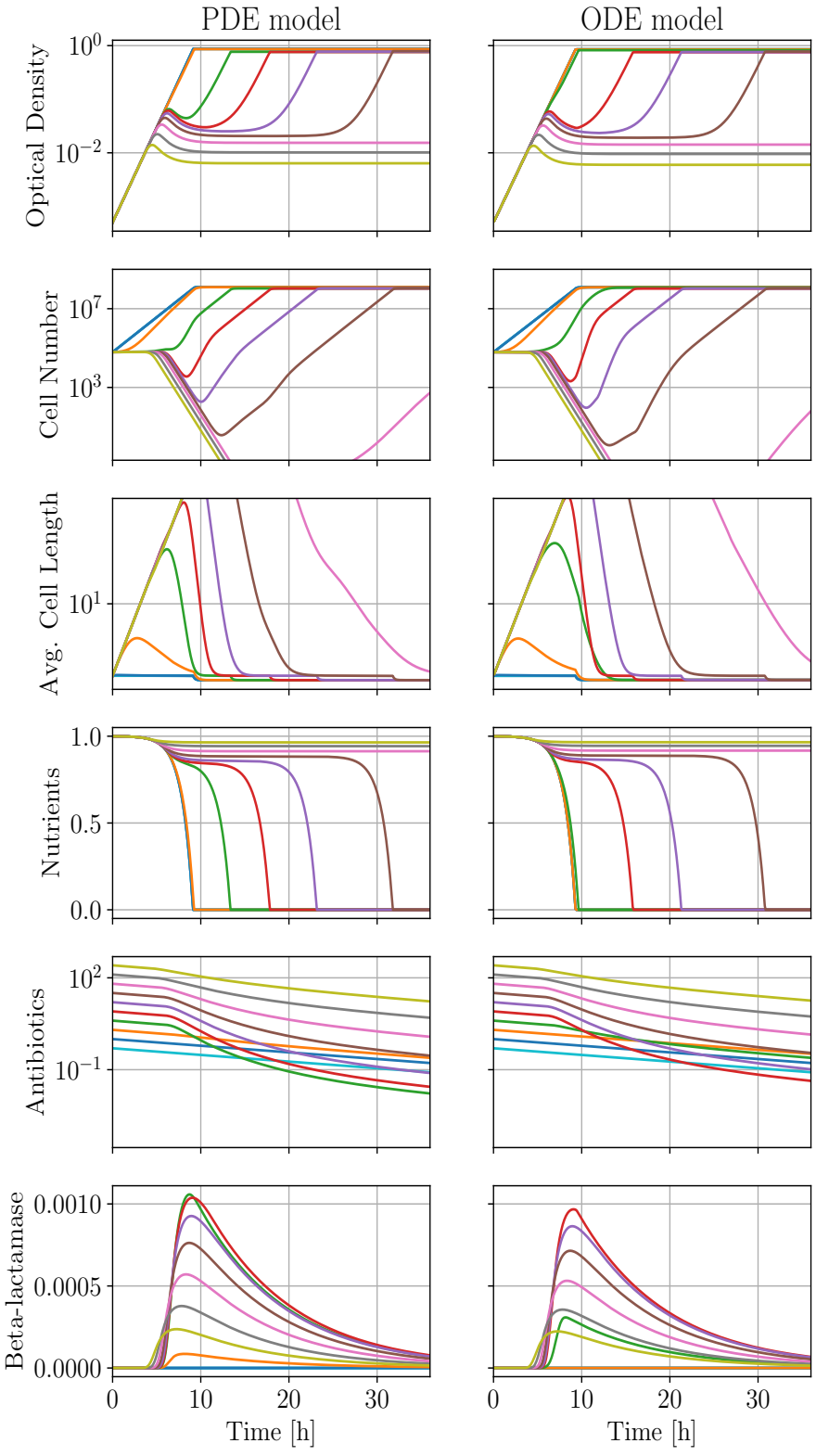

Figure 3.14: Comparison of the PDE and ODE models on the same parameters, chosen to exhibit all of the model features.

In retrospect, the fact that we were able to make this dimensionality reduction: going from a 1-dimensional PDE model to a 0-dimensional ODE one without losing too much information, means that the original problem was very constrained. In this case, the whole shape of the distribution of cell lengths at any time can be almost completely specified by a couple of scalar variables. However, from a modelling perspective, it is far from obvious how it would have been possible to come up with the reduced model, or another one with similar features, without first developing the population model.

3.4 VALIDATION OF THE MODEL

Numerous previous studies made an ensemble of observations on the response of bacteria to β-lactams. In this section, we check if the model satisfies these constraints and whether it can help acquire new insight with respect to these previous observations.

3.4.1 Combined OD, cell number and length predictions

The link between OD and cell number during β-lactam treatment is a notoriously difficult problem because of cell filamentation. As a result, β-lactam-resistance models either conflate number of cells with optical density, or do not attempt to model the temporal dynamics of the response. Interpreting the OD as a number of cells can lead to wrong parameters or erroneous conclusions. Moreover, the ability to quickly and reliably measure length distributions is only recent (Fredborg et al. 2015). Now that specialized devices allow for successive whole cell length distributions to be acquired quickly and automatically, there is a need for models able to incorporate data coming from multiple observables: optical density readings (for measurement of biomass), viable cell counts (for measurement of cell number), and length distributions. We do not have the ability to reliably measure the average cell length, but our simultaneous measurements on OD and cell number are well-matched by the model, as shown in figure 3.15.

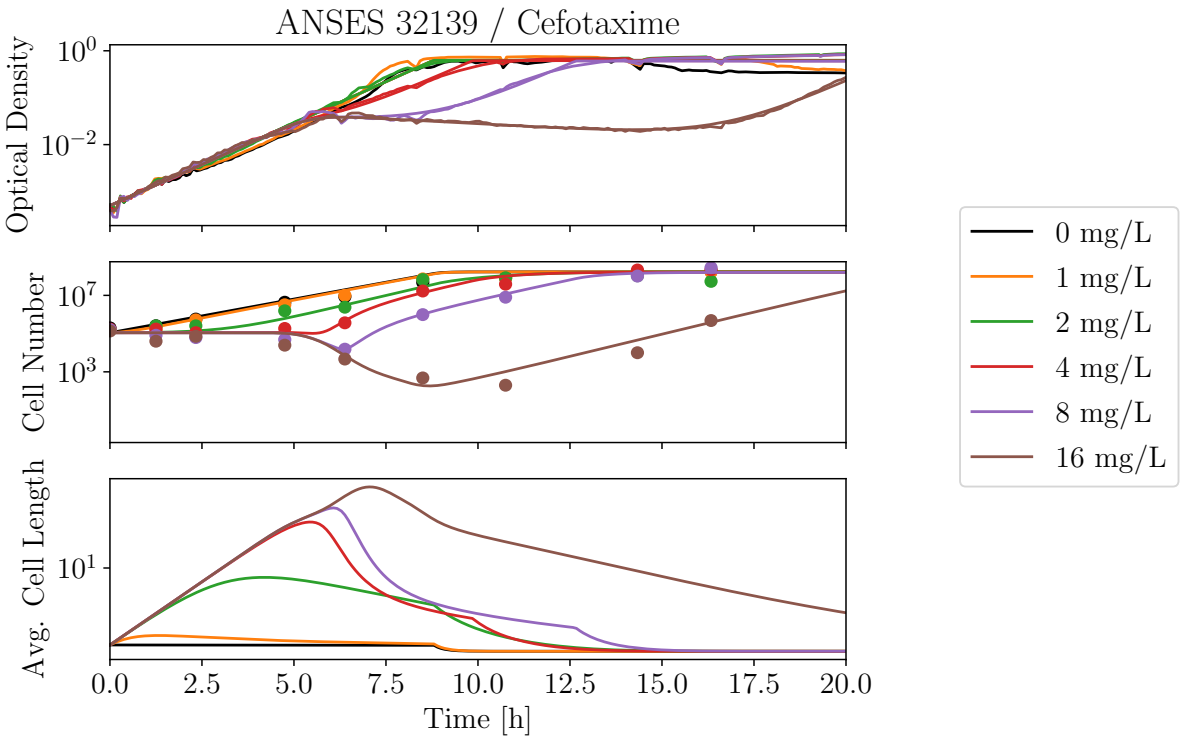

Figure 3.15: ODE model fit to both optical density and cell number for a resistant strain.

3.4.2 Inoculum effect

Active antibiotic degradation is known to cause what is called the inoculum effect. First described by Kirby (1945), this effect relates to the decrease of antibiotic efficacy as the initial cell density increases. It is seen as one of the effects of collective antibiotic tolerance (Vega and Gore 2014; Hannah R. Meredith 2015). The understanding and quantitative characterization of this effect has been the subject of several studies (Artemova et al. 2015; Salas et al. 2020), as the precise knowledge of this effect would give an edge for the development of optimal treatments (Hannah R. Meredith et al. 2015).

Figure 3.16 shows a resistant strain treated with the same antibiotic doses, starting from three different cell densities. The model, plotted over the measured OD, shows that it is able to exhibit a behaviour compatible with the inoculum effect (observe in particular how the regrowths of 4, 8 and 16 mg/L are predicted and observed at different times for the two lowest

ODs, and how the OD curves for the highest initial condition are indistinguishable from untreated cells).

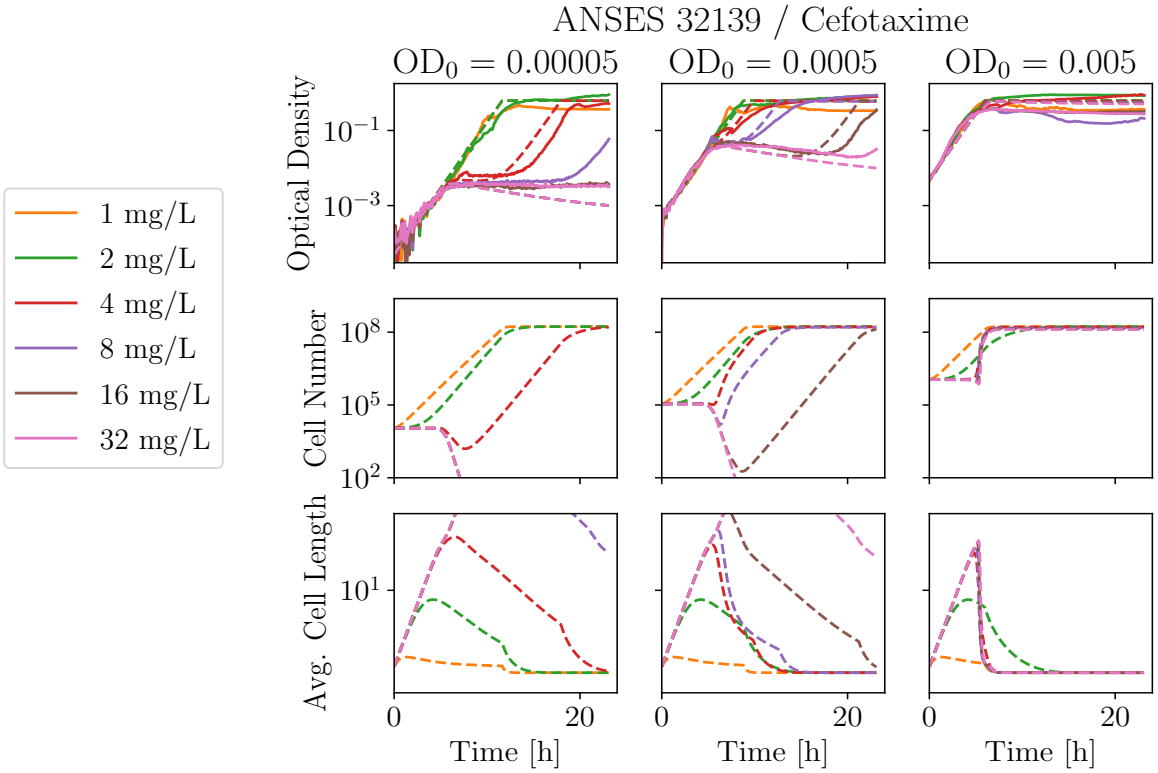

Figure 3.16: Representation of the inoculum effect. The dose of antibiotic sufficient to inhibit the growth of cells during 20 hours increases dramatically as the cell inoculum increases. The model is shown in dashed lines and data for OD in plain lines.

3.4.3 Single-cell MIC

Modelling attempts of the inoculum effect are often phenomenological: Salas et al. (2020) for example study which of six general functions can better account for the relation between the MIC and the starting cell density. However, Artemova et al. (2015) manage to explain this relation with a simple model of antibiotic diffusion through the cell wall, the assumption being that cells start dying when their internal antibiotic concentration crosses a threshold. They also introduce the single-cell MIC (scMIC), the limit of the MIC when the inoculum tends to zero. Their model predicts an exponential increase of the MIC with the inoculum at low inocula, and a linear increase at high inocula. This is in

exact agreement with figure 3.17 which shows the prediction of the ODE model for increasing inocula.

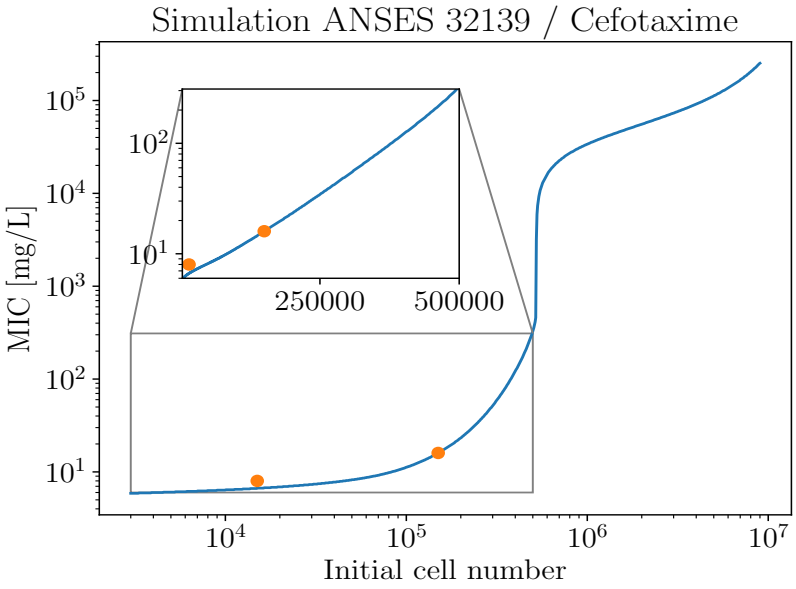

Figure 3.17: Extrapolation of MIC measurements for increasing inocula of a resistant strain. The two orange points are the actual measurements that correspond to figure 3.16. The model shows what MICs it predicts for very large inocula, if these hypothetical antibiotic concentrations were achievable in practice. The inset for small inocula shows the exponential behaviour of the MIC in this region. With these parameters, the scMIC is 5.8 mg/L.

3.4.4 Proportionality of lysis and growth rates

Another remarkable property of the bacterial response to β-lactams, reported as early as by G. L. Hobby, Meyer, and Chaffee (1942); Gladys L. Hobby and Dawson (1944) and further studied by E. Tuomanen et al. (1986) and Lee et al. (2018), is the relationship between the lysis rate and the growth rate. As put by Gladys L. Hobby and Dawson (1944), "Conditions which increase the rate of growth of bacteria increase the rate at which penicillin acts. Conditions which decrease the rate of growth decrease also the rate at which penicillin acts. Penicillin is most effective when active multiplication takes place." The effect of penicillin was quantified in this study by counting viable cell numbers at different times after addition of the antibiotic. E. Tuomanen et al. (1986) did the study on cultures experiencing balanced growth, in chemostat, also by counting cell numbers.

Lee et al. (2018) exploited an automated handling robot to make the same study, this time on batch cultures, and through OD measurements.

Since our model allows easy access to number of cells as well as OD, it is an ideal candidate to test this relationship. Because of the filamentation of cells, the quantitative effects of the antibiotic on N or on the OD are not similar and whether we consider the growth rate of N or of the OD might lead to different conclusions: we will then study these two quantities. The OD of the model includes the OD of dead biomass, so we will also consider the growth rate of a third quantity, the live biomass ($N\,L$).

It is useful to first compute the instantaneous net growth rate of these three quantities. From the ODE model,

$$\begin{aligned}
\frac{1}{N}\frac{\mathrm{d}N}{\mathrm{d}t} &= f\left(\frac{L}{\ln 2}-1\right)-\gamma\,Y_{>}\\
\frac{1}{N\,L}\frac{\mathrm{d}N\,L}{\mathrm{d}t} &= g-\gamma\frac{L_{>}}{L}\\
\frac{1}{OD}\frac{\mathrm{d}OD}{\mathrm{d}t} &= g-\frac{g\,(c+c_{\mathrm{r}})+d_{\mathrm{c}}\,c}{OD}
\end{aligned}$$

The three net growth rates have the form of the difference of two terms: the normal growth rate, and the antibiotic-induced lysis rate. We can then define the three lysis rates:

$$L_{\mathrm{N}}=\gamma\,Y_{>},\quad L_{\mathrm{NL}}=\gamma\,\frac{L_{>}}{L}\quad\text{and}\quad L_{\mathrm{OD}}=\frac{g\,(c+c_{\mathrm{r}})+d_{\mathrm{c}}\,c}{OD}$$

Lee et al. (2018) suggest studying the maximum lysis rate occurring during the course of an experiment. Applying this definition, we obtain figure 3.18 which shows that although the maximum lysis rates increases with the basal growth rate of the cells μ, it hits a threshold of value γ in the case of L_{N} and L_{NL}. Only the lysis rate measured through the optical density is a linear function of μ on an extended range. This graph also shows for the OD lysis rate a similar dependency to the antibiotic dose as noted by Lee et al. (2018): "The slope becomes smaller and the y-intercept becomes larger with increasing antibiotic concentrations."

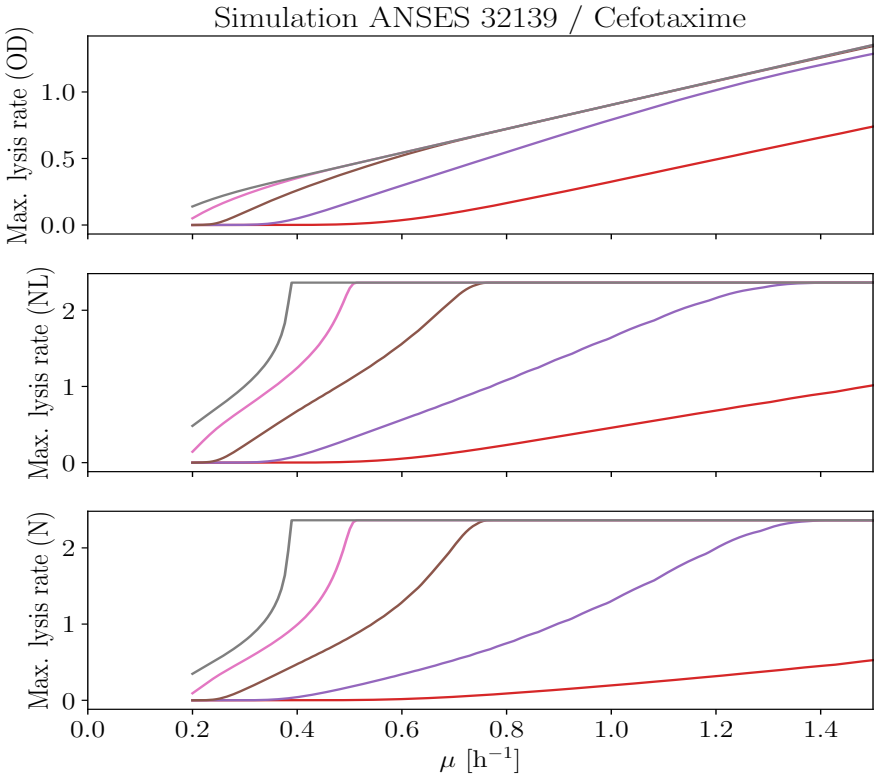

Figure 3.18: Maximum lysis rates of OD, live biomass and number of cells shown as a function of the basal growth rate of the cells.

3.5 CHAPTER SUMMARY

Because cell length changes dramatically during antibiotic treatment, the measured OD is not an accurate representation of the number of cells. In order to disentangle the complex link between these two quantities, a growth-fragmentation PDE model based on Hall and Wake (1989) was derived (section 3.2.1). The main assumptions are an exponential elongation unperturbed by the antibiotic treatment (3.2.2), a division rate directly affected by the antibiotic (3.2.3), a death rate dependent on the length of the cell (3.2.4), and that filamented cells are able to divide into several small cells once the antibiotic is gone (3.2.5). The model of action of antibiotic: inhibition of division and blocking of the cell wall repair mechanism, is justified by its molecular binding with two different enzymes: respectively PBP3 and PBP1.

The model is able to fit experimental data, as well as exhibit several notable features reported in the literature (3.4).

However, the simulation of the PDE system being computationally expensive, we found approximations to reduce the simulation of the whole length distribution to the simulation of only two scalar variables: the total number of cells, and their average length (section 3.3). Both PDE and ODE models share exactly the same parameters, and agree on validation experiments.

4 MODEL CALIBRATION

The resistance models contains 17 parameters, unique to each combination of bacterial strain and antibiotic used. In order to make the model perform predictions relevant to clinical isolates, it should be used with the appropriate parameters. However, although some parameters can be calibrated independently of the others, a large proportion cannot, and taking literature values for those is not possible because of the wide range that they span in wild strains. For the parameters that cannot be measured easily, or only through complex or expensive methods, the only possibility is to simulate an experiment with the model repeatedly with different parameter values, compare the output of the simulation to the real experiment, and choose the parameter set that provides the best fit. A naive approach would be to select a few values in the plausible variation range of each parameter, and try all these combinations. But this approach is only realistic at low dimensions: for 17 parameters, even choosing only 3 values for each, the time needed to simulate all these combinations is counted in years.

Besides the computational challenge, there is also an information problem. The model contains 7 state variables: number of cells, average length, nutrients, antibiotic, β-lactamase, and two kinds of cell debris. Most of these quantities are in principle observable, but some are much easier than others. As explained in the introduction, we deliberately chose to focus on the plate reader as main measurement instrument. However, the readings of optical density are combined readings of four of the state variables of the model: number of cells, length, and the debris. Another possible observable is the number of cells, but from dilutions, calibrations, and repetitions, to counting tens of thousands of cells on plates, the amount of tedious work involved in frequent measurements of the number of cells could be done for a couple of strains at maximum, during the development of the model, but not to characterize unknown strains. The question is then whether and how it is possible to estimate the model parameters, and make accurate predictions for all the state variables, based solely on the optical density.

Furthermore, unlike what the chapter division of this document suggests, the processes of model development and model calibration cannot simply be split into separated processes that are done one after the other. These processes are done simultaneously and feed one another, they are actually also interleaved with data acquisition. This makes model calibration an essential lever of model development itself: the inability for a model to fit experimental data can be interpreted as a sign of a mistake in the modelling or the implementation. Therefore, reliability and efficiency are indispensable features of the model calibration framework. In this particular case, the scale of the model, its subtle dynamics, and the data available all participate in making this problem even more challenging.

This chapter explains how we tackled these problems. First, we explain our whole setup of optimization methods for parameter inference. Then, we assess the identifiability of the model on restricted data.

4.1 DESIGN OF A ROBUST AND EFFICIENT MODEL CALIBRATION FRAMEWORK

The adjustment of a model to data is an optimization problem consisting in finding a set of parameters θ^* minimizing the distance between the predicted and observed data points, for some notion of distance.

Linear least square formulations can be used not only for linear regressions, but for any model linear in the parameters to fit, for example $y = a\,x^2 + b\,\log x$.

The best known problem of this type is linear regression, where the model consists of an affine relation with two parameters $y = a\,x + b$. One can define here the residuals, the differences between the data and the model at each data point. It is common to use the sum of squared residuals to assess the quality of the fit. Some algorithms to solve this type of problems are known under the name of linear least squares and allow to find the globally optimal solution efficiently.

The jacobian of a multi-valued and multi-parameter function is the matrix of first derivatives of the values relatively to the parameters. Here, it expresses the dependency of each residual on the parameters to fit.

However, most complex models, or models involving ODEs, are not linear in their parameters and require other optimizers. The first generalization of linear least squares methods is nonlinear least squares methods, that rely on the knowledge of the jacobian of the model. The jacobian can either be given by the user in analytical form when it is tractable, or estimated numerically.

Alternatively, a general scalar optimization algorithm can be used to minimize the sum of the squares of the residuals. Some scalar algorithms need a way to know or estimate the gradient vector (analogue of the jacobian for a scalar multi-parameter function), and some also use, or compute on the fly the Hessian matrix, which informs on the second derivatives of the function with respect to its parameters. Algorithms known as "black-box" do not require any information about the derivatives of the function.

There is a gradation between algorithms who require deep knowledge about the function to minimize and its derivatives, and exploit it to converge efficiently to a local optimum, and algorithms who only use the values of the function, but are sometimes better at finding global optima. It can be counterintuitive to think that the algorithms using fewer data can find better optima, but this is because derivatives are local information and are of little use to explore the parameter space. Unless in special cases, there is in general no way to reliably reach the global optimum of a non-linear optimization problem.

Although simulated annealing converges to the global optimum of even non-linear problems with certainty under some conditions, it is a mainly theoretical result, since the time required for this is completely prohibitive in practice.

The choice of algorithm can be daunting. Even the choice of the cost function needs careful consideration. In the next subsection, we will describe the choices that we made relatively to the fitting strategy. In order to reliably obtain good fits, it is crucial to put thought in the three components of fitting a given model to data besides the model itself: the data, the parameters, and the fitting algorithms. Then, we will elaborate on the intrinsic difficulty of the task of fitting this particular model. Finally, we will consider the problem of fitting this model with only optical density data.

4.1.1 Choice of the cost function

The purpose of the cost function is to quantify the match between the simulated model for a given parameter set, and the experimental data points. The data points are available from two sources: the plate reader, reading the optical density of wells at regular intervals of time, and the CFU counts, giving access to the number of living cells in each well. The CFU counts are done manually, which limits the frequency of observation, compared to the optical density measurements. Formally, we can have K_{OD} OD measurements OD_i made on times t^i_{OD}, and K_{N} CFU counts N_j performed on times t^j_{N}. The numerical simulation of the model gives access to continuous functions $OD(t)$

and $N(t)$ which we ideally want as close as possible from the experimental data points.

In the general case, let's assume that we have N observations y_i taken at times t_i, each marred by independent normal observation noise of standard deviation σ_i. One can then define the likelihood $\mathcal{L}(\theta)$ of a set of parameters θ: $\mathcal{L}(\theta) = f(y|\theta)$ where $f(y|\theta)$ is the probability density of making the observations y_i from a model parameterized by θ:

$$\mathcal{L}(\theta) = \frac{1}{\sqrt{2\,\pi}^N} \prod_i \frac{1}{\sigma_i} \mathrm{e}^{-\frac{(y_\theta(t_i)-y_i)^2}{2{\sigma_i}^2}} \tag{4.1}$$

The objective of the parameter search is to find θ that maximizes the likelihood, this is the Maximum Likelihood Estimator (MLE). For numerical reasons, because of the range of variation of the likelihood, one often maximize instead the logarithm of $\mathcal{L}$ (Andreas Raue et al. 2013):

$$\log \mathcal{L}(\theta) = cst - \frac{1}{2} \sum_i \frac{(y_\theta(t_i) - y_i)^2}{{\sigma_i}^2} = cst - \text{cost} \tag{4.2}$$

where the constant term is independent on θ. Maximizing the likelihood then amounts to minimizing the second term, that we will from now call the cost.

If this is a mathematically well-defined problem, there is a number of details that one needs to take care of to allow its easier numerical resolution.

Noise model

Determining the uncertainty of the observed data can be crucial to the success of the optimization function. The uncertainty distributions on the cell counts have been the object of section 2.1.5, where we derived a distribution, which is not normal, but which can be very satisfyingly approximated by a normal distribution. The standard deviations σ_{N}^j for the numbers of cells are then estimated through this distribution.

Concerning the OD, the measurement noise of the plate reader can be estimated with repeated OD measures of colloidal solutions. We found that it can be approximated with the sum of a 2 % multiplicative gaussian noise and an additive gaussian noise of standard deviation 10^{-4}. Formally, we modelled the observed value y_i as $y(t_i) + \delta_i$ with δ_i a random value distributed

according to a normal law of zero mean and standard deviation $\sigma^i_{\text{OD}} = \frac{y(t_i)}{50} + 10^{-4}$.

However, the measurement noise alone does not account for all the variations observed experimentally on technical replicates. The preparation of the experiment introduces experimental errors related to the handling of fluids by micropipettes. Micropipette constructors advertise both accuracy and precision of their instruments to a few percents. Following this specification, adding a multiplicative noise of 5 % to the initial number of cells and antibiotic concentration produces results consistent with the observed experimental noise, of up to 20 % on the time of regrowth, as shown on figure 4.1.

The distribution error (see 2.1.5) is here negligible in front of the dilution error, by a factor 20.

The results of adding this noise only to N or a are comparable. Hence, these two variables contribute equally to the dilution noise.

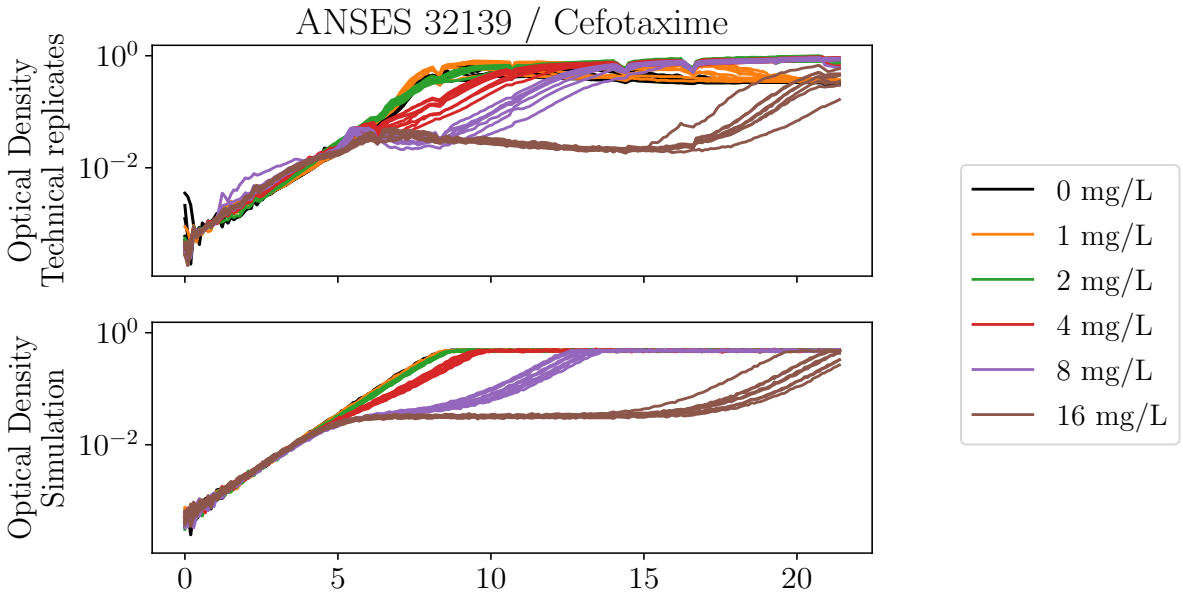

Figure 4.1: Top: technical replicates, bottom: simulation of the experiment. The noise model on the simulation consists of a 2 % multiplicative gaussian noise on the OD, and 5 % on the initial values of a and N.

Factoring this dilution noise in the likelihood function is doable, but requires another nested optimization procedure, as described in appendix A. Further code optimization is needed to make this feasible in practice. Until then, unless specified otherwise, the only noise considered is the measurement noise through σ^i_{OD} and σ^j_{N}.

Residuals scaling

The first question to consider is the natural scaling of the data. There are theoretical and practical reasons to argue that OD and number of cells should be considered on a logarithmic scale.

First, the number of bacteria N in a well can vary, in principle, from 1 to billions: over 9 decimal orders of magnitude. Accurately representing variations of this order is impossible with a linear scale, which can hardly display information spanning more than 1 or 2 orders of magnitude.

Secondly, the simplest equation to describe the unrestricted growth of a cell population is the exponential equation which indicates that the derivative of N is directly proportional to N, and therefore spans a range as wide as N itself: $\frac{\mathrm{d}N}{\mathrm{d}t} = \mu N$.

This equation can be rewritten in order to exhibit the derivative of the logarithm of N, which is now just constant and equal to the intensive variable μ. This is arguably the most natural formulation: $\frac{\mathrm{d}\ln N}{\mathrm{d}t} = \mu$.

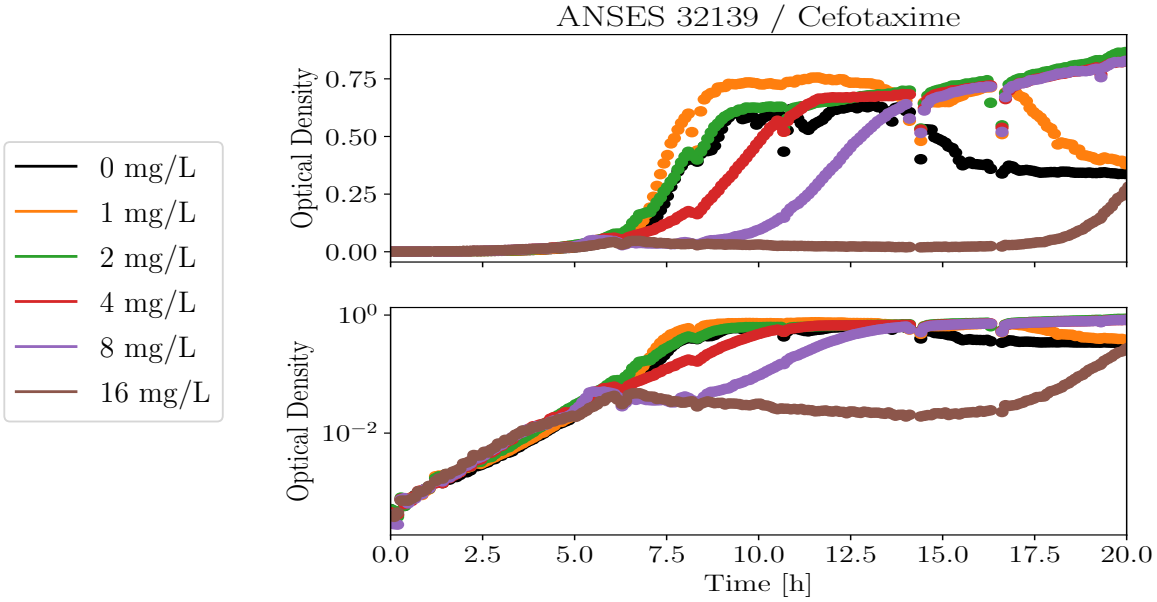

Figure 4.2: Top: linear, bottom: logarithmic scaling. With linear scaling, the exponential growth is invisible, as well as the low stationary level of the 16 mg/L curve (above 10^{-2}). With logarithmic scaling, everything is visible, and less importance is given to the late stationary phase which is not the focus of the model.

Experimentally, as demonstrated by figure 4.2, a linear scale disproportionately emphasizes the late features of the growth

curves, while masking the early exponential phase, as well as fine but important points such as the optical density reached at 6 h when the curves start to split, and the stationary level where the 16 mg/L establishes while the antibiotic dose is still too high to allow regrowth.

If the logarithmic scale is the natural scale of these quantities, it is more relevant to take $y = \log OD$, in the least squares equation, instead of $y = OD$, and to adapt the uncertainties appropriately. With X the random variable representing the measured value of optical density or number of cells, we need then to compute $\mu_{\log X}$ and $\sigma_{\log X}$, the average and standard deviation of $\log X$, as a function of μ_X and σ_X, average and standard deviation of X. Given in these terms, this problem is ill-posed, because X being normally distributed, it can take negative values, which prevents in principle to take its logarithm. However, under the assumption that the negative support of X is negligible, a first-order Taylor expansion of $\log(\mu_X + (X - \mu_X))$ allows deriving:

$$
\begin{aligned}
\mu_{\log X} &= \mathrm{E}[\log(X)] \\
&= \mathrm{E}[\log(\mu_X + (X - \mu_X))] \\
&\approx \mathrm{E}\left[\log(\mu_X) + \frac{X - \mu_X}{\mu_X}\right] \\
&\approx \mathrm{E}[\log(\mu_X)] + \mathrm{E}\left[\frac{X - \mu_X}{\mu_X}\right] \\
\mu_{\log X} &\approx \log(\mu_X)
\end{aligned}
$$

$$
\begin{aligned}
\sigma_{\log X} &= \sqrt{\mathrm{Var}[\log(X)]} \\
&= \sqrt{\mathrm{Var}[\log(X + (X - \mu_X))]} \\
&\approx \sqrt{\mathrm{Var}\left[\log(\mu_X) + \frac{X - \mu_X}{\mu_X}\right]} \\
&\approx \sqrt{\frac{\mathrm{Var}[X]}{\mu_X^2}} \\
\sigma_{\log X} &\approx \frac{\sigma_X}{\mu_X}
\end{aligned}
$$

These average and standard deviation are those of the normal noise model on $\log X$ approximating the best, at first order, the normal noise model on X. With our noise model of $\sigma^i_{\text{OD}} = \frac{y(t_i)}{50} + 10^{-4}$ (see 4.1.1), this approximation becomes increasingly wrong for smaller ODs (when the negative support of the normal distribution cannot be neglected any more), because $\sigma_{\log \text{OD}}$ diverges whereas σ_{OD} should tend to a finite value. Fortunately, the main measurement range for optical densities spans 10^{-3} to 10^{-1}, where this problem is not the most important.

Besides the scaling of the data, another point to consider, since the variance of the noise depends on the data, is whether to use the simulated point $y(t_i)$ or the experimental point y_i to compute the noise.

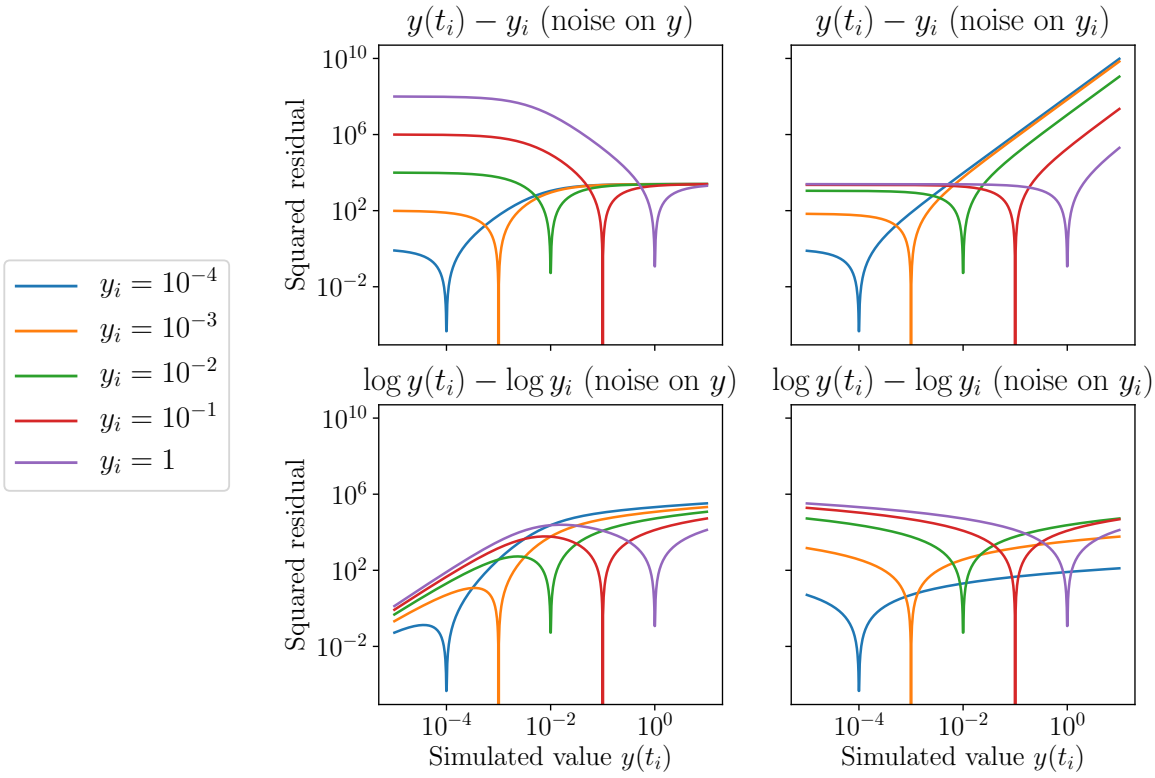

Figure 4.3: For five different experimental values y_i, this figure shows the behaviour of the squared residual as a function of the simulated value $y(t_i)$. Top: linear OD, bottom: logarithmic OD. Left: noise applied on $y(t_i)$, right: noise applied on y_i.

Although these four different noise models all allow the residuals to admit the value 0 when the simulation agrees with the experiment, they have different behaviours when the simulation and data do not agree perfectly, as shown on figure 4.3. The op-

timization algorithm heavily relies on the behaviour of the cost function away from the optimum to find a way to the optimum. Consequently, when possible, it is important to optimize this behaviour in order to facilitate the optimization. In general, the cost function should be continuously decreasing towards its minimum, like a funnel.

Both linear versions are flat on at least one side, which can prevent convergence. The first logarithmic version presents two minima and could then drag the optimizer into nonsensical regions. The second logarithmic version is very well-behaved for optimization: a unique minimum, and slopes on both sides to guide the optimization like in a funnel. This is the one that we used. Finally, the residuals for OD and N are written:

As a matter of fact, when using the top right noise model, it is not uncommon to see some simulated ODs lower than the data. The optimizer misses these points because their cost function is locally flat.

$$r^i_{\mathrm{OD}} = \frac{\log OD(t^i_{\mathrm{OD}}) - \log OD_i}{(\frac{OD_i}{50} + 10^{-4})/OD_i} \quad \text{and} \quad r^j_{\mathrm{N}} = \frac{\log N(t^j_{\mathrm{N}}) - \log N_j}{\sigma^j_N / N_j}$$

Finally, both non-linear least squares optimization algorithms (who work on the whole array of residuals) and scalar function optimization algorithms (who only take a scalar cost) then minimize the same function, extracted from 4.2:

$$\mathrm{cost} = \frac{1}{2}\left(\sum_i {r^i_{\mathrm{OD}}}^2 + \sum_j {r^j_{\mathrm{N}}}^2\right)$$

4.1.2 Parameter scaling

The 17 parameters of the model have widely different ranges of biologically relevant units and values. For example, λ, the conversion factor from cells to nutrients, is a quantity on the order of $0.5\,\mathrm{L/g}$, while K_s, the half-velocity nutrient constant, is around $1\,\mathrm{mg/L}$. Some are better known than others: this is the case for λ which is easy to estimate from any curve; inversely K_s has a range of different reported values in the literature spanning 3 orders of magnitude, and in this range has little effect on the simulations, which leads to uncertain estimations of this parameter.

All 17 parameters: concentrations, rates, lengths or Hill exponents, are bounded below by zero. Some of them are bounded above, like p_c, by 1. The others do not really have an upper limit, but one can define biologically plausible regions outside which it is not useful to search. The restriction of the search

to reasonable bounded regions does not only make for a more efficient parameter search, it also limits the risk of numerical instabilities caused in the integration of the ODE system by excessive parameter values, which could perturb or even stop the parameter search before its term.

However, the diversity in units and uncertainty ranges in the parameters is transposed in the axes of the resulting 17-dimensional box where the search is to be conducted. Simultaneously estimating parameters over disproportionate regions is known to pose numerical problems to most optimizers. Therefore, a parameter preconditioning is needed to rescale the rectangular box into a hypercube.

For similar reasons as for the data, the natural scale of some parameters is logarithmic, notably the parameters assimilable with an antibiotic concentration: k_1 and k_2. The parameters k_b et K_s, that can vary within large ranges, are also better expressed with a logarithmic scaling. On the contrary, Hill exponents like h_1 and parameters that have limited ranges of variation between strains, like μ and λ, are best fit within a linear space.

It is convenient to distinguish unscaled parameters, as they appear in the model, and scaled parameters, as they are used in the search, by the respective notions of "phenotype" and "genotype." The genotype versions of the parameters are all bounded between 0 and 10.

This convention, and genotype bounds, are suggested by the author of CMA-ES, and should not be attributed any biological meaning.

In order to convert parameters from phenotype p (with lower bound lb and upper bound ub) to genotype g and inversely, one of the following linear or logarithmic transformations is applied, depending on the parameter:

$$g = \begin{cases} 10\frac{p-lb}{ub-lb} & \text{linear} \\ 10\frac{\log(p/lb)}{\log(ub/lb)} & \text{logarithmic} \end{cases}$$

$$p = \begin{cases} lb + (ub-lb)\frac{g}{10} & \text{linear} \\ lb\left(\frac{ub}{lb}\right)^{g/10} & \text{logarithmic} \end{cases}$$

4.1.3 Integration of the ODE

The ODE model is implemented in Python and solved with the function `solve_ivp` using the method `LSODA`, which is a widely used integration algorithm implemented in FORTRAN (Hind-

marsh 1983). `LSODA` automatically detects the stiffness of the problem, and switches appropriately between the explicit Adams integration method, and the implicit BDF for stiff parts (Petzold 1983). The problem is stiff notably around the time of exhaustion of glucose when g, and several derivatives change abruptly.

The proper way to precondition a model for numerical integration would actually be to make it completely dimensionless by dividing all the variables and parameters by the appropriate combinations of parameters of the model.

However, even stiff solvers fail to integrate the model as it is, because of the disproportion between its variables. The variable N represents a number of cells, and can then take values up to 10^9, whereas the variables representing concentrations like s, a and b take much smaller values (typically lower than 1) in the units chosen for them. Numerical solvers cannot be simultaneously accurate over such a range of magnitudes. For this reason, we pass to the numerical solver a rescaled version of the model, with several variables changed in order to make their ranges similar: $\hat{N} = \eta\, N$, $\hat{\lambda} = \eta\, \lambda$, $\hat{B_{\text{in}}} = B_{\text{in}}/\eta$, $\hat{\eta} = 1$, $\hat{c} = \eta\, c$, $\hat{c}_{\text{r}} = \eta\, c_{\text{r}}$.

4.1.4 Choice of fitting algorithms

The scientific computing library `scipy` provides a variety of diverse optimization algorithms, among which local optimization algorithms for scalar functions through the function `minimize`, local least-squares methods through `least_squares`, and global optimization methods for scalar functions such as `basinhopping`, `dual_annealing` or `differential_evolution`. Another powerful optimization algorithm for scalar functions is Covariance Matrix Adaptation Evolution Strategy (CMA-ES) (Hansen 2006), implemented in the python package `cma`.

Several of these algorithms can be leveraged for different purposes. Searching for the best fit in a vast and multi-dimensional parameter space can be decomposed in two successive tasks: first, finding a region where parameters produce good fits, and secondly, finding the best fit in this region. The first task requires a global optimization algorithm, whereas the second needs a local algorithm.

A comprehensive comparison of optimization methods for a simpler biological problem can be found in (Andreas Raue et al. 2013). For our case, we found experimentally that three strategies worked well for the search of the first approximate fit:

- CMA-ES setup to initially span the whole parameter hypercube ($\sigma = 2$);

- the `basinhopping` algorithm of `scipy`, modified in order to use a non-linear least squares method as local optimizer;
- "multistart local search" consisting of successively calling `least_squares(method='trf')` from several predetermined initial positions, generated with Latin Hypercube Sampling (LHS) of the search region.

Latin Hypercube Sampling is a method to place a given number of random points in a multidimensional region while ensuring a uniform covering of the region.

These three methods were the most successful at finding fits, generally within 5 or 10% of the estimated optimum (best fit ever found). In order to refine these first fits, the modified `basinhopping` algorithm with smaller step size and temperature settings was sometimes used.

Finally, as developed in 4.2.1, profile likelihood computations require numerous successive parameter readjustments starting from very close initial positions. For this application, we can make the hypothesis that with sufficiently small steps, the local minimum does not change from an iteration to the next, and that it is then sufficient to call a local solver such as `least_squares(method='trf')` at each step, starting from the best fit at the previous iteration, which is two orders of magnitude faster than the full fitting procedure from scratch.

4.2 ASSESSMENT OF THE MODEL IDENTIFIABILITY

It is not always possible to infer all the parameters of a model from the observation of its behaviour. Parameters whose values cannot be inferred are called *unidentifiable*, for two kinds of reasons: *structural* and *practical*.

Structural unidentifiability is a mathematical property of the model that expresses that no estimate of the value of a parameter is possible to be made from a given set of observations. This might be because the parameter is only involved in an observable that cannot be measured, or because the parameter is mixed with another one such that only a relation between these two parameters can be inferred but not their individual values.

Practical unidentifiability concerns parameters that are mathematically identifiable, but whose estimation with the available data can be done at best with an uncertainty interval so large that it is unexploitable. This happens in cases where a parameter plays a very small, but non-zero, role in the behaviour of

the model, and this role is masked by measurement or intrinsic noise.

Model unidentifiabilities are in general to avoid, because if the value of a parameter cannot be determined, then a simpler model that would not include this parameter would probably fit the data just as well, and be more satisfying from the point of view of model parsimony. From a computational point of view, an optimization problem in a multi-dimensional space degenerated by unidentifiabilities can be much more difficult than in the space restricted to the identifiable parameters.

Finally, parameter identifiability depends on the available set of observables. We will consider for all this section that under the noise model described in 4.1.1, we have access to:

- a temporal series of OD readings,
- a temporal series of CFU counts of the number of cells N,
- the initial glucose concentration $s(0)$,
- the initial antibiotic concentration $a(0)$.

In these conditions, there exists a structural unidentifiability in the model, concerning the parameters B_{in} and k_{b}. Indeed, those are the only parameters that relate to the concentration of β-lactamase of the culture medium, b, but b is not observable with our experimental platform. With no way to make any measurement involving the concentration of β-lactamase, no parameters measured in units involving the concentration of this enzyme can be estimated. Dimensional analysis additionally suggests that their product is the quantity that could be identifiable. This can be shown rigorously by performing the change of variables $\hat{b} = b/B_{\text{in}}$ and $\hat{k_{\text{b}}} = k_{\text{b}} B_{\text{in}}$, which completely removes B_{in} from the model. Without knowledge of the values of k_{b} or b, this prevents recovering the one of B_{in}. It is then useless to search for both k_{b} and B_{in}, and we could fix the value of either without loss of generality.

Besides B_{in} and k_{b}, the conception of the model already hid another unidentifiability, related to the actual length of the cells. Since we cannot take reliable measurements of cell length, all parameters involving lengths would share an unidentifiability. This is the reason why we chose to make ℓ dimensionless.

The identifiability of a model also depends on the data values themselves. Taking the example of the mechanism of debris elimination: one of the hypotheses of the model is that when a cell lyses, it creates a proportion p_{c} of debris that never degrade, while the rest has a half-life d_{c}. We can imagine a strain with $p_{\text{c}} = 1$, or $d_{\text{c}} = 0$: in these cases, the other parameter, respectively p_{c} or d_{c}, would not be identifiable.

Both of these hypothetical strains would be described equally well with a subset of the original model. Actually, we will

see later that this phenomenon will play a large role in the explanation of the data.

The PDE and ODE models share exactly the same parameters, that interact in the same ways. Without access to experimental length distributions, they are then equivalent with respect to parameter identifiability, and although the simulations in this section have been performed with the ODE model, similar results should be expected with the former.

Most complex biological models are partially unidentifiable, and this one is not an exception. This problem is particularly intensified by the use of less data, as in our OD-based approach. Therefore, before using it, and trusting its inferred parameter values, we need to understand what is, or is not identifiable.

4.2.1 Profile likelihood

Although structural unidentifiabilities can be detected by examining the mathematical structure of the model, practical unidentifiabilities are dependent on the quality of the data fed to the model. A way to quantify practical identifiability is to link it to confidence intervals, a parameter θ_i being said unidentifiable if its confidence interval Θ_i^α with confidence level α is infinite, or too large to be useful.

Deciding whether a parameter is inside an interval or outside is a problem known as nested model discrimination. This is typically solved with a likelihood-ratio test, as following. Let H_0, the null hypothesis, be that the value of the parameter θ_i is outside of the α confidence interval for this parameter Θ_i^α. Then, we can define the following ratio:

$$\lambda_{\mathrm{LR}} = -2 \log \frac{\sup_{\theta_i \notin \Theta_i^\alpha} \mathcal{L}(\theta)}{\sup_\theta \mathcal{L}(\theta)}$$

The numerator is the maximum of the likelihood for θ_i outside of its confidence interval. The likelihood reaches its maximum on the boundaries of this confidence interval $\theta_{i\pm}^\alpha$. The denominator is the maximum of the likelihood, without restriction on θ_i. We will note it $\mathcal{L}(\theta^*)$, θ^* being the optimal parameter set. Introducing the cost function with equation 4.2, we can then write:

$$\lambda_{\mathrm{LR}} = 2 \log \frac{\mathcal{L}(\theta^*)}{\mathcal{L}(\theta_{i\pm}^\alpha)} = 2\big(\mathrm{cost}(\theta_{i\pm}^\alpha) - \mathrm{cost}(\theta^*)\big)$$

The theory of the likelihood-ratio test states that under the null hypothesis, λ_{LR} converges to be χ^2-distributed (Wilks 1938). Consequently, to compute the values of the boundaries of the confidence interval with the level of confidence α and df degrees of freedom, we need to solve the following equation:

$$\text{cost}(\theta^{\alpha}_{i\pm}) - \text{cost}(\theta^*) = \frac{\chi^2(\alpha, df)}{2} \tag{4.3}$$

From here, two approaches can be followed: the asymptotic approximation, and the profile likelihood method. The asymptotic approximation consists of approaching the cost function with its 2nd-order Taylor expansion around θ^*_i, the value of θ_i in θ^*.

$$\text{cost}(\theta^*_i) \approx \text{cost}(\theta^*) + \frac{\partial^2 \text{cost}}{\partial {\theta_i}^2}(\theta_i - \theta^*_i)^2$$

with no linear term, and a non-negative quadratic coefficient because θ^*_i is a minimum of the cost function.

We can now look at the extrapolation of the cost function from this curvature, and compare this to the critical χ^2 value from equation 4.3. This leads to expressions of the bounds of the uncertainty interval Θ^{α}_i:

$$\theta^{\alpha}_{i\pm} = \theta^*_i \pm \sqrt{\frac{\chi^2(\alpha, df)}{2\,\frac{\partial^2 \text{cost}}{\partial {\theta_i}^2}}}$$

This approach is convenient because all it requires is the knowledge of the optimal parameter set θ^*, and the curvature matrix of the cost function around this point, which some optimization solvers estimate during their work, and can return as a side-product of the optimization.

To compute a reliable estimate of the curvature matrix, `least_squares` has to be called with the option `jac='3-point'`. Even better, one could use autodifferentiation or a sensitivity solver like CVODES.

However, in the presence of limited data, and when the observables are non-linear functions of the parameters θ, this approximation is often not accurate. A. Raue et al. (2009) showed that the direct exploitation of equation 4.3 allows a better detection of the structural and practical unidentifiabilities of a model in degraded conditions. Repeatedly optimizing the cost function along in one direction allows to generate a profile of the likelihood along this axis, hence the name of the method.

These profiles can then be compared to a threshold defined as in equation 4.3. The parameter α sets the difficulty of the test: it is easier to randomly pass the test for a 68% confidence interval than for a 95% interval. The parameter df has classically one of two values: 1 or $\#\theta$, the number of parameters

in the model. Selecting a value of 1 gives so-called *pointwise* confidence intervals: the intervals that hold for each parameter separately. A value equal to the number of parameters in the system allows to compute the *simultaneous* confidence intervals, that hold for each parameter considering the possible variations of the others. Allowing the values of other parameters to change enlarges the confidence interval of parameters. We chose to judge identifiability of parameters against the simultaneous 95% confidence intervals.

4.2.2 Model calibration restricted to OD and N

To check our ability to reliably and accurately infer the parameters of an unknown model, we generated synthetic data with the ODE model, a set of parameters with biologically plausible values, and the full noise model identified in 4.1.1: with both measurement noise and dilution error. We also generated data only stained with measurement noise, and no dilution error, since this reflects the construction of the cost function (see 4.1.1).

The data was generated in order to simulate a real experiment: an exponential scale of antibiotics spanning from 0.5 mg/L to 512 mg/L was used as initial doses, with a starting cell inoculum of $5 \cdot 10^{-4}$ OD.

A possible improvement would be to generate data with two different initial densities, in order to feed the fit with data related to inoculum effect, instead of leaving it to be predicted by the model.

Plate reader OD measurements were simulated to be taken every 5 minutes, at the same frequency as actual measurements, and cell counts were simulated to be performed every 2 hours, the maximal frequency that a human experimenter can perform this tedious manual task over 24 hours.

The following table presents the initial values of parameters, and the best fits obtained, on data (OD and N) generated without and with dilution noise.

Parameter	Reference value	Meas. noise only	Dil. + Meas. noise
γ (1/h)	1.65	1.65	1.65
β (1/h)	5	5.03	5.37
μ (1/h)	0.8	0.800	0.800
K_s (g/L)	10^{-4}	$1.07 \cdot 10^{-4}$	$1.06 \cdot 10^{-4}$
λ (L/g)	$8.5 \cdot 10^{7}$	$8.54 \cdot 10^{7}$	$8.41 \cdot 10^{7}$
k_1 (mg/L)	1.2	1.19	1.05
h_1 (1)	8	8.02	7.24
k_2 (mg/L)	42	41.42	40.7
B_{in} (mg/L)	10^{-10}	$9.91 \cdot 10^{-10}$	$1.47 \cdot 10^{-10}$
k_b (L/mg/h)	300	300	209
d_a (1/h)	0.05	0.0511	0.0560
d_b (1/h)	0.1	0.100	0.107
d_c (1/h)	15	15.15	12.5
p_c (1)	0.2	0.201	0.202
L_{min} (1)	5	5.10	5.07
L_{max} (1)	120	120	117
η (1)	10^{-8}	$9.96 \cdot 10^{-9}$	$1.01 \cdot 10^{-8}$
—	—	—	—
cost (meas.)	1794.2	1785.2	
cost (dil.+meas.)	47468		6281.9

The best fit of noisy data remains in the vicinity of the parameter set used to generate the data. This test does not show anything about unidentifiability, because a fit almost as good or exactly as good could possibly have been generated with vastly different parameters. However, it shows that at least for these particular parameter values, dilution noise present in the data (as in the last column) and fitted with a cost function that ignores this error (see 4.1.1) does not in principle prevent the recovery of the cell parameters.

Profile likelihood analysis was performed on these two datasets and results are presented in the next pages. The dataset with measurement noise only is the easiest to interpret (figure 4.4).

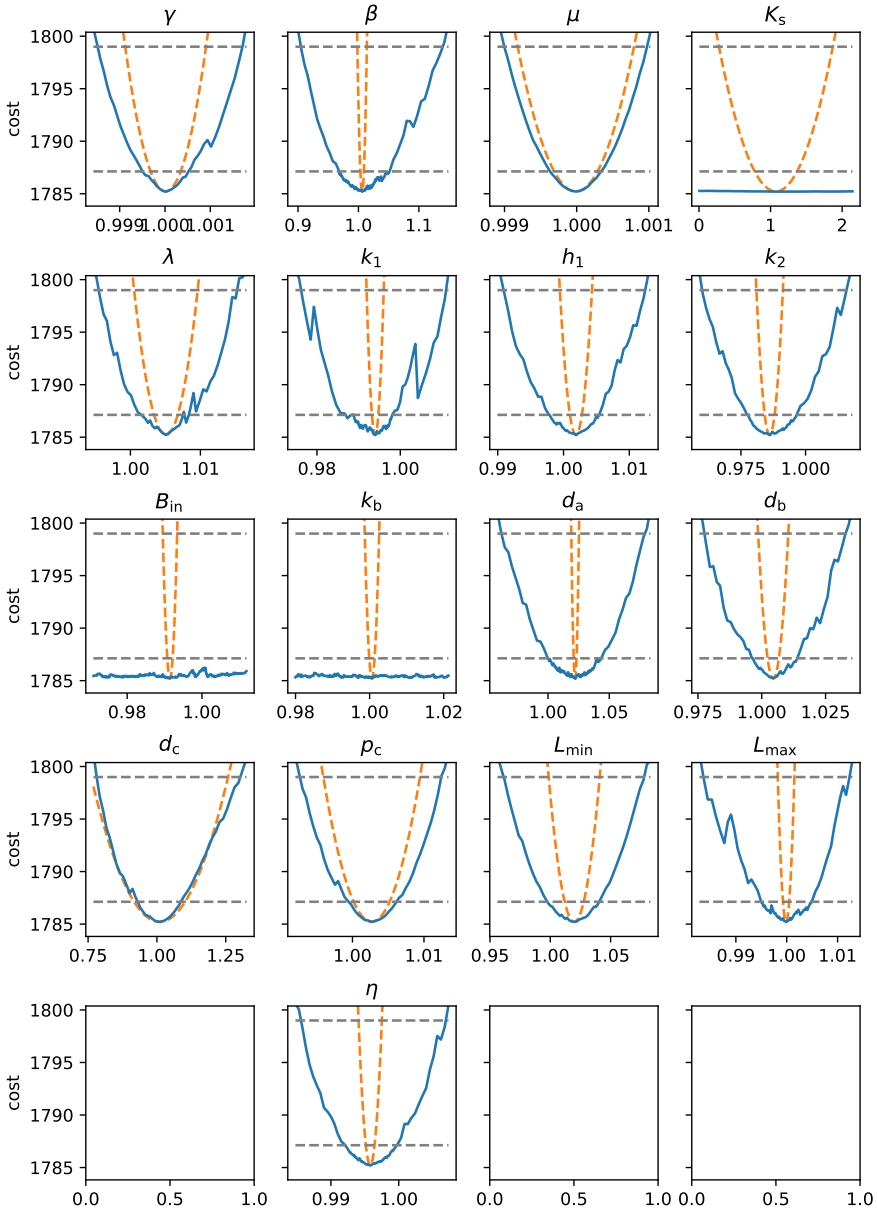

Figure 4.4: Identifiability analysis on synthetic data (OD and N) with measurement noise and no dilution noise. The orange dashed line is the parabolic approximation from the diagonal of the curvature matrix at minimum. The blue solid line is the profile likelihood. The two dashed gray horizontal lines are the two thresholds for identifiability: pointwise (lower) and simultaneous (higher) at $\alpha = 0.95$ confidence level. Parameter values are normalized with respect to the reference value.

Here, we can see that the two measures of identifiability (quadratic approximation and profile likelihood) give similar tight confidence intervals for γ, μ, λ, d_c, p_c, L_{min}. For β, k_1, h_1, k_2, d_a,

d_b, L_{max} and η the quadratic approximation slightly underestimates the range of the confidence interval, which might be either caused by an error of estimation of the curvature matrix, or by interplay with other parameters. Finally, K_s, B_{in}, k_b are fully unidentifiable, despite tight confidence intervals estimated by the parabolic approximation for B_{in} and k_b. These two parameters sharing an unidentifiability (their product is constrained), it is understandable that both of their individual variances are limited, the other being fixed. This is what is represented by the parabolic approximation. In the case of K_s however, the asymptotic approximation gives a huge confidence interval, which is only limited by the fact that it reaches 0.

Although the parabolic approximation underestimates the confidence intervals, its off-diagonal elements give information that the profile likelihood does not, related to the correlations between parameters. Indeed, correlations can be computed from the curvature matrix, giving insight into the structure of the model and the pairs of unidentifiable parameters.

On this synthetic data, the two highest correlation coefficients in absolute values are:

- $\rho_{B_{in},k_b} = -1$, which reflects the structural unidentifiability between the parameters B_{in} and k_b. The sign of the correlation indicates that an identifiable parameter can be formed with their product (if the correlation was positive, it is their quotient that would be involved).
- $\rho_{\eta,\lambda} = -0.97$ close to -1, this correlation indicates a practical unidentifiability. It says that the product of η and λ is approximately conserved in good fits neighbouring the optimal. This comes from the fact that to increase the OD of the culture, one can either decrease the conversion factor from nutrients to cells λ (to create more biomass from the same quantity of nutrients), or increase the proportionality constant between biomass and OD. These factors are difficult to disentangle in these experimental conditions, however, the two parameters remain identifiable as attested by their profile likelihood.

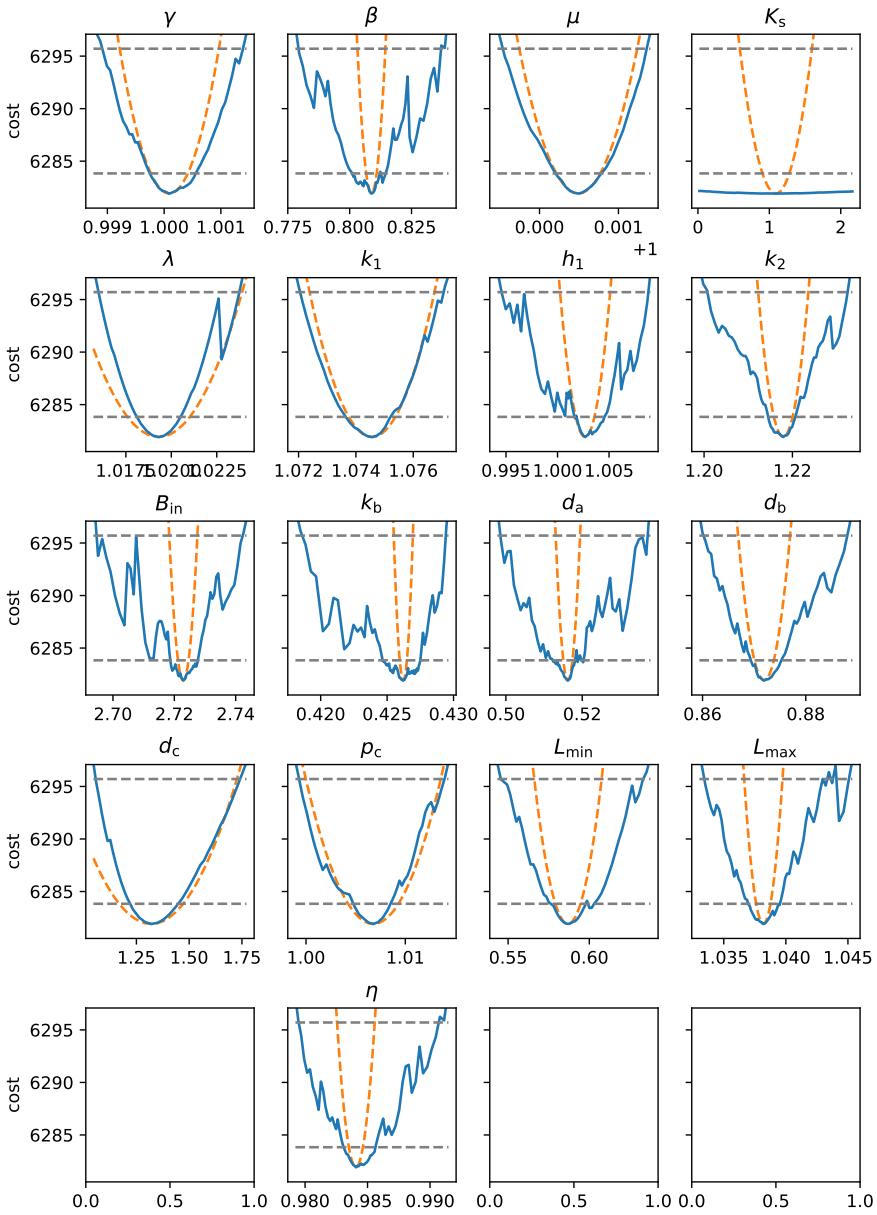

Figure 4.5: Identifiability analysis on synthetic data with measurement and dilution noise.

To test the influence of the dilution noise on the identifiability of the parameters, we also ran the profile likelihood analysis on the data generated with dilution noise (figure 4.6).

The results are a bit more difficult to interpret, probably because the optimization problem solved to compute the profile likelihood at each point is more difficult. However, parameters identified as identifiable remain identifiable. There seems to be a tendency for parameters to appear more identifiable than they really are in this setting, because of shortcomings in the

optimization procedure that gets stuck more easily in local minima. This is particularly noticeable for the parameter k_1 whose 95% confidence interval is ten times smaller with dilution noise than without. Likewise, the unidentifiable parameters B_{in} and k_b, nonetheless display a semblant of identifiability. It is unclear if this really comes from the inability of the search function to follow the global minimum, or from some more fundamental reason.

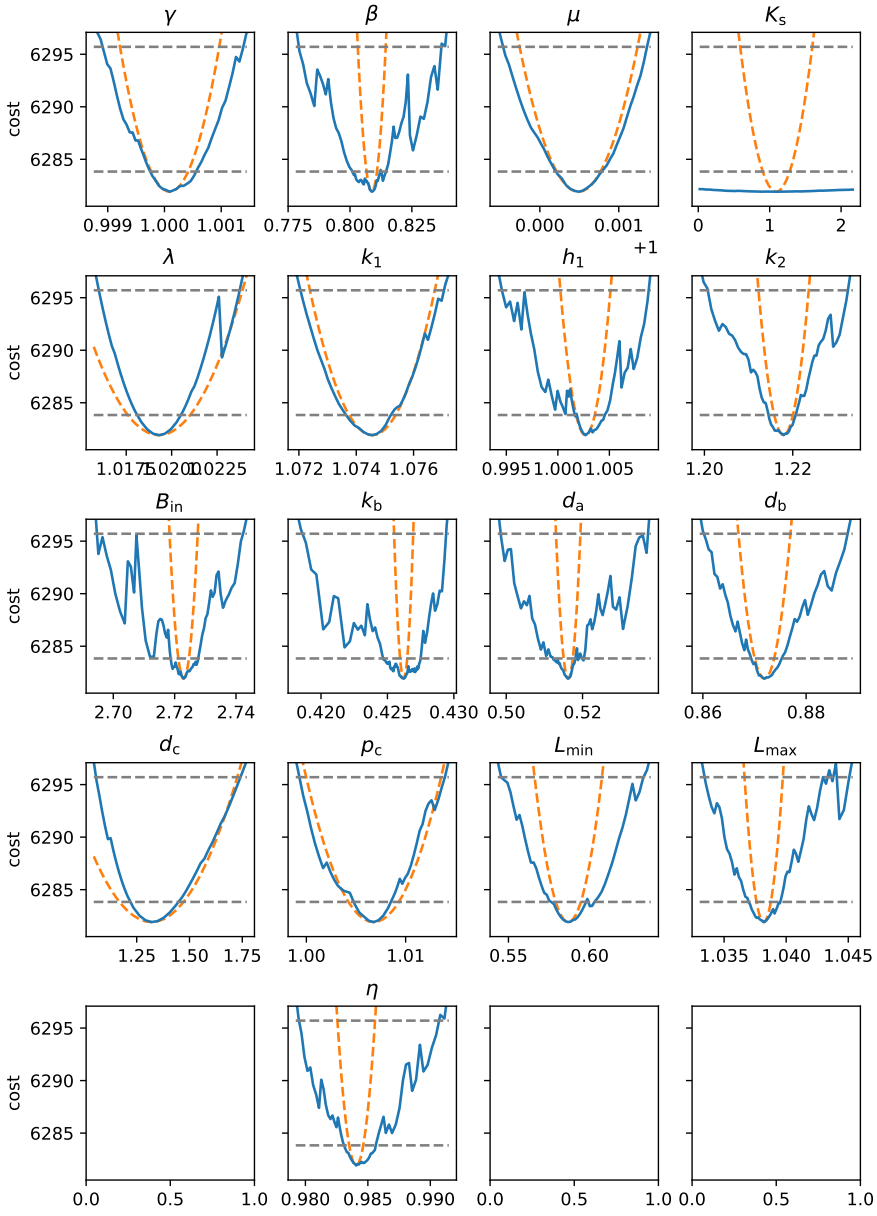

Figure 4.6: Identifiability analysis on synthetic data with measurement and dilution noise.

Values of K_s are very difficult to measure in batch, and are usually determined in continuous cultures.

We already knew from section 4.2 that in the absence of any measurement of b, B_{in} and k_b form a structurally unidentifiable pair. The parameter K_s is not surprising, since it only affects the slow down of growth when the nutrient concentration is similar to K_s, which happens very shortly during the last cell generation and then has in general very little effect on the output of the model[1]. The parameters k_b and d_a acting both on antibiotic degradation, k_b by active degradation caused by β-lactamase, and d_a by natural degradation, it is possible that both form a practically unidentifiable pair.

4.2.3 Model calibration restricted to OD only

As explained earlier (general introduction, and introduction of this chapter), the ambition of the approach is to be deployable in a context that does not allow more measurements than optical density growth curves. As we saw in the last section, calibrating a model of this complexity on only OD and N data is a challenging problem, so calibrating it on OD only is probably even more difficult. To assess this, we performed the same tests as in the last section, on the same synthetic experiments, but without including the data on cell number in the cost function. First, we searched for the globally best fits.

Parameter	Reference value	Meas. noise only	Dil. + Meas. noise
γ (1/h)	1.65	1.65	1.64
β (1/h)	5	5.37	4.41
μ (1/h)	0.8	0.800	0.800
K_s (g/L)	10^{-4}	$1.06 \cdot 10^{-4}$	$1.43 \cdot 10^{-4}$
λ (L/g)	$8.5 \cdot 10^{7}$	$8.41 \cdot 10^{7}$	$6.66 \cdot 10^{7}$
k_1 (mg/L)	1.2	1.05	1.18
h_1 (1)	8	7.25	9.98
k_2 (mg/L)	42	40.7	45.1

1 Seeing the almost nonexistent influence of K_s in the model of growth, one could wonder whether it was judicious to choose Monod's growth model instead of a logistic growth model, since the logistic growth model only requires one parameter, the growth rate μ, and no K_s. It does seem necessary, because the advantage of Monod's model is not only to better model the slow down of the growth when the nutrients get depleted, it also allows to track the level of nutrients, whereas the logistic model only slows down the growth based on the number of cells. In presence of antibiotics and important death, the difference between these two approaches matters.

Parameter	Reference value	Meas. noise only	Dil. + Meas. noise
B_{in} (mg/L)	10^{-10}	$1.47 \cdot 10^{-10}$	$5.03 \cdot 10^{-11}$
k_{b} (L/mg/h)	300	209	723
d_{a} (1/h)	0.05	0.0560	0.0632
d_{b} (1/h)	0.1	0.107	0.0664
d_{c} (1/h)	15	12.48	14.1
p_{c} (1)	0.2	0.202	0.201
L_{min} (1)	5	5.07	3.33
L_{max} (1)	120	117	119
η (1)	10^{-8}	$1.01 \cdot 10^{-8}$	$1.28 \cdot 10^{-8}$
—	—	—	—
cost (meas.)	1706.0	1702.2	
cost (dil.+meas.)	51179		2956.7

Then, we computed profile likelihood around these two optima (figure 4.7)..

Without data from cell number, it is understandably more difficult to infer parameters, and more unidentifiabilities will form. In fact, the correlation matrix showed the same two correlations as for the case fitted with OD and N ($\rho_{\eta,\lambda} = -1$, $\rho_{B_{\text{in}},k_{\text{b}}} = -0.56$), plus some others.

- $\rho_{d_{\text{c}},p_{\text{c}}} = -0.95$. Both parameters are related to dead biomass. This means that without the information of live cells provided by N, the model has more difficulty to recognize whether the OD is constituted of live cells or dead biomass.
- There is a cluster of five parameters linked by strong correlation coefficients ($|\rho| > 0.85$): d_{a}, d_{b}, k_1, k_2 and h_1. This is the marker of a cluster of unidentifiable parameters. The correlations are positive between d_{a} and d_{b}, and inside the trio k_1, k_2 and h_1. All the other relations are negative. Dimensionally, d_{a} and d_{b} share the same units, so do k_1 and k_2, and h_1 is dimensionless. From this dimensional argument, but also from the signs of the correlations, we can conclude that the invariant related to this unidentifiability is a function of the three quantities $d_{\text{a}}/d_{\text{b}}$, k_1/k_2 and h_1. Further study could reveal the shape of this function.

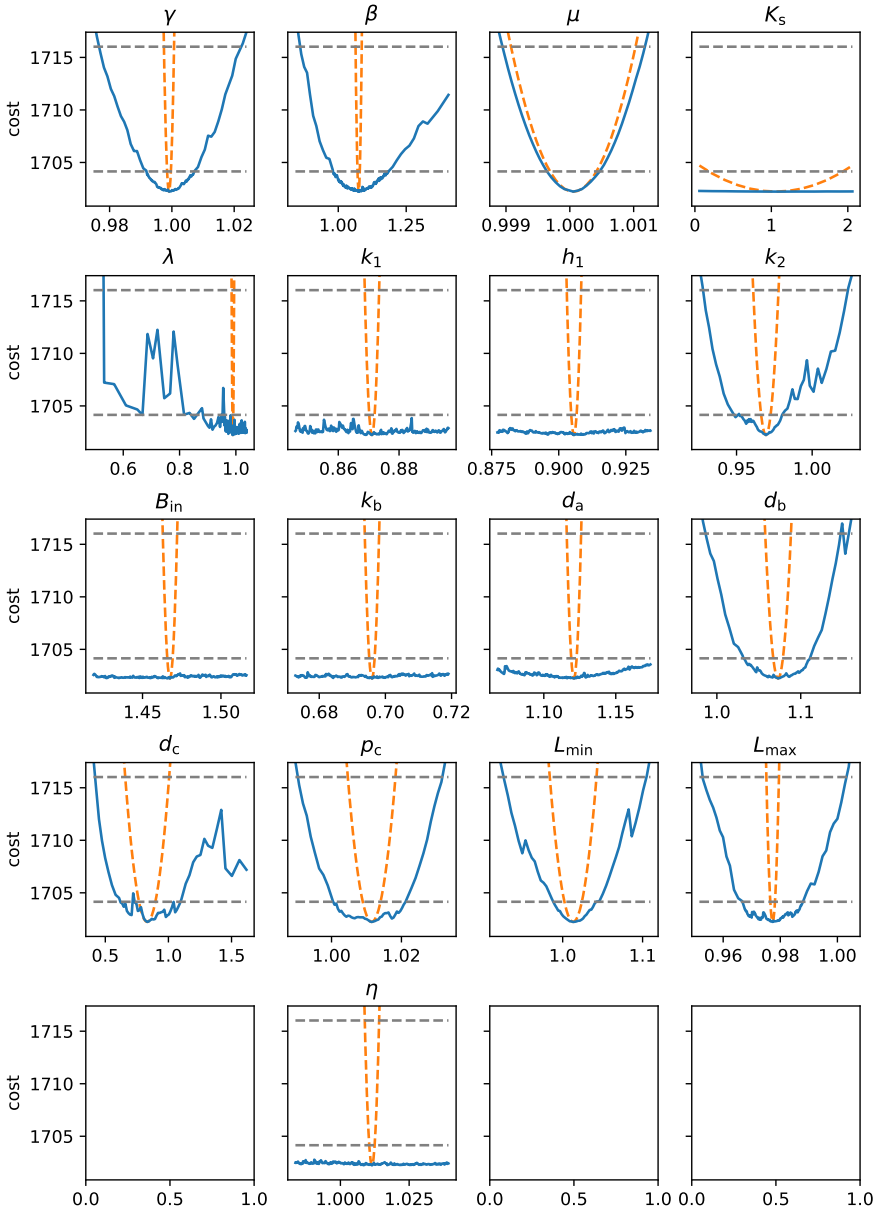

Figure 4.7: Identifiability analysis on synthetic data with measurement and no dilution noise, on optical density data only.

For completeness, we also run the profile likelihood analysis on the same dataset, with only OD and no cell number, but with dilution noise. The results are shown on figure 4.8.

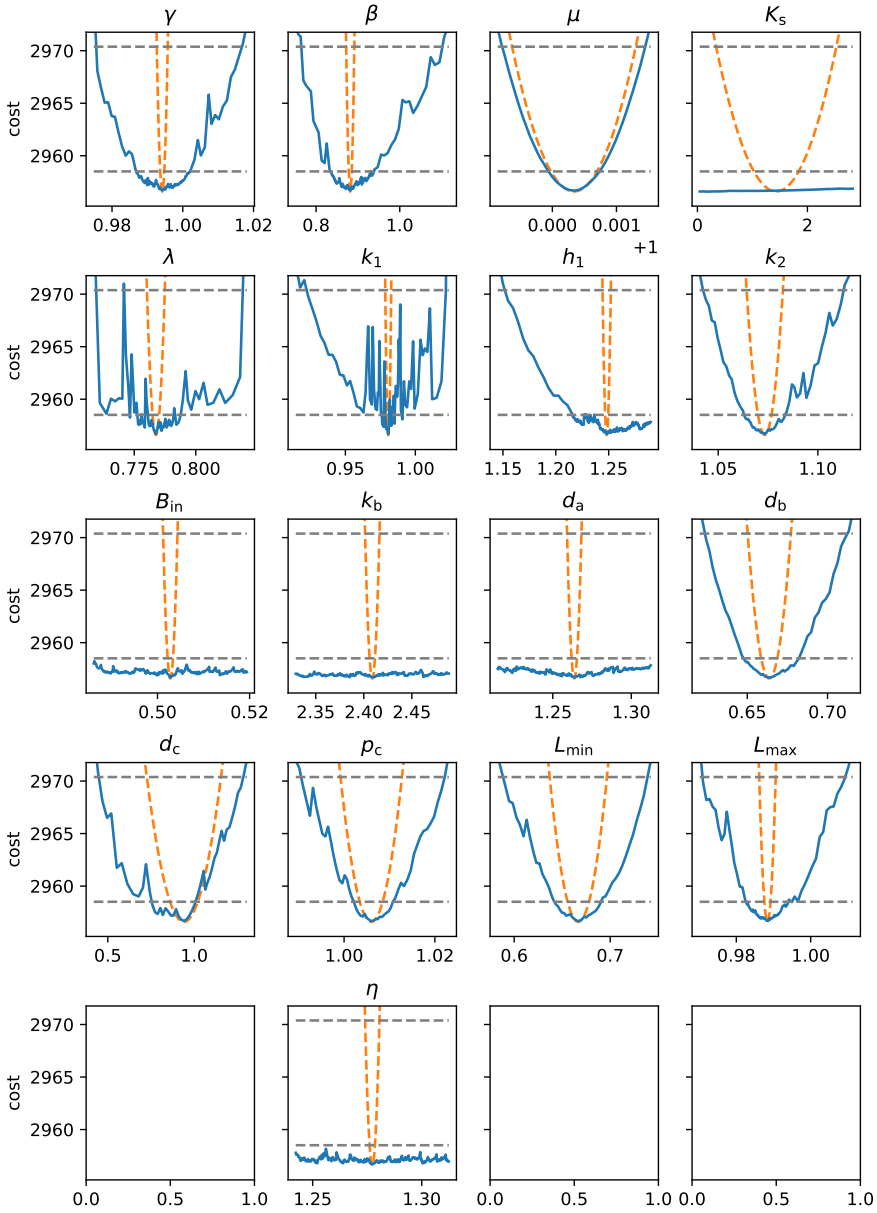

Figure 4.8: Identifiability analysis on synthetic data with measurement and dilution noise, on optical density data only.

Obviously, unidentifiable parameters do not become identifiable thanks to the noise, but identifiable parameters without dilution noise remain identifiable with it, which is a good sign for the parameter inference strategy.

4.2.4 The role of unidentifiabilities in the model

Seeing unidentifiabilities in the model, one could be tempted to reformulate it until it becomes completely identifiable. Except

for structural unidentifiabilities like B_{in} and k_b, the merits of this strategy are not obvious. Actually, a parameter identifiable on one dataset can be unidentifiable on another. The problem is one of model calibration with restricted information, on strains that often exhibit only subsets of the model, but different subsets depending on the strain.

For example, L_{min} cannot be estimated if we do not probe the system with antibiotic concentrations higher than k_2. We might not be able to do that if the strain is very resistant. Likewise, the efficiency of the β-lactamase cannot be determined precisely on very sensitive strains. It is possible to find strains and experimental conditions to make every parameter identifiable, but most isolates exploit only a subset of the model. It is then important to not reduce the model too much, to not lose its generality. We will actually find in section 5.3.2 that we can exploit the parameter unidentifiabilities as recognizable signatures of the isolates.

4.3 CHAPTER SUMMARY

This chapter enables to build the link between the data and the model, in fact, to find the set of parameters with which the model best reproduces a given experimental growth curve. This problem can be tackled with one or several techniques from an overwhelming diversity of optimization methods. However, some algorithms perform better than others depending on the problem.

In a first part, we describe the parameter inference infrastructure, that we engineered in order to satisfy variable goals: robustness for the global parameter inference problems, and efficiency for the local ones. In a second part, we use these methods to tackle the problem of model identifiability. Because the data is poor and noisy, some parameters cannot be fit accurately, and we determine which ones, on synthetic data as close as possible from the real data. We show that most parameters are identifiable notwithstanding the noise, and on data limited to OD only.

5 EXPERIMENTAL CALIBRATION OF CLINICAL ISOLATES

The number of different β-lactamases synthesised by bacteria is expressed in hundreds. Their kinetic parameters and affinity to various β-lactam antibiotics are the object of numerous studies (Felici et al. 1993; Nitanai et al. 2010; Page 2008). Among them, some of the most active on a diversity of β-lactams are classified as Extended Spectrum β-lactamases (ESBLs). ESBL-producing bacteria being resistant to several classes of β-lactams, infections involving ESBLs are particularly dreaded in the clinic. However, there is not a country in the world not plagued by a 5% to 30% prevalence of ESBL-producing strains in the wild and in medical centres (Paterson and Bonomo 2005). Some studies even report that up to 70% of the population of healthy adults of some countries are ESBL carriers (Savard and Perl 2012). This prevalence makes of ESBLs-producing bacteria one of the main actors of bacterial infections globally, and places them at the centre of medical attention.

Special dispositions can be taken in hospitals to avoid the spread of some classes of ESBLs-producing bacteria. To apply these measures as efficiently as possible, effective and sensitive detection protocols are required. One of the most widely used screening techniques is the disk diffusion method, or antibiogram. Paper disks soaked with antibiotics are deposited at the surface of a lawn of bacteria on a gel. A region of inhibition is formed around each paper disk, and its measured diameter can be compared to tabulated values (EUCAST 2020a) to determine the status (sensitive, intermediate, resistant) of this strain to the antibiotics tested. The commercial Etest relies on the same principle but allows a direct reading of the MIC of the strain on a paper strip. These methods require 18 to 24 hours of incubation. Other commercial tests such as Vitek or Phœnix can give an answer in 4 to 15 hours. The common characteristics of these tests is that they all take decisions based on the phenotypic behaviour of the strain at a single point in time.

Relying on a single point to characterize the behaviour of a strain can separate resistant from sensitive strains, but it does not allow to differentiate between different response mechan-

isms, in particular resistance, tolerance, persistence or resilience. Indeed, if a strain is shown to have grown after an antibiotic treatment, it could be because the population is resistant to the antibiotic (few cells died), or because it is tolerant and resilient (some cells died, but some survived, and the population recovered to untreated levels before the end of the incubation). In this example, although the resistant population did not respond to the treatment, the tolerant and resilient population showed a response that could be exploited in the design of a treatment. Such behaviours are often characteristic of strains neither sensitive nor resistant but qualified as intermediate.

In the context of the resistance crisis, intermediate strains are increasingly considered as cases where a high concentration antibiotic treatment could be attempted. Distinguishing resistant from intermediate strains, and accurately characterizing intermediate strains, is then a current problem.

Besides phenotypic approaches detecting either bacterial growth or the presence of a beta-lactamase, the second realm of ESBL detection is genotypic. The complete sequencing of a strain allows to detect all known genes coding for a resistant trait in the genome of this strain. However, this approach could potentially miss unknown resistance genes, as well as report the presence in the genome of resistance genes that are not expressed in a particular isolate, or that are not as potent as expected, because of interactions with other mechanisms. It is a mostly qualitative, and not quantitative approach: the same gene in two different strains could lead to two different phenotypical responses.

Between the MIC, a quantitative measurement relying on a unique datapoint, and a full sequencing, difficult to relate to a quantitative response, we need another approach that can articulate the differences between the different types of response: resistance, resilience, tolerance and persistence, while considering all the scales of this response: molecular, cell and population-level. The ambition of our approach is that our model could help dissect the behaviour of cells at all of these levels, strengthening the intuitive understanding of what could happen for a given strain treated with different doses.

In this chapter, after an introduction on the biology of β-lactamases, we will present the nine strains of our collection, their antibiotic resistance properties, and the antibiotics that we chose to test them. In a second part, we will present all the original data that we collected and that helped us to develop the model as it is. In a third part, we will show the parameter sets

inferred on all the strains, discuss their compatibility with the genetic information that we have on the strains, and show that we can identify three main types of response, that correspond to sensitive, tolerant/resilient, and resistant strains.

Panorama of β-lactamases

Since the early reports of the first β-lactamase by Abraham and Chain (1940), at least 5000 others have been observed (Naas et al. 2017). Expressed by various bacterial strains, they fall into two different but largely correlated classification schemes: the Ambler classification (Ambler, Baddiley, and Abraham 1980), describing four classes based on their molecular structure, and the Bush-Jacoby-Medeiros classification (Bush 1989; Bush, Jacoby, and Medeiros 1995; Bush and Jacoby 2010), identifying in its last version 3 groups and 16 subgroups distinguished by functional characteristics.

The review of Tooke et al. (2019) is useful to acquire a general vision of the Ambler classification. Without diving into unnecessary detail, β-lactamases can be structurally separated into two distinct groups: serines and metallo-β-lactamases. Serines correspond to the molecular classes A, C and D of the Ambler classification, and are chemical analogues of the PBPs, target enzymes of the β-lactams. They compete with PBPs for the binding of β-lactams, and hydrolyse antibiotics with an acyl-enzymatic reaction (Bush and Sykes 1986). Class A contains the better studied of these enzymes, and regroups families of enzymes among which CTX-M, TEM, SHV are some of the best known. They are in general held not by the chromosome of the bacteria, but by a plasmid. In contrast, class C enzymes are chromosomic and contain CMY, FOX, AmpC among others. Class D enzymes are the most diverse and least understood of the β-lactamases. The most famous class D enzyme family is OXA, which regroups almost a thousand β-lactamases, some of them showing a particular activity against carbapenems.

In contrast, β-lactamases of class B are unrelated to PBPs, and bear the name of metallo-β-lactamases because of the zinc atoms that participate in their structure. Class B enzymes such as VIM, IMP or NDM are known to be effective against an exceptionally broad spectrum of β-lactams, including carbapenems, with kinetics that can also be modelled as acyl-enzymatic (Felici et al. 1993).

The second, orthogonal classification is functional: it groups families of β-lactamases together based on their relative activities against different β-lactams, and their resistance to β-lactamase inhibitors such as clavulanic acid, tazobactam or Etylenediaminetetraacetic acid (EDTA). It is mostly correlated with the molecular classification. Updated twice, the latest revision is described in details by the authors (Bush and Jacoby 2010).

The mode of action of β-lactamase on β-lactam is known to match one of an acyl-enzyme, where the β-lactamase is the enzyme and the antibiotic is the substrate. In a first reversible step, the enzyme binds to the antibiotic to form a Michaelis complex. This complex can commit to the hydrolysis reaction through a succession of two irreversible steps, releasing eventually the regenerated enzyme and the inactivated antibiotic molecule (the product of the reaction) (Bush and Sykes 1986).

The rate of this reaction follows Michaelis-Menten kinetics, which can be expressed as

$$v = -\frac{\mathrm{d}[A]}{\mathrm{d}t} = V_{\max}\frac{[A]}{K_\mathrm{M} + [A]} = k_{\mathrm{cat}}[B]_0\frac{[A]}{K_\mathrm{M} + [A]}$$

where $[A]$ is the molar concentration of antibiotic and $[B]_0$ is the molar concentration of enzyme, free or in a complex. The two constants k_{cat} and K_M are respectively the maximal number of hydrolysis events that a single molecule of β-lactamase can perform per unit of time, and the concentration of antibiotic that allows the enzyme to work at half of this speed.

For antibiotic concentrations exceeding K_M, the dynamics becomes of order 0 in the antibiotic, which is to say that it decreases linearly, and we have

$$\frac{\mathrm{d}[A]}{\mathrm{d}t} = -k_{\mathrm{cat}}[B]_0$$

For antibiotic concentrations negligible in front of K_M, the dynamics appears of order 1 in the antibiotic, or of order 2 if we include the enzyme, and we have

$$\frac{\mathrm{d}[A]}{\mathrm{d}t} = -\frac{k_{\mathrm{cat}}}{K_\mathrm{M}}[B]_0[A]$$

where the constant $k_{\mathrm{cat}}/K_\mathrm{M}$, the apparent 2nd-order constant, is often reported as well as k_{cat} and K_M in biochemical studies.

These constants are of course unique to every pair of β-lactamase and β-lactam. They are biochemical constants that reflect the behaviour of a simple chemical reaction. To make this

information clinically relevant, one also needs to consider not only the biology of the organism that expresses the β-lactamase, but also its population response.

5.1 BIOLOGICAL MATERIAL

5.1.1 Strains

With the help of Philippe Glaser, we could access a part of the collection of isolates of the French National Reference Centre for antibiotic resistance. We chose several strains expressing a panel of different families of β-lactamases, including carbapenemases, and some expressing several of them simultaneously. As shown in section 5.3, the chosen strains range from fully sensitive to highly resistant. All are *Escherichia coli* ST410. From all the strains used to develop and calibrate the model, five strains are human isolates from the reference centre, four are isolates of animal origin from the ANSES collection, and one is a reference strain supplied by the Collection of Institut Pasteur. The nine isolates have been the object of previous studies (Patiño-Navarrete et al. 2020).

Table 5.1: Designation of the nine isolates.

ID	Other references
IB31 / #256	ANSES 28668
IB32 / IB36 / #259	ANSES 32139
IB34 / #257	ANSES 29401
IB35 / #258	ANSES 30599
IB37 / #281	CNR 49A5
IB38 / #152	CNR 94G8
IB39 / #273	CNR 82A2
IB310 / #130	CNR 84G4
IB311 / #144	CNR 92B5

Most strains contain gene mutations contributing to β-lactam response, such as mutations on ftsI (gene coding for PBP3, protein responsible for cell division), ompC, ompF (genes coding for porins, proteins restraining the diffusion of antibiotic through the cell membrane), displayed below (see appendix B for the

full description of the strains). Each mutation has been reported to decrease the susceptibility of the strain to β-lactams. YRIK is a mutation that appears on top of YRIN_349-532, and therefore is even more effective than YRIN_349-532.

Table 5.2: Mutations contributing to β-lactam susceptibility, detected in the strains.

ID	ftsI	ompC	ompF
IB31	none	none	none
IB32	none	none	none
IB34	none	none	none
IB35	none	none	none
IB37	YRIK	none	none
IB38	YRIK	none	none
IB39	YRIN_349-532	R195L	-46; C->T (OmpR F3)
IB310	YRIN_349-532	R195L	-46; C->T (OmpR F3)
IB311	YRIN_349-532	R195L	-46; C->T (OmpR F3)

They also contain genes coding for several β-lactamases, which are reproduced in the table below.

Table 5.3: β-lactamases, including carbapenemases*, expressed by the strains.

β-lactamase	IB31	IB32	IB34	IB35	IB37	IB38	IB39	IB310	IB311
CTX-M-1	x								
CTX-M-15		x			x	x			
CTX-M-55							x	x	
TEM-1	x	x	x	x	x			x	x
NDM-5*					x				
CMY-2							x	x	x
CMY-42					x	x			
OXA-1*		x			x		x	x	
OXA-181*						x	x	x	x

5.1.2 Antibiotics

The antibiotics chosen to challenge these strains are ampicillin and cefotaxime, two widely used β-lactams, both figuring among the WHO Essential Medicines List (WHO 2019b), and the Critically Important Antimicrobials for Human Medicine (WHO 2019a). They are recommended as first or second-line drugs.

Both are relatively inexpensive, and available as generic medication. Their wide range of action allows their use in a variety of situations: respiratory or urinary tract infections, meningitis, joint infections or pneumonia, among others.

Because some selected strains are carbapenem-resistant, it would be interesting, but more expensive, to also include a carbapenem in this drug arsenal.

Within β-lactams, ampicillin and cefotaxime belong to two different families: extended-spectrum penicillins for ampicillin, and 3rd generation cephalosporins for cefotaxime. We hoped to cover a number of situations as representative as possible in limited time, with only two β-lactams. Ampicillin turned out to have little effect on the strains other than the most sensitive ones. Consequently, a majority of experiments was carried out with cefotaxime.

5.1.3 β-lactamases

The strains of the collection express several β-lactamases, acting on the antibiotics with different efficiencies. All these β-lactamases are well known and have been extensively studied.

Classification

Using the β-lactamase database (Naas et al. 2017), we could determine that the β-lactamases expressed by the strains in our possession belong to three different groups in both classification schemes, molecular and functional.

Table 5.4: Classification of the β-lactamases, including carbapenemases*, expressed by the strains.

β-lactamase	Molecular class	Functional group
CTX-M-1	A	2be
CTX-M-15	A	2be
CTX-M-55	A	2be
TEM-1	A	2b
NDM-5*	B1	3a

β-lactamase	Molecular class	Functional group
CMY-2	C	1 & 1e
CMY-42	C	1 & 1e
OXA-1*	D	2d
OXA-181*	D	2df

From this table, NDM-5 is a metallo-β-lactamase and the eight others are serines. The functional group 2be is characterized by a particular activity against oxymino-β-lactams, including cefotaxime. The functional group 2df targets particularly carbapenems. The group 3a is characterized by a broad activity spectrum, including on carbapenems (Bush and Jacoby 2010).

Reaction kinetics on ampicillin

Besides the qualitative summary given by the Bush-Jacoby classification, kinetic parameter values help to understand the differences between the enzymes in a more quantitative way. As explained in section 5, the hydrolysis action of β-lactamases on β-lactams can be quantified by two values: k_{cat} and K_M, respectively the maximal number of hydrolysis events that a single molecule of β-lactamase can effectuate per unit of time, and the concentration of antibiotic that allows the enzyme to function with half of its efficiency. Whereas K_M is usually given in molar units, we chose here to express it in massic units, to relate more easily to the concentrations measured in the wet lab. The molar mass of ampicillin used for these calculations is $m_{AMP} = 349.406\,\mathrm{g\,mol^{-1}}$.

Table 5.5: Kinetic constants of some of the β-lactamases expressed, with respect to ampicillin.

β-lactamase	k_{cat}	$m_{AMP}\,K_M$	k_{cat}/K_M	Reference
CTX-M-1	$94\,\mathrm{s^{-1}}$	$9\,\mathrm{mg/L}$	$3.5\,\mathrm{s^{-1}\,\mu M^{-1}}$	Pérez-Llarena et al. (2011)
CTX-M-15	$57\,\mathrm{s^{-1}}$	$5\,\mathrm{mg/L}$	$3.8\,\mathrm{s^{-1}\,\mu M^{-1}}$	Faheem et al. (2013)
CTX-M-55	$423\,\mathrm{s^{-1}}$	$40\,\mathrm{mg/L}$	$3.7\,\mathrm{s^{-1}\,\mu M^{-1}}$	Shen et al. (2017)

β-lactamase	k_{cat}	$m_{AMP}\,K_M$	k_{cat}/K_M	Reference
NDM-5	$103\,s^{-1}$	148 mg/L	$0.2\,s^{-1}\,\mu M^{-1}$	Liu et al. (2018)
OXA-1	$520\,s^{-1}$	7.3 mg/L	$25\,s^{-1}\,\mu M^{-1}$	Leonard et al. (2008)
OXA-181	$200\,s^{-1}$	45 mg/L	$1.5\,s^{-1}\,\mu M^{-1}$	Potron et al. (2013)

Reaction kinetics on cefotaxime

The following table displays the kinetic parameters of the β-lactamases in our collection against cefotaxime. The molar mass of cefotaxime used for these calculations is $m_{CTX} = 455.465\,g\,mol^{-1}$.

Table 5.6: Kinetic constants of the β-lactamases expressed, with respect to cefotaxime.

β-lactamase	k_{cat}	$m_{CTX}\,K_M$	k_{cat}/K_M	Reference
CTX-M-1	$1141\,s^{-1}$	59 mg/L	$8.8\,s^{-1}\,\mu M^{-1}$	Pérez-Llarena et al. (2011)
CTX-M-15	$222\,s^{-1}$	27 mg/L	$3.7\,s^{-1}\,\mu M^{-1}$	Faheem et al. (2013)
CTX-M-55	$126\,s^{-1}$	8 mg/L	$7.6\,s^{-1}\,\mu M^{-1}$	Shen et al. (2017)
TEM-1	$2.1\,s^{-1}$	683 mg/L	$0.0014\,s^{-1}\,\mu M^{-1}$	Palzkill (2018)
NDM-5	$19\,s^{-1}$	9 mg/L	$0.95\,s^{-1}\,\mu M^{-1}$	Liu et al. (2018)
CMY-2	$0.01\,s^{-1}$	0.0023 mg/L	$2\,s^{-1}\,\mu M^{-1}$	Hentschke et al. (2011)
CMY-42	$0.2\,s^{-1}$	0.036 mg/L	$2.9\,s^{-1}\,\mu M^{-1}$	Hentschke et al. (2011)
OXA-1	$5.3\,s^{-1}$	16 mg/L	$0.15\,s^{-1}\,\mu M^{-1}$	Leonard et al. (2008)
OXA-181	$4\,s^{-1}$	34 mg/L	$0.055\,s^{-1}\,\mu M^{-1}$	Potron et al. (2013)

Seeing that some of the values of antibiotic used in experiments (0.5 g/L to 512 g/L) cannot be neglected in front of K_M, one could wonder whether the choice to take the order 2 dynamic was a judicious one. For reminder, we chose to model the dynamics of the antibiotic as

$$\frac{da}{dt} = -k_b\, a\, b - d_a\, a$$

but as explained in section 5, this is an approximation that only holds well for $a \ll K_M$.

However, most strains express more than one β-lactamase, while the model only has one variable b. The modelled dynamics is then already an approximation of the real one, which does not really have any reason to look more like Michaelis-Menten than mass-action law. By parsimony, we preferred the model with fewer parameters.

5.2 DATA USED TO DEVELOP AND CHALLENGE THE MODEL

As much as the model is used to predict the data, the data tells a story that develops the model. In our case, the model was in the making for several years and as data was being produced, some modelling choices imposed themselves. Starting from our early work (Hannah R. Meredith et al. 2018), we knew that the response of the population was mediated by at least two different processes: resistance and resilience. Resistance is the individual ability of cells to grow unperturbed by the antibiotic. Resilience is the collective ability of the population to recover from a perturbation. We also knew that a simple model considering only the number of cells was failing to explain the initial pre-crash phase, because of antibiotic-induced filamentation. This phase is less trivial than it seems and is starting to be understood as a driver of antibiotic tolerance (Yang, Blair, and Salama 2016; Zahir et al. 2020).

The purpose of this section is to exhibit the succession of new observations that led to the current model.

5.2.1 First scan of clinical isolates

A first scan of 9 clinical isolates with OD growth curves was done with two different initial cell densities and 11 initial antibiotic concentrations spaced by factors of 2, covering 3 decades of concentration.

This scan revealed differences between resistant and resilient strains exhibiting the familiar crash and recovery pattern, and sensitive strains showing a pattern that we did not see anywhere before. Figure 5.1 shows four representative strains: one sensitive, two resilient, one highly resistant.

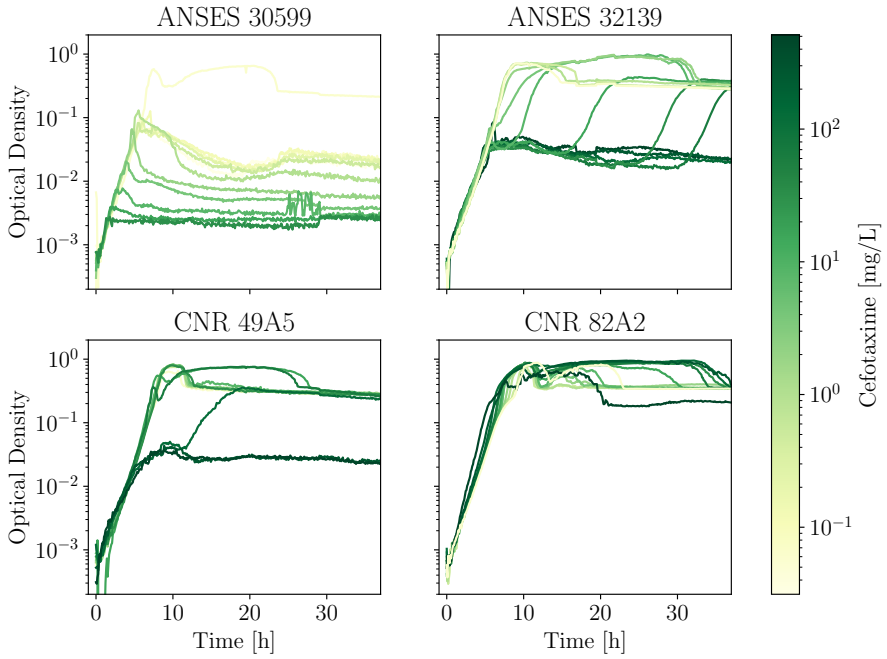

Figure 5.1: Representative growth curves from the first scan of the collection of clinical isolates. The cells were submitted to a scale of initial antibiotic concentrations ranging 3 orders of magnitude by factors of 2, with two different initial cell densities (only $OD_0 = 5 \cdot 10^{-4}$ is shown here).

5.2.2 Wider scan of sensitive isolates

To investigate whether these two behaviours could be understood together, increasingly smaller doses of antibiotics were applied to sensitive strains.

As shown on figure 5.2, three regimes appear distinctively on these curves. The first regime is the one where the cells are unperturbed by the low antibiotic concentration (yellow).

Cells finish with a high optical density (around 0.2). The second regime, intermediary, is pictured by curves in light green and leaves the final optical density at 0.02 on the top, 0.002 on the bottom. The last regime is the one of high antibiotic concentration (dark green) and the cells finish with the lowest optical density.

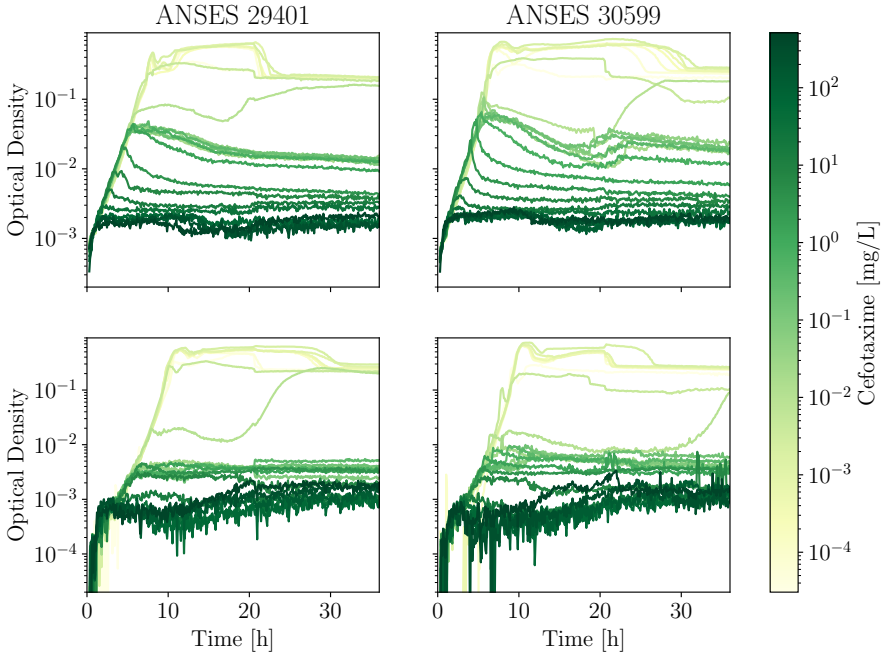

Figure 5.2: Two sensitive strains submitted to a scale of initial antibiotic concentrations ranging 6.5 orders of magnitude by factors of 2, with two different initial cell densities (top $OD_0 = 5 \cdot 10^{-4}$, bottom $OD_0 = 5 \cdot 10^{-5}$).

The transitions between the three regimes are interesting to observe. While the transition between the first two regimes is sharp (done within a factor 2 to 4 of antibiotic for the two strains of figure 5.2, from 0.008 mg/L to 0.031 mg/L), the transition between the last two is much more gradual (4 to 5 curves, which corresponds to a factor 16 to 32 in antibiotic, for figure 5.2 from 1 mg/L to 16 mg/L).

The three distinct regimes, including the unperturbed one, are a sign that two different processes triggered at different antibiotic doses. Knowing that β-lactams mode of action is to inhibit PBPs, we tried to identify the relevant PBPs based on the inhibition thresholds: from observation of the figure 5.2, the first transition occurs around 0.016 mg/L while the second one occurs around 4 mg/L. Kocaoglu and Carlson (2015) measured the IC50 (concentration of antibiotic inhibiting half of the target)

of inhibition of all PBPs in E. coli by various β-lactams, including cefotaxime (reproduced below).

The values observed on the graph point to PBP3 for the PBP responsible for the first transition, and PBP1 for the second transition.

Table 5.7: Half-maximal inhibitory concentrations for the main PBPs by cefotaxime.

PBP	PBP1a	PBP1b	PBP2	PBP3	PBP4
IC50 by CTX (mg/L)	0.9	0.2	3	0.01	3

The transitions between them also give hints on the nature of these processes. Indeed, the sharp transition between the first two regimes shows that PBP3, inhibited first, is either active or inhibited, whereas the gradual transition between the last two regimes shows that the PBPs targetted at these doses can function partially.

Furthermore, the first two regimes now look a bit like the pattern observed for resistant strains (see top right or bottom left panels of figure 5.1). Noting this similitude, we started to understand a global view that can be schematically explained with figure 5.3.

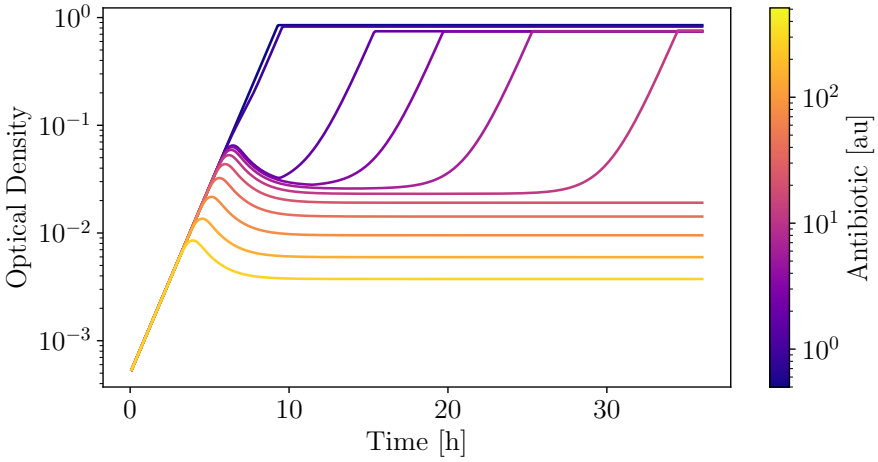

Figure 5.3: Schematic view of the general behaviour of a strain treated with increasing concentration of β-lactams.

Highly resistant strains such as CNR 82A2 observe, for all antibiotic doses, a behaviour similar to untreated cells (blue curve). Resilient strains (like ANSES 32139 or CNR 49A5) obey the pattern of the top half of the figure, and further increasing

the antibiotic concentration does not seem to generate the lower half. Finally, sensitive strains, in general do not recover: they are not resilient. Sensitive strains skip the pattern of resistant cells and only behave as in the lower half of the figure. Resilient as well as sensitive strains can be qualified tolerant, because they are able to survive a transient lethal dose of antibiotics.

Another interesting observation is the consistency of the *crash*, the point where the OD leaves the initial exponential growing phase, between all the isolates and antibiotics tested. Except for highly resistant strains where the crash is not observed, sensitive and moderately resistant strains alike show a crash that happens between 6 and 7 hours of the addition of antibiotic. This time did not depend neither upon the initial cell density. As explained in section 3.2.4, this could be interpreted either by a time delay or a critical length. However, literature points in the direction of a critical length, by showing that the time to lysis is inversely proportional to the growth rate, which we also observed when replaced the minimal medium M9 with a richer medium LB, as shown on figure 2.1: with approximately twice the growth rate, the crash happened in half the time. Another hypothesis, suggested by Yao, Kahne, and Kishony (2012), is related with the formation of a bulge. However, it is a bit more difficult to see what would be the underlying reason for the synchronization of the formation of the bulges.

All cells belonging to the *E. coli* ST410 cell type, it is reasonable to assume that this critical length is one that filaments cannot sustain any more, and that it depends on cell type. On *K. pneumoniae* and cefotaxime with a similar growth rate, the crash consistently happened at 3 hours rather than 6-7 (Hannah R. Meredith et al. 2018).

5.2.3 Microscope snapshots

To better confirm our understanding of the morphological changes occurring during the initial filamentation phase, we sampled wells containing a resistant strain (ANSES 32139) at different times following an antibiotic treatment, and observed the cells under an optical microscope. Some pictures are shown on figure 5.4.

We clearly observed filamentation, even at sub-MIC antibiotic concentrations. Higher drug concentrations led to longer cells, up to more than 100 times the size of the smallest cells observed. After an initial global increase of the size of cells, the regrowth of

the population was mediated by the reappearance of normally sized cells, in between long filaments (see the pictures taken at 8 hours, notably for 2 mg/L). A quantitative analysis of these pictures could be insightful to access the length distributions of cells, but would require a segmenting software able to deal with cells with highly atypical morphologies.

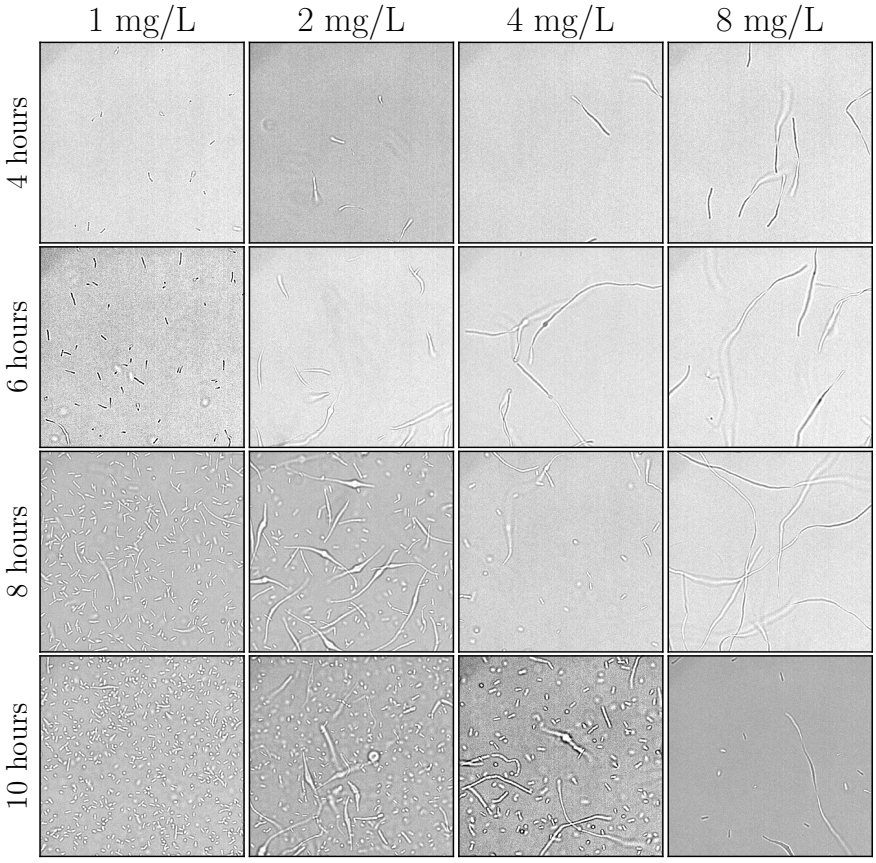

Figure 5.4: Microscope pictures (x600) of samples of batch cultures of ANSES 32139, taken using IBIDI slides at different times after treatment with cefotaxime. Image processing with help of Anđela Davidović.

This bimodal distribution challenged our intuitive idea of the notion of an average length increasing then decreasing, as shown by Fredborg et al. (2015), and led us to decide that the distribution of lengths in the population should be properly modelled in order to grasp an understanding of the processes at play.

We found in section 3.3.2 that the PDE model indeed generates a bimodal population at regrowth.

5.2.4 CFU experiments

Knowing that the OD and number of cells are decorrelated, measuring the optical density was not sufficient to understand the behaviour of the system, and we needed to find another quantitative observable. The length of cells can be observed semi-quantitatively with a microscope, but the number of cells is accessible through CFU counts, albeit less automatically than the OD. We then carried out experiments with regular sampling of cells, that we diluted by a proper factor before spreading on agar plates, and this every two hours for 16 to 22 hours. After 12 to 16 hour incubation, colonies growing on the agar plates could be counted, and we obtained like that simultaneous readings of optical density and number of cells for two isolates and six initial antibiotic concentrations. One of these isolates was presented on figure 3.2, the other is on figure 5.5.

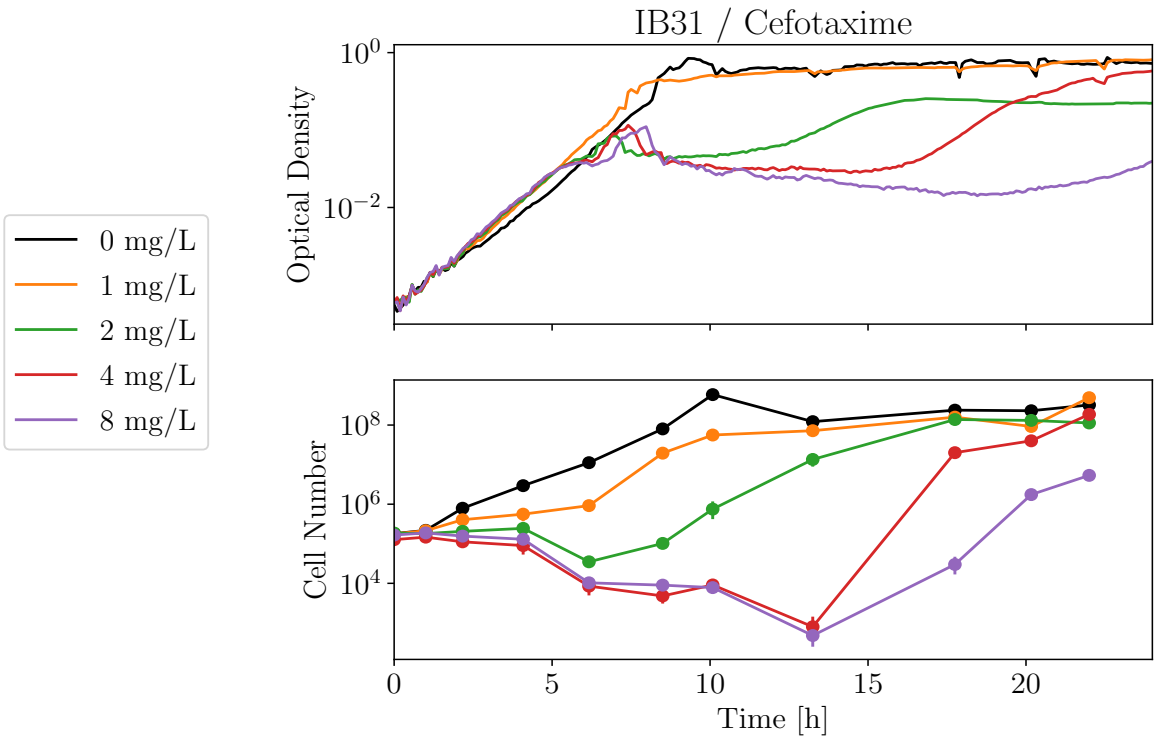

Figure 5.5: Simultaneous OD and number of cells measurements for IB31. The error bars are the 95% confidence intervals computed with the method presented in section 2.1.5.

It is clear on these figures that the initial increase of OD is not necessarily caused by an increase in the number of cells. Actually, for initial concentrations higher or equal than 2 mg/L

for this strain, the number of cells remains constant for the first five hours, and only starts to decrease later. This led us to the mechanism described in section 3.2 of an immediate inhibition of division (by inactivation of PBP3), followed by cell lysis when a certain length is reached (this critical length being affected by PBP1, that can also be inhibited with higher antibiotic doses).

Besides, the observation of cell number reveals other behaviours invisible on the OD curve. Firstly, judging by the OD, the cells are unperturbed by a concentration of antibiotics of 1 mg/L (yellow curve). The cell number curve shows that it is not the case. Secondly, as it is apparent for the green and purple curves (probably for the red also: the low red point could be an experimental mistake), the regrowth of the population can start several hours before it is picked up by the plate reader, this is because the regrowth is driven by a small number of cells concealed within a larger amount of dying biomass.

Understanding this, it seems interesting to split the treatment in two, and reserve the second half for the moment where the cells are few, because we know, with the inoculum effect, that this is when the antibiotic is the most efficient. This is why we then passed to multidosing experiments.

5.2.5 Multidosing

Multidosing experiments are important because the ability of the model to predict the response of the population after multiple injections of antibiotic is a requirement in order to exploit it to compute optimal treatment profiles. However, it is not obvious to think that a model developed through the observation and interpretation of growth curves following a unique initial treatment will be capable to handle the addition of antibiotics after time zero. Moreover, one can wonder whether growth curves of initial treatments with no drug reinjections are informative enough to enable parameters inferred only on them, to make accurate predictions on dynamics that they did not see during the calibration.

This is why we thought that multitreatment experiments were an ideal test of the model and parameter estimation strategy. We then configured the custom driver `platerider` (see section 2.2.2) to apply multiple treatments to the cells. To test the most of the model, while the plate reader measured OD, we also sampled regularly the plate to count cells.

For five total antibiotic amounts, three treatment strategies have been implemented:

- All the antibiotic was present in the culture at start;
- All the antibiotic was injected in the culture 4 hours after the beginning of the experiment;
- Half was present from the beginning, and the other half was injected at 4 hours.

All these situations have been represented on figure 5.6. The standard situation with only the initial dose is on the left column. Both OD and cell numbers follow the experimental points. The time shifts are within the range of experimental dilution mistakes of up to 5% in both inoculum and antibiotic concentration, as explained in section 4.1.1.

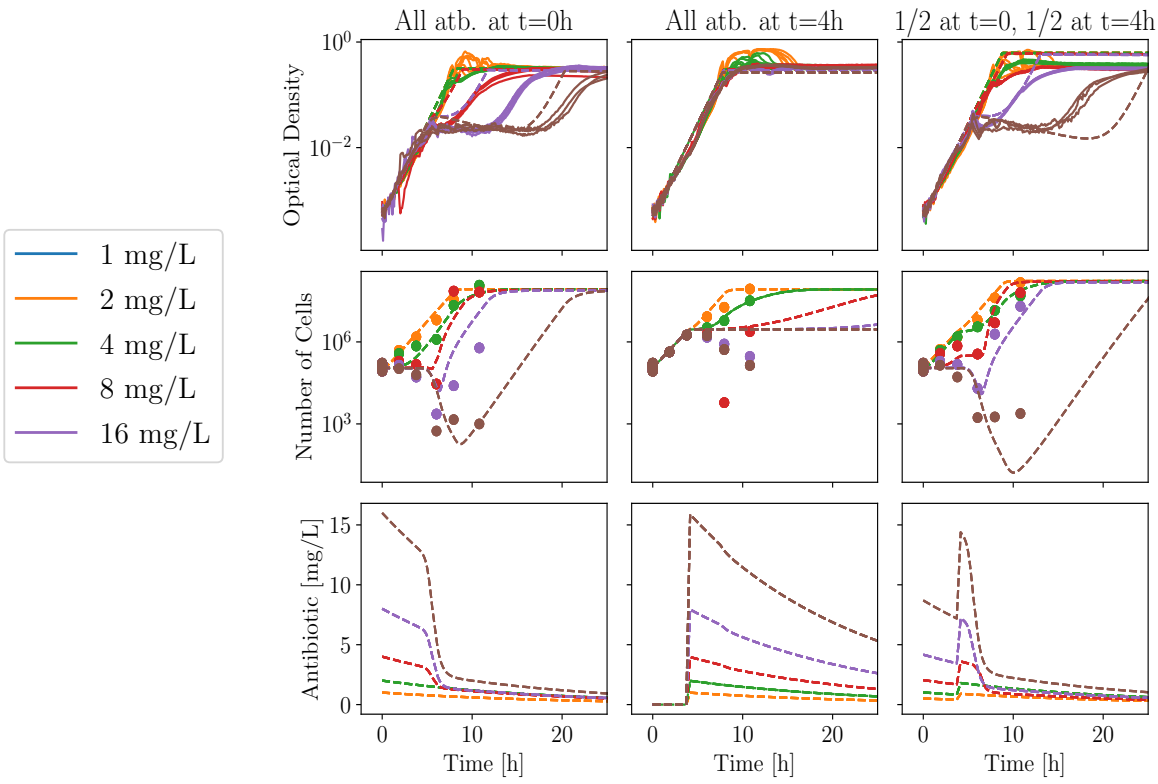

Figure 5.6: Different multidosing strategies, compared for OD and number of cells. Dashed lines are the model predictions.

The situation with a unique injection of antibiotic at 4 hours is in the middle column. During this initial delay, cells grew by 5 generations. Because of the inoculum effect, the injection of this dose, on an inoculum 32 times larger, affected the population less than the previous situation. The prediction of the OD is

not different from untreated cells, we can see that the number of cells is perturbed. For 8 mg/L and above, the experimental data suggests that the number of live cells is actually decreasing after 6 hours (the low green point is most certainly a fluke). The model predicts a stop of the growth of these cells at the same time. One can note that the model also predicts that the antibiotic is not flushed in these conditions.

The third situation, with two injections of antibiotics, corresponds to the column on the right. As shown by the predicted antibiotic course, the initial dose of antibiotics is sufficient to inhibit PBP3 and trigger filamentation, but the antibiotic is not degraded in the first four hours because no cell deaths happened yet. The second dose is injected shortly before the cells reach their critical length, and we then find ourselves in a situation similar to the left column, with as much antibiotic to degrade, which explains why the time to regrowth is similar in these two situations.

These experiments are preliminary, and there would be many other multidosing strategies to test. However, the success of these predictions was a good sign of the relevance of the model and encouraged us to try applying it to optimal treatment problems.

5.3 CHARACTERIZATION OF STRAINS

Numerical fits were performed on 9 of the 10 clinical isolates described in section 5.1.1. As shown in section 5.2.1, various behaviours have been observed, and there would be several ways to cluster the isolates. A first, classical classification is based on MIC as defined by EUCAST (2020a), and allows to sort the strains into Sensitive, Intermediate or Resistant. However, as explained in the introduction of this chapter, this phenotypical classification relies on one unique data point per strain, which reveals itself challenging to describe a complex panorama of resistance, tolerance and resilience. Our approach uses complete OD data over 36 hours, and extracts from this data 17 parameters per model. Not all parameters in these 17 are linked to antibiotics resistance (for example the growth rate μ or the conversion factor λ), but one could cluster the strains based on some of these parameters of interest. In this section, we will see if we can find notable phenotypical differences between the strains of

our collections, which would all be classified "R" by EUCAST, except IB34 and IB35 which would be labelled "S."

5.3.1 Clustering with parameter values

Figure 5.7 is a graphical representation of all the parameters fitted on all the strains, one by one. IB31N and IB32N are fits of IB31 and IB32, including also the number of cells, because we have them for these strains. All the others are fitted on only OD.

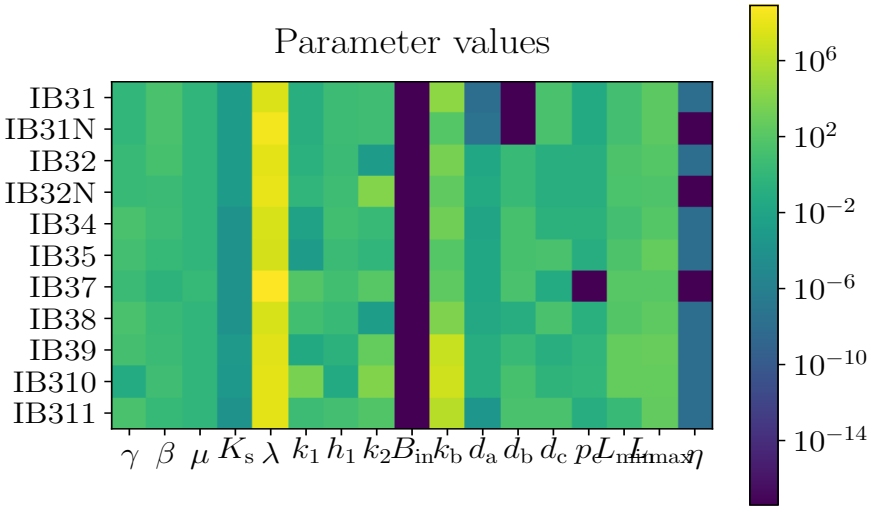

Figure 5.7: Values of the best fits found on the isolates.

It is difficult to identify related strains by eye. One difficulty comes from the presence of unidentifiable parameters: because no value is significantly better than the others, these parameters are assigned values influenced by all the noise and undeterminism in the system, essentially random values.

Nonetheless, a natural idea would be to cluster strains according to parameter values. Figure 5.8 shows the result of Principal Component Analysis (PCA) applied to the logarithms of the parameters.

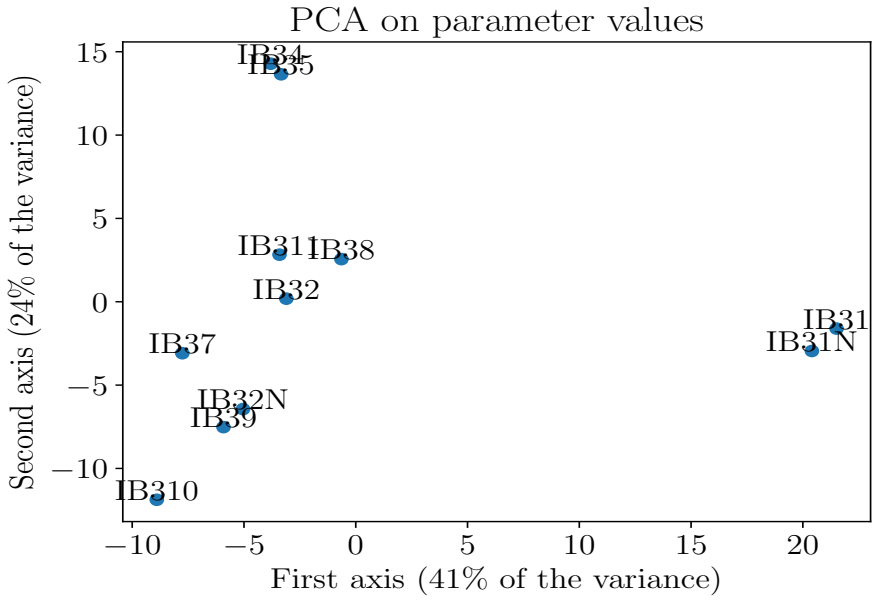

Figure 5.8: PCA on (the logarithms of) the parameter values.

This PCA splits the isolates into three groups: IB31 alone, a cluster of IB34 and IB35, and the rest of the strains. Although IB34 and IB35 are the two least resistant strains of the group (expressing only TEM-1, a weak β-lactamase, as shown in section 5.1.1), singling out IB31 is a bit more difficult to understand. Although it is the only one to express the β-lactamase CTX-M-1, its phenotypical profile is very resemblant to IB32.

It turns out that the parameter values of IB31 are very different from the rest of the values, because the fit of the model on this strain is the worst of all the strains. For some reason, either because the global optimum was not found by the search, or because the model does not describe accurately the behaviour of this strain, the fit is not as good as for the others, and the parameters are consequently significantly different, which explains why the PCA isolated it.

PCA being a linear dimensionality reduction technique, it is notably sensitive to outliers, like IB31. The parameters of IB31 are so different from the others that this strain "steals" the first axis of the PCA. This calls for the use of t-distributed Stochastic Neighbour Embedding (t-SNE), a non-linear dimensionality reduction technique, which can isolate outliers without compromising too much the rest of the elements. Figure 5.9 shows a result of t-SNE on the same dataset.

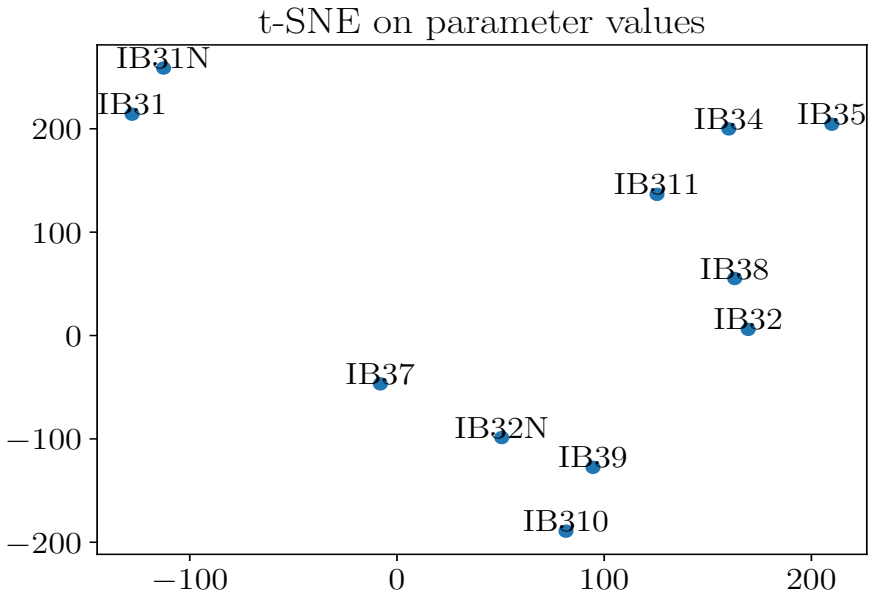

Figure 5.9: t-SNE on (the logarithms of) the parameter values.

IB31 is still isolated, and the rest is split into two groups. One contains notably IB34, IB35 and IB311, strains that show profiles similar to the sensitive isolates described in section 5.2.2. The other contains, among others, IB39 and IB310, the two most resistant strains of the collection. IB32 and IB32N appear separated, which seems difficult to explain.

Actually, it is probable that this clustering is heavily biased by the values of unidentifiable parameters, which can take a wide range of values, as we have seen in sections 4.2.2 and 4.2.3. Hence, relying only on the estimates on the parameter values to categorize clinical isolates is difficult.

5.3.2 Clustering with parameter uncertainties

We saw on the previous section that the uncertainties on the parameter estimates can work against an efficient dimensionality reduction of the space of parameter values. However, there is a correlation between the true parameter values and the unidentifiability of the parameters. Indeed, for a highly resistant strain, mostly unperturbed by antibiotic treatments, most parameters linked to PBPs are unidentifiable, because the dynamics following the inhibition of these enzymes are never observed.

Uncertainties in the parameter estimates could then work better than the parameter values themselves to categorize strains.

Figure 5.10 shows the values of the half-width of the 95% confidence intervals, estimated with the asymptotic approximation described in section 4.2.1.

True profile likelihood would have been more accurate, but much more expensive computationally.

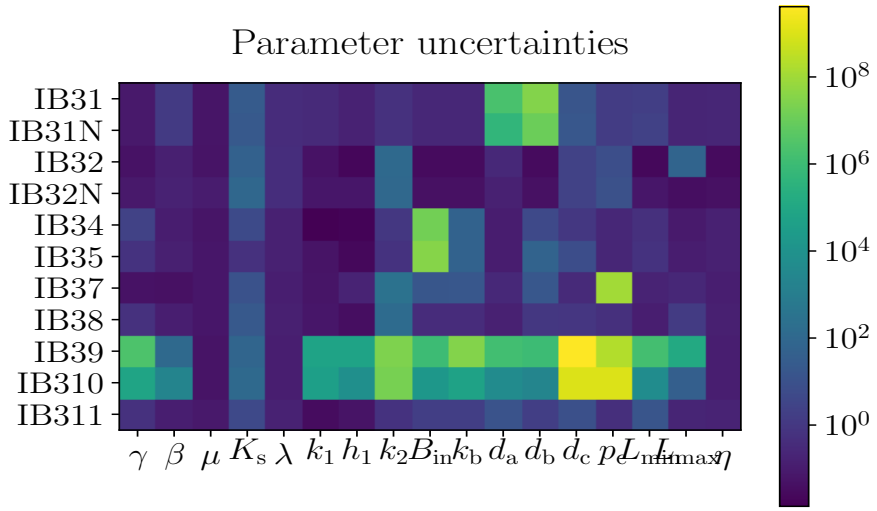

Figure 5.10: Half width of the 95% global confidence intervals on the best fits for each isolate, computed with the asymptotic method.

Similarly, a PCA can be computed on these uncertainties. The first two axes are presented on figure 5.11.

Another idea would be to compute these dimensionality reductions on the full covariance matrix of parameters at the optimum, not only on its diagonal like we do here.

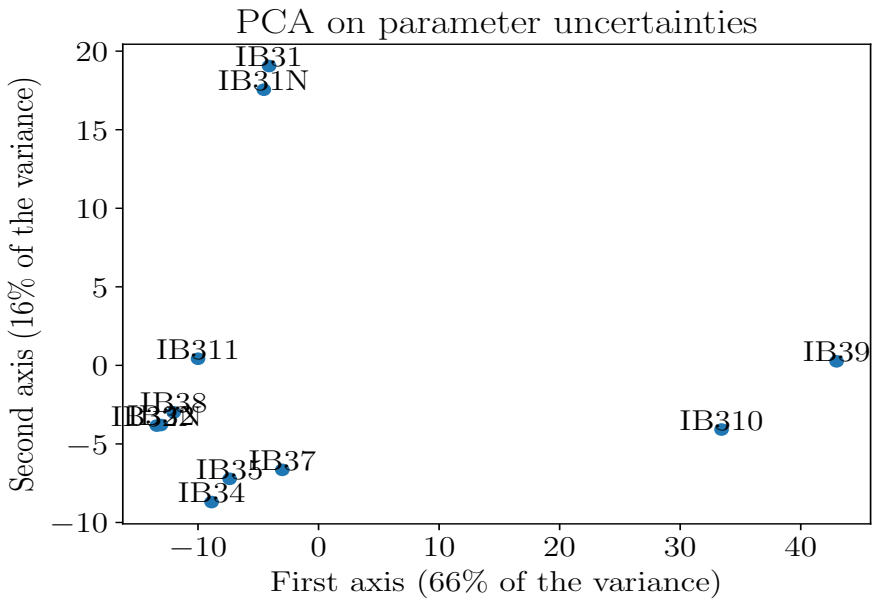

Figure 5.11: PCA on (the logarithms of) the parameter uncertainties.

Like for the parameter values (figure 5.8), the outlier IB31 is isolated. Another group is formed of IB39 and IB310, the two

most resistant strains in the group. The rest of the strains forms a compact third group.

To reduce the influence of the outlier IB31, we also performed a t-SNE analysis on the uncertainties, shown on figure 5.12.

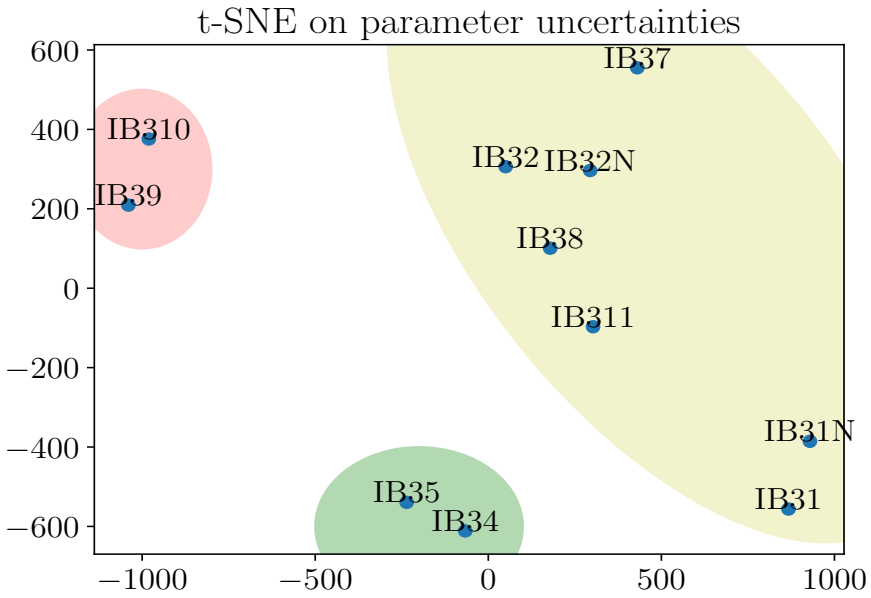

Figure 5.12: t-SNE on (the logarithms of) the parameter uncertainties.

Unlike all others approaches, three distinct and robust clusters emerge from this dimensionality reduction. A cluster is constituted of IB34 and IB35, the two most sensitive strains (green). Another is made of IB39 and IB310, the two most resistant strains (red). The last group contains the rest of the strains, of similar behaviour (yellow). Finally, both IB31 and IB31N, and IB32 and IB32N, are neighbours, which reassures both on the ability to fit the model on OD only, and on the relevance of the clustering approach which correctly manages to put them together.

5.3.3 Comparison of measured and inferred β-lactamase efficiency

Because we had access through the literature to the kinetic constants of all the β-lactamases expressed by the isolates in our collection (see section 5.1.3), we wanted to compare them to the values that our model inferred for these quantities.

Because most strains express several β-lactamases, but our model only assumes one, we chose to compare the value of

our model to the sum of the k_{cat}/K_M of all the β-lactamases expressed by a strain.

The corresponding model variable is k_b, but it forms a structurally unidentifiable pair with B_{in}, the concentration of β-lactamase inside one cell (see section 4.2). Their product represents the β-lactamase efficacy contributed by one bacterium. This is the variable that we chose to compare against the tabulated β-lactamase efficiency.

The correlation is actually between the literature value and the logarithm of the inferred parameter, which we don't know how to explain.

As shown on figure 5.13, we found a clear correlation between the literature and the parameter estimates from the model.

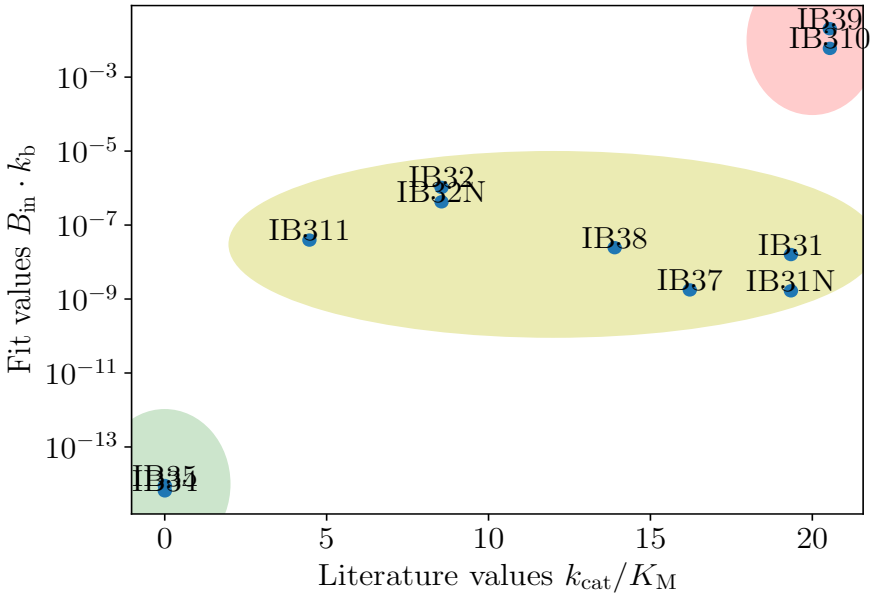

Figure 5.13: Comparison of the efficiency of β-lactamase per cell, from the model and from the literature. The Pearson correlation coefficient between k_{cat}/K_M and $\log(B_{in} \cdot k_b)$ is 0.72, and the associated p-value of correlation is 0.013.

The same three groups also emerge here: the sensitive strains IB34 and IB35, producing few and very weak β-lactamases, the highly resistant IB39 and IB310 characterized by the expression of CTX-M-55, a powerful β-lactamase on cefotaxime, and the rest of the strains with intermediate resistance. We can also note that for IB31 and IB32, fitting with or without the cell number data seems to make little difference.

Figures 5.12 and 5.13 suggest a separation into three groups: sensitive strains (IB34 and IB35), highly resistant (IB39 and IB310), and the rest. We will detail their respective parameters and behaviours in the next three sections.

5.3.4 Sensitive strains

The following table shows the best fit found for two strains that we can qualify as sensitive. In the following three tables, stars* indicate a parameter constrained by a bound of the search space.

Parameter	IB34	IB35
β	4.4	1.7
γ	20*	11
μ	0.81	0.90
K_s	10^{-4}	10^{-4}
λ	$2.1 \cdot 10^{7}$	$1.7 \cdot 10^{7}$
k_1	0.006	0.001
h_1	8.6	3.3
k_2	2.5	0.86
B_{in}	10^{-18}	10^{-16}
k_b	1634	102
d_a	0.0094	0.023
d_b	20*	16
d_c	0.35	20*
p_c	0.34	0.097
L_{min}	10	34
L_{max}	87	468
η	$1.5 \cdot 10^{-8}$	$2.0 \cdot 10^{-8}$

The common characteristic of these strains is that they both carry only the resistance enzyme TEM-1, a weak β-lactamase. As shown by figure 5.13, the product of the pair of unidentifiable parameters $B_{in} \cdot k_b$, which informs on the effectiveness of the β-lactamase produced by one cell, is correctly almost zero for these isolates.

For these two strains, k_1 and k_2 correspond to the order of magnitude of the respective inhibition of PBP3 (0.01 mg/L) and PBP1 (0.9 mg/L) by cefotaxime, as shown in table 5.7. This indicates that for these strains, these PBPs are likely inhibited at these antibiotic concentrations.

5.3.5 Tolerant and resilient strains

Because these strains do not exhibit the sensitive-like pattern of the bottom half of figure 5.3, the parameters k_2 and L_{min} are not observable.[1]

Parameter	IB31	IB32	IB37	IB38	IB311
β	20*	3.6	0.36	2.2	1.7
γ	1.0	2.8	3.2	20*	20*
μ	0.79	0.81	1.56	0.79	0.86
K_s	10^{-4}	10^{-4}	10^{-4}	10^{-4}	10^{-4}
λ	$3.0 \cdot 10^{8}$	$1.2 \cdot 10^{8}$	$7.1 \cdot 10^{7}$	$7.1 \cdot 10^{7}$	$7.1 \cdot 10^{7}$
k_1	0.16	0.83	77	8.5	4.2
h_1	4.6	5.6	9.4	3.0	10*
k_2	7.0	9893	125	0.002	54
B_{in}	$1.6 \cdot 10^{-11}$	$1.5 \cdot 10^{-9}$	$7.7 \cdot 10^{-12}$	$3.6 \cdot 10^{-12}$	10^{-14}
k_b	104	283	229	6788	$1.2 \cdot 10^{6}$
d_a	$3.5 \cdot 10^{-8}$	0.051	0.019	0.029	0.00026
d_b	$6.0 \cdot 10^{-9}$	2.2	20*	20*	20*
d_c	20*	0.12	0.06	20*	20*
p_c	0.05	0.13	10^{-9}	0.18	0.094
L_{min}	10	30	115	79	2.3
L_{max}	170	51	115	213	354
η	$2.0 \cdot 10^{-9}$	$5.3 \cdot 10^{-9}$	$6.3 \cdot 10^{-10}$	$1.9 \cdot 10^{-8}$	$7.1 \cdot 10^{-9}$

Even though k_2 is random because unidentifiable for these isolates, k_1 should be observed because it corresponds to the inhibition of PBP3 (which causes filamentation), which occurs within the range of antibiotics concentrations tested. However, for these strains, unlike for the sensitive ones, the values of k_1

1 In principle, for these strains, k_2 is higher than k_1, because the inhibition of PBP3 is observed but not of PBP1. However, the model needs L_m that is decided by L_{min}, L_{max} and k_2. For this class of strains, L_m is constant over the range of antibiotics used, meaning that the optimization will push k_2 to either very high or very low values compared to the range of antibiotics used experimentally. If k_2 is high, $L_m \approx L_{max}$, which is what should be; but if by chance during the parameter estimation, k_2 becomes small, then $L_{max} \approx L_{min}$. In which case one should interpret the value returned by the optimizer for L_{min} as L_{max}.

do not correspond any more to the literature value for the inhibition of PBP3 reported in table 5.7. This is because for strains expressing efficient β-lactamases, the concentration of antibiotic in the periplasm, at the contact of the PBPs, is much lower than the concentration of antibiotics outside the cell. However, we only model the outside antibiotic concentration, so the model overestimates the periplasmic antibiotic concentration, which should actually depend on the quantity of β-lactamase inside the cell, B_{in}, and its efficiency, k_{b}.

In the current model, all of this complexity is hidden into k_1 and k_2, which become compound parameters expressing the susceptibility of the PBPs to the *outside* antibiotic concentration.

If k_1 is influenced by other resistance mechanisms of the strain, it should be possible to explain its variations in this table by the presence of mutations, or antibiotic resistance genes. Indeed, the two highest values of k_1 correspond to the strains IB37 and IB38, which, according to table 5.2, possess the mutation "YRIK" of ftsI (the gene coding for PBP3) decreasing strongly the sensitivity of PBP3 to β-lactams. The third highest value of k_1 is given to IB311, which also features a mutation of ftsI, "YRIN_349-352," less effective than "YRIK," and also mutated porins, which slow down the entry of antibiotics in the cell.

5.3.6 Resistant strains

Because these strains almost do not react to the antibiotic, the dynamics is little informative and many parameters are unidentifiable, notably the parameters related to inhibition of PBPs: the only piece of knowledge earned about them is that they must be higher than the highest concentration of antibiotics used experimentally. L_{min} and L_{max} are completely unidentifiable, as well as the degradation rates of antibiotics, β-lactamase and cell debris, but also γ because no death is observed.

Parameter	IB39	IB310
β	3.3	7.0
γ	16	0.06
μ	0.86	0.87
K_{s}	$6 \cdot 10^{-4}$	$4 \cdot 10^{-4}$
λ	$5.5 \cdot 10^{7}$	$6.2 \cdot 10^{7}$
k_1	0.036	4228

Parameter	IB39	IB310
h_1	0.30	0.04
k_2	453	9169
B_{in}	$4.2 \cdot 10^{-9}$	$6.4 \cdot 10^{-10}$
k_{b}	$4.9 \cdot 10^{6}$	$9.3 \cdot 10^{6}$
d_{a}	0.10	0.093
d_{b}	1.9	18
d_{c}	0.16	0.51
p_{c}	0.86	0.98
L_{min}	490	444
L_{max}	607	513
η	$8.7 \cdot 10^{-9}$	$9.0 \cdot 10^{-9}$

The distinctive characteristic of these strains in our collection is that they carry the β-lactamase CTX-M-55, especially efficient against cefotaxime. As a result, from OD data only restricted to the range 0.5 mg/L to 512 mg/L, few parameters are identifiable. We only know that the β-lactamase is effective, as attested by the product $B_{\text{in}} \cdot k_{\text{b}}$. However, this antibiotic range was not able to perturb the system enough to identify the other antibiotic-related parameters.

5.4 UNEXPLAINED AND INTERESTING DATA

Although the model explains the main trends present in the data, some details escaped our understanding so far.

5.4.1 Stationary phase behaviour

The first is related to the behaviour of cells depleting the environment and reaching stationary phase. We observed a behaviour common to almost all strains of the collections, and reproducible one day to the next. Several examples are shown on figure 5.14, for two sensitive strains and two resistant.

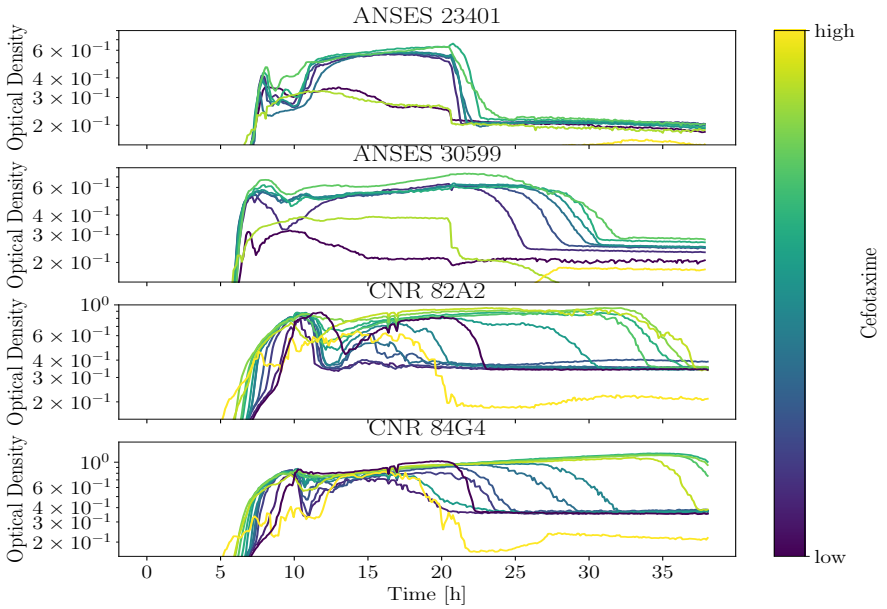

Figure 5.14: Zoom on the stationary phase of the growth curves of different stains submitted to different concentrations of antibiotics.

It looks like the population hesitates between two carrying capacities, spaced by a factor of 3. It eventually settles for the lower one, after a time that seems to increase with the initial antibiotic concentration. This looks like the transition between stationary phase and long-term stationary phase, which is a death phase, as shown in (Navarro Llorens, Tormo, and Martínez-García 2010; Pletnev et al. 2015). However, the reason why the death phase is further delayed by increasing quantities of antibiotics is unknown.

5.4.2 Partial regrowth for a sensitive strain

One of the sensitive strains, ANSES 30599 (IB35), seemed to exhibit a reproducible partial regrowth around 20 hours after the beginning of the experiment for some antibiotic concentrations, as shown on figure 5.15 (teal curves).

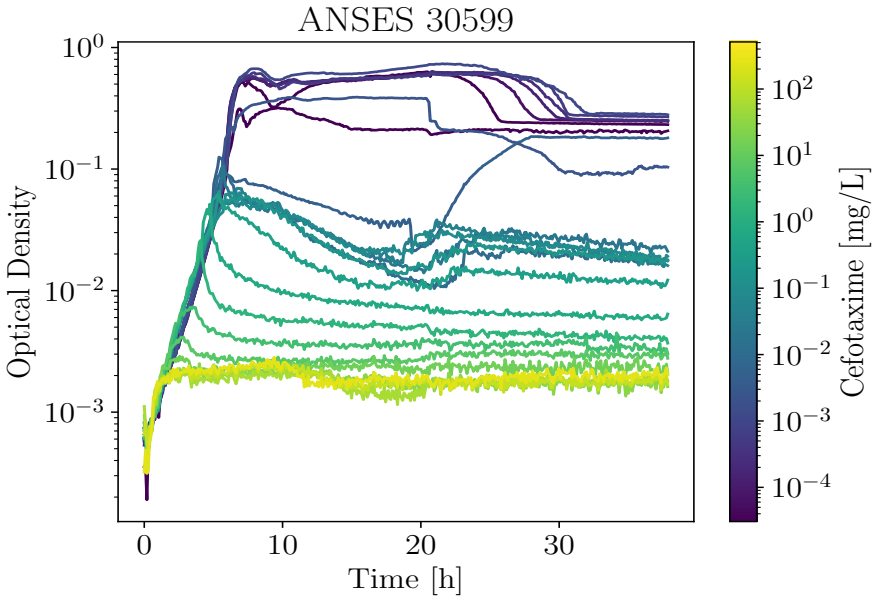

Figure 5.15: Apparent partial regrowth in the optical density, 16 to 20 hours after the initial treatment.

The hypothesis that appears the most likely is that this regrowth is linked to the degradation of the antibiotic, either by its natural decay rate, or by the effect of the weak β-lactamase TEM-1 produced by these cells. Following this decay, cell division is restored, which allows filamenting cells to divide into smaller cells and the growth of the population to restart. However, this regrowth does not reach the carrying capacity of the population, by at least one order of magnitude. This could for example result from a change of the medium preventing cells to consume all the nutrients.

5.5 CHAPTER SUMMARY

A collection of *E. coli* clinical isolates, each of them expressing multiple β-lactamases, including carbapenemases, was constituted (5.1). We described the series of experiments done on these strains that led us to developing the antibiotic resistance model described in chapter 3: growth curves observed through optical density (5.2.1 and 5.2.2), number of cells (5.2.4) and microscope snapshots (5.2.3). We could relate macroscopic observations to molecular properties of cell-wall enzymes, and specific parameters of the model (5.2.2). The model was also verified on a

multiple dosing experiment, which enables its use for optimal treatment design (5.2.5).

Inferring parameters for all nine strains, we proposed a method of clustering in presence of unidentifiable parameters, based on the parameter confidence intervals (5.3.2). We showed that the parameter values inferred on OD only, or on OD and number of cells were consistently neighbours, meaning that it is possible to calibrate the data with OD only. This clustering method allowed us to distinguish cells into three categories: sensitive, tolerant/resilient and resistant (5.3.4, 5.3.5 and 5.3.6). We exhibited a link between the inferred values of k_1, the parameter associated to the inhibition of PBP3, and mutations of ftsI (the gene coding for PBP3) detected in the genome of the strains. We also verified a correlation between the inferred values of B_{in} and k_{b}, and their literature values (5.3.3).

Finally, we proposed hypotheses for two experimental observations not captured by the model (5.4).

6 DISCUSSION AND CONCLUSION

In this chapter, after a brief summary of the contributions of this thesis, we will discuss the model and how it helps to explain the response of cell populations to antibiotic treatments. We will raise several points that the model does not address, and discuss its generality and applications. A conclusion follows.

6.1 THESIS SUMMARY

In the first chapter, we formulated the central problem of this thesis: getting a more informative assessment of antibiotic resistance by exploiting the whole growth curve, while limiting ourselves to optical density to simulate the conditions of a hospital laboratory.

We introduced a growth-fragmentation model accounting for the filamentation of cells, which is a mechanism of tolerance. We then derived a companion ODE model more amenable for optimization and parameter inference.

Calibrating a model of this size and complexity is not trivial. This led us to develop an efficient and robust optimization framework, which we exploited for an in-depth analysis of the unidentifiabilities of the model with the profile likelihood method.

We applied this approach to *E. coli* treated with cefotaxime, and found that the parameters inferred correspond to biochemical properties of the proteins expressed by the strains. We showed that these parameters can lead to a more meaningful classification than SIR in terms known by the community: sensitive, tolerant/resilient, and resistant strains.

Finally, we demonstrated that this model, based on a limited number of simple hypotheses, provides a comprehensive picture of the enzyme-mediated response of bacteria to β-lactam treatments.

6.2 A UNIFYING MODEL OF ANTIBIOTIC RESPONSE

6.2.1 Modelling assumptions and model overview

All β-lactams inhibit PBPs to various levels: the order described here (PBP3 then PBP1) is specific to some of them, including at least AMP and CTX.

We proposed in this thesis a model of tolerance, resistance and resilience of a population of cells to a β-lactam treatment. Although its derivation is mathematically involved, the model as its core relies on a limited number of simple biological hypotheses on cell physiology, and can be schematically illustrated by figure 6.1.

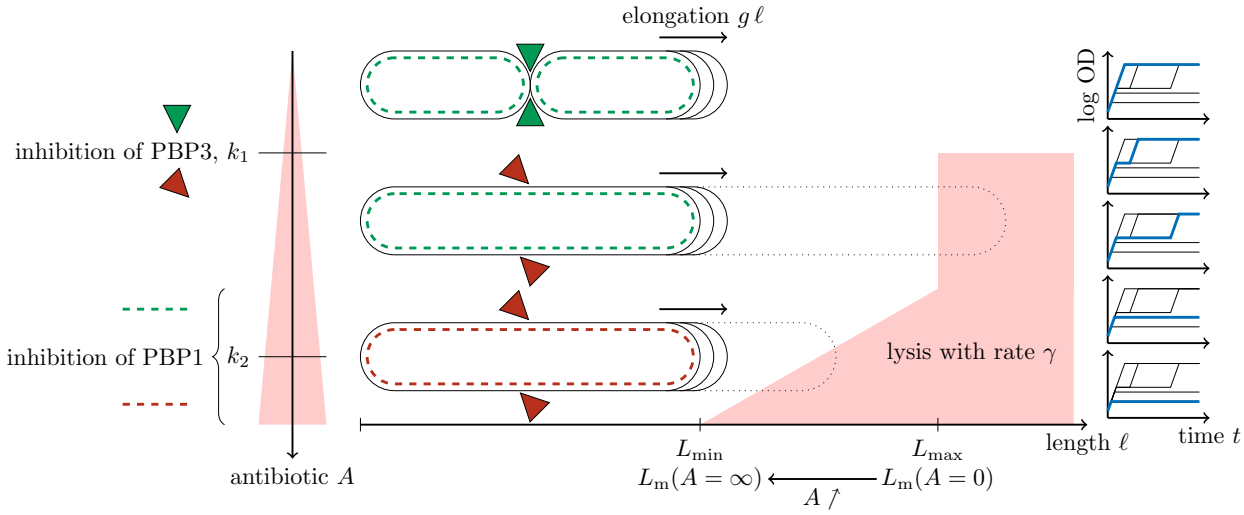

Figure 6.1: Graphical representation of the core principles of the model. Elongation proceeds at a speed $g\,\ell$ that depends only on the nutrients. Above a concentration k_1, the antibiotic inhibits PBP3, which deprives the cells from their capacity to divide. Cells who cannot divide filament until they reach a critical length $L_{\max}$ where they experience a death rate γ. Higher concentrations of antibiotics, around k_2, inhibit PBP1 which has for effect to reduce this critical length, hence cells die earlier. On the right are pictured schematic representations of the OD of the cell culture with the corresponding initial dose of antibiotic.

The core hypotheses of the model are the following:

- Growth: the rate of biomass formation per cell (elongation) is proportional to the cell length, and *not affected by the antibiotic*.
- Division: the antibiotic, through its action on PBP3, affects the ability of the cells to divide. Therefore, β-lactams act

as a switch to direct the neverstopping biomass formation into either new cells ($A < k_1$) or filamenting cells ($A > k_1$).
- Death: the antibiotic is *not the direct cause of cell death*. Cell death is mediated *solely by their length*: above a critical length, cells experience a constant death rate. This critical length can eventually be decreased by large doses of antibiotic, when this one becomes sufficient to disrupt the activity of the wall-repairing enzyme PBP1 (gradient around k_2).

Most of these hypotheses are standard and rather well known in the field, but the most original is the one related to death. The mechanism that it describes is extremely simple, yet manages to account for most experimental observations.

The rest of the model is less original, and made of very standard hypotheses including the action of β-lactamases that enables CAT:

- β-lactamases: cells produce enzymes that reduce their susceptibility. They are also released into the environment upon cell lysis and hydrolyse the antibiotic there.
- Both β-lactam and β-lactamase also follow natural exponential decay.
- Growth follows Monod's law.

6.2.2 Absent players: persisters

One dimension of antibiotic response is absent from this model: persistence. Persistence is an extreme case of tolerance and corresponds to a subpopulation of cells with a distinctively different phenotype than the rest of the population: a substantially lower, or even null growth rate. We understand that cells who do not elongate at all are not concerned by length-induced lysis. They can then persist under an arbitrary concentration of antibiotic for as long as necessary, until a persister stochastically awakens and switches to a normally growing phenotype. If this switch happens after the antibiotic disappeared, the population experiences regrowth.

The multidimensionality of antibiotic response prompted Brauner et al. (2016) to propose a framework for the measurement of resistance, tolerance and persistence. This framework exploits the MIC but also the Minimum Duration for Killing (MDK) to categorize strains into sensitive, resistant, tolerant or persistent. However, this framework does not seem adapted to strains

expressing enzymes degrading the antibiotic. Indeed, it does not mention the possibility of regrowth of the population, assuming that the cells either die (above the MIC) or thrive (below the MIC). It is unclear how to follow their framework in the case of resilient strains. The same article also describes biphasic kill curves as a sign of existence of a persistent subpopulation, killed less efficiently. In our system, the kill curve is monophasic, until the antibiotic is flushed and the population regrows.

The fact that persisters do not seem part of the dynamics of this system, and that our model is able to explain it without persistence, shows that resistance, tolerance and persistence are not the only axes of antibiotic response, and that a sufficiently tolerant population, even homogeneous in growth rate, can also exhibit the ability "to survive exposure to high concentrations of an antibiotic," a trait characteristic of persistence (Brauner et al. 2016).

6.2.3 Mathematical formulation of the ODE model

Although the model is conceptually rather simple (as seen on figure 6.1), its mathematical expression under the ODE form can be slightly surprising, for at least two reasons. The first is the factor $\ln 2$ in the differential equations for N and L, the second is the expression of the partial moments $Y_> = \int_{L_m}^{\infty} y(\ell)\,\mathrm{d}\ell$ and $L_> = \int_{L_m}^{\infty} \ell\, y(\ell)\,\mathrm{d}\ell$, for reminder:

$$\begin{aligned}\frac{\mathrm{d}N}{\mathrm{d}t} &= N\left[f\left(\frac{L}{\ln 2}-1\right)-\gamma Y_>\right]\\ \frac{\mathrm{d}L}{\mathrm{d}t} &= L\left[g-f\left(\frac{L}{\ln 2}-1\right)\right]-\gamma(L_>-L\,Y_>)\end{aligned}$$

$$Y_>\left(x=\frac{L}{L_0L_m}\right)=\begin{cases}\frac{x}{\nu}\left(x^\nu-\left(\frac{x}{2}\right)^\nu\right) & \text{for } x\le 1\\ x-1+\frac{x}{\nu}\left(1-\left(\frac{x}{2}\right)^\nu\right) & \text{for } 1\le x\le 2\\ 1 & \text{for } 2\le x\end{cases}$$

$$\frac{L_>}{L_0L_m}\left(x=\frac{L}{L_0L_m}\right)=\begin{cases}\frac{x}{\nu\ln 2}\left(x^\nu-\left(\frac{x}{2}\right)^\nu\right) & \text{for } x\le 1\\ x\frac{\ln x}{\ln 2}+\frac{x}{\nu\ln 2}\left(1-\left(\frac{x}{2}\right)^\nu\right) & \text{for } 1\le x\le 2\\ x & \text{for } 2\le x\end{cases}$$

The inelegant factor $\ln 2$ can be understood as resulting from the simplification of the increase of the division factor with the length of the filamented cell, as described in figure 3.6. It could probably be concealed by rescaling L. A better but harder approach could be to make the calculations with the original linear scale.

The dependency of these derivatives on $Y_>$ and $L_>$ can be understood intuitively. The partial moments have γ in factor, and are then clearly related to cell death, γ being the death rate above L_m. Reading this equation as $\frac{\mathrm{d}N}{\mathrm{d}t} = \cdots - \gamma\, Y_>\, N$, we can interpret $\gamma\, Y_>$ as a death rate applying on N, proportional to the proportion of cells longer than L_m.

However, death is in reality not applied uniformly on the population, but just to the longest cells. Killing the longest cells makes the average cell length L decrease, and this is what is expressed by the term $-\gamma(L_> - L\, Y_>)$ in the second equation. It is possible to show from the definitions of the partial moments that this term can only be negative, which confirms this intuitive interpretation.

Moreover, the limit cases where no cell is longer than L_m ($Y_> = 0$ and $L_> = 0$), or wher all cells are longer than L_m ($Y_> = 1$ and $L_> = L$), correspond to cases where this term is zero, leading to no change on the average length L, which is what we expect from these cases.

As for the involved mathematical expression of the partial moments $Y_>$ and $L_>$, one can wonder if it counts towards the model complexity. It can be argued that the complexity of the model lies only in its hypotheses, and in the number of its parameters. These two mathematical functions are approximations of the real dynamics contained in the PDE model, and do not introduce extra parameters. Moreover, they are used to reduce the number of variables of the model, from an uncountable number (PDE model), to a finite number (ODE model). Therefore, it can even be argued that the ODE model, despite taking more space on paper, is actually less complex than the PDE model.

6.2.4 Generality of the model

The model was designed for *in vitro* batch experiments. This is a convenient condition for an experimentalist, but it is not necessarily very realistic with respect to the location of the infection: typically a human organ. More realistic conditions could involve a periodic influx of nutrients, spatial heterogeneity, in-

teractions with the immune system of the host organism, and more involved drug dynamics. However, the multi-scale aspect of interaction between the molecular, cell and population levels is present in both of these conditions. Most of the constituents are there, and it should be possible to plug components to this model, or to couple it with a Pharmacokinetic/Pharmacodynamic (PK/PD) model to have a first approximation of the response to treatment of an infection in some organs where spatial heterogeneities are not an issue, for example the bladder.

It however makes strong assumptions on the physiology of cells, notably that filamentation is the driver of tolerance. However, filamentation is just observed on certain strains and certain antibiotics: in general, enterobacteriae (such as *E. coli*, used through this work, and *K. pneumoniae*, used in the beginning of this thesis with a similar model (Hannah R. Meredith et al. 2018)) treated with some β-lactams such as ampicillin, cefotaxime, or ceftazidime. Some other β-lactams, binding to PBPs in a different order, cause not filamentation but the formation of spheroplasts (spherical cells without a wall). In this case, biomass is still being formed at the same rate as normal cells, but the cell morphology is different. It remains to be seen if this model can be transposed to this setting too.

An obvious and immediate test of the generality of the model would be to try more strains (including Gram Positive) and more β-lactams (including antibiotics known to cause spheroplast formation rather than filamentation). It could also be valuable to make more counting cell experiments, to get more data on N. Other observables could also be considered in order to confirm the model predictions, like the antibiotic concentration or the proportion of dead cells.

One of the least satisfying parts of the model is the omission of the fact that β-lactamases protect not only the environment once released, but also the cells themselves when they are in their periplasm. So B_{in}, the amount of β-lactamase in a cell, and k_{b}, its efficiency, should be involved in the division rate f and in the critical length L_{m}. In this way, k_1 and k_2 would really represent the susceptibility of PBPs to antibiotics, and not be overestimated because of the presence of β-lactamase. It should be possible to arrange the model in the direction that is explained by Livermore (1997).

6.2.5 Perspectives: optimal experimental design and optimal treatment

The work done on section 4.2.1 on profile likelihood and identifiability analysis showed that parameter identifiability depend not only on the strain tested, but also on the experiments done on the strain. A fascinating direction of research lies in optimal experimental design. This consists in solving the problem of finding an optimally informative experiment, given time and resource constraints. The availability of a programmable plate reader capable of injecting antibiotic on request in certain wells, which was made possible by the `platerider` library, introduced in section 2.2, enables the implementation of arbitrarily complex experiments.

For example, one can decide *a priori* on a sequence of injections engineered to be informative on most expected strains. While performing this experiment on a given strain, as the first few measurement points become available, an optimization solver connected to the plate reader can refine the sequence of injections to adapt it more specifically to the strain being tested. The new instructions are sent to the plate reader that carries on with the experiment with the updated instructions. With our experimental platform, this "measure, learn, optimize" loop could occur every 5 minutes over 24 hours, or until the strain parameters are perfectly identified. Experiments taking place in 96-well plates, one can of course also envision performing this in parallel, with several parallel experiments on the same strain, or by experimenting on different strains at the same time.

Optimal treatment also comes to mind as a direct application of the model, at least in the conditions of the experiments: *in vitro* and for batch experiments. Antibiotic treatments are not innocuous, most drug being susceptible to cause undesirable side effects at high dose. It was even shown that inappropriate treatments can facilitate the evolution of resistance (Gould and MacKenzie 2002; Wistrand-Yuen et al. 2018; Levin-Reisman et al. 2017). The criteria to optimize treatments could be for example to minimize the total dose of antibiotic used, or the time it takes, or the time spent above the MIC, to reduce the number of cells under a defined threshold. We already computed optimal treatments on a previous model, appearing in (Hannah R. Meredith et al. 2018), but computing them on the model presented in this thesis, and testing them *in vitro*, should be doable. A success of the optimal treatment would confirm the relevance of the model,

and be a concrete demonstration of the information earned on the clinical isolate through parameter inference.

6.3 CONCLUSION

Antibiotic resistance is a challenging and threatening problem spanning multiple fields of research: pharmacology, biochemistry, microbiology, biophysics, medicine, epidemiology and more. Although research is being done in each of them individually, the key to this global problem is crosswork. For this, communication is needed across disciplines. In this respect, reviews and consensus papers are needed to push for the use of a shared vocabulary (Balaban et al. 2019).

The literature is a mine of data on almost all the elements in the system. For example, is easy to find two or three references for almost any kinetic parameter concerning any particular β-lactamase or PBP. But it seems that this enormous and valuable amount of data is not exploited as it could. It cannot, unless we try explaining the data with a view transcending the layers (Greulich et al. 2015). Often however, biology is more complex than one β-lactamase or one PBP, or even one antibiotic. In this case, the way forward is to understand how several elements interact (Bollenbach 2015).

With this work, we try to provide an explanation of the response of enterobacteriae to β-lactams, encompassing the dimensions of resistance, tolerance, and resilience. It is evidently not a final view on the question, as some aspects are missing, and some others are not optimally represented. However, it seems possible to start building on this to start improving how we both intuitively and quantitatively understand the dynamics of this system, which can lead to progress in the design of treatments more efficient and less susceptible to increase the overall antibiotic resistance.

7 REFERENCES

Abraham, Edward P., and Ernst Chain. 1940. "An Enzyme from Bacteria Able to Destroy Penicillin." *Nature* 146 (3713): 837. https://doi.org/10.1038/146837a0.

Allen, Rosalind, and Bartłomiej Waclaw. 2016. "Antibiotic Resistance: A Physicist's View." *Physical Biology* 13 (4): 045001. https://doi.org/10.1088/1478-3975/13/4/045001.

Alonso, Antonio A., Ignacio Molina, and Constantinos Theodoropoulos. 2014. "Modeling Bacterial Population Growth from Stochastic Single-Cell Dynamics." *Applied and Environmental Microbiology* 80 (17): 5241–53. https://doi.org/10.1128/AEM.01423-14.

Ambler, R. P., James Baddiley, and Edward Penley Abraham. 1980. "The Structure of β-Lactamases." *Philosophical Transactions of the Royal Society of London. B, Biological Sciences* 289 (1036): 321–31. https://doi.org/10.1098/rstb.1980.0049.

Artemova, Tatiana, Ylaine Gerardin, Carmel Dudley, Nicole M Vega, and Jeff Gore. 2015. "Isolated Cell Behavior Drives the Evolution of Antibiotic Resistance." *Molecular Systems Biology* 11 (7). https://doi.org/10.15252/msb.20145888.

Baker, Monya. 2016. "1,500 Scientists Lift the Lid on Reproducibility." *Nature News* 533 (7604): 452. https://doi.org/10.1038/533452a.

Balaban, Nathalie Q., Sophie Helaine, Kim Lewis, Martin Ackermann, Bree Aldridge, Dan I. Andersson, Mark P. Brynildsen, et al. 2019. "Definitions and Guidelines for Research on Antibiotic Persistence." *Nature Reviews. Microbiology* 17 (7): 441–48. https://doi.org/10.1038/s41579-019-0196-3.

Baym, Michael, Tami D. Lieberman, Eric D. Kelsic, Remy Chait, Rotem Gross, Idan Yelin, and Roy Kishony. 2016. "Spatiotemporal Microbial Evolution on Antibiotic Landscapes." *Science (New York, N.Y.)* 353 (6304): 1147–51. https://doi.org/10.1126/science.aag0822.

Beal, Jacob, Natalie G. Farny, Traci Haddock-Angelli, Vinoo Selvarajah, Geoff S. Baldwin, Russell Buckley-Taylor, Markus Gershater, et al. 2019. "Robust Estimation of Bacterial Cell Count from Optical Density." *bioRxiv*, October, 803239. https://doi.org/10.1101/803239.

Ben-David, Avishai, and Charles E. Davidson. 2014. "Estimation Method for Serial Dilution Experiments." *Journal of Microbiological Methods* 107 (December): 214–21. https://doi.org/10.1016/j.mimet.2014.08.023.

Ben-Jacob, Eshel, Ofer Schochet, Adam Tenenbaum, Inon Cohen, Andras Czirók, and Tamas Vicsek. 1994. "Generic Modelling of Cooperative Growth Patterns in Bacterial Colonies." *Nature* 368 (6466): 46–49. https://doi.org/10.1038/368046a0.

Berg, Stuart, Dominik Kutra, Thorben Kroeger, Christoph N. Straehle, Bernhard X. Kausler, Carsten Haubold, Martin Schiegg, et al. 2019. "Ilastik: Interactive Machine Learning for (Bio)image Analysis." *Nature Methods* 16 (12, 12): 1226–32. https://doi.org/10.1038/s41592-019-0582-9.

Bertani, Giuseppe. 1951. "Studies on Lysogenesis." *Journal of Bacteriology* 62 (3): 293–300. https://www.ncbi.nlm.nih.gov/pmc/articles/PMC386127/.

Bhat, Nayana G., and S. Balaji. 2020. "Whole-Cell Modeling and Simulation: A Brief Survey." *New Generation Computing* 38 (1): 259–81. https://doi.org/10.1007/s00354-019-00066-y.

Bollenbach, Tobias. 2015. "Antimicrobial Interactions: Mechanisms and Implications for Drug Discovery and Resistance Evolution." *Current Opinion in Microbiology*, Antimicrobials • Microbial systems biology, 27 (October): 1–9. https://doi.org/10.1016/j.mib.2015.05.008.

Boman, H. G., and K. G. Eriksson. 1963. "Penicillin Induced Lysis in Escherichia Coli." *Journal of General Microbiology* 31 (3): 339–52. https://doi.org/10.1099/00221287-31-3-339.

Botta, G A, and J T Park. 1981. "Evidence for Involvement of Penicillin-Binding Protein 3 in Murein Synthesis During Septation but Not During Cell Elongation." *Journal of Bacteriology* 145 (1): 333–40. https://doi.org/10.1128/JB.145.1.333-340.1981.

Brauner, Asher, Ofer Fridman, Orit Gefen, and Nathalie Q. Balaban. 2016. "Distinguishing Between Resistance, Tolerance and Persistence to Antibiotic Treatment." *Nature Reviews Microbiology* 14 (5, 5): 320–30. https://doi.org/10.1038/nrmicro.2016.34.

Brugger, Silvio D., Christian Baumberger, Marcel Jost, Werner Jenni, Urs Brugger, and Kathrin Mühlemann. 2012. "Automated Counting of Bacterial Colony Forming Units on Agar Plates." *PLoS ONE* 7 (3). https://doi.org/10.1371/journal.pone.0033695.

Buchanan, Robert E. 1918. "Life Phases in a Bacterial Culture." *Journal of Infectious Diseases* 23 (2): 109–25. https://doi.org/10.1086/infdis/23.2.109.

Buijs, J., A. S. M. Dofferhoff, J. W. Mouton, J. H. T. Wagenvoort, and J. W. M. van der Meer. 2008. "Concentration-Dependency of β-Lactam-Induced Filament Formation in Gram-Negative Bacteria." *Clinical Microbiology and Infection* 14 (4): 344–49. https://doi.org/10.1111/j.1469-0691.2007.01940.x.

Bush, Karen. 1989. "Characterization of β-Lactamases." *ANTIMICROB. AGENTS CHEMOTHER.* 33: 5.

———. 2018. "Past and Present Perspectives on β-Lactamases." *Antimicrobial Agents and Chemotherapy* 62 (10). https://doi.org/10.1128/AAC.01076-18.

Bush, Karen, and George A. Jacoby. 2010. "Updated Functional Classification of β-Lactamases." *Antimicrobial Agents and Chemotherapy* 54 (3): 969–76. https://doi.org/10.1128/AAC.01009-09.

Bush, Karen, George A. Jacoby, and Antoine A. Medeiros. 1995. "A Functional Classification Scheme for Beta-Lactamases and Its Correlation with Molecular Structure." *Antimicrobial Agents and Chemotherapy* 39 (6): 1211–33. https://www.ncbi.nlm.nih.gov/pmc/articles/PMC162717/.

Bush, Karen, and Richard B. Sykes. 1986. "Methodology for the Study of β-Lactamases." *Antimicrobial Agents and Chemotherapy* 30 (1): 6–10. https://www.ncbi.nlm.nih.gov/pmc/articles/PMC176424/.

Cadena-Herrera, Daniela, Joshua E. Esparza-De Lara, Nancy D. Ramírez-Ibañez, Carlos A. López-Morales, Néstor O. Pérez, Luis F. Flores-Ortiz, and Emilio Medina-Rivero. 2015. "Validation of Three Viable-Cell Counting Methods: Manual, Semi-Automated, and Automated." *Biotechnology Reports* 7 (September): 9–16. https://doi.org/10.1016/j.btre.2015.04.004.

Centers for Disease Control and Prevention (U.S.). 2019. "Antibiotic Resistance Threats in the United States, 2019." Centers for Disease Control and Prevention (U.S.). https://doi.org/10.15620/cdc:82532.

Chambers, H F, M J Sachdeva, and C J Hackbarth. 1994. "Kinetics of Penicillin Binding to Penicillin-Binding Proteins of Staphylococcus Aureus." *Biochemical Journal* 301 (July): 139–44. https://www.ncbi.nlm.nih.gov/pmc/articles/PMC1137153/.

Cho, Hongbaek, Tsuyoshi Uehara, and Thomas G. Bernhardt. 2014. "β-Lactam Antibiotics Induce a Lethal Malfunctioning of the Bacterial Cell Wall Synthesis Machinery." *Cell* 159 (6): 1300–1311. https://doi.org/10.1016/j.cell.2014.11.017.

Chung, Hak Suk, Zhizhong Yao, Nathan W. Goehring, Roy Kishony, Jon Beckwith, and Daniel Kahne. 2009. "Rapid β-Lactam-Induced Lysis Requires Successful Assembly of the Cell Division Machinery." *Proceedings of the National Academy of Sciences* 106 (51): 21872–77. https://doi.org/10.1073/pnas.0911674106.

Clarke, Matthew L., Robert L. Burton, A. Nayo Hill, Maritoni Litorja, Moon H. Nahm, and Jeeseong Hwang. 2010. "Low-Cost, High-Throughput, Automated Counting of Bacterial Colonies." *Cytometry Part A* 77A (8): 790–97. https://doi.org/10.1002/cyto.a.20864.

Cochran, William G. 1950. "Estimation of Bacterial Densities by Means of the "Most Probable Number"." *Biometrics* 6 (2): 105. https://doi.org/10.2307/3001491.

Collins, J. F., and M. H. Richmond. 1962. "Rate of Growth of Bacillus Cereus Between Divisions." *Journal of General Microbiology* 28 (1): 15–33. https://doi.org/10.1099/00221287-28-1-15.

Colquhoun, David. 2014. "An Investigation of the False Discovery Rate and the Misinterpretation of p-Values." *Royal Society Open Science* 1 (3). https://doi.org/10.1098/rsos.140216.

Combs, Gerald. 2020. *Wireshark* (version 3.2). Wireshark Foundation. https://code.wireshark.org/review/wireshark.

Condrey, Richard E. 1982. "The Chemostat and Blackman Kinetics." *Biotechnology and Bioengineering* 24 (7): 1705–9. https://doi.org/10.1002/bit.260240720.

Cullum, John, and Miguel Vicente. 1978. "Cell Growth and Length Distribution in Escherichia Coli." *Journal of Bacteriology* 134 (1): 330–37. https://www.ncbi.nlm.nih.gov/pmc/articles/PMC222250/.

Daniels, H. E. 1954. "Saddlepoint Approximations in Statistics." *Annals of Mathematical Statistics* 25 (4): 631–50. https://doi.org/10.1214/aoms/1177728652.

DeBlois, Ralph W., and Charles P. Bean. 1970. "Counting and Sizing of Submicron Particles by the Resistive Pulse Technique." *Review of Scientific Instruments* 41 (7): 909–16. https://doi.org/10.1063/1.1684724.

Eagle, Harry. 1948. "A Paradoxical Zone Phenomenon in the Bactericidal Action of Penicillin in Vitro." *Science* 107 (2767): 44–45. https://doi.org/10.1126/science.107.2767.44.

Eagle, Harry, and A. D. Musselman. 1948. "The Rate of Bactericidal Action of Penicillin in Vitro as a Function of Its Concentration, and Its Paradoxically Reduced Activity at High Concentrations Against Certain Organisms." *The Journal of Experimental Medicine* 88 (1): 99–131. https://doi.org/10.1084/jem.88.1.99.

Egli, Thomas, Urs Lendenmann, and Mario Snozzi. 1993. "Kinetics of Microbial Growth with Mixtures of Carbon Sources." *Antonie van Leeuwenhoek* 63 (3-4): 289–98. https://doi.org/10.1007/BF00871224.

Elf, Johan, Karin Nilsson, Tanel Tenson, and Måns Ehrenberg. 2006. "Bistable Bacterial Growth Rate in Response to Antibiotics with Low Membrane Permeability." *Physical Review Letters* 97 (25): 258104. https://doi.org/10.1103/PhysRevLett.97.258104.

EUCAST. 2020a. "Breakpoint Tables for Interpretation of MICs and Zone Diameters." https://www.eucast.org/fileadmin/src/media/PDFs/EUCAST_files/Breakpoint_tables/v_10.0_Breakpoint_Tables.pdf.

———. 2020b. "EUCAST Reading Guide for Broth Microdilution." https://www.eucast.org/fileadmin/src/media/PDFs/EUCAST_files/Disk_test_documents/2020_manuals/Reading_guide_BMD_v_2.0_2020.pdf.

Faheem, Mohammad, Md Tabish Rehman, Mohd Danishuddin, and Asad U. Khan. 2013. "Biochemical Characterization of CTX-M-15 from Enterobacter Cloacae and Designing a Novel Non-β-Lactam-β-Lactamase Inhibitor." Edited by Hendrik W. van Veen. *PLoS ONE* 8 (2): e56926. https://doi.org/10.1371/journal.pone.0056926.

Felici, Antonio, Gianfranco Amicosante, Arduino Oratore, Roberto Strom, Philippe Ledent, Bernard Joris, Laurence Fanuel, and Jean-Marie Frère. 1993. "An Overview of the Kinetic Parameters of Class B β-Lactamases." *Biochemical Journal*, no. 291: 151–55.

Finberg, Robert W., Robert C. Moellering, Francis P. Tally, William A. Craig, George A. Pankey, E. Patchen Dellinger, Michael A. West, et al. 2004. "The Importance of Bactericidal Drugs: Future Directions in Infectious Disease." *Clinical Infectious Diseases* 39 (9): 1314–20. https://doi.org/10.1086/425009.

Fisher, R. A., H. G. Thornton, and W. A. Mackenzie. 1922. "The Accuracy of the Plating Method of Estimating the Density of Bacterial Populations." *Annals of Applied Biology* 9 (3-4): 325–59. https://doi.org/10.1111/j.1744-7348.1922.tb05962.x.

Frasier, Kaitlin E., Marie A. Roch, Melissa S. Soldevilla, Sean M. Wiggins, Lance P. Garrison, and John A. Hildebrand. 2017. "Automated Classification of Dolphin Echolocation Click Types from the Gulf of Mexico." Edited by Herve Glotin. *PLOS Computational Biology* 13 (12): e1005823. https://doi.org/10.1371/journal.pcbi.1005823.

Fredborg, Marlene, Flemming S. Rosenvinge, Erik Spillum, Stine Kroghsbo, Mikala Wang, and Teis E. Sondergaard. 2015. "Automated Image Analysis for Quantification of Filamentous Bacteria." *BMC Microbiology* 15 (1). https://doi.org/10.1186/s12866-015-0583-5.

Geissmann, Quentin. 2013. "OpenCFU, a New Free and Open-Source Software to Count Cell Colonies and Other Circular Objects." *PLOS ONE* 8 (2): e54072. https://doi.org/10.1371/journal.pone.0054072.

Gould, I. M., and F. M. MacKenzie. 2002. "Antibiotic Exposure as a Risk Factor for Emergence of Resistance: The Influence of Concentration." *Journal of Applied Microbiology* 92 (s1): 78S–84S. https://doi.org/10.1046/j.1365-2672.92.5s1.10.x.

Greenland, Sander, Stephen J. Senn, Kenneth J. Rothman, John B. Carlin, Charles Poole, Steven N. Goodman, and Douglas G. Altman. 2016. "Statistical Tests, P Values, Confidence Intervals, and Power: A Guide to Misinterpretations." *European Journal of Epidemiology* 31 (4): 337–50. https://doi.org/10.1007/s10654-016-0149-3.

Greenwood, David. 1977. "Response Profiles: A Method of Evaluating the Activity of β-Lactam Antibiotics Against Enterobacteria." *Chemotherapy* 23 (1): 11–18. https://doi.org/10.1159/000221965.

Greenwood, David, and Adrian Eley. 1982. "A Turbidimetric Study of the Responses of Selected Strains of Pseudomonas Aeruginosa to Eight Antipseudomonal β-Lactam Antibiotics." *Journal of Infectious Diseases* 145 (1): 110–17. https://doi.org/10.1093/infdis/145.1.110.

Greulich, Philip, Matthew Scott, Martin R. Evans, and Rosalind J. Allen. 2015. "Growth-Dependent Bacterial Susceptibility to

Ribosome-Targeting Antibiotics." *Molecular Systems Biology* 11 (3). https://doi.org/10.15252/msb.20145949.

Greulich, Philip, Bartłomiej Waclaw, and Rosalind J Allen. 2012. "Mutational Pathway Determines Whether Drug Gradients Accelerate Evolution of Drug-Resistant Cells." *PHYSICAL REVIEW LETTERS*, 5.

Hall, Alistair J., and Graeme C. Wake. 1989. "A Functional Differential Equation Arising in Modelling of Cell Growth." *The Journal of the Australian Mathematical Society. Series B. Applied Mathematics* 30 (4): 424–35. https://doi.org/10.1017/S0334270000006366.

Hansen, Nikolaus. 2006. *The CMA Evolution Strategy: A Comparing Review*.

Harms, Alexander, Etienne Maisonneuve, and Kenn Gerdes. 2016. "Mechanisms of Bacterial Persistence During Stress and Antibiotic Exposure." *Science* 354 (6318): aaf4268. https://doi.org/10.1126/science.aaf4268.

Hashimoto, Mikihiro, Takashi Nozoe, Hidenori Nakaoka, Reiko Okura, Sayo Akiyoshi, Kunihiko Kaneko, Edo Kussell, and Yuichi Wakamoto. 2016. "Noise-Driven Growth Rate Gain in Clonal Cellular Populations." *Proceedings of the National Academy of Sciences* 113 (12): 3251–56. https://doi.org/10.1073/pnas.1519412113.

Hazan, Ronen, Yok-Ai Que, Damien Maura, and Laurence G Rahme. 2012. "A Method for High Throughput Determination of Viable Bacteria Cell Counts in 96-Well Plates." *BMC Microbiology* 12 (November): 259. https://doi.org/10.1186/1471-2180-12-259.

Hedges, Alan J. 2002. "Estimating the Precision of Serial Dilutions and Viable Bacterial Counts." *International Journal of Food Microbiology* 76 (3): 207–14. https://doi.org/10.1016/S0168-1605(02)00022-3.

Hentschke, Moritz, Stathis D. Kotsakis, Manuel Wolters, Peter Heisig, Vivi Miriagou, and Martin Aepfelbacher. 2011. "CMY-42, a Novel Plasmid-Mediated CMY-2 Variant AmpC Beta-Lactamase." *Microbial Drug Resistance* 17 (2): 165–69. https://doi.org/10.1089/mdr.2010.0137.

Hilsenbeck, Oliver, Michael Schwarzfischer, Dirk Loeffler, Sotiris Dimopoulos, Simon Hastreiter, Carsten Marr, Fabian J. Theis, and Timm Schroeder. 2017. "fastER: A User-Friendly Tool for Ultrafast and Robust Cell Segmentation in Large-Scale Microscopy." *Bioinformatics (Oxford, England)* 33 (13): 2020–28. https://doi.org/10.1093/bioinformatics/btx107.

Hindmarsh, Alan C. 1983. "ODEPACK, A Systematized Collection of ODE Solvers." *Scientific Computing*, IMACS Transactions on Scientific Computation, 1: 55–64. https://computing.llnl.gov/casc/nsde/pubs/u88007.pdf.

Hiroshi, Nikaido. 2009. "The Limitations of LB Medium." Small Things Considered. November 9, 2009. http://schaechter.asmblog.org/schaechter/2009/11/the-limitations-of-lb-medium.html.

Hobby, G. L., K. Meyer, and E. Chaffee. 1942. "Observations on the Mechanism of Action of Penicillin." *Experimental Biology and Medicine* 50 (2): 281–85. https://doi.org/10.3181/00379727-50-13773.

Hobby, Gladys L., and Martin H. Dawson. 1944. "Effect of Rate of Growth of Bacteria on Action of Penicillin." *Experimental Biology and Medicine* 56 (2): 181–84. https://doi.org/10.3181/00379727-56-14643.

Hogan, Deborah, and Roberto Kolter. 2002. "Why Are Bacteria Refractory to Antimicrobials?" *Current Opinion in Microbiology* 5 (5): 472–77. https://doi.org/10.1016/S1369-5274(02)00357-0.

Houle, David, Christophe Pélabon, Günter P. Wagner, and Thomas F. Hansen. 2011. "Measurement and Meaning in Biology." *The Quarterly Review of Biology* 86 (1): 3–34. https://doi.org/10.1086/658408.

Ioannidis, John P. A. 2005. "Why Most Published Research Findings Are False." *PLoS Medicine* 2 (8). https://doi.org/10.1371/journal.pmed.0020124.

Jennison, Marshall W., and George P. Wadsworth. 1940. "Evaluation of the Errors Involved in Estimating Bacterial Numbers by the Plating Method." *Journal of Bacteriology* 39 (4): 389–97. https://doi.org/10.1128/JB.39.4.389-397.1940.

Jett, Bradley D., Kenneth L. Hatter, Mark M. Huycke, and Michael S. Gilmore. 1997. "Simplified Agar Plate Method for Quantifying Viable Bacteria." *BioTechniques* 23 (4): 648–50. https://doi.org/10.2144/97234bm22.

Johnston, Grace. 2010. "Automated Handheld Instrument Improves Counting Precision Across Multiple Cell Lines." *BioTechniques* 48 (4): 325–27. https://doi.org/10.2144/000113407.

Khan, Arif ul Maula, Angelo Torelli, Ivo Wolf, and Norbert Gretz. 2018. "AutoCellSeg: Robust Automatic Colony Forming Unit (CFU)/Cell Analysis Using Adaptive Image Segmentation

and Easy-to-Use Post-Editing Techniques." *Scientific Reports* 8 (1): 7302. https://doi.org/10.1038/s41598-018-24916-9.

Kirby, William M. M. 1945. "Bacteriostatic and Lytic Actions of Penicillin on Sensitive and Resistant Staphylococci." *Journal of Clinical Investigation* 24 (2): 165–69. https://www.ncbi.nlm.nih.gov/pmc/articles/PMC435445/.

Kocaoglu, Ozden, and Erin E. Carlson. 2015. "Profiling of β-Lactam Selectivity for Penicillin-Binding Proteins in Escherichia Coli Strain Dc2." *Antimicrobial Agents and Chemotherapy* 59 (5): 2785–90. https://doi.org/10.1128/AAC.04552-14.

Koch, Arthur L. 1961. "Some Calculations on the Turbidity of Mitochondria and Bacteria." *Biochimica Et Biophysica Acta* 51 (3): 429–41. https://doi.org/10.1016/0006-3002(61)90599-6.

———. 1968. "Theory of the Angular Dependence of Light Scattered by Bacteria and Similar-Sized Biological Objects." *Journal of Theoretical Biology* 18 (1): 133–56. https://doi.org/10.1016/0022-5193(68)90174-4.

———. 1970. "Turbidity Measurements of Bacterial Cultures in Some Available Commercial Instruments." *Analytical Biochemistry* 38 (1): 252–59. https://doi.org/10.1016/0003-2697(70)90174-0.

Lee, Anna J., Shangying Wang, Hannah R. Meredith, Bihan Zhuang, Zhuojun Dai, and Lingchong You. 2018. "Robust, Linear Correlations Between Growth Rates and β-Lactam–mediated Lysis Rates." *Proceedings of the National Academy of Sciences* 115 (16): 4069–74. https://doi.org/10.1073/pnas.1719504115.

Lendenmann, Urs, Heinrich Senn, Mario Snozzi, and Thomas Egli. 2000. "Dynamics of Mixed Substrate Growth of Escherichia Coli in Batch Culture: The Transition Between Simultaneous and Sequential Utilisation of Carbon Substrates," July, 11.

Lendenmann, Urs, Mario Snozzi, and Thomas Egli. 2000. "Growth Kinetics of Escherichia Coli with Galactose and Several Other Sugars in Carbon-Limited Chemostat Culture." *Canadian Journal of Microbiology* 46 (1): 72–80. https://doi.org/10.1139/cjm-46-1-72.

Leonard, David A, Andrea M Hujer, Brian A Smith, Kyle D Schneider, Christopher R Bethel, Kristine M Hujer, and Robert A Bonomo. 2008. "The Role of OXA-1 β-Lactamase Asp66 in the Stabilization of the Active-Site Carbamate Group and in Substrate Turnover," 8.

Levin-Reisman, Irit, Irine Ronin, Orit Gefen, Ilan Braniss, Noam Shoresh, and Nathalie Q. Balaban. 2017. "Antibiotic Tolerance Facilitates the Evolution of Resistance." *Science* 355 (6327): 826–30. https://doi.org/10.1126/science.aaj2191.

Levy, Stuart B, and Bonnie Marshall. 2004. "Antibacterial Resistance Worldwide: Causes, Challenges and Responses." *Nature Medicine* 10 (S12): S122–29. https://doi.org/10.1038/nm1145.

Li, Chen, Marco Donizelli, Nicolas Rodriguez, Harish Dharuri, Lukas Endler, Vijayalakshmi Chelliah, Lu Li, et al. 2010. "BioModels Database: An Enhanced, Curated and Annotated Resource for Published Quantitative Kinetic Models." *BMC Systems Biology* 4 (June): 92. https://doi.org/10.1186/1752-0509-4-92.

Liu, Zhihai, Jiyun Li, Xiaoming Wang, Dejun Liu, Yuebin Ke, Yang Wang, and Jianzhong Shen. 2018. "Novel Variant of New Delhi Metallo-β-Lactamase, NDM-20, in Escherichia Coli." *Frontiers in Microbiology* 9. https://doi.org/10.3389/fmicb.2018.00248.

Livermore, David M. 1997. "β-Lactamases: Quantity and Resistance." *Clinical Microbiology and Infection* 3 (January): 4S10–19. https://doi.org/10.1016/S1198-743X(14)65031-X.

Lopatkin, Allison J., and James J. Collins. 2020. "Predictive Biology: Modelling, Understanding and Harnessing Microbial Complexity." *Nature Reviews Microbiology*, May, 1–14. https://doi.org/10.1038/s41579-020-0372-5.

Ltd, Tecan Group. n.d. "Multimode Microplate Reader, Live Cell Assays." Accessed June 17, 2020. https://lifesciences.tecan.com/multimode-plate-reader.

Lukačišinová, Marta, and Tobias Bollenbach. 2017. "Toward a Quantitative Understanding of Antibiotic Resistance Evolution." *Current Opinion in Biotechnology* 46 (August): 90–97. https://doi.org/10.1016/j.copbio.2017.02.013.

Madigan, Michael T., Kelly S. Bender, Daniel H. Buckley, W. Matthew Sattley, and David A. Stahl. 2017. *Brock Biology of Microorganisms*. 15 edition. NY, NY: Pearson.

McCrady, M. H. 1915. "The Numerical Interpretation of Fermentation-Tube Results." *The Journal of Infectious Diseases* 17 (1): 183–212. https://www.jstor.org/stable/30083495.

Merck. n.d. "M9, Minimal Salts, 5x M6030." M9 media. Accessed July 1, 2020. https://www.sigmaaldrich.com/catalog/product/sigma/m6030.

Meredith, Hannah R. 2015. "Collective Antibiotic Tolerance: Mechanisms, Dynamics and Intervention." *Nature Chemical Biology* 11: 7.

Meredith, Hannah R., Virgile Andreani, Helena R. Ma, Allison J. Lopatkin, Anna J. Lee, Deverick J. Anderson, Gregory Batt, and Lingchong You. 2018. "Applying Ecological Resistance and Resilience to Dissect Bacterial Antibiotic Responses." *Science Advances* 4 (12): eaau1873. https://doi.org/10.1126/sciadv.aau1873.

Meredith, Hannah R., Allison J. Lopatkin, Deverick J. Anderson, and Lingchong You. 2015. "Bacterial Temporal Dynamics Enable Optimal Design of Antibiotic Treatment." *PLOS Computational Biology* 11 (4): e1004201. https://doi.org/10.1371/journal.pcbi.1004201.

Miles, A. A., S. S. Misra, and J. O. Irwin. 1938. "The Estimation of the Bactericidal Power of the Blood." *The Journal of Hygiene* 38 (6): 732–49. https://www.ncbi.nlm.nih.gov/pmc/articles/PMC2199673/.

Monod, Jacques. 1941. "Recherches sur la croissance des cultures bactériennes." Paris: Hermann.

———. 1949. "The Growth of Bacterial Cultures." *Annual Review of Microbiology* 3 (1): 371–94. https://doi.org/10.1146/annurev.mi.03.100149.002103.

Munafò, Marcus R., Brian A. Nosek, Dorothy V. M. Bishop, Katherine S. Button, Christopher D. Chambers, Nathalie Percie du Sert, Uri Simonsohn, Eric-Jan Wagenmakers, Jennifer J. Ware, and John P. A. Ioannidis. 2017. "A Manifesto for Reproducible Science." *Nature Human Behaviour* 1 (1): 0021. https://doi.org/10.1038/s41562-016-0021.

Murphy, James T., Ray Walshe, and Marc Devocelle. 2008. "A Computational Model of Antibiotic-Resistance Mechanisms in Methicillin-Resistant Staphylococcus Aureus (MRSA)." *Journal of Theoretical Biology* 254 (2): 284–93. https://doi.org/10.1016/j.jtbi.2008.05.037.

Naas, Thierry, Saoussen Oueslati, Rémy A. Bonnin, Maria Laura Dabos, Agustin Zavala, Laurent Dortet, Pascal Retailleau, and Bogdan I. Iorga. 2017. "Beta-Lactamase Database (BLDB) – Structure and Function." *Journal of Enzyme Inhibition and Medicinal Chemistry* 32 (1): 917–19. https://doi.org/10.1080/14756366.2017.1344235.

Navarro Llorens, Juana María, Antonio Tormo, and Esteban Martínez-García. 2010. "Stationary Phase in Gram-Negative

Bacteria." *FEMS Microbiology Reviews* 34 (4): 476–95. https://doi.org/10.1111/j.1574-6976.2010.00213.x.

Neidhardt, Frederick C. 1999. "Bacterial Growth: Constant Obsession with dN/Dt." *Journal of Bacteriology* 181 (24): 7405–8. https://www.ncbi.nlm.nih.gov/pmc/articles/PMC94194/.

Nitanai, Yasushi, Tatsuro Shimamura, Takuro Uchiyama, Yoshikazu Ishii, Michiyo Takehira, Katsuhide Yutani, Hiroshi Matsuzawa, and Masashi Miyano. 2010. "The Catalytic Efficiency (Kcat/Km) of the Class A β-Lactamase Toho-1 Correlates with the Thermal Stability of Its Catalytic Intermediate Analog." *Biochimica Et Biophysica Acta (BBA) - Proteins and Proteomics* 1804 (4): 684–91. https://doi.org/10.1016/j.bbapap.2009.10.023.

Page, M. G. P. 2008. "Extended-Spectrum β-Lactamases: Structure and Kinetic Mechanism." *Clinical Microbiology and Infection* 14 (January): 63–74. https://doi.org/10.1111/j.1469-0691.2007.01863.x.

Palzkill, Timothy. 2018. "Structural and Mechanistic Basis for Extended-Spectrum Drug-Resistance Mutations in Altering the Specificity of TEM, CTX-M, and KPC β-Lactamases." *Frontiers in Molecular Biosciences* 5 (February): 16. https://doi.org/10.3389/fmolb.2018.00016.

Pamphilon, Derwood, Eileen Selogie, David McKenna, Jose A. Cancelas-Peres, Zbigniew M. Szczepiorkowski, Ron Sacher, John McMannis, et al. 2013. "Current Practices and Prospects for Standardization of the Hematopoietic Colony-Forming Unit Assay: A Report by the Cellular Therapy Team of the Biomedical Excellence for Safer Transfusion (BEST) Collaborative." *Cytotherapy* 15 (3): 255–62. https://doi.org/10.1016/j.jcyt.2012.11.013.

Pasteur, Louis (1822-1895) Auteur du texte. 1922–1939. *Oeuvres de Pasteur. Tome 2 / Réunies Par Pasteur Vallery-Radot,...* https://gallica.bnf.fr/ark:/12148/bpt6k7357p.

Paterson, David L., and Robert A. Bonomo. 2005. "Extended-Spectrum β-Lactamases: A Clinical Update." *Clinical Microbiology Reviews* 18 (4): 657–86. https://doi.org/10.1128/CMR.18.4.657-686.2005.

Patiño-Navarrete, Rafael, Isabelle Rosinski-Chupin, Nicolas Cabanel, Lauraine Gauthier, Julie Takissian, Jean-Yves Madec, Monzer Hamze, Remy A. Bonnin, Thierry Naas, and Philippe Glaser. 2020. "Stepwise Evolution and Convergent Recombination Underlie the Global Dissemination of Carbapenemase-

Producing Escherichia Coli." *Genome Medicine* 12 (1): 10. https://doi.org/10.1186/s13073-019-0699-6.

Patterson, Manford K. 1979. "Measurement of Growth and Viability of Cells in Culture." In *Methods in Enzymology*, 58:141–52. Cell Culture. Academic Press. https://doi.org/10.1016/S0076-6879(79)58132-4.

Petzold, Linda. 1983. "Automatic Selection of Methods for Solving Stiff and Nonstiff Systems of Ordinary Differential Equations." *SIAM Journal on Scientific and Statistical Computing* 4 (1): 136–48. https://doi.org/10.1137/0904010.

Pérez-Llarena, Francisco José, Frédéric Kerff, Olga Abián, Susana Mallo, María Carmen Fernández, Moreno Galleni, Javier Sancho, and Germán Bou. 2011. "Distant and New Mutations in CTX-M-1 β-Lactamase Affect Cefotaxime Hydrolysis." *Antimicrobial Agents and Chemotherapy* 55 (9): 4361–68. https://doi.org/10.1128/AAC.00298-11.

Phelps, Earle B. 1908. "A Method of Calculating the Numbers of B. Coli from the Results of Dilution Tests." *American Journal of Public Hygiene* 18 (2): 141–45. https://www.ncbi.nlm.nih.gov/pmc/articles/PMC2543481/.

Pienaar, Elsje, Scott E. Whitney, Hendrik J. Viljoen, and Nicolaas F. J. van Rensburg. 2009. "A Model of the Complex Response of Staphylococcus Aureus to Methicillin." *Journal of Theoretical Biology* 257 (3): 438–45. https://doi.org/10.1016/j.jtbi.2008.12.003.

Pletnev, P., I. Osterman, P. Sergiev, A. Bogdanov, O. Dontsova, Moscow State University, Chemistry Department, Moscow, 119991, Russia, A. Bogdanov, Moscow State University, Chemistry Department, Moscow, 119991, Russia, O. Dontsova, and Moscow State University, Chemistry Department, Moscow, 119991, Russia. 2015. "Survival Guide: Escherichia Coli in the Stationary Phase." *Acta Naturae* 7 (4): 22–33. https://doi.org/10.32607/20758251-2015-7-4-22-33.

Potron, Anaïs, Emilie Rondinaud, Laurent Poirel, Olivier Belmonte, Sophie Boyer, Sabine Camiade, and Patrice Nordmann. 2013. "Genetic and Biochemical Characterisation of OXA-232, a Carbapenem-Hydrolysing Class D β-Lactamase from Enterobacteriaceae." *International Journal of Antimicrobial Agents* 41 (4): 325–29. https://doi.org/10.1016/j.ijantimicag.2012.11.007.

PyUSB (version 1.0). 2020. https://github.com/pyusb/pyusb.

Raue, A., C. Kreutz, T. Maiwald, J. Bachmann, M. Schilling, U. Klingmüller, and J. Timmer. 2009. "Structural and Prac-

tical Identifiability Analysis of Partially Observed Dynamical Models by Exploiting the Profile Likelihood." *Bioinformatics* 25 (15): 1923–29. https://doi.org/10.1093/bioinformatics/btp358.

Raue, Andreas, Marcel Schilling, Julie Bachmann, Andrew Matteson, Max Schelke, Daniel Kaschek, Sabine Hug, et al. 2013. "Lessons Learned from Quantitative Dynamical Modeling in Systems Biology." *PLOS ONE* 8 (9): e74335. https://doi.org/10.1371/journal.pone.0074335.

Rolinson, G. N. 1980. "Effect of β-Lactam Antibiotics on Bacterial Cell Growth Rate." *Journal of General Microbiology* 120 (2): 317–23. https://doi.org/10.1099/00221287-120-2-317.

Roser, Max, Hannah Ritchie, and Esteban Ortiz-Ospina. 2013. "World Population Growth." *Our World in Data*, May. https://ourworldindata.org/world-population-growth.

Salas, Jessica R., Majid Jaberi-Douraki, Xuesong Wen, and Victoriya V. Volkova. 2020. "Mathematical Modeling of the 'Inoculum Effect': Six Applicable Models and the MIC Advancement Point Concept." *FEMS Microbiology Letters* 367 (5). https://doi.org/10.1093/femsle/fnaa012.

Salvatier, John, Thomas V. Wiecki, and Christopher Fonnesbeck. 2016. "Probabilistic Programming in Python Using PyMC3." *PeerJ Computer Science* 2 (April): e55. https://doi.org/10.7717/peerj-cs.55.

Sauvage, Eric, Frédéric Kerff, Mohammed Terrak, Juan A. Ayala, and Paulette Charlier. 2008. "The Penicillin-Binding Proteins: Structure and Role in Peptidoglycan Biosynthesis." *FEMS Microbiology Reviews* 32 (2): 234–58. https://doi.org/10.1111/j.1574-6976.2008.00105.x.

Savard, Patrice, and Trish M. Perl. 2012. "A Call for Action: Managing the Emergence of Multidrug-Resistant Enterobacteriaceae in the Acute Care Settings." *Current Opinion in Infectious Diseases* 25 (4): 371–77. https://doi.org/10.1097/QCO.0b013e3283558c17.

Senn, Heinrich, Urs Lendenmann, Mario Snozzi, Geoffrey Hamer, and Thomas Egli. 1994. "The Growth of Escherichia Coli in Glucose-Limited Chemostat Cultures: A Re-Examination of the Kinetics." *Biochimica Et Biophysica Acta (BBA) - General Subjects* 1201 (3): 424–36. https://doi.org/10.1016/0304-4165(94)90072-8.

Serres, Margrethe H., Shuba Gopal, Laila A. Nahum, Ping Liang, Terry Gaasterland, and Monica Riley. 2001. "A Functional Update of the Escherichia Coli K-12 Genome." *Genome*

Biology 2 (9): research0035.1. https://doi.org/10.1186/gb-2001-2-9-research0035.

Sezonov, G., D. Joseleau-Petit, and R. D'Ari. 2007. "Escherichia Coli Physiology in Luria-Bertani Broth." *Journal of Bacteriology* 189 (23): 8746–49. https://doi.org/10.1128/JB.01368-07.

Shallue, Christopher J., and Andrew Vanderburg. 2018. "Identifying Exoplanets with Deep Learning: A Five-Planet Resonant Chain Around Kepler-80 and an Eighth Planet Around Kepler-90." *The Astronomical Journal* 155 (2): 94. https://doi.org/10.3847/1538-3881/aa9e09.

Shen, Zhen, Baixing Ding, Yingmin Bi, Shi Wu, Su Xu, Xiaogang Xu, Qinglan Guo, and Minggui Wang. 2017. "CTX-M-190, a Novel β-Lactamase Resistant to Tazobactam and Sulbactam, Identified in an Escherichia Coli Clinical Isolate." *Antimicrobial Agents and Chemotherapy* 61 (1). https://doi.org/10.1128/AAC.01848-16.

Spratt, B. G. 1975. "Distinct Penicillin Binding Proteins Involved in the Division, Elongation, and Shape of Escherichia Coli K12." *Proceedings of the National Academy of Sciences* 72 (8): 2999–3003. https://doi.org/10.1073/pnas.72.8.2999.

Srimani, Jaydeep K., Shuqiang Huang, Allison J. Lopatkin, and Lingchong You. 2017. "Drug Detoxification Dynamics Explain the Postantibiotic Effect." *Molecular Systems Biology* 13 (10): 948. https://doi.org/10.15252/msb.20177723.

Stevenson, Keiran, Alexander F. McVey, Ivan B. N. Clark, Peter S. Swain, and Teuta Pilizota. 2016. "General Calibration of Microbial Growth in Microplate Readers." *Scientific Reports* 6 (December): 38828. https://doi.org/10.1038/srep38828.

"Tackling Drug-Resistant Infections Globally: Final Report and Recommendations." 2016. https://amr-review.org/sites/default/files/160525_Final%20paper_with%20cover.pdf.

Takahasi, K., S. Ishida, and M. Kurokawa. 1964. "Statistical Considerations on Sampling Errors in Total Bacterial Cell Count." *Japanese Journal of Medical Science & Biology* 17 (June): 73–86. https://doi.org/10.7883/yoken1952.17.73.

Tanouchi, Yu, Anand Pai, Heungwon Park, Shuqiang Huang, Nicolas E. Buchler, and Lingchong You. 2017. "Long-Term Growth Data of Escherichia Coli at a Single-Cell Level." *Scientific Data* 4 (1): 1–5. https://doi.org/10.1038/sdata.2017.36.

Tooke, Catherine L., Philip Hinchliffe, Eilis C. Bragginton, Charlotte K. Colenso, Viivi H. A. Hirvonen, Yuiko Takebayashi,

and James Spencer. 2019. "β-Lactamases and β-Lactamase Inhibitors in the 21st Century." *Journal of Molecular Biology* 431 (18): 3472–3500. https://doi.org/10.1016/j.jmb.2019.04.002.

Transcriptic. n.d. "Powering On-Demand Biology." Transcriptic. Accessed August 30, 2020. https://transcriptic.com/.

Tsao, George T., and Thor P. Hanson. 1975. "Extended Monod Equation for Batch Cultures with Multiple Exponential Phases." *Biotechnology and Bioengineering* 17 (11): 1591–98. https://doi.org/10.1002/bit.260171104.

Tuomanen, E., R. Cozens, W. Tosch, O. Zak, and A. Tomasz. 1986. "The Rate of Killing of Escherichia Coli by β-Lactam Antibiotics Is Strictly Proportional to the Rate of Bacterial Growth." *Journal of General Microbiology* 132 (5): 1297–1304. https://doi.org/10.1099/00221287-132-5-1297.

Tuomanen, Elaine. 1986. "Phenotypic Tolerance: The Search for β-Lactam Antibiotics That Kill Nongrowing Bacteria." *Reviews of Infectious Diseases* 8 Suppl 3 (July): S279–291. https://doi.org/10.1093/clinids/8.supplement_3.s279.

Vega, Nicole M, and Jeff Gore. 2014. "Collective Antibiotic Resistance: Mechanisms and Implications." *Current Opinion in Microbiology*, Antimicrobials, 21 (October): 28–34. https://doi.org/10.1016/j.mib.2014.09.003.

Vigouroux, Antoine, Baptiste Cordier, Andrey Aristov, Laura Alvarez, Gizem Özbaykal, Thibault Chaze, Enno Rainer Oldewurtel, et al. 2020. "Class-A Penicillin Binding Proteins Do Not Contribute to Cell Shape but Repair Cell-Wall Defects." Edited by Anna Akhmanova, Jie Xiao, Jie Xiao, and Tobias Dörr. *eLife* 9 (January): e51998. https://doi.org/10.7554/eLife.51998.

Wang, C. Houston, and Arthur L. Koch. 1978. "Constancy of Growth on Simple and Complex Media." *Journal of Bacteriology* 136 (3): 969–75. https://doi.org/10.1128/JB.136.3.969-975.1978.

Wang, Jue D., and Petra A. Levin. 2009. "Metabolism, Cell Growth and the Bacterial Cell Cycle." *Nature Reviews Microbiology* 7 (11): 822–27. https://doi.org/10.1038/nrmicro2202.

Wang, Ping, Lydia Robert, James Pelletier, Wei Lien Dang, Francois Taddei, Andrew Wright, and Suckjoon Jun. 2010. "Robust Growth of Escherichia Coli." *Current Biology* 20 (12): 1099–1103. https://doi.org/10.1016/j.cub.2010.04.045.

Wanner, Ursula, and Thomas Egli. 1990. "Dynamics of Microbial Growth and Cell Composition in Batch Culture." *FEMS Mi-*

crobiology Letters 75 (1): 19–43. https://doi.org/10.1016/0378-1097(90)90521-Q.

Wehrens, Martijn, Dmitry Ershov, Rutger Rozendaal, Noreen Walker, Daniel Schultz, Roy Kishony, Petra Anne Levin, and Sander J. Tans. 2018. "Size Laws and Division Ring Dynamics in Filamentous Escherichia Coli Cells." *Current Biology* 28 (6): 972–979.e5. https://doi.org/10.1016/j.cub.2018.02.006.

WHO. 2019a. *Critically Important Antimicrobials for Human Medicine*. 6th revision. https://www.who.int/foodsafety/publications/antimicrobials-sixth/en/.

———. 2019b. "Report of the 22nd WHO Expert Committee on the Selection and Use of Essential Medicines." WHO Headquarters, Geneva. https://apps.who.int/iris/bitstream/handle/10665/325773/WHO-MVP-EMP-IAU-2019.05-eng.pdf.

Wilks, S. S. 1938. "The Large-Sample Distribution of the Likelihood Ratio for Testing Composite Hypotheses." *Annals of Mathematical Statistics* 9 (1): 60–62. https://doi.org/10.1214/aoms/1177732360.

Windels, Etthel M., Zacchari Ben Meriem, Taiyeb Zahir, Kevin J. Verstrepen, Pascal Hersen, Bram Van den Bergh, and Jan Michiels. 2019. "Enrichment of Persisters Enabled by a SS-Lactam-Induced Filamentation Method Reveals Their Stochastic Single-Cell Awakenin." *Communications Biology* 2 (1, 1). https://doi.org/10.1038/s42003-019-0672-3.

Wistrand-Yuen, Erik, Michael Knopp, Karin Hjort, Sanna Koskiniemi, Otto G. Berg, and Dan I. Andersson. 2018. "Evolution of High-Level Resistance During Low-Level Antibiotic Exposure." *Nature Communications* 9 (April). https://doi.org/10.1038/s41467-018-04059-1.

Wood, Thomas K., Stephen J. Knabel, and Brian W. Kwan. 2013. "Bacterial Persister Cell Formation and Dormancy." *Applied and Environmental Microbiology* 79 (23): 7116–21. https://doi.org/10.1128/AEM.02636-13.

Wu, Siva, Xiaojin Li, Manjula Gunawardana, Kathleen Maguire, Debbie Guerrero-Given, Christoph Schaudinn, Charles Wang, Marc M. Baum, and Paul Webster. 2014. "β-Lactam Antibiotics Stimulate Biofilm Formation in Non-Typeable Haemophilus Influenzae by Up-Regulating Carbohydrate Metabolism." *PLOS ONE* 9 (7): e99204. https://doi.org/10.1371/journal.pone.0099204.

Wyant, Zae Northrup. 1921. "A Comparison of the Technic Recommended by Various Authors for Quantitative Bacteri-

ological Analysis of Soil." *Soil Science* 11 (April): 295–304. https://doi.org/10.1097/00010694-192104000-00005.

Yang, Desirée C., Kris M. Blair, and Nina R. Salama. 2016. "Staying in Shape: The Impact of Cell Shape on Bacterial Survival in Diverse Environments." *Microbiology and Molecular Biology Reviews: MMBR* 80 (1): 187–203. https://doi.org/10.1128/MMBR.00031-15.

Yao, Zhizhong, Daniel Kahne, and Roy Kishony. 2012. "Distinct Single-Cell Morphological Dynamics Under β-Lactam Antibiotics." *Molecular Cell* 48 (5): 705–12. https://doi.org/10.1016/j.molcel.2012.09.016.

Zahir, Taiyeb, Dorien Wilmaerts, Sabine Franke, Bram Weytjens, Rafael Camacho, Kathleen Marchal, Johan Hofkens, Maarten Fauvart, and Jan Michiels. 2020. "Image-Based Dynamic Phenotyping Reveals Genetic Determinants of Filamentation-Mediated β-Lactam Tolerance." *Frontiers in Microbiology* 11. https://doi.org/10.3389/fmicb.2020.00374.

Zwietering, M. H., I. Jongenburger, F. M. Rombouts, and K. van 't Riet. 1990. "Modeling of the Bacterial Growth Curve." *Applied and Environmental Microbiology* 56 (6): 1875–81. https://www.ncbi.nlm.nih.gov/pmc/articles/PMC184525/.

A DILUTION ERROR IN LIKELIHOOD

In section 4.1.1, we described a noise model consistent with the experimental data. Besides the measurement noise, the main source of day-to-day variability is the dilution noise due to the handling of micropipettes. This dilution error can be modelled by a 5 % multiplicative gaussian noise on the initial optical density, and antibiotic concentration. Figure A.1, reproduced here from the main text, shows the two sources of noise.

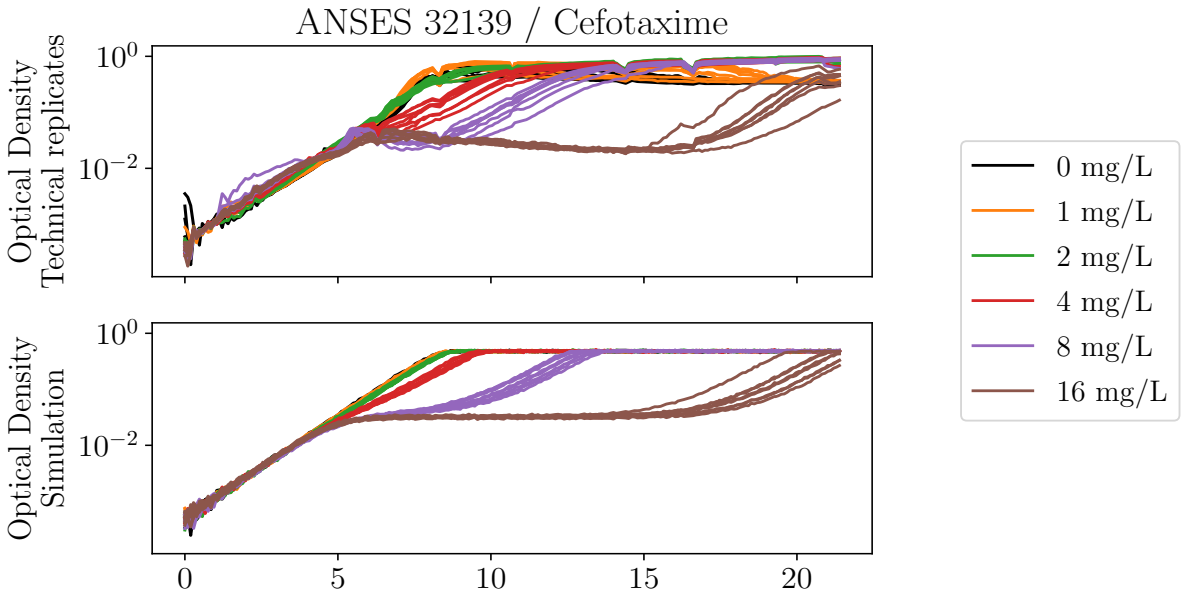

Figure A.1: Top: technical replicates, bottom: simulation of the experiment. The noise model on the simulation consists of a 2 % multiplicative gaussian noise on the OD, and 5 % on the initial values of a and N.

The strategy for the parameter estimations was to neglect the dilution noise; however this noise can influence the regrowth time of a replicate to up to 20 %. The purpose of this section is to explain how this dilution error could be taken into account in the likelihood function.

We will assume that we are estimating the parameters of the model based on the data, OD and number of cells, from several

experiments, with L different initial antibiotic doses and M different initial ODs.

The noise model described in 4.1.1 specifies that the actual values of a_0 and N_0, $\hat{a}_0$ and $\hat{N}_0$, are linked with the desired values a_0 and N_0 by the equations $\hat{a}_0 = a_0(1 + \sigma x)$ and $\hat{N}_0 = N_0(1 + \sigma y)$, with x and y two random values, specific to each experiment, and distributed according to a standard normal distribution.

A.1 ADDING VARIABLES

The first straightforward approach is to estimate the noise at the same time as the model parameters. For this, each experiment adds its two variables x_{lm} and y_{lm} to the set of parameters to be estimated. To specify that x_{lm} and y_{lm} should be distributed on a standard normal distribution, one should just append each of them to the existing array of residuals to be minimized.

For two initial ODs and 12 initial antibiotic conditions, this methods amounts to adding 48 variables to the 17 of the model. A non-linear optimization problem of this size is at the edge of the possible, in the best case. Given the relative difficulty of already estimating 17 parameters, this does not seem a reasonable approach.

A.2 DIRECT LIKELIHOOD ESTIMATION

Another approach does not require to add parameters. Here, for a given set of parameters of the model θ, we want to estimate the likelihood $\mathcal{L}(\theta)$:

$$\begin{aligned}\mathcal{L}(\theta) &= f(\text{data}|\theta) \\ &= \prod_{lm} f(\text{data}_{lm}|\theta) \\ &= \frac{1}{2\pi}\prod_{lm}\iint f(\text{data}_{lm}|\theta, x_{lm}, y_{lm})\mathrm{e}^{-\frac{x_{lm}{}^2}{2}}\mathrm{e}^{-\frac{y_{lm}{}^2}{2}}\mathrm{d}x_{lm}\mathrm{d}y_{lm}\end{aligned}$$

where $f(data_{lm}|\theta, x_{lm}, y_{lm})$ is the density probability to observe the data of the experiment lm with the initial antibiotic dose

specified by x_{lm} and the initial OD given by y_{lm}, according to equation 4.1. We can continue the derivation

$$\begin{aligned}\mathcal{L}(\theta) &= \frac{1}{\sqrt{2\,\pi}^{N+2}} \prod_{lm} \iint \prod_{i} \frac{1}{\sigma_{lmi}} \mathrm{e}^{-\frac{(\mathrm{model}_{\theta,x_{lm},y_{lm}}(t_i)-\mathrm{data}_{lmi})^2}{2\,{\sigma_{lmi}}^2}} \mathrm{e}^{-\frac{{x_{lm}}^2}{2}} \mathrm{e}^{-\frac{{y_{lm}}^2}{2}} \mathrm{d}x_{lm}\mathrm{d}y_{lm} \\ &= \frac{1}{\sqrt{2\,\pi}^{N+2} \prod_{lmi} \sigma_{lmi}} \prod_{lm} \iint \mathrm{e}^{-\sum_i \frac{(\mathrm{model}_{\theta,x_{lm},y_{lm}}(t_i)-\mathrm{data}_{lmi})^2}{2\,{\sigma_{lmi}}^2} - \frac{{x_{lm}}^2}{2} - \frac{{y_{lm}}^2}{2}} \mathrm{d}x_{lm}\mathrm{d}y_{lm} \\ &= \frac{1}{\sqrt{2\,\pi}^{N+2} \prod_{lmi} \sigma_{lmi}} \prod_{lm} \iint \mathrm{e}^{-g_{\theta lm}(x_{lm},y_{lm})} \mathrm{d}x_{lm}\mathrm{d}y_{lm}\end{aligned}$$

where $g_{\theta lm}(x_{lm}, y_{lm}) = \sum_i \frac{(\mathrm{model}_{\theta,x_{lm},y_{lm}}(t_i) - \mathrm{data}_{lmi})^2}{2\,{\sigma_{lmi}}^2} + \frac{{x_{lm}}^2}{2} + \frac{{y_{lm}}^2}{2}$

The log-likelihood of this function is then the following:

$$\log \mathcal{L}(\theta) = cst + \sum_{lm} \log \iint \mathrm{e}^{-g_{\theta lm}(x_{lm},y_{lm})} \mathrm{d}x_{lm}\mathrm{d}y_{lm}$$

With a fixed θ, each integral is independent and can then be computed independently, by integrating on the pair of variables x_{lm} and y_{lm}. However, the integrals should be done on the infinite plane, and the exponential in the integrand can pose numerical stability issues, so we need a more direct method to compute these integrals.

The saddlepoint approximation allows to approximate an infinite integral based on the information around a unique point!

A classical method to integrate exponentials is the saddlepoint approximation (Daniels 1954). Because of the fast decrease of the exponential, the whole integral is dominated by the point where $g_{\theta lm}$ is minimal. In two dimensions, if $x^*_{\theta lm}$, $y^*_{\theta lm}$ are the coordinates of the point where $g_{\theta lm}$ takes its minimum, and $H_{\theta lm}$ is the hessian of $g_{\theta lm}$ on that point, then

$$\iint \mathrm{e}^{-g_{\theta lm}(x_{lm},y_{lm})} \mathrm{d}x_{lm}\mathrm{d}y_{lm} = \mathrm{e}^{-g_{\theta lm}(x^*_{\theta lm},y^*_{\theta lm})} \frac{2\,\pi}{\sqrt{|H_{\theta lm}|}}$$

So we can write

$$\log \mathcal{L}(\theta) = cst - \sum_{lm} g_{\theta lm}(x^*_{\theta lm}, y^*_{\theta lm}) - \frac{1}{2} \sum_{lm} \log |H_{\theta lm}|$$

This means that to compute the log-likelihood of a set of parameters of the model, we need to know in what point each of the $g_{\theta lm}$ reach their minimum, and their hessian. These 2-dimensional optimization problems can be efficiently solved with non-linear least squares solvers, that can also return the hessian at the minimum, since they typically estimate this matrix during the optimization.

However, these albeit short 2D optimizations should be done for each parameter set, which multiplies the number of integrations of the ODE system by a factor between 20 and 100. However, they can be done in parallel, so on a 12-core computer, the overhead of this method compared to the one that we used, can be brought back to an order of magnitude only. Because of time constraints, the optimization and parallelization of the code necessary to make this method feasible could not be done, and we did not attempt to estimate parameters with this likelihood.

B CHARACTERISTICS OF STRAINS

The strains used in this work and described in section 5.1.1 have been sequenced as part of another study (Patiño-Navarrete et al. 2020), hence their full genetic information is available and all antibiotic-related genes and mutations are known.

The β-lactamases have been enumerated in section 5.1.1, but the strains also exhibit several other mutations and genes modifying their antibiotic susceptibility. For completeness, the full information is detailed here.

ftsI is the gene coding for PBP3. In these tables, it can have three possible states: "none," indicating wild type, "YRIN_349-532," indicating a mutation, and "YRIK," indicating a mutation occuring over "YRIN_349-532" and conferring an even reduced susceptibility of PBP3 to β-lactams.

ompC and ompF respectively code for a precursor of the outer membrane porins C and F. Their mutations can play a role on antibiotic susceptibility because they might prevent the entrance of antibiotic molecules in the cell.

gyrA and parC are genes coding for a DNA gyrase and topoisomerase, enzymes that participate in the winding and unwinding of DNA. These mutations are not involved in the resistance to β-lactams, but rather to fluoroquinolones.

- IB31 / ANSES 28668
  - carbapenemases: none
  - β-lactamases: CTX-M-1, TEM-1A
  - other genes contributing to antibiotic susceptibility: aadA5, aadA1, mph(B), sul2, dfrA1, sul1, dfrA17, tet(A), tet(M)
  - mutations contributing to antibiotic susceptibility:

ftsI	ompC	ompF	gyrA	parC
none	none	none	S83L/D87N	S80I

- IB32 / ANSES 32139

  - carbapenemases: OXA-1
  - β-lactamases: CTX-M-15, TEM-1B
  - other genes contributing to antibiotic susceptibility: aac(6')Ib-cr; dfrA17; sul2; aadA5; aac(3)-IId; strA; sul1; strB; tet(B); mph(A)
  - mutations contributing to antibiotic susceptibility:

ftsI	ompC	ompF	gyrA	parC
none	none	none	S83L/D87N	S80I

- IB34 / ANSES 29401
  - carbapenemases: none
  - β-lactamases: TEM-1B
  - other genes contributing to antibiotic susceptibility: strB; sul2; aph(3')-Ia; strA; tet(A)
  - mutations contributing to antibiotic susceptibility:

ftsI	ompC	ompF	gyrA	parC
none	none	none	none	none

- IB35 / ANSES 30599
  - carbapenemases: none
  - β-lactamases: TEM-1B
  - other genes contributing to antibiotic susceptibility: aph(3')-Ia; sul2; strA; strB; tet(A)
  - mutations contributing to antibiotic susceptibility:

ftsI	ompC	ompF	gyrA	parC
none	none	none	none	none

- IB37 / CNR 49A5
  - carbapenemases: NDM-5, OXA-1
  - β-lactamases: CTX-M-15, TEM-1B, CMY-42
  - other genes contributing to antibiotic susceptibility: aadA2; dfrA17; aac(6')Ib-cr; tet(A); erm(B); strA; tet(B); sul1; sul2; aadA5; strB; mph(A); qepA; dfrA12

  - mutations contributing to antibiotic susceptibility:

ftsI	ompC	ompF	gyrA	parC
YRIK	none	none	S83L/D87N	S80I/E84

- IB38 / CNR 94G8
  - carbapenemases: OXA-181
  - β-lactamases: CTX-M-15, CMY-42
  - other genes contributing to antibiotic susceptibility: QnrS1; sul2; mph(A); tet(A); sul1; aadA5; dfrA17
  - mutations contributing to antibiotic susceptibility:

ftsI	ompC	ompF	gyrA	parC
YRIK	none	none	S83L/D87N	S80I/E84

- IB39 / CNR 82A2
  - carbapenemases: OXA-1, OXA-181
  - β-lactamases: CTX-M-55, CMY-2
  - other genes contributing to antibiotic susceptibility: strB; QnrS1; catA2; aac(6')Ib-cr; mph(A); sul2; aac(3)-IId; tet(B); strA
  - mutations contributing to antibiotic susceptibility:

ftsI	ompC	ompF	gyrA	parC
YRIN_349-532	R195L	-46; C->T (OmpR F3)	S83L/D87N	S80I/E84

- IB310 / CNR 84G4
  - carbapenemases: OXA-1, OXA-181
  - β-lactamases: TEM-1B, CMY-2, CTX-M-55
  - other genes contributing to antibiotic susceptibility: QnrS1; catA2; dfrA17; mph(A); aac(6')Ib-cr; sul2; aadA5; aac(3)-IId; strA; sul1; strB; tet(B)
  - mutations contributing to antibiotic susceptibility:

ftsI	ompC	ompF	gyrA	parC
YRIN_349-532	R195L	-46; C->T (OmpR F3)	S83L/D87N	S80I/E84

- IB311 / CNR 92B5
  - carbapenemases: OXA-181
  - β-lactamases: TEM-1B, CMY-2
  - other genes contributing to antibiotic susceptibility: QnrS1; tet(B); dfrA17; mph(A); sul2; aadA5; aac(3)-IId; strA; sul1; strB
  - mutations contributing to antibiotic susceptibility:

ftsI	ompC	ompF	gyrA	parC
YRIN_349-532	R195L	-46; C->T (OmpR F3)	S83L/D87N	S80I/E84

Si tu vas à Paris,
Dis bonjour aux amis.
Dis bonjour à la Seine,
Au bois de Vincennes.
Va revoir ma chambre, sous les toits,
D'où l'on voit les étoiles.
Porte à tous de bonnes nouvelles de moi,
Dis-leur : « Il reviendra. »
Pose-toi dans le ciel,
En haut de la tour Eiffel,
Au printemps qui sourit,
Et chante avec tous les oiseaux de Paris.

— Charles Trénet, *Les Oiseaux de Paris*

DOCTORAL SCHOOL

Titre : Modélisation et caractérisation efficace de la réponse bactérienne aux antibiotiques

Mots clés : résistance aux antibiotiques, tolérance par filamentation, modèle de croissance-fragmentation, identifiabilité de paramètres, *E. coli*, β-lactames

Résumé : La résistance aux antibiotiques est connue comme l'un des plus grands dangers de santé publique. Dans les hôpitaux, la susceptibilité d'une souche à un antibiotique est quantifiée par sa Concentration Minimale Inhibitrice (CMI) : la dose minimale d'antibiotique nécessaire pour inhiber la croissance de la souche pendant 24 heures. Cette valeur joue un rôle central dans les décisions de traitements. Or, la CMI est une mesure reposant sur un unique point de temps. Pourrait-on obtenir une évaluation plus informative de la résistance d'une souche, en exploitant sa courbe de croissance entière, observée par densité optique (DO) ? Cette donnée pourrait être disponible dans un contexte clinique, ce qui est nécessaire pour la pertinence de l'approche. Le problème est complexe, notamment parce que les antibiotiques β-lactames provoquent la filamentation des cellules, ce qui décorrèle la DO du nombre de cellules vivantes.

Dans cette thèse, nous développons un modèle mathématique de la réponse de populations bactériennes à des β-lactames, qui rassemble les différents types de résistance. Unifiant les échelles moléculaire, de la cellule et de la population, ce modèle offre des prédictions simultanées de la DO et du nombre de cellules. Son cœur est un modèle de croissance-fragmentation : une équation aux dérivées partielles considérant explicitement la distribution des tailles des cellules. Or, le modèle à EDP n'est pas idéal pour l'optimisation numérique, et notamment pour l'inférence de paramètres. Nous décrivons donc le passage à un modèle compagnon à équations différentielles ordinaires, pour une calibration efficace. Après calibration de ce modèle sur un ensemble d'isolats cliniques à l'aide d'un pilote sur mesure permettant l'automatisation d'un lecteur de plaques, nous montrons que nous pouvons relier plusieurs paramètres du modèle aux gènes et mutations contribuant à la résistance des souches aux antibiotiques. Nous proposons ensuite une méthode permettant de catégoriser les souches, en dépit de la présence de paramètres non identifiables, et observons l'émergence de trois classes : les souches sensibles, les souches tolérantes et résilientes, et les résistantes. En comparaison avec le système classique définissant les souches susceptibles, intermédiaire, et résistantes, ces classes fournissent une explication plus riche du comportement des isolats, et offrent un débouché direct sur l'optimisation de traitements.

Title : Modelling and Efficient Characterization of Enzyme-Mediated Response to Antibiotic Treatments

Keywords : antibiotic resistance, tolerance by filamentation, growth-fragmentation model, parameter identifiability, *E. coli*, β-lactams

Abstract : Antibiotic resistance is widely recognized as one of the biggest threats to global health.

In hospitals, the susceptibility of a strain to an antibiotic is quantified by its Minimum Inhibitory Concentration (MIC): the minimal concentration of antibiotic necessary to inhibit the growth of the strain during 24 hours. This value plays a central role for treatment decisions.

However, the MIC is a measure relying on a unique timepoint. Could we get a more informative assessment of antibiotic resistance by exploiting the whole growth curve, observed by optical density? This information could be available in a clinical context, which is a requirement of the approach. The problem is complex, notably because β-lactam antibiotics induce cell filamentation, which decorrelates the optical density from the number of live cells.

In this thesis, we build a mathematical model of the response of bacterial populations to β-lactams, encompassing the different kinds of antibiotic resistance under a unifying framework. Bridging the three scales: molecular-, cell-, and population-level, this model provides simultaneous predictions of the optical density and the number of cells. Its core is a growth-fragmentation equation: a partial differential equation that considers explicitly the distribution of cell lengths. The PDE model is not very practical for numerical optimization, notably for parameter inference. Therefore, we describe the passage to a companion ODE model for efficient calibration.

After calibrating this model on a library of clinical isolates with the help of a custom driver allowing the programmable use of a commercial plate reader, we show that we can relate several parameters to the antibiotic resistance genes and mutations present in the strains. We then propose a method to cluster the strains despite the presence of unidentifiable parameters, and show that three classes emerge: sensitive, tolerant/resilient, and resistant strains. In comparison with the classical system susceptible, intermediate, and resistant, these classes provide a richer explanation of the behaviour of the isolates, and allow a direct exploitation for treatment optimization.

Institut Polytechnique de Paris
91120 Palaiseau, France